DEPARTAMENTO DE ASTROFISICA

Stellar chemo-kinematics of isolated Local Group dwarf galaxies

A thesis submitted by
Salvatore Taibi
in fulfillment of the requirements for the degree of
Doctor of Philosophy in Astrophysics
at the Universidad de La Laguna

Supervisor: Dr. Giuseppina Battaglia
Tutor: Dr. Carme Gallart

INSTITUTO Đ ASTROFISICA Đ CANARIAS
Septiembre de 2020

BATTAGLIA GIUSEPPINA - Y3480619C
Digitally signed by BATTAGLIA GIUSEPPINA - Y3480619C
Date: 2020.09.03 18:28:26 +01'00'

A mio Nonno

Abstract

The study of dwarf galaxies is of great importance to understand galaxy formation and evolution on the smallest mass scales. According to the current cosmological paradigm, galaxies grows hierarchically from the accretion of smaller systems. The dwarf galaxies that we observe today are therefore a living record of the building blocks that drove the formation of larger galactic systems. Being the first galaxies to be formed, they may provide information about the nature of dark matter, the formation of first stars and the era of reionization.

In the Local Group, our galactic neighbourhood, dwarf galaxies can be studied in great details. Apparently simple, these systems have actually proven to cover a variety of properties, be them kinematic, chemical, and structural. They also span a wide range in stellar masses, inhabit different environments, and show complex star formation histories.

There are currently almost a hundred dwarf galaxies known to be part of the Local Group, more than half of which have been discovered in the last two decades only. The majority of these systems are gas-poor spheroidals usually found as satellites of the largest spirals, namely the Milky Way and M31, while the rest are gas-richer systems, typically found in the field. Due to their small masses, the formation and evolution of dwarf galaxies could be strongly influenced by internal and environmental effects. In particular, the evolution of satellite dwarfs have been probably influenced by their host galaxy. The isolated systems then, having spent much of their time in a more benign environment, offer a valuable opportunity to better understand what are the intrinsic properties of dwarf galaxies.

In this thesis we have studied a sample of Local Group dwarf galaxies found in isolation. From the analysis of sizeable samples of spectroscopic data for individual stars in each of these systems, we have obtained accurate line-of-sight velocity and metallicity measurements from their individual stars distributed over a wide spatial area. We were able to determine the galaxies chemo-kinematic

properties, along with their internal mass content. The obtained results enabled us to perform a comparison with the other dwarf galaxies that populate the Local Group, drawing general conclusions on the evolutionary role played by the environment and their internal mechanisms.

In the first part of this work, we present results from the analysis of Cetus and Tucana, two of the three dwarf spheroidals of the Local Group found in isolation. These systems are of great interest because they are directly comparable to their satellite counterparts. We analysed spectroscopic data of individual target stars mainly collected with the FORS2 instrument on the Very Large Telescope. Results from the kinematic analysis showed that their internal motion is dominated by velocity dispersion, with no significant signs of rotation. Making use of extensive mock-tests, we also showed that an eventual rotation signal inside the half-light radius would be weak and not capable of producing the observed ellipticity of these systems.

In the case of Tucana, previous spectroscopic works reported results substantially different from ours. We re-reduced and homogeneously analysed these archival data, reporting consistent results among the datasets. In particular, the velocity dispersion value resulted much smaller than what was previously found, implying a lower dark matter content and a less centrally-concentrated dark-matter-halo, now in line with similarly luminous systems.

The internal kinematics of Cetus and Tucana therefore resembles that of the Milky Way satellites, challenging those models wherein the evolution of dwarf spheroidals has been strongly influenced by the repeated interaction with a larger galaxy. The chemical properties resulted normal for these systems. Cetus showed a radial metallicity gradient, like other dwarf galaxies of similar luminosity but inhabiting very different environments.

The second part of the text is devoted to the analysis of the gas-rich isolated systems IC 1613 and Aquarius, finally completed by a comparison between the observed kinematic, chemical and mass properties of the dwarf galaxies of the Local Group.

The study of IC 1613 focused on the analysis of a large spectroscopic dataset obtained with the integral-field-unit MUSE instrument, also on the Very Large Telescope. We performed the spectral classification and determination of radial velocities for more than 800 stars. At the same time we obtained metallicities for a selected subsample of red giant branch stars. The kinematic analysis confirmed for the first time the presence of a strong stellar rotation signal with a high statistical significance. Stars appeared to rotate in the same direction, and with a similar intensity, as the neutral gas. From the chemical analysis, we find no signs of a radial metallicity gradient, as observed in other systems with a similar luminosity.

On the other hand, the study of Aquarius also showed the presence of a significant internal rotation, which resulted however peculiarly misaligned with respect to that of the neutral gas, being the first time that such effect is observed in the Local Group for a dwarf galaxy of this luminosity.

In the comparative analysis, we showed that the dynamical masses obtained for our sample add to those of the other Local Group systems that reside in dark-matter-halos less massive than predicted by dark-matter-only simulations. This issue, also known as the too-big-to-fail problem, therefore persists regardless of the environment in which dwarf galaxies reside. We also performed a homogeneous analysis of the dwarf systems in the Local Group aimed at finding spatial variations in their metallicity measurements. Several dwarfs showed indeed mild metallicity gradients, with a large scatter of values among the fainter systems. The brightest dwarfs instead had values often consistent with zero. In general, we found that the environment seems to play a minor role in the formation of such gradients, while past mergers are the probable cause of the steepest slopes.

The work carried out during this thesis led to the following publications:

- "The Tucana dwarf spheroidal galaxy: not such a massive failure after all", Taibi, S. et al.; 2020, A&A, 635, A152
- "Kinematic and metallicity properties od the Aquarius dwarf galaxy from FORS2 MXU spectroscopy", Hermosa-Muñoz, L.; Taibi, S. et al., 2020, A&A, 634, A10
- "The mass of our Galaxy from satellite proper motions in the Gaia era", Fritz, T. K. et al., incl. Taibi, S., 2020, MNRAS, 494, 5178F
- "Gaia DR2 and VLT/FLAMES search for new satellites of the LMC", Fritz, T. K. et al., incl. Taibi, S., 2019, A&A, 623, A129
- "Stellar chemo-kinematics of isolated dwarf spheroidal galaxies", Taibi, S. et al.; 2019, Proceedings of the International Astronomical Union, IAUS, 344, 222
- "Stellar chemo-kinematics of the Cetus dwarf spheroidal galaxy", Taibi, S. et al., 2018, A&A, 618, A122

Resumen

El estudio de las galaxias enanas resulta de gran importancia para comprender la formación y evolución de galaxias en las escalas de masa más pequeñas. Según el paradigma cosmológico actual, las galaxias crecen jerárquicamente a partir de la acumulación de sistemas más pequeños. Las galaxias enanas que observamos hoy en día son, por tanto, un registro vivo de los bloques constitutivos que impulsaron la formación de sistemas galácticos mayores. Al ser las primeras galaxias en formarse, pueden proporcionar información acerca de la naturaleza de la materia oscura, la formación de las primeras estrellas y la era de la reionización.

En el Grupo Local, nuestro vecindario galáctico, las galaxias enanas pueden ser estudiadas en gran detalle. Estos sistemas aparentemente simples han demostrado cubrir una gran variedad de propiedades, tanto cinemáticas como químicas o estructurales. También abarcan un amplio rango de masas estelares, habitan en ambientes diversos y muestran historias de formación estelar complejas.

Actualmente se sabe que existen casi cien galaxias enanas formando parte del Grupo Local, más de la mitad habiendo sido descubiertas tan solo en las dos últimas décadas. La mayoría de estos sistemas presentan estructura esferoidal y poca abundancia de gas y se encuentran normalmente como satélites de galaxias espirales de mayor tamaño, como pueden ser la Vía Láctea y M31, mientras que el resto de sistemas más ricos en gas se encuentran típicamente más lejos y aislados. Debido a sus bajas masas, la formación y evolución de galaxias enanas podría estar fuertemente influenciada por efectos internos y ambientales. En particular, la evolución de enanas satélites ha sido probablemente influenciada por su galaxia anfitriona. Los sistemas aislados entonces, habiendo pasado gran parte de su tiempo en un entorno más benigno, ofrecen una valiosa ventana de oportunidad para comprender mejor las propiedades intrínsecas de las galaxias enanas.

En esta tesis se ha estudiado una muestra de galaxias enanas del Grupo Local aisladas. En cada uno de estos sistemas, y a partir del análisis de muestras considerables de datos espectroscópicos de estrellas individuales, hemos obtenido mediciones precisas de la velocidad de línea de visión y de la metalicidad de cada estrella distribuida en una amplia área espacial. Hemos sido capaces de determinar las propiedades quimio-cinemáticas de estas galaxias, junto con su contenido de masa interna. Los resultados obtenidos permitieron la realización de una comparación con otras galaxias enanas que pueblan el Grupo Local, obteniendo conclusiones genéricas sobre el rol evolutivo que juegan el medio ambiente y los propios mecanismos internos.

En la primera parte de este trabajo, se presentan los resultados obtenidos del análisis de Cetus y Tucana, dos de las tres esferoidales enanas del Grupo Local encontradas en aislamiento. Estos sistemas resultan de gran interés porque son directamente comparables con sus homólogos satelitales. Analizamos los datos espectroscópicos de estrellas individuales recogidos especialmente con el instrumento FORS2 del Very Large Telescope. Los resultados del análisis cinemático mostraron que su movimiento interno está dominado por la dispersión de velocidad, sin signos significativos de rotación. Mediante el uso de extensos mock-tests, también mostramos que una señal eventual de rotación dentro del radio efectivo sería demasiado débil e incapaz de producir la elipticidad observada en estos sistemas.

En el caso de Tucana, algunos trabajos espectroscópicos previos han comunicado resultados sustancialmente diferentes a los nuestros. Volvimos a reducir y analizar homogéneamente estos datos de archivo, obteniendo resultados consistentes entre los dos conjuntos de datos. En particular, el valor de la dispersión de velocidad resultó mucho menor que el encontrado previamente, lo que implica un menor contenido en materia oscura y un halo de materia oscura menos concentrado en el centro, en línea con sistemas de luminosidad similar.

Por tanto, la cinemática interna de Cetus y Tucana se asemeja a la de los satélites de la Vía Láctea, en contraposición a aquellos modelos en los que la evolución de esferoidales enanas ha sido fuertemente influida por la repetida interacción con una galaxia de mayor tamaño. Las propiedades químicas resultaron normales para estos sistemas. Cetus mostró un gradiente radial de metalicidad, al igual que otras galaxias enenas de luminosidad similar habitando en entornos muy diferentes.

La segunda parte de la tesis está dedicada al análisis de los sistemas aislados ricos en gas IC 1613 y Aquarius, para finalmente concluir con una comparativa de las propiedades cinemáticas, químicas y masivas observadas en las galaxias enanas del Grupo Local.

El estudio de IC 1613 se centró en el análisis de una gran muestra de datos

espectrocópicos obtenida con el instrumento de campo integral MUSE, también en el Very Large Telescope. Realizamos la clasificación espectral y determinación de la velocidad radial de más de 800 estrellas. Al mismo tiempo, obtuvimos las metalicidades de una selección de muestras de estrellas de la rama de gigantes rojas. El análisis cinemático confirmó por primera vez la presencia de una fuerte señal de rotación estelar con una significancia estadística elevada. Las estrellas parecen rotar en la misma dirección, y con una intensidad similar, a la del gas neutro. A partir del análisis químico, no hemos encontrado signos de un gradiente radial de metalicidad, como había sido observado en otros sistemas de luminosidad similar.

Por otra parte, el estudio de Aquarius también mostró la presencia de una significante rotación interna, encontrándose ésta sin embargo particularmente desalineada con respecto a la del gas neutral, siendo la primera vez que tal efecto es observado en el Grupo Local en una galaxia enana de esta luminosidad.

En el análisis comparativo, demostramos que las masas dinámicas obtenidas para nuestra muestra se suman a aquellas de otros sistemas del Grupo Local que residen en halos de materia oscura menos masivos que los predichos por las simulaciones que sólo tienen en cuenta la materia oscura. Este problema, también conocido como el *too-big-to-fail problem*, persiste por tanto independientemente del ambiente en el que residan las galaxias enanas.

Finalmente, realizamos un análisis homogéneo de los sistemas enanos en el Grupo Local dirigido a la búsqueda de variaciones espaciales en sus medidas de metalicidad. De hecho, varias enanas mostraron ligeros gradientes de metalicidad con una gran dispersión de valores entre los sistemas más débiles. Por el contrario, las enanas más brillantes presentaban valores a menudo consistentes con cero. En general, encontramos que el ambiente parece jugar un rol menor en la formación de dichos gradientes, mientras que fusiones pasadas son la causa más probable de las pendientes más pronunciadas.

Riassunto

Lo studio delle galassie nane è di grande importanza per comprendere la formazione e l'evoluzione dei sistemi galattici alle scale di massa più piccole. Secondo l'attuale paradigma cosmologico, le galassie crescono in maniera gerarchica dall'unione di sistemi più piccoli. Le galassie nane che osserviamo oggi sono quindi una testimonianza vivente dei blocchi che hanno guidato la formazione dei sistemi galattici più grandi. Come prime galassie in essersi formate, esse possono fornire informazioni sulla natura della materia oscura, sulla formazione delle prime stelle e sull'era della reionizzazione.

Nel Gruppo Locale, il nostro vicinato galattico, le galassie nane possono essere studiate con grande dettaglio. Questi sistemi all'apparenza semplici coprono in realtà un'ampia gamma di proprietà, siano esse cinematiche, chimiche o strutturali. Inoltre, hanno masse stellari che spaziano vari ordini di grandezza, vivono in intorni differenti e mostrano storie di formazione stellare complesse.

Al momento si conoscono un centinaio di galassie nane che fanno parte del Gruppo Locale, più della metà delle quali scoperte solo negli ultimi due decenni. La maggior parte di questi sistemi sono di tipo sferoidale e poveri di gas interno, trovati di solito come satelliti delle galassie più grandi, cioè la Via Lattea e M31, mentre il resto sono sistemi più ricchi di gas, trovati di solito più distanti e in isolamento. Dovuto alle loro masse ridotte, la formazione e l'evoluzione delle galassie nane può essere fortemente influenzata da effetti sia interni che esterni. In particolare, l'evoluzione dei sistemi satellite è stata probabilmente condizionata dalla galassia intorno a cui orbitano. I sistemi isolati quindi, avendo passato la maggior parte del loro tempo in un intorno più benigno, offrono la preziosa opportunità di capire meglio quali sono le proprietà intrinseche delle galassie nane.

In questa tesi si presenta lo studio di un insieme di galassie nane isolate del Gruppo Locale. Dall'analisi di un campione significativo di dati spettroscopici per ognuno di questi sistemi, abbiamo ricavato misure accurate della velocità

lungo la linea di visione e della metallicità per le loro stelle individuali distribuite su un'ampia area spaziale. Siamo stati quindi in grado di determinare le proprietà chimico-cinematiche di queste galassie, insieme al loro contenuto di massa interna. I risultati ottenuti ci hanno permesso di eseguire un confronto con le altre galassie nane del Gruppo Locale, traendo conclusioni generali sul ruolo evolutivo svolto dai loro meccanismi interni e dall'ambiente.

Nella prima parte di questo lavoro vengono presentati i risultati dell'analisi di Cetus e Tucana, due delle tre galassie nane sferoidali isolate del Gruppo Locale. Questi sistemi sono di grande interesse perché direttamente paragonabili alle loro controparti satellitari. Ne abbiamo analizzato i dati spettroscopici ottenuti principalmente con lo strumento FORS2 del Very Large Telescope. I risultati dell'analisi cinematica hanno mostrato che il loro moto interno è dominato dalla dispersione di velocità, senza segni significativi di rotazione. Facendo un uso estensivo di mock-test, abbiamo inoltre dimostrato che un eventuale segnale di rotazione all'interno del raggio a metà luce sarebbe debole e non in grado di produrre l'ellitticità osservata di questi sistemi.

Nel caso di Tucana, i precedenti lavori spettroscopici hanno riportato risultati sostanzialmente diverso dai nostri. Abbiamo dunque ri-ridotto e analizzato in modo omogeneo questi dati d'archivio, ottenendo risultati consistenti tra i diversi set di dati. In particolare, il valore della velocità di dispersione è risultato molto più piccolo di quello trovato in precedenza, implicando un alone di materia oscura meno massivo e con una densità centrale inferiore, adesso in linea con quello di altri sistemi analogamente luminosi.

Pertanto, la cinematica interna di Cetus e Tucana è simile a quella dei satelliti della Via Lattea, sfidando quei modelli per i quali l'evoluzione delle nane sferoidali è stata fortemente influenzata dall'interazione ripetuta con una galassia più grande. Le proprietà chimiche sono risultate normali per questi sistemi. Cetus ha mostrato un gradiente radiale di metallicità, com'è il caso di altre galassie nane di luminosità analoga che occupano però un intorno molto diverso.

La seconda parte del testo è dedicata all'analisi di due sistemi isolati ricchi di gas noti come IC 1613 ed Aquarius, completata infine dal confronto tra le proprietà cinematiche, chimiche e di massa delle galassie nane del Gruppo Locale.

Lo studio di IC 1613 si è incentrato sull'analisi di un grande set di dati spettroscopici ottenuti con lo strumento a unità di campo integrale MUSE, anch'esso sul Very Large Telescope. Abbiamo eseguito la classificazione spettrale e la determinazione delle velocità radiali per più di 800 stelle. Allo stesso tempo abbiamo ottenuto le metallicità per un sottocampione di stelle appartenenti al ramo delle giganti rosse. L'analisi cinematica ha confermato per la prima volta

la presenza di un forte segnale di rotazione stellare con un'elevata significatività statistica. Le stelle appaiono ruotare nella stessa direzione e con un'intensità simile a quella del gas neutro. Dall'analisi chimica, non abbiamo trovato segni di un gradiente di metallicità radiale, come osservato in altri sistemi con una luminosità simile.

D'altra parte, anche lo studio di Aquarius ha mostrato la presenza di una significativa rotazione interna, che tuttavia è risultata disallineata rispetto a quella del gas neutro, essendo la prima volta che tale peculiare effetto viene osservato nel Gruppo Locale per una galassia nana di questa luminosità.

L'analisi comparativa ha mostrato come i valori della massa dinamica ottenuti per il nostro campione si sommano a quelle di altri sistemi del Gruppo Locale che risiedono in aloni di materia oscura meno massicci rispetto a quanto previsto dalle simulazioni numeriche di sola materia oscura. Questo problema, noto anche come *too-big-to-fail problem*, persiste quindi indipendentemente dall'ambiente in cui risiedono le galassie nane.

Infine abbiamo effettuato un'analisi omogenea dei sistemi nani del Gruppo Locale, con l'obiettivo di trovare variazioni spaziali nelle loro misure di metallicità. Diverse nane hanno mostrato infatti lievi gradienti di metallicità, con una grande dispersione di valori tra i sistemi più deboli. Le nane più brillanti hanno mostrato invece valori spesso consistenti con zero. In generale, abbiamo scoperto che l'ambiente sembra giocare un ruolo minore nella formazione di tali gradienti, mentre le fusioni passate sono la probabile causa dei profili radiali di metallicità più marcati.

Contents

1

Introduction

Dwarf galaxies are elusive objects. Although their presence in the sky was evident to the first humans inhabiting the southern hemisphere, thanks to the Magellanic Clouds, it was only in the past century that astronomers understood their (extra-)galactic nature and started to discover more of these systems[1]. Today, the study of dwarf galaxies is still an expanding field and an extensive observational effort has been devoted to obtaining details about their dynamic, chemical and structural properties. Moreover, they are of great importance for the validation of theoretical works dedicated to understand how galaxies form and evolve.

In this thesis, we focus on the study of four dwarfs belonging to the Local Group of galaxies. State-of-the-art spectroscopic and photometric observations of individual stars, together with advanced methods of analysis, have been used to improve our knowledge of these systems. Their retrieved properties are then compared to those of the other dwarf galaxies of the Local Group.

[1]The first written record of the Magellanic Clouds, and therefore of any dwarf galaxies, dates back to 964 by the Persian astronomer Abd al-Rahman al-Sufi, as noted in his work *Book of fixed stars*. Almost a millennium had to pass before Shapley (1938) was puzzled by the discovery in Sculptor of a resolved stellar cluster of the globular type but of galactic dimensions, like the Magellanic Clouds without the bright stars and gas, a nearby spheroidal galaxy of very low surface brightness, what is known today as the Sculptor dwarf spheroidal galaxy. For an historical introduction on dwarf galaxies, see e.g. Tammann (1994).

1.1 Dwarf galaxies: a definition

The work definition of a dwarf galaxy is that of a galactic system fainter than $M_V \approx -17$ (Tolstoy, Hill, & Tosi, 2009). This definition is not related to a particular physical property, but helps to separate these systems from larger ones in order to better understand the specific aspects of galaxy formation and evolution at smaller scales. In fact, their dynamical, chemical and structural properties show a continuity with those of other galaxy types.

As shown in Fig. 1.1, the surface-brightness, absolute magnitude and physical size values of dwarf galaxies appear to overlap with those of larger early- and late-type systems, along with faint spiral galaxy disks, while they are clearly distinct from the ellipticals. Dwarf galaxies also differ from globular clusters, being more spatially extended. It is true, however, that the so-called ultra-faint dwarfs have structural properties and luminosities that overlaps with those of faint star clusters, which makes them hard to identify as galaxies. In fact, ultra-faint systems challenge a size-based identification of galaxies, which has raised the question of what a galaxy is in the first place. According to Willman & Strader (2012), a galaxy is defined as *a gravitationally bound collection of stars whose properties cannot be explained by a combination of baryons and Newton's laws of gravity*. When studied in detail, dwarf galaxies appear indeed to host complex stellar populations, show signs of chemical enrichment and their internal kinematics implies a dynamical mass significantly larger than the baryonic one (Tolstoy, Hill, & Tosi, 2009). Taken together, these criteria clearly distinguish dwarf galaxies from star clusters. In addition, they indicate that dwarf systems are also embedded in a dark matter halo massive enough to prevent significant metal-loss through supernovae ejecta and to ensure large mass-to-light ratios (see Simon, 2019, also for a review on the ultra-faint dwarfs)[2].

Therefore, dwarf galaxies are dark-matter-dominated systems, with the fainter ones showing the largest mass-to-light ratios (e.g. McConnachie, 2012; Simon, 2019). On the other hand, their chemical properties show they are generally metal-poor (i.e. with a sub-solar average metallicity) following the well-known stellar luminosity-metallicity relation (e.g. Kirby et al., 2013b). This implies that the fainter a dwarf galaxy is, the more metal-poor it will be (on average), independently of being an early- or late-type (see e.g. Fig 5.7).

[2]Having to consider a large amount of non-baryonic (or dark) matter to explain the observed properties of galaxies could indicate a deeper problem with our understanding of how gravity actually works. A modification of Newton's laws, called MOND theory, has been proposed to account for the observations and solve some of the small-scale problems that the current cosmological paradigm is facing (Milgrom, 2002, and McGaugh, 2015). At the moment, however, this theory lacks of a cosmological model and a parent relativistic framework.

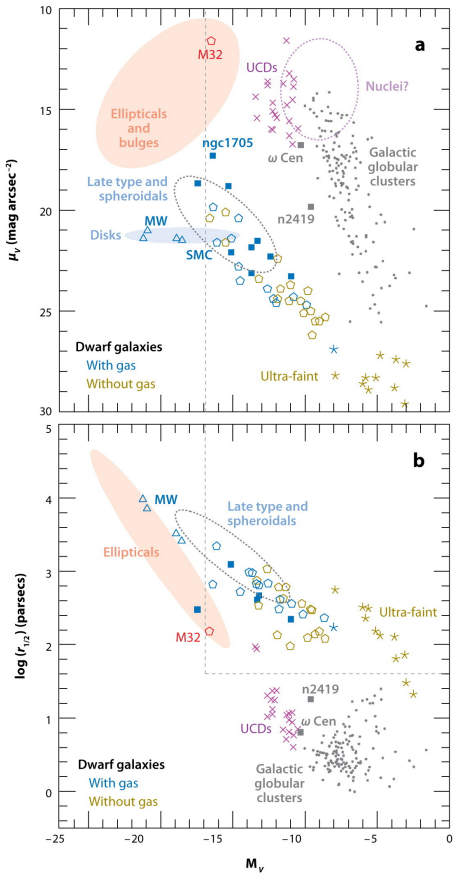

FIGURE 1.1— Structural properties of different galactic and stellar systems. In panel *a* the absolute magnitude M_V vs. the central surface brightness μ_V, while in *b* vs. the half-light radius $r_{1/2}$. Dashed lines indicate the limits of the dwarf galaxy class as defined by Tammann (1994). Coloured ellipses mark typical locations of different galaxy types. Galactic globular clusters are marked as grey dots, blue-compact dwarfs as blue solid squares, and ultra-compact dwarfs as magenta crosses. Local Group dwarf galaxies are plotted as open pentagons, blue for systems with gas and green for those without gas. Ultra-faint dwarfs follow the same colour-scheme, but are given star symbols. Figure taken from Tolstoy, Hill, & Tosi (2009).

Kirby et al. (2013b) also showed how this relation is roughly continuous with observations from larger galaxies (up to stellar masses $M_* \sim 10^{12} M_\odot$), despite their larger scatter.

Dwarf galaxies are abundant in the Universe. They are observed to preferentially cluster around much larger systems, like the Milky Way (MW) or M31, while they are also present in the field. It is likely that their proximity to a large host galaxy may have influenced their evolution. Due to their shallow potential wells, internal mechanisms may also have had a significant impact on their observed properties. To understand which are the main drivers of dwarf galaxy evolution, it may be useful to study those systems found in isolation. In fact, they have evolved mainly in a more benign environment. Contrasting their observed properties with those of satellite systems offers a unique window to understand what the intrinsic features of dwarf galaxies are. However, due to their distance, a considerable observational effort is needed to obtain data of a comparable quality to that of the closest systems. In the next sections, we will see better the results of observations on this subject, and how predictions from simulations compare to them.

1.2 Dwarf galaxies in a cosmological context

According to the current cosmological paradigm, the Universe is dominated today by the so-called dark energy ($\Omega_\Lambda \approx 70\%$) and cold dark matter ($\Omega_{\rm CDM} \approx 25\%$), while all the observable baryons contribute only to the $\Omega_{\rm b} \approx 5\%$ of the total energy density budget (Planck Collaboration et al., 2016). This model is consistent with observations ranging from the very large scales to those typical of galactic systems. In the latter case, dark matter is of particular importance because it is required to explain the observed properties of galaxies that cannot be fully justified only by their baryonic content (e.g. Willman & Strader, 2012).

In the Λ-CDM framework, structures form hierarchically (e.g. White & Rees, 1978; Peebles, 1982; Blumenthal et al., 1984), with small halos forming first to then merge into larger structures. Dark matter is assumed to be in the form of weakly interacting particles with non-relativistic (i.e. cold) velocities, which allows them to collapse on small scales at the time of structure formation. Dwarf galaxies then are predicted to be the first galactic systems to have formed. Furthermore, observations show that they are highly dark-matter-dominated, with mass-to-light ratios within the half-light radius that could exceed 1000 $M_\odot/L_\odot$ in the fainter objects (McConnachie, 2012, but see also Walker et al., 2009b; Wolf et al., 2010). Therefore, dwarf galaxies are excellent laboratories for testing Λ-CDM at the smallest scales.

A wealth of cosmological dark-matter-only numerical simulations, exploring how structures form and evolve, have provided several robust predictions that are of general validity in the mark of Λ-CDM. Dark matter halo density profiles follow a nearly universal form over all masses that is well described by the so-called Navarro-Frenk-White (from Navarro, Frenk, & White, 1997) profile. The NFW functional form increases steadily towards the centre, taking the form of a cusp profile. Furthermore, simulations predict not only that small halos are more abundant than the larger ones, but also individual dark matter halos are full of substructures (or sub-halos) that survived the hierarchical merging process. For a MW-sized halo, simulations predict that $\sim 20\%$ of its mass resides in substructures, implying a large number ($\sim 500 - 1000$ with $M_{\rm sub} > 10^7 M_\odot$) of satellites (see Bullock & Boylan-Kolchin, 2017, and references therein).

These predictions have been problematic to verify on small galactic scales, like those of the Local Group and its systems. Perhaps, the most striking problem is that the number of satellites observed around the MW (but the same is true for M31) is almost one order of magnitude lower than that predicted by simulations. This "missing satellite" problem (Moore et al., 1999; Klypin et al., 1999) has started to be alleviated by the recent discoveries of many ultra-faint dwarfs around the MW and M31 (see the on-line catalogue of McConnachie, 2012, for an up-to-date compilation). From a theoretical point of view, it appears that star formation becomes increasingly inefficient at lower masses, with the smallest halos remaining dark due to UV-feedback from the reionization epoch (Bullock & Boylan-Kolchin, 2017). Therefore, one way to potentially solve the missing-satellite problem has been to associate the largest sub-halos with the brightest satellites, assuming that the smallest ones have not been able to form stars. However, the bigger substructures result to have central masses that are too high compared to those inferred from the kinematics of MW satellites. This is known as the "too-big-to-fail" problem (Boylan-Kolchin et al., 2012), which remain valid also when taking into account the other dwarf galaxies of the Local Group (e.g. Kirby et al., 2014; Tollerud et al., 2014) and more distant low-mass field systems (Ferrero et al., 2012; Papastergis et al., 2015; Papastergis & Shankar, 2016). Somewhat related is a third problem, that is the internal dynamics of many dwarf galaxies (either inferred from their HI rotation curves or their stellar motion) is better described by a density profile that is cored in the central regions, instead of the usual NFW cusp profile (e.g. Battaglia et al., 2008a; de Blok et al., 2008; Oh et al., 2011; Walker & Peñarrubia, 2011; Amorisco & Evans, 2012b; Oh et al., 2015; Oman et al., 2015; Read et al., 2016; Strigari et al., 2018, among others).

Only recently, advanced cosmological hydrodynamic simulations taking into account the effects of baryons have shown how the internal stellar feedback

(e.g. from episodic star formation and supernova-driven winds), together with environmental effects (i.e. tidal and ram-pressure mass-stripping, disk shocking) for the closer and less-massive systems, could potentially solve part of the above problems (Bullock & Boylan-Kolchin, 2017, but also Zolotov et al., 2012; Arraki et al., 2014; Brooks & Zolotov, 2014; Brook & Di Cintio, 2015; Wetzel et al., 2016; Sawala et al., 2016; Dutton et al., 2016; Fattahi et al., 2018; Buck et al., 2019; Fattahi et al., 2020). These simulations, however, have not found a definitive solution that match with the observed properties for the entire Local Group systems. For example, (Sawala et al., 2016) showed that environmental interactions are key to lower the central densities of their simulated dwarfs, being able to solve the too-big-to-fail problem, while maintaining a canonical cusp density profile. According to these results, satellites should systemically differ from the isolated systems, although observations (e.g. Kirby et al., 2014) have shown that this is not the case (see also discussion in Ch. 5). Clearly, future simulations need to better explore the low-mass regime of dwarf galaxies.

1.3 The dwarf galaxy population of the Local Group

The Local Group (LG) of galaxies is defined as our extra-galactic neighbourhood. It comprises few bright spirals, the MW, M31 and M33, but almost a hundred of dwarf galaxies (from the October 2019 update of McConnachie, 2012, and references therein). Historically, they have been classified according to their observed morphology. Three main groups can be identified. Those that contain gas and are currently forming stars, such as WLM or IC 1613 (Ch. 4), are called irregular dwarfs (dIrr). Those that are instead devoid of gas and no longer form stars, like Fornax, Sculptor and Draco, are classified as spheroidal dwarfs (dSph). An intermediate type of systems are called transition dwarfs (dTr), like Pegasus and Phoenix, because they contain gas and a young population of stars, but no active star forming regions. Other types that deserve a mention are the dwarf ellipticals (dE) around M31, which appear as large dSphs, and the ultra-faint dwarfs (uFd) introduced in the first section, which form an extension of the dSphs to the lowest stellar masses[3]. As a whole, LG dwarf galaxies span almost six orders of magnitude in stellar masses, as shown in Fig 1.2, which could led to a different classification based on their brightness (see e.g. Bullock & Boylan-Kolchin, 2017).

[3]The uFds take a different denomination for historical reasons, since they were started to be discovered in digital sky surveys (e.g. SDSS), unlike the dSphs which were found mainly through the inspection of photographic plates. In particular, those dSphs found as satellites of the MW are called *classical*, for convenience. They are Carina, Draco, Fornax, Leo I, Leo II,

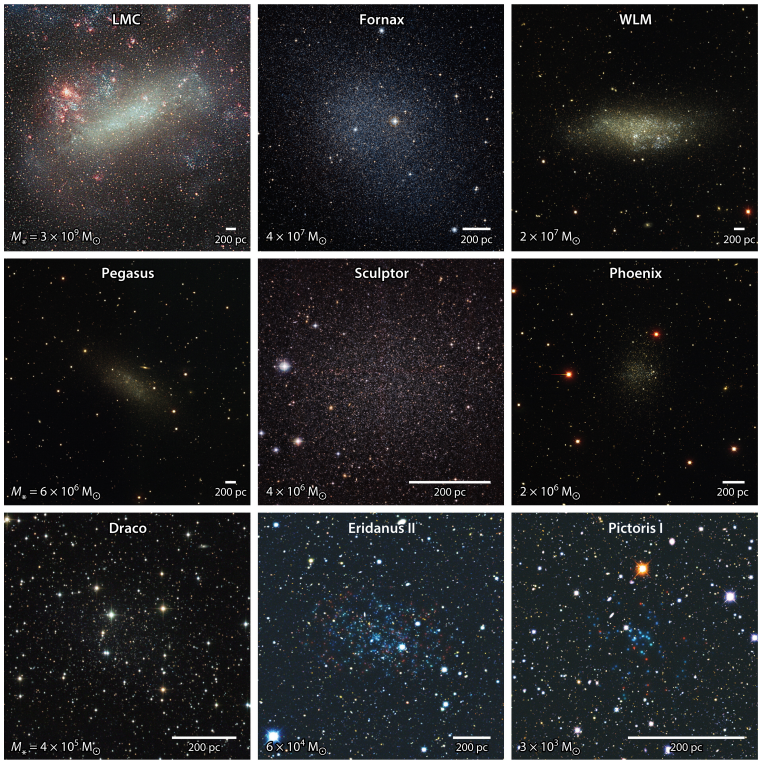

FIGURE 1.2— Dwarf galaxies ordered as a function of stellar masses. The Large Magellanic Cloud, although classified as an irregular galaxy, is taken as reference for the brightest dwarfs. Names, stellar masses and spatial scales are shown in each panel. Figure taken from Bullock & Boylan-Kolchin (2017).

The majority of LG dwarf galaxies are of the early type (i.e. they are dEs, dSphs, uFds), preferentially found as satellites of the MW or M31, while the late-types (i.e. dIrrs and dTr) are typically found in isolation. This so-called morphology-density relation (Einasto et al., 1974; van den Bergh, 1994) has raised the question of whether the different types of dwarf galaxies shared similar progenitors, but evolved differently due to environmental effects. Indeed, many numerical simulations have shown that the prolonged action of tidal and ram-pressure stripping from a host-galaxy on an accreted highly-rotating gas-rich system is able to remove its gas and angular momentum, and transform it into a gas-free dispersion-supported dSph (the so-called "tidal stirring" model, see Mayer, 2010, review). These simulations have shown that specific conditions, like eccentric orbits and small pericentric distances from the host-galaxy, are required for a complete transformation (Kazantzidis et al., 2011). Thanks to recent *Gaia*-DR2 observations the orbital properties for many MW-satellites have been derived from their systemic proper motions (see e.g. Gaia Collaboration et al., 2018; Fritz et al., 2018; Simon, 2018). They indicate that many satellites could have experienced several pericentric passages. However, the low orbital eccentricities and relatively large pericentric distances recovered for classic dSphs seem to discourage their possible tidal stirring origin (Gaia Collaboration et al., 2018).

Furthermore, the presence of dSphs found in isolation, such as Cetus and Tucana, is not fully accounted by tidal stirring models, particularly if they were to exhibit properties similar to those of satellite systems. It has been shown that the isolated dSphs could be probable "backsplash galaxies", which implies that they may have passed just once near a large host-galaxy, but without becoming bound (e.g., Sales et al., 2007; Teyssier et al., 2012, but also Buck et al., 2019). According to tidal stirring models, a short interaction would mean a lower degree of transformation for these isolated systems, implying significant differences in their internal properties compared to their satellite companions (e.g. a higher degree of stellar rotation). The study of the isolated dSphs is then an important test bed for tidal stirring models, but it is also useful to understand the impact of environmental interactions in general.

Another question that arises with respect to the evolution of dwarf galaxies comes from a careful inspection of their full star formation histories (SFH). Gallart et al. (2015) showed that there is no univocal connection between the present-day morphological type of a dwarf galaxy and its evolutionary history. They observed that some dwarfs formed most or all of their stars in an early and dominant period of star formation lasted only few Gyrs; they labelled them

Sculptor, Sextans and Ursa Minor. See Walker (2013); Simon (2019).

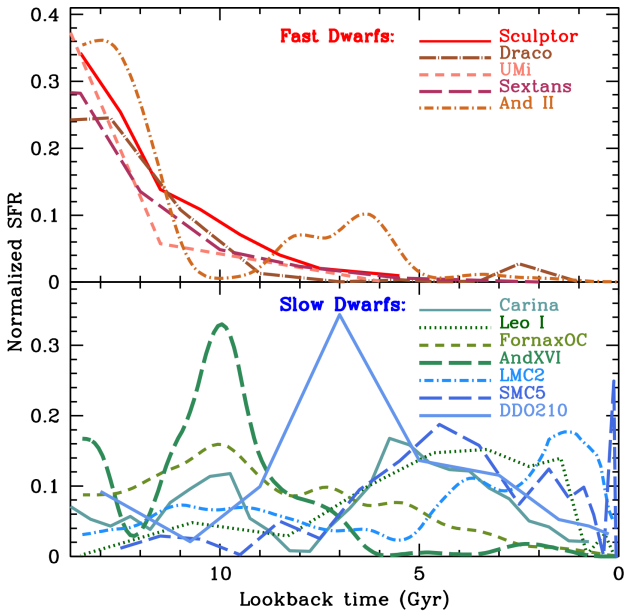

FIGURE 1.3— Full star formation histories of Local Group dwarf galaxies. Those plotted in the upper panel are labelled as fast dwarfs, while those in the lower panel are called slow dwarfs. We note how dSphs are present in both panels, while dIrrs (and dTrs) only in the lower one. Figure taken from Gallart et al. (2015).

as *fast* dwarfs. The other systems instead formed only a fraction of their stellar mass at early epochs, but continued to form stars until (or almost) the present-days; these were called *slow* dwarfs. Indeed, looking at Fig 1.3, it is easy to see how dSphs are not exclusively old systems (like Sculptor and Sextans), but they may contain intermediate-young age stars too (e.g. Carina and Fornax). The SFHs of these latter systems, in particular, are similar to those of dIrrs (and dTrs) for most of their lifetimes.

These evidences led Gallart et al. (2015) to propose that dwarf galaxies may actually born different, with their evolutionary paths influenced by early conditions at their formation. This scenario implies that those dwarfs born in a high-density environment, such as the surroundings of a large host-galaxy, could

have accreted more material and formed most of their stars at early times, with their SFHs eventually stopped after a few Gyrs due to the combined effects of reionization and internal stellar feedback. Slow dwarfs, on the other hand, may have formed in low-density environments, with their evolution affected by slow mass assembly, which implies milder stellar feedback and slow gas-loss favouring a prolonged SFH. Those satellites dSphs labelled as slow dwarfs may have lost their last gas reservoir due to tidal and ram-pressure stripping during their late entry into the host-galaxy potential.

Knowing the actual infall time of satellite dwarfs into the host-galaxy potential and comparing it with their quenching time (i.e. the time when a system stopped to form new stars), could potentially help to better understand the aforementioned scenarios. However, the recovery of the full orbital history and first infall time for the satellite dwarfs is hampered by the unknown form of the MW's potential and its past merging history (e.g. Lux et al., 2010). Comparisons with the assembly history of MW-like hosts in full cosmological simulations suggest that most of the MW-satellites were accreted at intermediate to early times (i.e. from 6 to 10 Gyr ago, see Rocha et al., 2012; Wetzel et al., 2015; Simpson et al., 2018). This could be too late compared to the quenching times of many MW-satellites, which instead would suggest a very early accretion (Weisz et al., 2014; Gallart et al., 2015, e.g., but see also Buck et al., 2019 results for a simulation with early accreted systems). Interestingly, an early accretion or a very late entry in the host-galaxy potential is required for ram-pressure stripping to be effective in quenching the SFH of the infalling dwarf galaxies, as showed in high-resolution hydrodynamical simulations conducted by Hausammann, Revaz, & Jablonka (2019). The recent *Gaia* measurements combined with analytical modelling or simulations should help to provide a better constraint on the infall times of MW-satellites (see e.g. preliminary results by Fillingham et al., 2019; Miyoshi & Chiba, 2020).

Modern cosmological simulations of the LG provide enough resolution to show how both internal and environmental mechanisms are required to match the observed properties of dwarf galaxies (Wetzel et al., 2016; Sawala et al., 2016; Dutton et al., 2016; Fattahi et al., 2018; Buck et al., 2019; Garrison-Kimmel et al., 2019b,a). Additionally, some of these simulations are aimed to understand the evolution of these systems when found in isolation (e.g. Revaz & Jablonka, 2018). In this context, it is of great importance to obtain details on the internal kinematics, chemical abundances and stellar ages for the isolated dwarf galaxies not only to contrast them with the properties of satellite systems, but also as a necessary complement to model predictions.

Any proposed scenario for the formation of the LG would eventually have to account for the observed morphology-density relation. We want to stress,

however, how this relation may not be universal, as observations of star forming satellites around MW-analogues suggest (Spencer et al., 2014; Geha et al., 2017, but see also Hausammann et al., 2019).

1.4 Spectroscopic studies for Local Group dwarfs

The possibility that individual stars can be resolved for the LG dwarf galaxies, makes them ideal targets for spectroscopic studies. Thanks to their vicinity, MW satellites are the best studied systems, with large datasets available for the brightest dwarfs (i.e. with ~ 1000 acquired targets, see e.g. Tolstoy et al., 2004; Battaglia et al., 2006, 2008a, 2011; Walker et al., 2009a, 2015; Kirby et al., 2011; Lemasle et al., 2012, 2014; Hendricks et al., 2014; Spencer et al., 2017). Other dwarf galaxies, like the M31 satellites and the isolated systems, have been also extensively studied, with sizeable spectroscopic samples acquired ($\sim 50 - 500$) despite their larger distances (Tollerud et al., 2012; Leaman et al., 2012, 2013; Collins et al., 2013; Ho et al., 2015; Swan et al., 2016; Kacharov et al., 2017; Kirby et al., 2014, 2017, 2020).

Most of the spectroscopic efforts have been devoted to observe individual red giant branch (RGB) stars in dwarf galaxies. They are very convenient targets, since most of the low mass stars undergoes the RGB phase. Having ages $>$ 1 Gyr, they basically cover (and are informative on) the entire formation history of the considered dwarf galaxy. Furthermore, they are the brightest stellar feature in the early-type systems, like the dSphs. They also show prominent spectral features, like the near-IR Ca II triplet lines (around 8600 Å), which are easily resolved even at low spectral resolution ($R \sim 1000$). Observing dwarf galaxies with multi-objects spectrograph, it is possible to obtain information from many stars at once distributed on a wide spatial area.

The spectral analysis allows to recover the line-of-sight (l.o.s.) velocity and chemical abundances from the individual stars. At high spectral resolution, abundances can be obtained from more than one element, although this is a time-consuming process particularly for systems placed at further distances than the MW-satellites. Otherwise, metallicity is generally reduced to the Fe abundance of the star (i.e. [Fe/H]), which is assumed to be representative of its total metal content[4]. An empirical relation between the equivalent width of the Ca II lines and [Fe/H] has been established for individual RGB stars (Battaglia et al., 2008b; Starkenburg et al., 2010; Carrera et al., 2013, e.g.). This relation holds over a large range of metallicities ($-4.0 \lesssim$ [Fe/H] $\lesssim -0.5$) and stellar ages

[4]By *metals* is meant all those elements heavier than helium.

($t > 1$ Gyr), and is particularly convenient for measuring metallicities in the distant galaxies of the LG.

The internal kinematic and chemical properties of dwarf galaxies can be derived then from the l.o.s. velocities and metallicities of their individual stars. By combining the chemo-kinematic information with the spatial distribution of the individual targets, it is possible to determine the presence of velocity and radial metallicity gradients, together with that of multiple stellar populations with distinct properties.

The kinematic status of a dwarf galaxy, in particular, is informative on its mass content. For rotating systems (like the brightest dIrrs), the mass content within a certain radius can be inferred by the circular motion of either their stellar or gas components (e.g. Leaman et al., 2012; Oh et al., 2015; Read et al., 2016). For dSphs, instead, the mass modelling has to rely on their stellar random motion, specifically on the velocity dispersion profile of the stellar tracer which amplitude depends on the gravitational potential of the system, but also on the stellar mass density profile and the velocity anisotropy parameter β[5]. This procedure, however, is not trivial because it may suffer of degeneracies in the mass estimation due to the difficulties involved in the determination of β. In fact, spectroscopic observations allow to accurately derive only the l.o.s. velocity dispersion profile, while the other two tangential components have to be derived using proper motion estimations. The determination of 3D velocities is currently achievable only for the closest dwarfs and on tiny spatial areas, as showed by studies using *Gaia* measurements (e.g. Massari et al., 2018, 2020). Another way to break the mass-anisotropy degeneracy is to detect multiple stellar components with different chemo-kinematic properties. Since they are independent tracers living in the same potential, modelling their velocity dispersion profiles may inform on the internal shape of the mass profile (i.e. if it is cuspy or cored, see e.g. Battaglia et al., 2008a; Walker & Peñarrubia, 2011; Amorisco & Evans, 2012b). Otherwise, it has been shown that the mass-anisotropy degeneracy is minimized approximately around the half-light radius of dispersion-supported systems, where the mass content can be obtained by their averaged l.o.s. velocity dispersion (Walker et al., 2009b; Wolf et al., 2010). This procedure has the advantage to be simple and easy to achieve even for the most distant systems, at the cost of knowing the mass content of a dwarf galaxy at only one spatial point. Nevertheless, this already allows to constrain theoretical predictions on the internal mass content of dwarf galaxies (see Ch. 5).

The spectroscopically derived chemo-kinematic quantities are of great im-

[5]The velocity anisotropy parameter is defined as: $\beta(r) = 1 - \frac{\sigma_\theta(r)^2 + \sigma_\phi(r)^2}{2\sigma_r(r)^2}$, where $\sigma_r, \sigma_\theta, \sigma_\phi$ are the 3D velocity dispersion components in spherical coordinates (Binney & Tremaine, 1987).

portance to identify similarities and differences between the various types of dwarf galaxies located in different environments, eventually helping us to understand which are the main drivers of their evolution. Since the evolution of satellite systems could have been influenced by their host-galaxies, the isolated dwarfs play a central role in our understanding of the intrinsic mechanisms that shape their internal properties. In particular, the comparison between dwarf galaxies of similar luminosity and SFH, yet inhabiting different environments, is facilitated by the analysis of similar stellar tracers, such as the RGB stars.

On the other hand, late-type dwarfs that are still forming stars (or have recently finished to do so) and have evolved in a more benign environment, offer the opportunity to study star formation processes at low-mass and low-metallicity scales, thanks to the combined presence of gas and stars of young and old age. In particular, the chance to observe these systems with an integral-field-unit (IFU) spectrograph, like the MUSE instrument on the Very Large Telescope, allows to simultaneously obtain a large dataset of stars in different evolutionary phases, giving the unique opportunity to link the young and old populations, and see how the stellar properties have changed over time.

1.5 Outline of this thesis

In this thesis we study a sample of Local Group dwarf galaxies found in isolation[6]. They have different morphologies (two early-types and two late-types) and stellar masses ($1 \lesssim M_*(10^6 M_\odot) \lesssim 100$). We conduct an analysis of novel spectroscopic data aimed to obtain accurate velocity and metallicity measurements from individual target stars distributed over a wide-area. To this end, we exploit data collected with the FORS2, FLAMES-GIRAFFE and MUSE instruments mounted on the Very Large Telescope, having a low-intermediate spectral resolution ($R \sim 2500 - 6500$). We then determine the kinematic and chemical properties of our systems according to the ages and spatial distribution of their stars, along with their internal mass content. The obtained results are finally compared to those of the other LG dwarf galaxies.

In Chapters 2 and 3, we study two of the three isolated LG dSphs, namely Cetus and Tucana. These systems are of great interest because directly comparable to satellite dSphs. Previous spectroscopic studies have not been conclusive on their internal properties, in particular on their current kinematic status. Our

[6]Throughout the text, we label as isolated those systems that are at more than one viral radius away from both MW and M31 (see e.g. Leaman et al., 2012, their Fig. 1). In particular, our sample systems show a tidal index $\Theta \lesssim 0$, as defined by Karachentsev et al. (2013), which implies that they are currently isolated from the nearest significant tidal disturber.

analysis shows how they are dispersion-supported systems with no significant signs of internal rotation. In particular, by conducting extensive mock-tests we show that if these systems were dominated by rotation within the half-light radius, we should have detected it with great statistical significance. Performing a homogeneous analysis comprising also literature data, the velocity dispersion value of Tucana results much smaller than what was previously reported, implying a lower dark matter content and a less centrally-concentrated dark-matter-halo, now in line with similarly luminous dSphs. The chemical analysis of Cetus and Tucana shows that they are metal-poor systems with a significant metallicity spread. In particular, Cetus hosts a radial metallicity gradient, similarly to what observed in other dwarf galaxies inhabiting very different environments. The obtained catalogues have been made publicly available.

Chapter 4 is dedicated to the study of the IC 1613 dIrr. We analyse a large spectroscopic dataset obtained with the integral-field-unit MUSE instrument mounted on the Very Large Telescope. We perform the spectral classification and determination of radial velocities for more than 800 stars. At the same time we obtain metallicities for a selected subsample of red giant branch stars. The obtained systemic velocity and velocity dispersion are in agreement with literature value, while this is the first time that a rotation signal for the stellar component is confirmed with high significance. The stars seem to rotate in the same direction, and with a similar intensity, as the neutral gas. We find no significant signs of a radial metallicity gradient, as observed in other systems with a similar luminosity.

In Chapter 5 we present the results of a comparison between the properties obtained for our sample and those of the other LG dwarf galaxies, along with the chemo-kinematic analysis of the Aquarius dTr. Results for the latter system show a significant internal rotation, which is peculiarly misaligned with respect to that of the neutral gas, being the first time that such effect is observed for a LG dwarf galaxy of this luminosity. In the comparative analysis of LG dwarf galaxies we focus on their internal kinematic and radial metallicity properties. In particular, the kinematic status of Cetus and Tucana is similar to that of MW-satellites, challenging tidal stirring models on the formation of dSphs. Dynamical masses obtained for our sample add to those of the other LG systems that reside in dark-matter-halos less massive than predicted by dark-matter-only simulations. The too-big-to-fail problem then persists, regardless of the environment in which these dwarf galaxies reside. Finally, we show results from a homogeneous analysis of LG dwarf systems aimed at finding radial variations in their metallicity measurements. Several dwarfs show indeed mild metallicity gradients, with a large scatter of values among the fainter systems. The brightest dwarfs show instead values that are often consistent with zero.

In general, the role that the environment could have played in the formation of such gradients seems limited, while the steepest slopes have been probably caused by past mergers.

2

Stellar chemo-kinematics of the Cetus dwarf spheroidal galaxy

The material included in this chapter has been published in:

Taibi, S.; Battaglia, G.; Kacharov, N.; Rejkuba, M.; Irwin, M.; Leaman, R.; Zoccali, M.; Tolstoy, E.; Jablonka, P., 2018, Astronomy & Astrophysics, 618, A122.

ABSTRACT

Aims. In order to minimize environmental effects and gain an insight into the internal mechanisms that shape the properties of dwarf galaxies, we study one of the few dwarf spheroidals of the Local Group found in isolation: Cetus. This system is of particular interest since it does not follow the Local Group morphology-density relation.

Methods. We obtained Very Large Telescope (VLT) FORS2 spectra ($R \sim 2600$) in the region of the Ca II triplet lines for 80 candidate red giant branch (RGB) stars. The analysis yielded line-of-sight velocities and metallicities ([Fe/H]) for 54 bona-fide member stars.

Results. The kinematic analysis shows that Cetus is a mainly pressure-supported ($\sigma_v = 11.0^{+1.6}_{-1.3}$ km s^{-1}), dark-matter-dominated system ($M_{1/2}/L_V = 23.9^{+9.7}_{-8.9} M_\odot/L_\odot$) with no significant signs of internal rotation. We find Cetus to be a metal-poor system with a significant metallicity spread (median [Fe/H] $= -1.71$ dex, median-absolute-deviation $= 0.49$ dex), as expected for its stellar mass. We report the presence of a mild metallicity gradient compatible with those found in other early-type dwarf galaxies of the same luminosity; we trace the presence of a stellar population gradient also in the spatial distribution of stars in different evolutionary phases in ancillary SuprimeCam photometric data. There are tentative indications of two chemo-kinematically distinct sub-populations, with the metal-poorer stars showing a hotter kinematics than the metal-richer ones. Furthermore, the photometric data reveals the presence of a foreground population that most likely belongs to the Sagittarius stream.[1]

[1]The averaged spectra (FITS files) used in this work are publicly available at the CDS

2.1 Introduction

The Cetus dwarf spheroidal galaxy (dSph) was discovered by Whiting, Hau, & Irwin (1999) from visual inspection of ESO/SRC survey photographic plates. Follow-up observations disclosed an early-type system, placed in isolation ($D_\odot > 600$ kpc) from both the MW and M31 galaxies. McConnachie et al. (2005) calculated a heliocentric distance of 755 ± 23 kpc using the tip of the red giant branch (TRGB) method, a result subsequently confirmed by Bernard et al. (2009) using RR-Lyrae stars ($D_\odot = 780 \pm 40$ kpc). Structural parameters estimated by McConnachie & Irwin (2006), revealed an extended galaxy with a half-light radius almost double that of MW dSphs of similar luminosity, and one of the largest nominal tidal radii of the LG[2].

From deep HST/ACS observations reaching below the oldest main sequence turnoff (oMSTO), Monelli et al. (2010) were able to derive the SFH of the Cetus dSph, finding that it is an old and metal-poor system ($\langle$[Fe/H]$\rangle \sim -1.7$ dex), with the SFH peaking around 12 Gyr ago and lasting approximately 2 Gyr, with no stars being formed in the last 8 Gyr; this makes Cetus comparable in age to some of the oldest dSph satellites of the MW, such as Sculptor (see e.g. Gallart et al., 2015). On the spatial scale of the HST/ACS data ($\lesssim 1.5$ half-light radii R_e, see Table 2.1), no age gradient is detected (Hidalgo et al., 2013). The analysis of a more spatially extended photometric dataset (Monelli et al., 2012, based on VLT/VIMOS observations) revealed the presence of a radial gradient in the RGB and horizontal branch (HB) morphologies, both of which become bluer when moving away from Cetus' center (approximately beyond the half-light radius). On the other hand, from the same VLT/VIMOS dataset, the RR-Lyrae stars did not show any spatial variation of their mean period properties. It appears then that the age and metallicity properties of Cetus are fairly homogeneous in the central regions, but might change in the outer parts.

The first spectroscopic study of individual stars in Cetus was conducted by Lewis et al. (2007), using Keck/DEIMOS data of ~ 70 stars selected from the red giant branch (RGB) of the galaxy and mainly distributed along its optical projected major axis. The spectroscopic analysis led to the first determination of the systemic velocity (-87 ± 2 km s^{-1}) and velocity dispersion (17 ± 2 km s^{-1}) of the galaxy, revealing also a hint of rotation (< 10 km s^{-1}). Furthermore the kinematic analysis excluded any association with nearby HI clouds, thus

via anonymous ftp to cdsarc.u-strasbg.fr (130.79.128.5) or via `http://cdsarc.u-strasbg.fr/viz-bin/qcat?J/A+A/618/A122`

[2]We note that here "nominal tidal radius" is to be understood as simply the relevant parameter resulting from a King profile fit to Cetus surface density profile; Cetus in fact shows no evidence of tidal truncation.

establishing that Cetus is devoid of gas given the actual observational limits. Metallicity estimates from Ca II triplet (CaT) lines resulted in agreement with the expectations based on photometry of finding a metal-poor stellar population ([Fe/H] ~ -1.9 dex).

A subsequent spectroscopic study conducted by Kirby et al. (2014) on a larger sample ($\sim$ 120 RGB targets), also obtained with the Keck/DEIMOS spectrograph, led to lower values of the systemic velocity (-83.9 ± 1.2 km s^{-1}) and velocity dispersion (8.3 ± 1 km s^{-1}), excluding at the same time any presence of internal rotation. The discrepant results with the previous work of Lewis et al. (2007) were attributed to the different membership selection method implemented and the higher signal-to-noise ratio (S/N) of their sample.

In this work, we present results of a new chemo-kinematic study of the stellar component of the Cetus dSph, based on wide-area VLT/FORS2 MXU spectroscopic observations in the region of the near-IR CaT for a sizable sample (80) of individual RGB stars. This is the first study that makes [Fe/H] estimates of stars in the Cetus dSph publicly available. The chapter is structured as follows. In Sect. 2.2 we present the data acquisition and reduction process. In Sect. 2.3 we describe the determination of line-of-sight velocities for the whole sample. Section 2.4 is dedicated to the criteria applied to select likely member stars to the Cetus dSph. Section 2.5 presents the kinematic analysis, where we determine the galaxy systemic velocity and the internal dispersion and search for the possible presence of rotation. In Sect. 2.6 we describe the determination of metallicities ([Fe/H]) and the subsequent chemical analysis. In Sect.2.7 we determine the structural properties of the Cetus dSph using ancillary Subaru/SuprimeCam photometric data, while in Sect. 2.8 we analyze a portion of the Sagittarius stream found in the foreground to the Cetus dSph in the same photometric dataset. Finally, Sect. 2.9 is dedicated to the summary and conclusions.

The parameters adopted for the Cetus dSph are summarized in Table 2.1.

TABLE 2.1— Parameters adopted for the Cetus dwarf galaxy.

Parameter	Units	Value	Ref.
$\alpha_{\rm J2000}$		$00^h26^m10.5^s$	(1)
$\delta_{\rm J2000}$		$-11°02'32''$	(1)
$\epsilon^{(a)}$		0.33±0.06	(1)
P.A.	deg	63 ± 3	(1)
$R_{\rm core}$	arcmin (kpc)	1.3 ± 0.1 (0.29 ± 0.02)	(1)
$R_{\rm tidal}$	arcmin (kpc)	32.0 ± 6.5 (7.1 ± 1.5)	(1)
$R_{\rm e}$	arcmin (kpc)	2.7 ± 0.1 (0.60 ± 0.02)	(1)
M_V		-11.3 ± 0.3	(1)
$I_{\rm TRGB}$		20.39 ± 0.03	(2)
E(B-V)		0.029	(2)
$D_\odot$	kpc	755 ± 23	(2)
$\bar{v}_{\rm hel}$	$\rm km\,s^{-1}$	$-78.9^{+1.7}_{-1.6}$	(3)
$\sigma_{\rm v}$	$\rm km\,s^{-1}$	$11.0^{+1.6}_{-1.3}$	(3)
[Fe/H]	dex	-1.71	(3)
$\sigma_{\rm [Fe/H]}$	dex	0.42	(3)

Notes. The table lists: the coordinates of the galaxy's optical center; the ellipticity; the position angle; the core, tidal and half-light geometric radii; the absolute magnitude in V-band; the tip of the red giant branch magnitude in I-band; the average reddening; the heliocentric distance; the average reddening along the line-of-sight; the chemo-kinematic parameters obtained in this work, i.e., the systemic velocity, the velocity dispersion, the median metallicity, and the intrinsic metallicity scatter. $^{(a)}\epsilon = 1 - b/a$.
References. (1) (1) McConnachie & Irwin (2006); (2) McConnachie et al. (2005); (3) this work.

2.2 Data acquisition and reduction process

2.2.1 Target selection and observations

The data were obtained using the FORS2 instrument (Appenzeller et al., 1998) mounted at the Cassegrain focus of the Very Large Telescope's (VLT) UT1 (Antu) at ESO Paranal Observatory in service mode over several nights of observations between December 2012 and November 2014, as part of the ESO Program 090.B-0284(B), PI: M. Zoccali.

The FORS2 instrument was set up with the Mask eXchange Unit (MXU), a solution that allows multi-object spectroscopy employing selectable masks with custom cut slits. The targets were selected from Subaru/SuprimeCam imaging data in the Johnson V- and I-band (Subaru Program S05A-015, PI: N. Arimoto), covering Cetus out to more than half its tidal radius ($0.5 \times R_{\rm tidal} = 16'$).

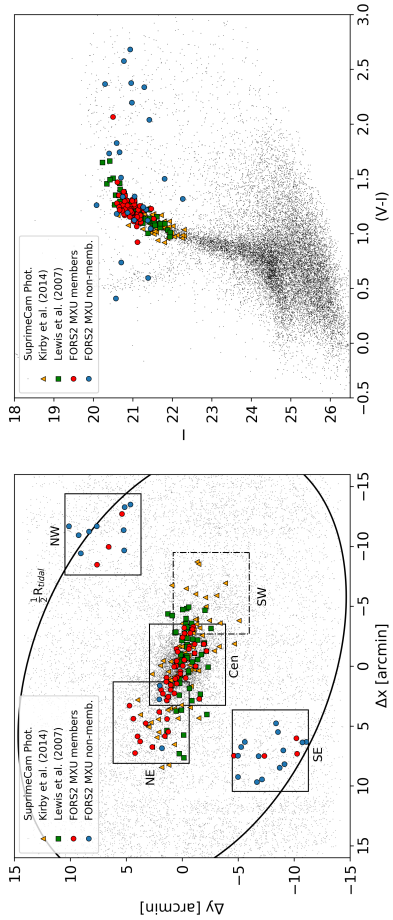

FIGURE 2.1— Spatial distribution in standard coordinates (x,y) projection (*left*) and color-magnitude diagram (*right*) of stars along the line-of-sight to the Cetus dSph. Black points represent the objects classified as stars in the Subaru/SuprimeCam photometric data (see main text); FORS2 MXU targets classified as members are marked with red dots, while the non-members are marked with blue dots. The large squares indicate the 4 observed FORS2 pointings, together with the not-observed SW pointing marked as a dot-dashed box. The ellipse indicates the galaxy half tidal radius (see value in Table 2.1). Overplotted are also spectroscopic targets classified as probable members in Kirby et al. (2014) (orange triangles) and Lewis et al. (2007) (green squares).

We selected all the sources flagged as stellar or probably stellar, and with magnitudes and colors compatible with RGB stars at the distance of the Cetus dSph (taken to be $D_{\odot} = 755 \pm 23$ kpc, McConnachie et al., 2005). Slits to which we could not assign likely RGB stars belonging to Cetus were allocated to random stars within the same magnitude range ($20.5 \lesssim I \lesssim 21.5$). To ensure precise slit allocations to our targets, we used short pre-imaging exposures obtained with FORS2 within the same program.

Figure 2.1 shows the targets spatial distribution and location on the color-magnitude diagram (CMD)[3], respectively. We have observed 83 objects distributed over four FORS2 pointings (see Fig. 2.1 left), of which the northeast (NE) is aligned along the projected major axis of the galaxy and partially overlaps with the Central field, while the southeast and northwest (SE and NW) are aligned with the projected minor axis. Among these objects, three were repeated on purpose on the overlapping Central-NE fields; therefore 80 different stars were observed. We had planned a further pointing along the major axis (namely the southwest one), which, however, was not observed. We refer the reader to Table 2.2 for the observing log: each reported science exposure corresponds to an individual observation block (OB). Several identical OBs were defined for each pointing in order to accumulate S/N necessary for velocity and metallicity measurements.

The instrumental setup and observing strategy we adopted is the same as in Kacharov et al. (2017) (hereafter K17), where the chemo-dynamical properties of the stellar component of the Phoenix dwarf transition type galaxy have been studied. Mask slits were designed to be $1''$ wide per $8''$ long ($7''$ in rare cases, to avoid overlap between two adjacent slits) for the Cen and NE fields, while $10''$ long for both the SE and NW. The instrumental setup included a mosaic of two red-sensitive 2k×4k MIT CCDs (pixel size of $15 \times 15 \mu m$) that together with the Standard Resolution Collimator and a 2×2 binning granted a pixel-scale of $\sim 0.25''\,\mathrm{pxl}^{-1}$ and a field of view of $6.8'' \times 6.8''$. We then used the 1028z+29 holographic grism in conjunction with the OG590+32 order separation filter to cover a wavelength range of $7700 - 9500$ Å with a binned spectral dispersion of 0.84 Å pxl^{-1} and a resolving power of $R = \lambda_{\mathrm{cen}}/\Delta\lambda = 2560$ at $\lambda_{\mathrm{cen}} = 8600$ Å. The two component chips worked in standard operation mode (high gain with 100 kHz readout) having a gain of 0.7 ADUs/e^- and readout noises of 2.9 e^- and 3.15 e^- for chips 1 and 2, respectively.

[3]Magnitudes and colors reported in this chapter were not corrected for extinction and reddening, since the photometric information for the RGB stars is only needed in the estimation of [Fe/H], that already takes these effects into account (see Sect. 2.6). However, we did consider extinction and reddening when looking at which isochrones were compatible with the Sagittarius stream feature spotted in the Subaru/SuprimeCam photometry (see Sect. 2.8).

Calibration data (biases, arc lamp, dome flat-field frames) and slit acquisition images were acquired as part of the FORS2 standard calibration plan.

2.2.2 Data reduction

We adopt the same data-reduction process as in K17, based on IRAF[4] routines and custom-made *python* scripts. We have also explored the dedicated FORS2 pipeline available for download from ESO[5]. Although the ESO pipeline allows for a faster and more automatic data reduction leading to satisfactory results, we put it aside in favor of the custom-made pipeline, because the latter allowed us more flexibility over the intermediate steps that are part of the reduction process, such as cosmic-ray removal and sky-subtraction methodology.

For our custom-made pipeline we have managed standard IRAF tasks in a *python* environment in order to organize and reduce each OB dataset independently. Bias and flat-field corrections were performed on each of the two-dimensional (2D) scientific and arc-lamp calibration images; master bias and normalized master flat-field were created by combining five individual bias and five screen flat-field frames, respectively, which were typically taken during the morning after the night observing run. Science frames also needed to be corrected for bad-rows and cleaned from cosmic rays. The former step was necessary since several 2D spectra, especially in chip-2 frames, were affected by bad rows. We therefore used the IRAF *fixpix* task to replace bad regions linearly interpolating with nearby rows, a solution that improved the subsequent sky subtraction and spectral extraction. To deal with cosmic rays instead we used several iteration of the *L.A. Cosmic* algorithm (van Dokkum, 2001) adapted to the spectroscopic case.

It is known that images of 2D multi-object slit spectra can show significant distortions both in the spatial direction, where slit traces appear curved (the so-called *S-distortion*), and in the dispersion one, along which the instrument disperser tends to impose a wavelength-dependent curvature of the spectral lines (*C-distortion*). In our case, this is particularly evident in the red spectral range ($\lambda > 7000$ Å), which presents numerous OH telluric emission lines. These distortions needed to be taken into account for our dataset in order to perform a correct wavelength calibration and obtain well-extracted 1D spectra with minimal sky residuals. We used a custom made IRAF script (a combination of IRAF *identify*, *reidentify* and *fitcoords* tasks acting along the spatial direction)

[4]IRAF is the Image Reduction and Analysis Facility distributed by the National Optical Astronomy Observatories (NOAO) for the reduction and analysis of astronomical data. `http://iraf.noao.edu/`

[5]`http://www.eso.org/sci/software/pipelines/`

TABLE 2.2— Observing log of VLT/FORS2 MXU observations of RGB targets along the line-of-sight to the Cetus dSph.

Field	Position (R.A., Dec) (J2000)	Date / Hour (UT)	Exp. time (sec)	Airmass	Seeing (arcsec)	Grade$^{(\star)}$	Slits
Central	00:26:10.43, -11:03:09.0	2012-12-11 / 01:11	2614	1.09	0.84	A	35
		2012-12-11 / 01:56	2614	1.20	0.84	A	
		2012-12-12 / 00:55	2614	1.08	0.88	A	
		2012-12-12 / 01:40	2614	1.16	0.94	A	
		2013-08-11 / 06:30	2614	1.09	0.71	A	
		2013-08-30 / 04:59	2614	1.11	0.94	A	
NE	00:26:30.16, -10:59:53.9	2013-09-06 / 05:45	2614	1.03	0.80	A	18
		2013-09-06 / 06:33	2614	1.04	0.83	A	
		2013-09-14 / 02:03	2614	1.63	0.87	C$^{(a)}$	
		2013-09-14 / 02:48	2614	1.34	0.82	B	
		2013-09-14 / 03:33	2614	1.18	0.71	B	
		2013-09-30 / 02:14	2614	1.23	0.64	A	
		2013-09-30 / 06:56	2614	1.25	0.58	A	
SE	00:26:39.71, -11:10:16.4	2014-09-30 / 02:58	2614	1.12	0.62	A	18
		2014-09-30 / 03:42	2614	1.06	0.61	A	
		2014-10-02 / 01:18	2614	1.45	0.83	B	
		2014-10-02 / 02:06	2614	1.23	0.85	B	
		2014-10-02 / 02:52	2614	1.11	0.98	B	
NW	00:25:26.11, -10:56:12.1	2014-10-02 / 03:53	2614	1.04	1.08	A	12
		2014-10-02 / 04:38	2614	1.03	1.55	A	
		2014-10-29 / 01:48	2614	1.05	1.02	B	
		2014-10-29 / 02:34	1277	1.03	1.08	C$^{(b)}$	
		2014-11-23 / 02:02	2900	1.07	1.19	B	
		2014-11-23 / 02:52	2900	1.15	0.90	B$^{(c)}$	
Total							83

Notes. From left to right, column names indicate: the pointing field name; the field center coordinates; observing date and starting time of the scientific exposure; the exposure time in seconds; the starting airmass; the average DIMM seeing during the exposure in arcsec; the ESO OB fulfillment grades (a full description is reported in the notes below); the number of slits/observed objects per mask. For each field, the mask design remained identical in each OB. The total number of slits (83) is reported in the last row of the table.
$^{(\star)}$ ESO OB fulfillment Grades: A) Fully within constraints – OB completed; B) Mostly within constraints, some constraint is 10% violated – OB completed; C) Out of constraints – OB must be repeated: $^{(a)}$ airmass out of constraints – OB repeated; $^{(b)}$ at 02:57 seeing increased to $> 1.0''$ during execution – OB aborted; $^{(c)}$ although classified as completed, the OB did not have visible stellar continua, and was therefore discarded and not reduced.

to trace slit apertures in the science and arc-lamp images in order to correct for the S-distortion. We then cut the individual rectified 2D spectra and perform the wavelength calibration on each of them separately. We used in sequence IRAF *identify*, *reidentify* and *fitcoords* tasks to identify the Hg-Cd-Ar-He-Ne emission lines in the arc-lamp spectra and find the wavelength calibration function to be applied on the science spectra using the task *transform*. We used a spline3 function of order 2 in *identify / reidentify* tasks, while in *fitcoords* we made use of a chebyshev function of orders 4 and 2 along the x- and y- axis respectively. The typical RMS accuracy of the wavelength solution was of the order of 0.03 Å. Performing the wavelength calibration in the 2D spectra leads to the correction of the C-distortion and therefore to the straightening of the sky lines orthogonal to the stellar continuum, important for limiting sky-subtraction residuals in the extracted 1D spectra.

For the last part of the reduction process we made use of the IRAF *apall* task to obtain background-subtracted and optimally extracted 1D spectra. Outputs included also the extracted sky-background and the error spectrum (i.e. the flux uncertainty at each pixel). Finally, we applied the IRAF *continuum* task to normalize the flux distribution of the extracted 1D spectra fitting a high-order polynomial to the stellar continuum. The median S/N calculated around the CaT for the individual exposures resulted in $\sim$9 pxl^{-1} for the Cen and NE fields and $\sim$7 pxl^{-1} for the SE and NW ones. An example of a single exposure extracted spectrum (with a S/N = 10 pxl^{-1}), obtained using both IRAF tasks and the ESO-pipeline, can be seen in Fig. 2.2.

Below are some notes on the reduced data products.

- The NE field had an aborted OB due to airmass out of constraints. Since the exposure time was complete, we have decided to reduce it anyway. The extracted spectra were suitable for the subsequent analysis.
- Each OB of aperture 2 in chip-2 of the NE field suffered from bad rows on the stellar continuum that we could not fix. The extracted spectra were therefore compromised and were excluded from the analysis.
- The last OB of the NW field (date/time: 2014-11-23/02:52h), although classified by the observer as complete, did not have visible stellar continua and was therefore discarded and not reduced.

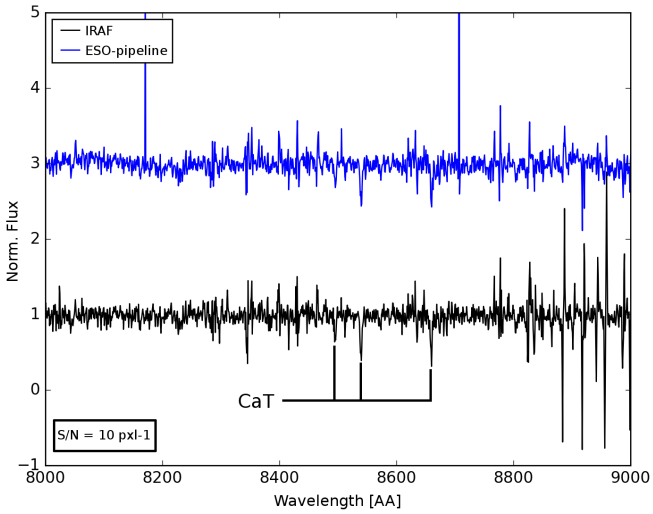

FIGURE 2.2— Example of output single-exposure normalized spectra obtained using the ESO-pipeline (upper blue spectrum) vs. IRAF tasks (lower black spectrum), for the same target star. The two spectra were offset on purpose for direct comparison. Although the IRAF reduced spectrum presents higher residual at redder wavelengths (where we note the presence of a telluric absorption band), around the CaT it turned out to be cleaner and less noisy than the ESO-pipeline reduced one.

2.3 Determination of line-of-sight velocities

We determined the line-of-sight (l.o.s.) velocities of the target stars on the combined spectra from the multiple science exposures. Prior to that, the spectra from the individual exposures had to be placed on a common zero-point by correcting them for offsets due to slight differences of the wavelength calibration, slit-centering shifts, and the different observing date.

We took advantage of having numerous OH emission lines in the extracted sky background to refine the wavelength calibration of the individual spectra. Scientific exposures, in fact, can suffer from instrument flexure that may introduce an offset with respect to calibration arc-lamp spectra, usually taken in

daytime with the telescope pointing at the zenith. We used the IRAF *fxcor* task to evaluate the offset between a reference sky spectrum and the object ones performing a Fourier cross-correlation over $8250 - 9000$ Å. The associated errors were calculated based on the fitted correlation peak height and the antisymmetric noise (Tonry & Davis, 1979). The calculated offsets, v_λ, varied between 5 and 22 $\mathrm{km\,s^{-1}}$ with a mean error of 2 $\mathrm{km\,s^{-1}}$ (equivalent to $0.2 - 0.8$ pxl; $1\,\mathrm{pxl} = 28\ \mathrm{km\,s^{-1}}$).

Most observations were taken under very good seeing conditions, with seeing smaller than the slit-width. If targets are not perfectly centered on their slits, there will be a systematic offset in wavelength calibration, and therefore on the velocity measurement. In order to calculate the slit-centering shift of the target stars, we made use of the through-slit images typically taken before each science exposure. The slit-offset was calculated as the difference in pixels between the center of the slit and the star centroid for every target in each mask. As shown in Fig. 2.3, for example, significant deviations were found at the borders of the frames, which were systematically present also on the other exposures, a fact that would make the mean shift per through-slit image an incomplete description of the situation. Therefore, we calculate an offset for each target as the median value of all the slit-shifts obtained for that target. The associated error is the scaled median absolute deviation (MAD) [6] of those values. Median shifts, v_{slit}, were found to be in the range $\pm 0.1 - 9\ \mathrm{km\,s^{-1}}$ with errors of $\pm 2 - 5\ \mathrm{km\,s^{-1}}$.

Finally, we used the IRAF *rvcorrect* task to calculate the heliocentric correction, v_ϕ, to apply to the individual spectra.

The spectra from the individual science exposures of each star were corrected for $\Delta v = v_\phi - v_\lambda - v_{\mathrm{slit}}$ with the IRAF *dopcor* task and finally averaged together weighting them by their associated σ-spectra. In order to associate error spectra to the stacked ones we have divided the individual σ-spectra by the polynomial used for the continuum normalization of the science spectra and combined them according to the formula for the error of the weighted mean [7]. We did this procedure for all the targets presented in our dataset.

The heliocentric velocity v_{hel} of each stacked spectra was obtained using the *fxcor* task by cross-correlating with an interpolated Kurucz stellar atmospheric model resembling a low-metallicity RGB star, similar to what we expect for our Cetus targets – $\log(g) = 1.0$, $T_{\mathrm{eff}} = 4000$ K, $[\mathrm{Fe/H}] = -1.5$ dex, convolved to have the same dispersion of our spectra and wavelength range between 8400 and 8700 Å (as in K17). The resulting final velocity errors have a mean value of $\pm 6\ \mathrm{km\,s^{-1}}$, with shift-related errors added in quadrature. Typical S/N values

[6] $MAD(X) = 1.48\ median(|X - median(X)|)$
[7] $\sigma^2(\lambda) = 1/\Sigma_i[1/\sigma_i^2(\lambda)]$

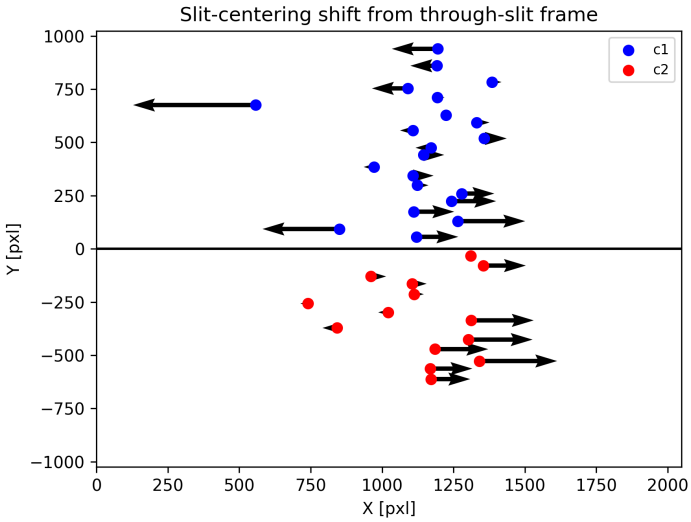

FIGURE 2.3— Arrow diagram showing slit-centering shifts from the through-slit frame associated with the first exposure of the central field: arrow lengths are the slit-centering shifts multiplied by a factor of 1000.

were ~ 20 pxl^{-1}.

A complete table with the velocity determinations for each target in our sample is reported in Appx. A.2, along with the corresponding field and slit information, RA-Dec coordinates, V- and I-band magnitudes, metallicity values obtained from the CaT lines as explained in Sect. 2.6, the S/N per pixel, and the membership status according to the criteria provided in Sect. 2.4.

2.3.1 Sanity checks

Our data reduction process has already been adopted and well tested in K17 using the same instrumental setup. However, our methodology differs from K17 in that the target velocities we obtained are from stacking the spectra of the individual exposures, rather than from the weighted mean of the velocities calculated on the individual science exposures. This choice was due to the fainter

magnitudes of our targets with respect to those in the Phoenix dwarf studied in K17, which yielded a lower S/N on the individual exposure spectra. We then performed a series of tests in order to assess the efficacy of our methodology.

We found that in the lower S/N regime, as for our individual exposure spectra, the velocity errors from *fxcor* appear underestimated. This was tested by injecting Poisson noise on a synthetic spectrum obtained from the Munari et al. (2005) library of spectra based on the Kurucz's code – log(g) = 2.5, $T_{\rm eff}$ = 4000 K, [M/H] = −2.5 dex to obtain a S/N ∼ 8 pxl^{-1}, then shifting the spectrum of a known quantity (2 Å ≡ 2.5 pxl ≡ 70 km s^{-1}) to simulate a l.o.s. velocity and finally cross-correlating with the CaT template. The process was repeated for 500 random realizations of the noise: while the median value of the recovered velocity was in excellent agreement with the input velocity (70.1 km s^{-1}), the median of associated errors calculated by *fxcor* was 8.2 km s^{-1}, much smaller than the MAD of the distribution of velocities (12.3 km s^{-1}). Therefore the errors calculated by *fxcor* were underestimated compared to the scatter in the velocity distribution from the simulated spectra.

We then repeated the previous test by stacking six synthetic spectra with the same shift and S/N as before, in order to reach a $S/N_{\rm sum} = \sqrt{6}$ S/N ∼ 20 pxl^{-1}, i.e., similar to that of our combined spectra. The shift was also very well recovered (71 km s^{-1}) and the median velocity error was now in much better agreement with the scatter of the velocity distribution (3.5 km s^{-1} and 4 km s^{-1}, respectively).

Furthermore, in the great majority of cases, each science exposure had a through-slit image associated to it, and taken immediately before. There were however a couple of exceptions among the consecutive exposures. In order to assess the reliability of velocity measurements from combined spectra with different (unknown) individual shifts, as for the exposures missing their own through-slit image, we repeated the previous test by stacking individual spectra, but this time assigning a slightly different velocity shift to each of them: the velocities are correctly recovered as long as the difference between individual shifts is less than 1 Å, which appears to be the case for our observations, as estimated from those consecutive exposures that *did* have their own through-slit frame associated. The above results then motivated our choice to derive the velocities, as well as the metallicities, directly from the stacked spectra.

We also verified the internal accuracy of our velocity measurements between the different pointings. For the Cen and NE fields, we used the three stars that they have in common: targets 17, 20, and 21 from Cen field corresponding to targets 10, 8, and 6 from the NE field, respectively (see Table A.4 for further details). The calculated heliocentric velocities for two of these stars resulted in very good agreement within 1-σ. However the heliocentric velocities of the

third star (target Cen-17/NE-8) were found to to agree only within 3.5-σ. We cannot exclude that the source of this discrepancy is due to the fact that this star is part of a binary system. Taking a look at the velocities obtained from single-exposure spectra as a function of the observing date, we obtain two blocks of measurements: those taken on December 2012 (with exposure from the Cen field only) show in general lower velocities than those taken between August and September, 2013 (comprising exposures from both the Cen and NE fields). Furthermore, this star is one of those in common with the Kirby et al. (2014) dataset (see Sect. 2.3.2): their observations were taken on the first two days of September 2013 and their reported heliocentric velocity was found to be in agreement with those we took in the same period. Nevertheless we have decided to not reject this star and average together the velocities from the two fields. The inclusion or exclusion of this target in the following kinematic analysis (see Sect. 2.5) did not have any significant impact on the final results. We did the same for the other two stars, since the velocity measurements between the two pointings were compatible with each other.

On the other hand, the SE and NW pointings do not overlap with the other ones. As another check of our internal zero points between different pointings, we derived the velocities of our stars also on the spectra reduced with the ESO pipeline, which is an entirely independent data reduction approach. We find that the velocities compare very well, except for a systematic offset of $\sim 2-3$ $\mathrm{km\,s^{-1}}$ ($\sim 0.07-0.1$ pxl) for all the fields. Since our reduction method has been consistently the same for all the exposures and fields, from this comparison we conclude that, at most, systematics between different pointings are negligible.

2.3.2 Comparison with other works

We have compared our l.o.s. velocities with those obtained in other works (Lewis et al., 2007, and Kirby et al., 2014). Primarily we compare with the work of Kirby et al. (2014) (hereafter K14), since the analysis made by Lewis et al. (2007), although performed using data of lower S/N, resulted in agreement with the former author.

We find 18 stars in common with K14, all of them classified as Cetus members. The l.o.s. velocity measurements overlap for 9 targets within the 1σ level of the quadratic sum of the errors, i.e. only 50% of the expected 68% if errors were perfectly estimated. Specifically, we examined the quantity $v/\varepsilon = (v_{\mathrm{hel},*} - v_{\mathrm{hel,K14}})/\sqrt{\varepsilon_*^2 + \varepsilon_{\mathrm{K14}}^2}$, which for random errors should resemble a normal distribution with mean and standard deviation $N(\mu,\sigma) \sim (0,1)$. In our case, the mean and standard deviation were found to be 1.2 and 1.6, respectively (see Fig. 2.4). If we exclude the highest deviant point with $v/\varepsilon > 5.0$, the v/ε

mean and dispersion reduce to 0.9 and 1.3, respectively. This was a justified choice since this measure in the K14 dataset has a low S/N (~ 5 Å^{-1}) compared to the average S/N of the other stars (~ 20 Å^{-1}), despite having a velocity error comparable to the dataset average value. We conclude that we mainly observe a systematic shift in the velocity measurements between the two datasets (~ 5 km s^{-1}), but estimate the velocity errors fairly well.

Moreover, we detected a slope when examining the velocity difference $\Delta V_{\rm hel} = v_{\rm hel,*} - v_{\rm hel,K14}$ versus our measured values $v_{\rm hel,*}$. In order to understand if this slope is due to a statistical fluctuation, we simulated a Gaussian velocity distribution with an intrinsic dispersion of 10 km s^{-1} from which we randomly selected 18 values. We then created two sets of values by further reshuffling the selected velocities according to the velocity error distributions measured in our sample and K14, respectively. We examined the two sets like we did for the common targets and calculated the slope by means of a least-square (LSQ) linear fit. We repeated this process 500 times, finding a median slope of 0.30 ± 0.15, where the error indicates the MAD scatter of the 500 measurements. The LSQ linear fit to the original data yields a slope of 0.67 ± 0.12, that is, $\sim$2-σ away from the simulated one. Also in this case, excluding the highest deviant point from the observed sample would bring the data and the mock sets into much better agreement ($\sim$1.5-σ). This appears to confirm that the main source of discrepancy between the two datasets is a systematic shift in the velocity measurements.

In the following kinematic analysis (see Sect. 2.5.3) we therefore expect to find at most a systematic displacement in the determination of the systemic velocity parameter between our sample and that of K14.

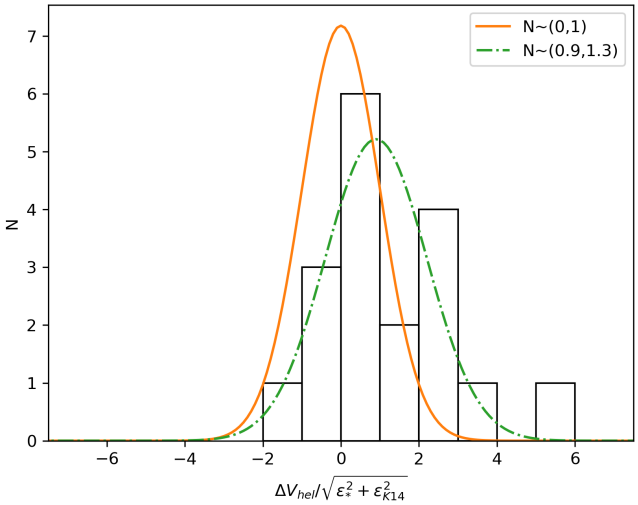

FIGURE 2.4— Distribution of velocity differences for stars in common between our dataset and that of Kirby et al. (2014). A normal distribution with mean and standard deviation $N(\mu,\sigma) \sim (0,1)$ is overplotted for direct comparison (continuous line), together with a normal distribution $N(\mu,\sigma) \sim (0.9, 1.3)$ (dot-dashed line) fitted to the velocity differences after discarding the most deviant measurement.

2.4 Membership selection

In order to perform an analysis of the properties of the Cetus stellar component, we need to identify the probable member stars and weed out possible contaminants from the sample. Our membership selection is based on the following criteria, applied step by step:

- In order to select only stars with magnitude and colors compatible with being RGB stars at the distance of the Cetus dSph, we compare the location of our targets on the color-magnitude diagram to expectations from theoretical isochrones shifted at Cetus' distance and broadly bracketing the range of stellar ages and metallicities expected from Cetus' stellar population from SFH determinations (Monelli et al., 2010). This step

is necessary because not all targets fall on the Cetus RGB (see Fig. 2.1 right) due to the allocation to random objects for some of the slits remaining otherwise empty. We selected all targets located between Padova isochrones (Girardi et al., 2000) with age $t_{\rm age} = 10$ Gyr and [Fe/H] ~ -2.3 dex (which sets the "blue" limit at $(V-I) \sim 0.9$), and age $t_{\rm age} = 8$ Gyr and [Fe/H] ~ -0.4 dex (which sets the "red" limit at $(V-I) \sim 2.0$). Our sample was reduced from 80 to 69 targets.

- We performed an initial kinematic selection on the sample of 69 targets, excluding all those with evidently outlying l.o.s. velocities, imposing the following velocity cut: $|v_{\rm hel,i} - median(v_{\rm hel})| \leq 5\ MAD(v_{\rm hel})$. We also excluded one target to which we could not associate a metallicity value (see Sect. 2.6): this choice was motivated by the fact that this target also has one of the highest velocity errors (~ 20 km s^{-1}) and the lowest S/N (~ 5 pxl^{-1}) in our sample. Our dataset was therefore reduced from 69 to 58 targets.
  We further performed a more strict kinematic selection, iteratively retaining those objects $|v_{\rm hel,i} - \bar{v}_{\rm hel}| \leq 3\sigma_{\rm v} + \varepsilon_{\rm i}$, where the heliocentric systemic velocity $\bar{v}_{\rm hel}$ and intrinsic velocity dispersion $\sigma_{\rm v}$, are derived as explained in Sect. 2.5. This step finally reduced the sample to 54 most probable members. Since the spread in the observed distribution of l.o.s. velocities is the result of both the intrinsic l.o.s. velocity dispersion of the system and the uncertainties in the velocity measurements, it could be argued that this last step is too strict and excludes genuine members. We have double-checked that making an iterative selection on $|v_{\rm hel,i} - \bar{v}_{\rm hel}| \leq 3\ MAD(v_{\rm hel})$ would lead to the same result.

According to the Besançon model (Robin et al., 2003), simulated in the direction of Cetus on a solid angle of 0.05 deg^2 (equivalent to the summed area of the four FORS2 pointings) and over a distance range up to 100 kpc, five MW contaminants could still have passed our photometric and kinematic selection criteria. This number can be considered as an upper limit since on the area surveyed the surface density of Cetus is higher than that of the Galaxy, therefore when allocating slits onto objects we are more likely to have sampled Cetus' population than the MW one.

2.5 Kinematic analysis

2.5.1 Systemic velocity and velocity dispersion

We have performed a Bayesian analysis to measure kinematic parameters for our dataset (such as Cetus' heliocentric systemic velocity and velocity dispersion) and investigate the possible presence of rotation. Due to the small angular scales we are exploring, no significant velocity gradient is expected due to the projection of the Sun and Local Standard of Rest (LSR) motion onto the l.o.s. of the individual stars (nor of the 3D motion of the galaxy), therefore in the following we continue working with velocities in the heliocentric reference frame, even if not explicitly mentioned.

First, we have carried out an initial analysis considering our system as being supported by dispersion only. Following Walker et al. (2006), we have assumed that the likelihood function for a distribution of N member stars with l.o.s. velocities $v_{\rm hel,i}$ and associated errors $\varepsilon_{\rm i}$ has the following form:

$$L\left(\{v_{\rm hel,1},\ldots,v_{\rm hel,N}\}\right)=\prod_{\rm i=1}^{\rm N}\frac{1}{\sqrt{2\pi(\varepsilon_{\rm i}^2+\sigma_{\rm v}^2)}}exp\left[-\frac{1}{2}\frac{(v_{\rm hel,i}-\bar{v}_{\rm hel})^2}{(\varepsilon_{\rm i}^2+\sigma_{\rm v}^2)}\right], \quad (2.1)$$

where $\sigma_{\rm v}$ is the intrinsic l.o.s. velocity dispersion of the system and $\bar{v}_{\rm hel}$ the l.o.s. systemic velocity.

These last two are the parameters of interest that we have numerically estimated using the *emcee* code (Foreman-Mackey et al., 2013), a *python* implementation of the Goodman & Weare (2010) affine-invariant Monte-Carlo Markov chain (MCMC) ensemble sampler. The code allowed us to calculate the posterior distributions associated to the parameters. As priors, we demanded positive and negative values, respectively, for the velocity dispersion and the systemic velocity (the latter is justified because we know from previous works (Lewis et al., 2007; Kirby et al., 2014) that Cetus is approaching the Sun). We initialized the sampler setting applying the median and the MAD of a Gaussian fit to the l.o.s. velocity distribution of probable member stars as starting guesses for our free parameters.

As explained in the previous section, the estimation of the parameters was an iterative process, repeated until convergence. We obtain a systemic velocity and velocity dispersion of $\bar{v}_{\rm hel}=-79.0^{+1.6}_{-1.7}$ and $\sigma_{\rm v}=11.0^{+1.5}_{-1.3}$, as shown in Fig. 2.5, where $\bar{v}_{\rm hel}$ and $\sigma_{\rm v}$ are the median of the corresponding posterior distributions, while the limits enclosing 68% of each distribution were set as the asymmetric 1-σ confidence intervals.

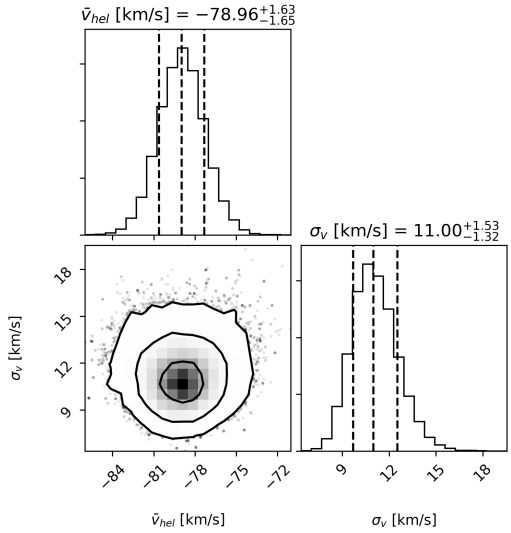

FIGURE 2.5— MCMC 2D and marginalized posterior probability distributions for the systemic velocity and velocity dispersion parameters. Dashed lines in the histograms indicate the 16th, 50th, and 84th percentiles. Contours are shown at 1, 2, and 3-σ level.

2.5.2 Rotation

The next step in the analysis was to search for evidence of rotation in our dataset, investigating different kinematic models. In order to do so, we modified the likelihood function introduced in Eq. 2.1, substituting the systemic velocity parameter for a relative velocity one:

$$\bar{v}_{\rm hel} \rightarrow v_{\rm rel,i} = \bar{v}_{\rm hel} + v_{\rm rot}(R_{\rm i})cos(\theta - \theta_{\rm i}), \tag{2.2}$$

where $(R_{\rm i}, \theta_{\rm i})$ are the angular distance from the galaxy center and position angle (measured from north to east) of the i-target star, θ is the position angle of the kinematic major axis[8] and $v_{\rm rot}(R_{\rm i})$ is the observed rotational velocity along

[8]The kinematic major axis indicates the gradient axis, i.e., the axis along which the l.o.s. velocities deviate furthest from $\bar{v}_{\rm hel}$; it is perpendicular to the axis of rotation.

this axis. A complementary parametrization of the rotation term explicitly based on the standard coordinates $(X_{\rm i}, Y_{\rm i})$ would be: $v_{\rm rot}(R_{\rm i})cos(\theta - \theta_{\rm i}) \equiv v_{\rm rot}(X_{\rm i}, Y_{\rm i})(X_{\rm i}sin\theta + Y_{\rm i}cos\theta)$, where $v_{\rm rot}(X_{\rm i}, Y_{\rm i}) = v_{\rm rot}(R_{\rm i})/R_{\rm i}$ (see e.g. Martin & Jin, 2010).

We considered three models for $v_{\rm rot}$:

- linear or solid-body rotation, $v_{\rm rot}(R_{\rm i}) = \frac{dV}{dR}R_{\rm i} = kR_{\rm i}$ with k a constant velocity gradient;
- flat or constant rotation, $v_{\rm rot}(R_{\rm i}) = v_{\rm c} = {\rm constant}$;
- no rotation, $v_{\rm rot}(R_{\rm i}) = 0$, with $v_{\rm rel,i}$ reducing to $\bar{v}_{\rm hel}$ i.e. to the dispersion-only case described above.

Subsequently we wanted to explore which model was to be preferred over the others. We recall the Bayes theorem, rewritten here to condition explicitly on the model under consideration:

$$P(\Theta|D, M) = \frac{P(D|\Theta, M)P(\Theta|M)}{P(D|M)}, \tag{2.3}$$

where $P(\Theta|D, M)$ is the posterior distribution of parameters Θ for model M given the observed data D, $P(D|\Theta, M)$ is the likelihood function accounting for model parameters, $P(\Theta|M)$ is the prior distribution representing our *a priori* knowledge of the considered model, and $P(D|M) = Z$ is the so-called *Bayesian evidence*, a normalization factor usually ignored for parameter estimation but of central importance for model selection. The Bayesian evidence represents the average of the likelihood over the prior for a specific model choice. If we have two models, M_1 and M_2, we can compare them through the *Bayes factor*, i.e., the ratio between their evidences: $Z_1/Z_2 = B_{1,2}$. A positive value tends to favor M_1 over M_2. The significance of one model with respect to another can be based on the Jeffrey's scale, computing the natural logarithm of $B_{1,2}$: values of (0-1), (1-2.5), (2.5-5), (5+) corresponds to inconclusive, weak, moderate and strong evidence favoring the first model over the second one (see also Wheeler et al., 2017).

The evaluation of Z is a nontrivial computational task. To do this, we used the *MultiNest* code (Feroz et al., 2009), a fast and efficient multi-modal nested sampling algorithm. The *nested sampling* (Skilling, 2006) is a Monte Carlo technique that allows to evaluate Bayesian evidence and at the same time provide posterior parameter estimation as a by-product. The MultiNest code is an implementation of this algorithm that produces posterior samples from distributions that could be multi-modal or degenerate at high dimensions.

TABLE 2.3— MultiNest output evidences and best-fitting parameters of the kinematic models applied to our dataset.

Models	$\log(Z)$	$\bar{v}_{\rm hel}$ ($\mathrm{km\,s^{-1}}$)	$\sigma_{\rm v}$ ($\mathrm{km\,s^{-1}}$)	k ($\mathrm{km\,s^{-1}\,arcmin^{-1}}$)	$v_{\rm c}$ ($\mathrm{km\,s^{-1}}$)	θ (deg)
Linear	-220.0	$-79.2^{+1.8}_{-1.7}$	$11.1^{+1.6}_{-1.4}$	$0.32^{+0.55}_{-0.53}$		$48.7^{+51.3}_{-54.2}$
Flat	-219.2	$-79.0^{+1.7}_{-1.7}$	$11.1^{+1.6}_{-1.3}$		$-1.28^{+2.7}_{-3.1}$	$154.2^{+46.6}_{-52.9}$
No rotation	-217.2	$-78.9^{+1.7}_{-1.6}$	$11.0^{+1.6}_{-1.3}$			

Notes. The reported values of the kinematic parameters represent the median of the corresponding marginalized posterior distributions, with 1-σ errors set as the confidence intervals around the central value enclosing 68% of each distributions.

In our case, we have calculated the evidences for all three models, together with their parameter estimation. We want to stress that the resulting values relative to the $v_{\rm rot}$ parameter represent a lower limit on the intrinsic value of the rotational velocity: this is due to $v_{\rm rot} = v_{\rm rot}^{\rm intrinsic}\sin(i)$, where i is the angle between the angular momentum vector and the line of sight direction. Since $\sin(i)$ is unconstrained in dwarf spheroidals, we refer simply to $v_{\rm rot}$. We specified the following prior ranges: $\bar{v}_{\rm hel} < 0$ $\mathrm{km\,s^{-1}}$, $\sigma_{\rm v} > 0$ $\mathrm{km\,s^{-1}}$, $-10 < k < 10$ $\mathrm{km\,s^{-1}\,arcmin^{-1}}$, $-20 < v_{\rm c} < 20$ $\mathrm{km\,s^{-1}}$. For the prior over θ we performed an iterative choice: we initially set the prior range $0 < \theta < \pi$, run the MultiNest code once for the rotational models performing a parameter estimation, took the maximum value from θ posterior distribution and used this value, $\theta_{\rm m}$, to update the prior range to $-\frac{\pi}{2} < \theta - \theta_{\rm m} < +\frac{\pi}{2}$, and run again the MultiNest code.

The resulting model evidences and relative estimated parameters are reported in Table 2.3. We found that the recovered velocity gradient k for the linear rotation model aligns roughly along the major axis, while for the flat rotation model the constant rotational velocity component $v_{\rm c}$ is recovered instead along the minor axis. We note however that both rotational signals are very weak and compatible with zero. Figure 2.6 displays the velocity distribution along the major and minor axis with the velocity estimated parameters from the two models overplotted accordingly.

Comparing the evidences of the linear rotation model against the flat rotation one we have $\ln B_{\rm lin,flat} = \ln Z_{\rm lin} - \ln Z_{\rm flat} = -0.8$, that is, the solid-body model is not favored over the other. If we compare now the evidence of the most favored rotational model (the constant rotation one) with the dispersion-only model, we have $\ln B_{\rm rot,disp} = \ln Z_{\rm rot} - \ln Z_{\rm disp} = -2.0$, that is, the model with rotation is not favored and the simplest dispersion-only model is to be preferred. Estimated parameters for the solid-body rotational model are shown

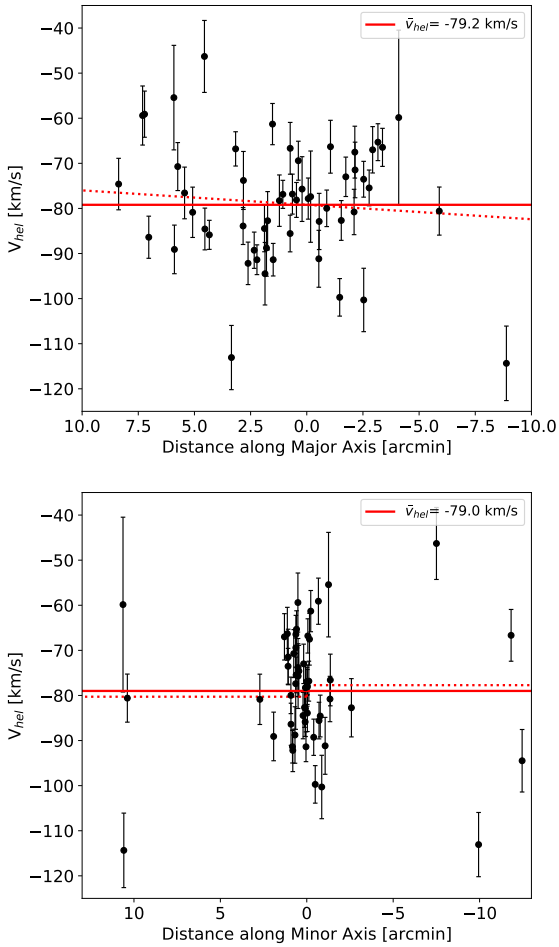

FIGURE 2.6— Line-of-sight velocity distributions of the probable members – *top panel*: along the optical major axis, with the systemic velocity (solid line) and the rotational component (dotted line) resulting from MultiNest run using the linear rotation model overplotted; *bottom panel*: along the minor axis, with the systemic velocity (solid line) and the rotational component (dotted line) resulting from MultiNest run using the flat rotation model overplotted. As can be seen from both panels the rotational component is negligible.

in Fig. 2.7. We note that the systemic velocity and velocity dispersion are in excellent agreement in all of the three cases analyzed.

Since we have found no evidence of rotation in the Cetus dSph, we can calculate its dynamical mass within the half-light radius using the Wolf et al. (2010) mass-estimator for pressure-supported spherical systems: $M_{1/2} = 3G^{-1}\sigma_{\rm v}^2 r_{1/2}$, where $r_{1/2}$ is the 3D de-projected half-light radius that can be well approximated by $\frac{4}{3}R_e$. Substituting the values[9], we obtained $M_{1/2} = 67^{+19}_{-16} \times 10^6 M_\odot$, that corresponds to a mass-to-light ratio within the half-light radius of $M_{1/2}/L_V = 23.9^{+9.7}_{-8.9} M_\odot/L_\odot$, assuming $L_V = 2.8 \pm 0.8 \times 10^6 L_\odot$ (obtained transforming the absolute magnitude value reported by McConnachie & Irwin, 2006). Our values of the dynamical mass $M_{1/2}$ and velocity dispersion $\sigma_{\rm v}$ were found to be compatible to those found for other galaxies of similar luminosity in the LG (see e.g., Kirby et al., 2017).

Using the K14 velocity dispersion value, Brook & Di Cintio (2015) found Cetus to be an outlier in its stellar-dark matter halo mass properties, where the latter was calculated taking into account modifications in the dark-matter halo density profile due to stellar feedback. This appears to be due to Cetus being more extended with respect to systems of similar luminosity and internal kinematics. Our new determination of Cetus' velocity dispersion would not imply a significant change in its dark-matter halo mass properties. Therefore Cetus would continue to be an outlier, showing a lower dark matter halo mass than expected. However, as recently reported by (Buck et al., 2019) analyzing results from the high-resolution NIHAO simulation, the position of Cetus on the stellar-dark matter halo mass diagram would be compatible with those of nearby isolated dwarf galaxies that experienced in the past a close encounter with a host-galaxy (i.e. the so-called "backsplash" systems), which resulted in a significant mass loss. This result shows how the halo mass properties of dwarf systems with stellar masses $\lesssim 10^{6.5} M_\odot$ are still part of an evolving picture.

We refer to Sect. 5.2.1 and 5.2.2, for a further discussion on the kinematic and mass properties of LG dwarf galaxies.

2.5.3 Comparison with other works

We have also run the MultiNest code on the Lewis et al. (2007) (hereafter L07) and Kirby et al. (2014) datasets. The values we recover for the systemic velocity and velocity dispersion for the dispersion-only case are in agreement (within the 1-σ errors) with the values reported by these authors. We therefore refer to their

[9] For the velocity dispersion we have used the *MultiNest* output value from the dispersion-only case.

values in the following discussion.

For the systemic velocity, we find a shift of ~ 5 km s^{-1} (~ 8 km s^{-1}) between the results of K14 (L07) and ours ($\bar{v}_{\rm hel,K14} = -83.9 \pm 1.2$ km s^{-1}; $\bar{v}_{\rm hel,L07} = -87 \pm 2$ km s^{-1}). As reported in Sect. 2.3.1, we are aware that our velocities might suffer from a 2-3 km s^{-1} systematic shift.

The velocity dispersion measured by K14 is $\sigma_{\rm v,K14} = 8.3 \pm 1.0$ km s^{-1}, differing from our measured value by approximatively 1.5-σ. This last discrepancy could be explained by the different spatial distribution of our targets with respect to those observed by K14, and the existence of a mild metallicity gradient in Cetus, with the metal-rich stars displaying a colder kinematics than the metal-poor ones (see Sect. 2.6.2). Indeed, if we select from our catalog only those targets in the central fields (i.e., Cen and NE) and perform again the parameter estimation, we recover $\sigma_{\rm v,inner} = 8.9^{+1.3}_{-1.2}$ km s^{-1}, which is in perfect agreement with the K14 value. However it is harder to reconcile L07 findings with ours and those of K14. Their reported velocity dispersion $\sigma_{\rm v,L07} = 17 \pm 2.0$ km s^{-1} deviates significantly from our value and that of K14 in particular, although the two datasets have a similar spatial distribution. We would therefore have expected a lower dispersion value. In their analysis, K14 reported that applying their membership selection criteria they were able to lower the $\sigma_{\rm v,L07}$ value to $12.0^{+2.0}_{-1.9}$ km s^{-1}. They explained the further discrepancy from their reported value with the fact that L07 data had in general a lower S/N. This value instead is in very good agreement with our velocity dispersion result.

When searching for the presence of velocity gradients, we did not find any evidence in support of rotation in the K14 dataset, as already reported by Wheeler et al. (2017) who performed a similar analysis to ours. In the case of Lewis et al. (2007) data instead, the flat rotational model is weakly favored over the others, confirming the authors impressions about a hint of rotation in Cetus.

2.5.4 MultiNest mock tests

We performed a series of mock tests to understand what classes of rotational properties we could have expected to detect, given the characteristics of the observational datasets, in terms of number statistics, velocity errors, and spatial coverage.

To this aim, we created separate mock catalogs of objects with the spatial positions and velocity error distributions similar to the spectroscopic catalogs of L07, K14, and ours; the velocities were randomly extracted from Gaussian velocity distributions centered around zero and with a fixed $\sigma_{\rm v} = 10$ km s^{-1}, to which we add a projected rotational component $v_{\rm rot}$, following the differ-

ent kinematic models described in Sect. 2.5.2. For our simulations, we tested $v_{\rm rot}/\sigma_{\rm v} = n$, where $n = \{0, 0.25, 0.5, 1, 2\}$ at the half-light radius $R_{\rm e}$ (2.7 arcmin). We note that for $n = 0$, we reduce to the dispersion-only case. These test rotational velocity values were chosen so as to explore different amounts of rotation versus dispersion support of the stellar component, i.e., $v_{\rm rot}/\sigma_{\rm v}$. For a galaxy of the ellipticity of Cetus ($e = 0.3$), the expectation for an oblate isotropic self-gravitating system flattened by rotation corresponds to a $v_{\rm rot}/\sigma_{\rm v}$ value of 0.5 (Binney, 1978); lower values would indicate that the system is flattened by anisotropy, while larger values indicate that the rotational support is dominant over the pressure support.

Specifically, for the linear rotation model, $v_{\rm rot} = kR_{\rm i}$, and the n-values of the velocity gradient k corresponding to the above $v_{\rm rot}/\sigma_{\rm v} = n$ at the half-light radius, would be $k = n\sigma_v/R_e = \{0, 0.9, 1.85, 3.7, 7.4\}$ [km s^{-1} arcmin^{-1}]. For the constant rotation model, $v_{\rm rot} = v_{\rm c} =$ constant, and we had $v_{\rm c} = n\sigma_{\rm v} = \{0, 2.5, 5, 10, 20\}$ [km s^{-1}].

We also explored different values for the kinematic axis position angle $\theta = \theta_{\rm C} + \{0°, 45°, 90°\}$, where $\theta_{\rm C} = 63°$ is the Cetus position angle. We subsequently ran the MultiNest code in order to calculate the evidences of each model (the two rotational and the dispersion-only ones) as done in Sect. 2.5.2, finding $\ln B_{\rm lin,flat}$ and $\ln B_{\rm rot,disp}$ and estimating the related parameters. Each case process was repeated N=100 times. All the results are reported in tabulated form in Appendix A.1.

The analysis showed that the three catalogs have a different sensitivity in the ability to detect rotation with high significance, according to the direction of the input kinematic major axis: for example, the K14 dataset distinguishes gradients along the projected major axis more easily, while our FORS2 dataset is better for detecting gradients along the projected minor axis; this is most likely due to the different spatial coverage.

For all the three spectroscopic catalogs and both rotational models, the analysis of the velocities yielded strong evidence in favor of there being rotation for the $n = 2$ case and recovered the correct rotational input model (with moderate evidence for the L07 catalog with constant input rotation).

For the $n = 1$ case, evidence in favor of rotation is still strong (or in a minority of cases, moderate or weak) with the three catalogs for both input models. However, in most cases, the correct input rotational model cannot be recovered with conclusive evidence if rotation is constant with radius. Nonetheless, the systemic velocity, internal dispersion, and position angle of the gradient appear reliably determined.

For the $n = 0.5$ case and linear model, there is still strong or moderate evidence for rotation in ours and K14's catalog, depending on the axis of the

input kinematic gradient. This indicates that the complementary information provided by our FORS2 and K14's catalogs would have made it possible to establish if Cetus had a rotational velocity at the half-light radius compatible with an isotropic rotator (and have its elliptical shape due to rotational flattening).

In general, rotation constant with radius was more difficult to detect with respect to solid-body rotation. This can be explained by the fact that mock velocities for the linear rotation model were calculated at the half-light radius $R_{\rm e}$, while the spatial coverage of all the considered catalogs reaches far beyond this value ($r_{\rm max} \sim 15'$). Therefore at larger radii than $R_{\rm e}$, the constant rotational component is more easily hidden by the velocity dispersion with respect to the linear model.

Finally, for case $n = 0$, i.e. dispersion-only, all catalogs indeed showed no evidence of rotation. This indicates that the Bayesian analysis using the *MultiNest* code is not biased in favor of rotational models.

These simulations have shown that if rotation in Cetus were significant, with the current sets of observations we would have already detected it. Instead, our analysis on the observed datasets has shown no evidence in favor of rotation, indicating that Cetus is mainly a dispersion-supported system where an eventual rotational component would be weak, and therefore not likely to cause the observed ellipticity. Furthermore, these results should be considered as conservative, taking into account the higher ellipticity value we have found when analyzing the structural properties of Cetus, as explained in Sect. 2.7: a higher ellipticity would require the presence of a stronger rotation signal to flatten the system, which is not the case as already described above.

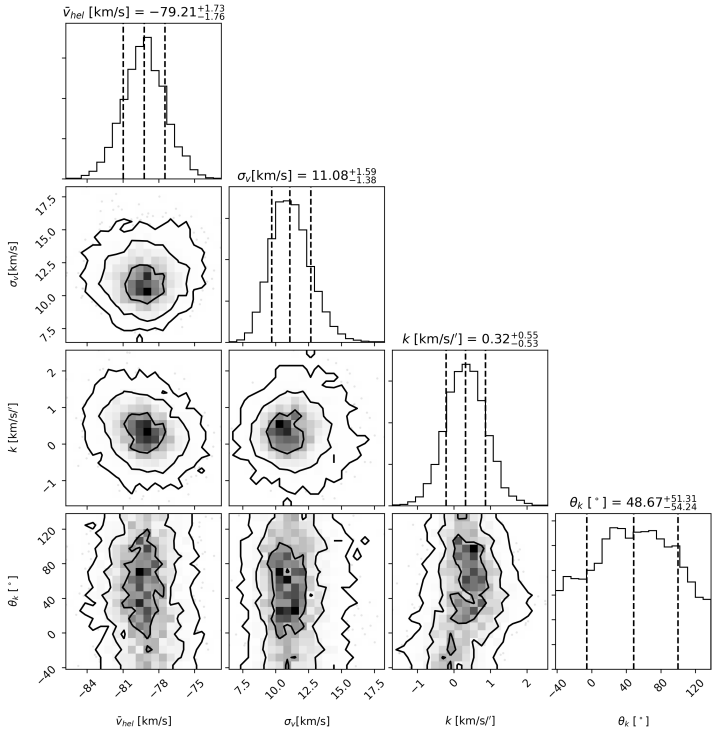

FIGURE 2.7— MultiNest 2D and marginalized posterior probability distributions for the solid-body rotational model parameters. Dashed lines in the histograms indicate the 16th, 50th and 84th percentiles. Contours are shown at 1, 2, and 3-σ level.

2.6 Metallicity properties

We have estimated metallicity ([Fe/H]) values for the probable Cetus members in our FORS2 sample measuring the strength of the CaT lines ($\lambda\lambda$ = 8498.02, 8542.09 and 8662.14 Å). Our measurements relied on the empirical calibration that connects a linear combination of the CaT lines equivalent widths (EW) and the star magnitude to the corresponding [Fe/H] values. The method has been widely applied in the literature for a variety of stellar systems, from MW globular and open clusters (e.g., Rutledge et al., 1997; Cole et al., 2004; Carrera, 2012) to LG dwarf galaxies (e.g., Tolstoy et al., 2001; Battaglia et al., 2008b; Ho et al., 2015), and tested and calibrated over a broad range of metallicities and stellar ages (e.g., Battaglia et al., 2008b; Starkenburg et al., 2010; Carrera et al., 2013; Vásquez et al., 2015).

Given that we share the same stellar target types and instrumental setup with K17, we adopted their approach. The authors examined various calibration methods, alongside testing the most suitable way for measuring the EW of CaT lines in the individual spectra, testing the results on calibrating globular clusters. Following their conclusions, we have used the Starkenburg et al. (2010) relation, using a Voigt fit for the estimation of the EW of the individual CaT lines (with the flux being integrated over a region of 15 Å around the CaT lines of interest) and linearly combining the EW of the two strongest CaT lines; for the $(V - V_{\rm HB})$ term, which allows for comparison of stars of different luminosities, making the calibration also reddening and distance independent, we adopted $V_{\rm HB} = 25.03$ (the mean visual magnitude of the RR-Lyrae stars from Bernard et al., 2009).

The EWs are determined from the continuum normalized stacked spectra, integrating the flux from the Voigt profile best-fit over a window of 15 Å around the CaT lines of interest and adopting the corresponding error-spectra as the flux uncertainty at each pixel in the fitting process. The errors on the EW measurements were calculated directly from the covariance matrix of the fitting parameters. As a test, we also calculated EW uncertainties using an analytical formula adapted from Cayrel (1988) and Battaglia et al. (2008b) based solely on the resolution and S/N of the spectra:

$$\Delta_{\rm EW} = 2.45\sqrt{\sigma_{\rm Gauss}}\ {\rm S/N}^{-1}, \tag{2.4}$$

where S/N is the signal-to-noise ratio per Å calculated in the continuum regions around the CaT and $\sigma_{\rm Gauss}$ is the 1-σ width obtained performing a Gaussian fit to the CaT lines, which we can assume as representative of the line broadening of the Voigt profiles. Uncertainties on [Fe/H] were calculated propagating the EW errors for both approaches. The two kind of errors were found to be correlated and have good agreement between them: the median value of those obtained

from the analytic estimates resulted in 0.09 dex, while for the uncertainties derived from the line-fitting covariance matrix resulted in a median value of 0.13 dex. We have decided therefore to use the latter as final [Fe/H] errors.

As done for the radial velocity measurements, the relative accuracy of the metallicity values has been assessed using the three stars in common between the Cen and NE pointings: all the calculated values resulted in excellent agreement and were then averaged together (see Table A.4).

From the [Fe/H] values we derived, we find that Cetus is a metal-poor system with a significant metallicity spread – median [Fe/H] = −1.71 dex, standard deviation = 0.45 dex, MAD = 0.49 dex [10]. This is the first time that metallicities derived from individual RGB stars in Cetus are being made publicly available (see Table A.4).

The derived median [Fe/H] value is in excellent agreement with integrated [Fe/H] quantity derived from SFH studies ($\langle$[Fe/H]$\rangle \sim -1.7$ dex, Monelli et al., 2010). Moreover, this value is in good agreement with the stellar luminosity-metallicity linear relation for LG dwarf galaxies reported by Kirby et al. (2013b), where the Cetus value lies below the relation, but within the rms scatter (see also Fig. 5.7). Looking at the metallicity spread, Leaman et al. (2013) have shown that the anti-correlation found by Kirby et al. (2011) between the mean metallicity of a dwarf galaxy and its intrinsic spread in [Fe/H] tends to saturate at high luminosities ($\gtrsim 10^5 L_\odot$) (see also Ho et al., 2015). The calculated spread in [Fe/H] may be inflated by uncertainties on the individual measurements. In order to obtain the intrinsic spread, we applied Eq. 8 of Kirby et al. (2011); this yielded $\sigma_{[Fe/H]} = 0.42 \pm 0.03$ dex, where the associated error is calculated as in the Appendix of Hargreaves et al. (1994). The intrinsic spread is in agreement with the value calculated by simply subtracting in quadrature the mean error in metallicity of the sample from the standard deviation of the metallicity distribution function. Our $\sigma_{[Fe/H]}$ value is then compatible with the saturated trend followed by the other dwarf galaxies of similar or higher luminosity. However, $\sigma_{[Fe/H]}$ is calculated on [Fe/H], which is a logarithmic quantity. Expressing [Fe/H] values in terms of linear metal fraction, $Z_i/Z_\odot = 10^{[Fe/H]_i}$, the flattened trend disappears, as shown in Leaman et al. (2012). Assuming Z uncertainties as $\delta Z_i/Z_\odot = (Z_i/Z_\odot)\ln(10)\delta[Fe/H]_i$, we got, in analogy to $\sigma_{[Fe/H]}$, the intrinsic $\sigma(Z/Z_\odot)^2 = 3.7 \times 10^{-4}$. This value is in very good agreement with the tight correlation between average linear metallicity $\bar{Z}$ and $\sigma(Z/Z_\odot)^2$ reported by Leaman et al. (2012).

[10] Median [Fe/H] value obtained transforming the metallicities to their corresponding Z values and then transforming back to [Fe/H] the calculated median Z value.

2.6.1 Signs of a metallicity gradient

We analyzed the spatial variation of the metallicity properties looking at the distribution of [Fe/H] as a function of elliptical radius: as shown in Fig. 2.8, we observe a decreasing trend, that is, the metal-richer members look spatially concentrated toward the galactic center. An error-weighted linear least-square fit to the data showed the presence of a mild metallicity gradient of $m = -0.033 \pm 0.014$ dex arcmin^{-1} (-0.15 ± 0.06 dex kpc^{-1} $= -0.09 \pm 0.04$ dex $R_{\rm e}^{-1}$, with distance and $R_{\rm e}$ values as reported in Table 2.1). The trend was also confirmed by a running-median: the gradient is almost constant inside $R_{\rm e}$, it gets steeper up to $\sim 3R_{\rm e}$ where it starts to flatten again.

The presence of a metallicity spread combined with the lack of a gradient within Cetus' half-light radius, and possible drop beyond that, is in excellent agreement with the analysis of deep photometric datasets: analyzing Cetus' SFH as a function of radius, Hidalgo et al., 2013 detected no population gradient inside the galaxy half-light radius $R_{\rm e}$. On the other hand, Monelli et al. (2012) have shown using photometry on a wider area (up to half of Cetus tidal radius $\sim 15'$) that the metal poorer population on the RGB starts to dominate at radii grater than $\sim R_{\rm e}$ and it is ubiquitous at all radii.

When considered at face value, the slope of the best least-square fit to the individual metallicities as a function of radius would suggest a much shallower metallicity gradient in Cetus than in the other LG dSphs, and make it more akin to what is seen for example in the WLM dIrr (see Leaman et al., 2013).

However, when looking at both simulations and observations in more detail, one finds that a simple linear fit is often not a complete description of the spatial variations of the metallicity properties. For example, in similarly luminous systems like Sculptor and VV 124, the mean metallicity remains fairly constant in the inner regions, then declines and is followed by a plateau (see Fig. 14 in Schroyen et al., 2013, and references therein). This is exactly the kind of trend that we see in Cetus, when considering a running median of the metallicity as a function of radius. For example, the slope of the declining region, expressed in dex $R_{\rm e}^{-1}$, is -0.16 for VV 124, -0.26 for Sculptor (both values as in Schroyen et al., 2013)[11] and -0.17 ± 0.08 for Cetus. In this respect, the wide-area metallicity properties of Cetus appear to resemble those of similarly luminous, pressure-supported dwarf galaxies, characterized by an early dominant period of star formation. It is interesting to note that these three systems

[11] We note that the metallicity values used for VV 124 in Schroyen et al., 2013 were too high by about 0.4 dex, as reported in the errata by Kirby et al., 2013a. However, using the updated metallicity values we find that the slope of the declining region remains unchanged, as do our conclusions.

span a range of environments: Sculptor is a MW satellite, VV 124 is extremely isolated ($D > 1$ Mpc), while Cetus is found in isolation at present, although it cannot be excluded that it might have experienced a pericentric passage around one of the large LG spirals.

An alternative approach to examine the general radial trend of metallicity data and at the same time provide meaningful error bars is the Gaussian process regression (GPR) analysis[12]. The GPR has the advantage of being a kernel-based non-parametric probabilistic method that makes it possible to compute empirical confidence intervals. Since we are looking for a smooth function, it performs better than a least-square fit in finding the general trend in the data, being similar in this sense to a running median. For the GPR analysis we used a Gaussian kernel together with a noise component to account for the intrinsic metallicity scatter. As shown in Fig. 2.8, the GPR result follows the trend marked by the running median. However, the large 1-σ confidence interval prevents a firm conclusion on the presence of a metallicity gradient in Cetus.

In this regard, we performed a simple simulation assuming that Cetus hosts no radial gradient. By approximating its metallicity distribution as a single Gaussian of mean -1.7 dex and standard deviation 0.5 dex, we randomly extracted [Fe/H] values at the radial positions of our data, further reshuffling them according to their observed errors, assumed to be Gaussian too. We performed then a least-square fit to the mock data, saving the slope value. The entire process was repeated 1000 times. Comparing the observed metallicity slope in Cetus with the recovered distribution of mock values, we obtained that the hypothesis of no gradient is rejected at only the 2-σ level. Considering, however, the reduced size of our dataset and the independent results from photometric studies reported above, we conclude that the presence of a metallicity gradient in Cetus is not to be excluded, although we would need more data, particularly for $R/R_e \gtrsim 3$, to pin its presence down.

We refer to Sect. 5.2.3, for a further discussion on the metallicity properties of LG dwarf galaxies and possible mechanisms that led to the formation of radial metallicity gradients.

2.6.2 Two chemo-kinematically distinct populations?

The occurrence of a metallicity gradient in Fig. 2.8 might also indicate the presence of sub-populations with different kinematics. We divided our dataset into a metal-poor (MP) and a metal-rich (MR) sample according to their [Fe/H] values being lower or greater than the median [Fe/H] (-1.71 dex), respectively. We

[12] https://scikit-learn.org/stable/modules/gaussian_process.html

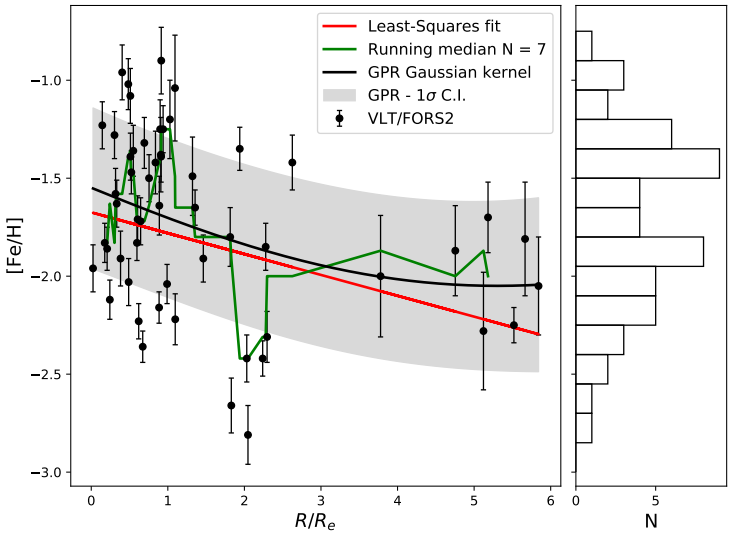

FIGURE 2.8— Individual metallicity measurement as a function of the elliptical radius scaled with R_e for Cetus probable member stars. The red line indicates the least-squares linear fit to the data, while the green line represents the running median boxcar having a 7-point kernel size. The black solid line is the result of a Gaussian process regression analysis using a Gaussian kernel and taking into account an intrinsic scatter; the gray band indicates the corresponding 1-σ confidence interval.

then ran the MultiNest code for both samples in order to estimate the associated velocity dispersion in the case of no rotation and obtained $\sigma_{\rm v,MR} = 8.7^{+1.9}_{-1.5}$ km s^{-1} and $\sigma_{\rm v,MP} = 13.8^{+2.7}_{-2.3}$ km s^{-1}. The two values are at 2-σ from each other. Although this is a tentative result, it seems that the different spatial distributions of Cetus metal-richer and metal-poorer stars are reflected in different kinematic properties. This is along the same line as what seen in some of the dSphs satellites of the MW, such as Sculptor, Fornax, Carina and Sextans, which have a spatially concentrated dynamically colder metal-rich stellar population together with a hotter and more extended metal-poorer one (e.g., Tolstoy et al., 2004; Battaglia et al., 2006, 2008a; Koch et al., 2008; Battaglia et al., 2011; Amorisco & Evans, 2012b).

As is the case for the majority of those LG dwarf galaxies where the evolved stellar population shows similar chemo-dynamical properties as seen here, it is difficult to ascertain whether this is due to the presence of chemo-dynamically distinct components or to a smooth variation of the spatial distribution of stellar populations of different mean metallicity. The SFH of Cetus and the other dwarf galaxies where this behavior has been detected does not show the presence of clear, separated bursts of star formation, which could be directly linked to two separate populations. Unfortunately, in exclusively old systems such as Cetus, given that uncertainties in age determination increase at old ages, it is typically challenging or impossible to detect separate bursts based on their relative strength and separation. So far the most clear case is that of Sculptor dSph, where the application of orbit-based dynamical modeling shows a distribution function that is bimodal in energy and angular momentum space for all of the best-fitting mass models explored, offering an independent and purely dynamically based confirmation of the existence of two physically distinct components (Breddels & Helmi, 2014; see also Zhu et al., 2016). The determination of the properties of chemo-dynamically distinct populations in dSphs is of strong interest not only to unravel the complex formation and evolution histories of these galaxies, but, importantly, also to shed light onto the dark-matter properties of these systems. In fact, by modeling the velocity dispersion profile of the distinct populations, which are independent stellar tracers living in the same potential, it is possible to know the internal shape of the mass profile, if for example it is cuspy or cored (Battaglia et al., 2008b; Walker & Peñarrubia, 2011; Amorisco & Evans, 2012a; Strigari et al., 2018).

2.7 Structural properties

Given the observed metallicity gradient and chemo-kinematic hint of two distinct stellar population, we combined the spectroscopic information with the Subaru/SuprimeCam photometric data to gain insight into Cetus' structural properties. We have already seen in the previous section that the MR sample of spectroscopically observed RGB stars is more spatially concentrated than the MP one (see Fig. 2.8). Furthermore, as can be seen from the CMD reported in Fig. 2.9, the spectroscopic members show a clear correlation between their colors and metallicities, with the MP stars having bluer colors than the MR ones. This information guided us to split the overall RGB population into a red and blue part in order to check whether there is evidence of different structural properties. We also checked for the structural properties of the entire RGB and HB populations, for completeness. The selection limits were defined as shown

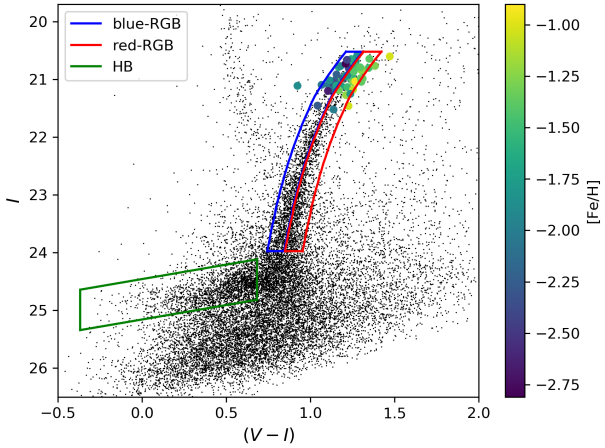

FIGURE 2.9— Color-magnitude diagram of the Cetus dSph from the Subaru/SuprimeCam photometric catalog. The FORS2 spectroscopic targets classified as probable members are overplotted, and color-coded according to their calculated [Fe/H]. Selection limits for the blue-RGB, red-RGB, and HB are marked as color boxes.

in Fig. 2.9, with the total RGB population corresponding to the sum of its blue and red parts.

Following the Richardson et al. (2011) formalism, we employed a maximum likelihood approach to analyze the spatial distribution of the considered populations and get their structural parameters (see also Cicuéndez et al., 2018 for further details). Assuming an exponential profile for the surface density distribution of the selected population, together with a constant contamination density, we had seven parameters to determine: the central surface density value (σ_0), the central coordinates (α_0, δ_0), the exponential scale length (r_0) measured on the semimajor axis, the position angle (P.A.), the ellipticity (ϵ) and the constant contamination density (σ_c). We have numerically estimated the posterior distributions associated to these parameters using the *emcee* code, already introduced in Sect. 2.5.1. We set Gaussian priors for the central coordinates and the P.A. centered around their initial values with dispersion of 0.05° and 35°, respectively, while for the ellipticity we set a flat prior between 0 and 1. As

initial values, we used those reported in Table 2.1. We also demanded positive values for the density parameters and the exponential scale length, while we fixed the ellipticity values to vary between 0 and 1. The derived structural parameters obtained from the marginalized posterior distributions are reported in Table 2.4.

The spatial distribution corresponding to each selection can be seen in Fig. 2.10. The different spatial extensions of the red and blue parts of the RGB can be distinguished, with the first one more centrally concentrated and less extended than the other. The HB population instead, although suffering from a higher level of contamination, is more extended and tends to resemble the blue RGB selection. This indicates, as expected, that the HB is dominated by an older population. The visual impression is confirmed by the determination of the structural parameters: we can see that the exponential radius tends to change within the selections, being smaller for the redder/more metal-rich selection on the RGB and larger for the bluer/more metal-poor one. It is however not obvious that there is a one-to-one correspondence between the bRGB and the HB selection, given the even less concentrated spatial distribution of the HB stars.

We note that in the previous work by McConnachie & Irwin (2006), by fitting the total RGB population, the authors obtained a geometric averaged exponential radius of 1.59 ± 0.05 arcmin. Our value of 2.19 ± 0.05 arcmin for the RGB fit, once changed from being measured on the semimajor axis to a geometric averaged radius, resulted in 1.53 ± 0.05 arcmin, in very good agreement. On the other hand, the P.A. and ellipticity were almost equal for all our selections: roughly 65° and 0.5, respectively. In this case the ellipticity value of 0.33 reported by McConnachie & Irwin (2006) is significantly lower than our calculated value, while the P.A. of 63° is compatible between the errors with our findings. We attribute this discrepancy to the fact that our photometric dataset is deeper than that used by McConnachie & Irwin (2006) in their study.

Also interesting to note in Fig. 2.10 is the elongated shape of the HB and the RGB along the major axis of the galaxy, a characteristic morphologically reminiscent of tidal tails. Even if the MW, or most likely M31, exerted tidal disturbance onto Cetus, it is difficult to explain how tidal features - if made by unbound stars - could still be visible at present. Assuming Cetus' motion is all in the radial direction moving away from M31 with a velocity of 46 $\mathrm{km\,s^{-1}}$ (McConnachie, 2012), the last pericentric passage around M31 could have occurred about 6 Gyr ago; this would correspond to > 200 internal crossing times (defined as in Peñarrubia et al., 2009), much in excess of the expectations for tidal tails to still be visible, as can be gathered in that same work. Curiously enough, elongations in the outer parts of the stellar component have also been

TABLE 2.4— MCMC-Hammer output structural parameters for each selected population.

Selections	σ_0 (stars arcmin^{-2})	(α_0, δ_0) (deg)	r_0 (arcmin)	P.A. (deg)	ϵ	σ_c (stars arcmin^{-2})
blue-RGB	$74.6^{+4.2}_{-4.0}$	6.549 ± 0.001, -11.038 ± 0.001	2.45 ± 0.08	65.2 ± 1.3	0.53 ± 0.02	0.17 ± 0.02
red-RGB	$99.8^{+5.6}_{-5.4}$	6.546 ± 0.001, -11.044 ± 0.001	$1.97^{+0.07}_{-0.06}$	65.2 ± 1.4	0.50 ± 0.02	0.14 ± 0.02
RGB	$159.5^{+6.7}_{-6.4}$	6.548 ± 0.001, -11.041 ± 0.001	2.19 ± 0.05	64.2 ± 1.0	0.51 ± 0.01	0.30 ± 0.02
HB	$47.1^{+2.9}_{-2.8}$	6.551 ± 0.002, -11.037 ± 0.001	$3.46^{+0.16}_{-0.15}$	65.6 ± 1.3	0.56 ± 0.02	0.54 ± 0.04

Notes. Reported values represent the median of the corresponding marginalized posterior distributions, with 1-σ errors set as the confidence intervals around the central value enclosing 68% of each distributions.

detected in an extremely isolated dwarf galaxy like VV124 (Kirby et al., 2012), perhaps pointing to an explanation other than tidal disturbances.

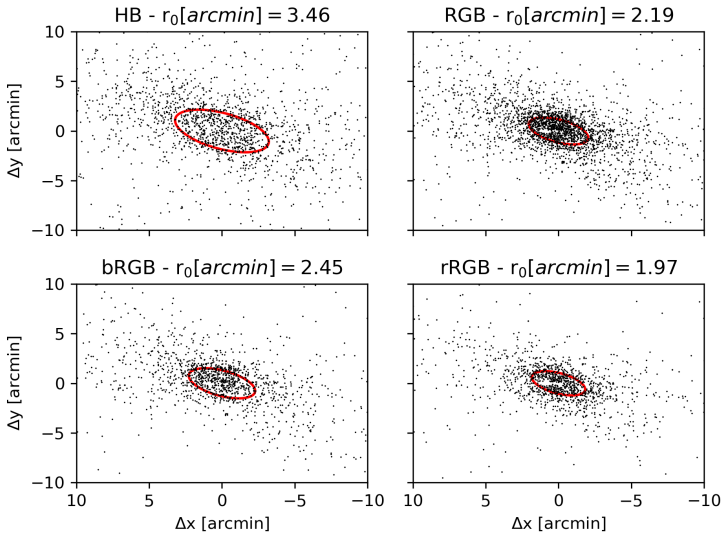

FIGURE 2.10— Spatial distribution of the selected HB, RGB, blue-RGB, and red-RGB populations. The ellipses have, as semimajor axis values, the calculated r_0 of the considered populations, together with their corresponding P.A. and ellipticity values. North is toward the top of each panel, east is to the left.

2.8 Tracing the Sagittarius stream in Cetus foreground

The CMD shown in the right part of Fig. 2.1 reveals the presence of an overdensity of main sequence turn-off (MSTO) stars in the foreground to the Cetus dSph (see region at $19 \lesssim I \lesssim 23$ and $0.4 \lesssim (V-I) \lesssim 0.7$).

In order to test whether that region of the CMD is more populated than what would be expected in a smooth model of the MW, we generated a synthetic catalog in the direction of Cetus using the Besançon model (Robin et al., 2003), encompassing the solid angle of the Subaru/SuprimeCam catalog (0.25 deg^2), a distance range up to 100 kpc and a magnitude error ± 0.05 mag in both bands, with default values. We have found that the number counts predicted by the Besançon model of the Galaxy in that range of magnitude and colors are not sufficient to explain the MSTO feature: indeed in the considered region we

observe 220 stars, while the Besançon model predicts only 132.

Therefore it is evident that we are crossing some sort of structure placed in the foreground. The MSTO sources have a homogeneous spatial distribution on our f.o.v. and do not show any tight spatial clustering; therefore they appear to be part of a wider structure.

In order to trace the upper part of the MSTO feature, we merged our catalog with the publicly available Sloan Digital Sky Survey (SDSS) DR13 Photometric catalog, which covers the Cetus area and probes a brighter magnitude range than the SuprimeCam dataset. Since the SDSS catalog is on a different photometric system, we searched for common targets and performed a rough photometric calibration to convert all magnitudes to the Johnson-Cousin system. This allowed us to set the upper part of the MSTO feature at $I \sim 19.5$.

We find that the MSTO feature is well described by a set of isochrones (from Girardi et al., 2000) of old age ($10 \leq$ t[Gyr] ≤ 12.6) that are metal-poor ($0.0004 \leq Z \leq 0.001$), or intermediate-young age ($2 \leq$ t[Gyr] ≤ 5.6) and metal-richer ($0.004 \leq Z \leq 0.019$), occupying an increasing heliocentric distance range that goes from 25 to 40 kpc.

Searching in literature to possibly constrain these values, it appears that multiple MW streams cross close to the location on the sky of the Cetus dSph. The Cetus Polar Stream (Yanny et al., 2009; Newberg et al., 2009; Koposov et al., 2012; Yam et al., 2013) intersects the Sagittarius trailing tail at $(l, b) \sim (140°, 70°)$, which was found by analyzing blue horizontal branch (BHB) stars in the Sloan data. Its distance was confined between $\sim$ 24 and 35 kpc, with most of its stars having metallicity of $-2.5 <$ [Fe/H] < -2.0. However, according to its position (e.g., as can be seen in Fig. 4 of Yam et al. (2013)) this stream is far enough from the Cetus dSph location and therefore should not be associated with our MSTO feature.

A narrow stellar stream was found by Koposov et al. (2014) in the ATLAS DR1 data, at least 12° long and $\approx 0.25°$ broad. Their optimal isochrones match was consistent with a metal-poor ([Fe/H]< -2.1) and old age (t $\sim$12.5 Gyr) stellar population positioned at a distance of $\sim$20 kpc. The stream great circle passes near the Cetus location (see Koposov et al. (2014), their Fig. 1) and therefore it may be associated to our MSTO feature, but being a very narrow structure its contribution should also be negligible.

Cetus appears to project onto the southern Sagittarius stream, halfway from both its bright and faint arms (see Slater et al. (2013) and Belokurov & Koposov (2016), their Fig. 1). Koposov et al. (2012) have shown that the two arms follow a similar distance gradient, going from $\sim$ 25 to 34 kpc across a sampled sky area of 30°, and present a spread in metallicity with [Fe/H] values between -2.0 and 0. At the location on the sky of Cetus, the Sagittarius arms are at a distance of

$\sim$25 kpc and present stars with [Fe/H]< -0.5 (Koposov et al., 2012) and ages > 5 Gyr (de Boer et al., 2015). It is therefore likely that the MSTO feature we detect belongs to the Sagittarius stream.

To further constrain the association of the MSTO feature to the Sagittarius stream, we analyzed the three FORS2 MXU targets that fall on this area of the CMD. However, just one of them was found to be a stellar object with a visible CaT feature. The measured heliocentric velocity from the normalized stacked spectrum resulted in -70.25 ± 8.1 km s^{-1}. This velocity in the Galactic Standard of Rest (GSR) system is equivalent to $v_{\rm GSR} \sim -13$ km s^{-1}. This is in agreement with the expectations from the Law & Majewski (2010) model of the Sagittarius stream at this location and heliocentric distance range.

We deem unlikely, though not completely excluded based on the comparison with isochrones, the hypothesis that the feature detected might be part of the smooth halo or be another feature other than Sagittarius. The Sagittarius stream dominates the faint MSTO features that appear when crossing a region of the sky around its orbital plane (Deason et al., 2011; Belokurov, 2013; de Boer et al., 2015), as is the case for the Cetus dSph. It should also be noted that the outer parts of the Galactic halo (i.e., at Galactocentric distances > 15 kpc) show in general a lower metallicity compared to the inner parts, with a metallicity distribution function peaking around [Fe/H]$= -2.3$ dex (e.g., Beers et al., 2012; Allende Prieto et al., 2014; Fernández-Alvar et al., 2015). Furthermore, the outer halo appears to be highly structured (Janesh et al., 2016), with the stellar streams being the main source of younger and more metal-rich stars with respect to the smooth halo component (see also Huxor & Grebel, 2015). This is also observed in M31 (Ibata et al., 2014). In our case, we suggest that the MSTO feature is most likely associated with the Sagittarius stream.

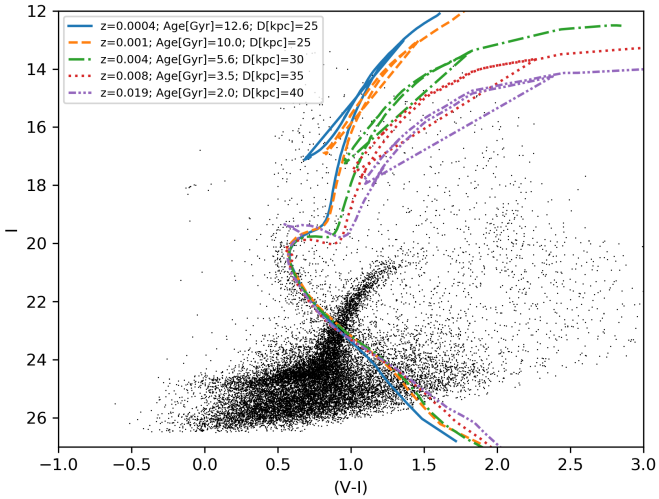

FIGURE 2.11— Isochrones overlaid on to the MSTO feature, probably belonging to the Sagittarius stream, on the color-magnitude diagram resulting from merging the photometric catalogs Subaru/SuprimeCam and the Sloan Digital Sky Survey (SDSS) DR13 in the Cetus dSph area. Extinction and reddening have been added to the isochrones (average extinction values calculated in the Cetus dSph area: $A_V = 0.076$, $A_I = 0.043$, Schlafly & Finkbeiner, 2011). The figure legend reports the metallicity Z, age, and distance of the corresponding isochrones.

2.9 Summary and Conclusions

In this chapter we present an analysis carried out on VLT/FORS2 multi-object spectroscopic observations of 80 individual targets in the Cetus dwarf spheroidal galaxy, of which 54 are probable RGB member stars. We have been able to characterize from this sample the internal kinematics of the galaxy and present the first spectroscopic determination of its wide-area metallicity properties.

The Bayesian analysis of the internal kinematics shows that Cetus is a mainly pressure-supported system ($\bar{v}_{\rm hel} = -78.9^{+1.7}_{-1.6}$ km s^{-1}, $\sigma_{\rm v} = 11.0^{+1.6}_{-1.3}$ km s^{-1}) with no significant signs of stellar rotation. Initially our results were found to be somewhat different from those reported in the previous studies of Lewis

et al. (2007) and Kirby et al. (2014). We attribute the difference in the systemic velocity to a small zero-point offset with respect to K14's study. The larger value that we obtained for the velocity dispersion with respect to K14 appears to be the result of the different spatial coverage of the two datasets combined with the presence of two chemo-kinematic stellar populations. Moreover, the tests we conducted on mock datasets showed that the exclusion of a significant rotation signal is robust, indicating that the presence of an eventual rotational component would be weak and not capable of producing the observed galaxy ellipticity. This is in agreement with what has already been found by Kirby et al. (2014) and Wheeler et al. (2017), although it contrasts with the Lewis et al. (2007) findings of a moderate rotation ($\sim 8\,\mathrm{km\,s^{-1}}$) along the major axis. We can attribute this discrepancy to a probable artifact caused by the low S/N and non-homogeneous distribution of Lewis et al. (2007) targets.

From the analysis of Cetus metallicity properties we establish that the galaxy is predominantly a metal-poor system with a significant metallicity spread (median $[\mathrm{Fe/H}] = -1.71$ dex, MAD $= 0.49$ dex). The derived values are in very good agreement with integrated quantities from SFH studies (Monelli et al., 2010; Hidalgo et al., 2013). In addition, the derived median [Fe/H] value agrees, between the 1-σ limits, with the L_V-[Fe/H] relation for LG dwarf galaxies reported by Kirby et al. (2013b). On the other hand, the intrinsic metallicity spread value ($\sigma_{[\mathrm{Fe/H}]} = 0.42 \pm 0.03$ dex) does not follow the linear anti-correlation found by Kirby et al. (2011) between the intrinsic [Fe/H] spread and the luminosity of a dwarf system, resulting instead in agreement with the saturated trend found for other dwarf galaxies of similar or higher luminosities by Leaman et al. (2013) and Ho et al. (2015).

Looking at the radial distribution of the individual metallicity measurements, a LSQ linear fit revealed a mild metallicity gradient of $m = -0.033 \pm 0.014\,\mathrm{dex\,arcmin^{-1}}$. This value would set Cetus apart from other LG dSphs, where, in general, steeper gradients have been observed. However a simple linear fit can often be an incomplete description of the radial metallicity distribution, as already seen in both simulations and observations (Schroyen et al., 2013 and Leaman et al., 2013, respectively). By comparing the running-median of the metallicity as a function of radius, we see a complex radial stellar population profile, comparable to other pressure-supported dSphs of similar luminosity but inhabiting a range of environments. The decreasing radial trend in metallicity was also confirmed by performing a Gaussian process regression analysis, while results from a mock simulation showed that the presence of a [Fe/H] gradient in Cetus is significant at the 2-σ level.

The detection of a radial metallicity gradient in an isolated dwarf galaxy would suggest that the formation of metallicity gradients in dwarf galaxies can

be mainly driven by internal parameters like mass and angular momentum, rather than being the result of environmental interactions with the large hosts of the LG (see also Kacharov et al., 2017 and the discussion in Ch. 5).

Albeit only at 2-σ significance, we have also found evidence of two chemo-kinematically distinct stellar populations, with more metal-rich stars showing a lower dispersion velocity than the metal-poor ones ($\sigma_{\rm v,MR} = 8.7^{+1.9}_{-1.5}$ km s^{-1} and $\sigma_{\rm v,MP} = 13.8^{+2.7}_{-2.3}$ km s^{-1}, respectively). Although tentative, this result is in line with what has already been found in other dSphs satellites of the MW (e.g., Tolstoy et al., 2004; Battaglia et al., 2006, 2008a; Koch et al., 2008; Battaglia et al., 2011; Amorisco & Evans, 2012b).

The presence of stellar population gradients is confirmed by our analysis of the photometric Subaru/SuprimeCam dataset, which reveals that the HB, blue (more-metal poor), and red (more metal-rich) portion of the RGB stars have decreasing values for the scale-length of the best-fitting exponential surface density profile. However, in our simple analysis, we do not find a one-to-one correspondence between the spatial distribution of the blue/metal-poor part of the RGB and the HB, as the latter has a significantly larger scale length than the former. This should be taken into account when adopting a spatial distribution for the tracer population in mass modeling studies that use multiple chemo-kinematic components. Intriguingly, features reminiscent of tidal tails are seen in the outer part of the system, although it is difficult to reconcile their presence with the timescales of a possible passage around M31 and the internal crossing times.

Finally, the ancillary photometric dataset used in this work from Subaru/SuprimeCam reveals the presence of a foreground population that most likely belongs to the Sagittarius stream, based both on the analysis of the color-magnitude diagram and on the agreement of the radial velocity measurement for one of the observed spectroscopic targets with the Sagittarius stream orbit properties from the literature (Law & Majewski, 2010).

This study has not only increased our knowledge of the internal chemo-kinematic properties of the Cetus dSph, but has also added an extra piece to our understanding of the mechanisms that drive the evolution of such small systems.

Authorship

This chapter is based on the published work of Taibi et al. (2018), where several authors has been involved. My contribution has been of the most relevant, from data reduction to the analysis and final writing of the manuscript.

3

The Tucana dwarf spheroidal galaxy: not such a massive failure after all

The material included in this chapter has been published in:

Taibi, S.; Battaglia, G.; Rejkuba, M.; Leaman, R.; Kacharov, N.; Iorio, G.; Jablonka, P.; Zoccali, M., 2020, Astronomy & Astrophysics, 635, A152.

ABSTRACT

Aims. Here we explore the internal kinematic and metallicity properties of Tucana, one of the few isolated dwarf spheroidal galaxy of the Local Group. This is an intriguing system, as it has been found in the literature to have an internal rotation of up to 16 $\mathrm{km\,s^{-1}}$, a much higher velocity dispersion than dwarf spheroidals of similar luminosity, and to be a possible exception to the too-big-too-fail problem.

Methods. We present results of a new spectroscopic dataset taken with FORS2 instrument on the Very Large Telescope (VLT) in the region of the Ca II triplet for 50 candidate red giant branch stars in the direction of Tucana. These yielded line-of-sight (l.o.s.) velocity and metallicity ([Fe/H]) measurements of 39 effective members that double the number of Tucana's stars with such measurements. In addition, we re-reduce and include in our analysis the other two spectroscopic datasets presented in the literature, the VLT/FORS2 sample by Fraternali et al. (2009), and the VLT/FLAMES one from Gregory et al. (2019).

Results. Across the various datasets analyzed, we consistently measure a l.o.s. systemic velocity of 180 ± 1.3 $\mathrm{km\,s^{-1}}$ and find that a dispersion-only model is moderately favored over models accounting for internal rotation. Our best estimate of the internal l.o.s. velocity dispersion is $6.2^{+1.6}_{-1.3}$ $\mathrm{km\,s^{-1}}$, much smaller than the values reported in the literature and in line with similarly luminous dwarf spheroidals; this is consistent with Tucana not being an exception to the too-big-to-fail problem, nor living in a dark matter halo much more massive than those of its siblings. As for the metallicity properties, we do not find anything unusual; there are hints of a radial metallicity gradient, but more data are needed to confirm its presence.

3.1 Introduction

Tucana is an early-type dwarf galaxy found at present in extreme isolation with a heliocentric distance of $D_\odot = 887 \pm 49$ kpc (Bernard et al., 2009), which places it at more than 1 Mpc away from M31 and the LG center, with only the Phoenix dwarf found within ∼500 kpc of it (McConnachie, 2012). Photometric observations have shown that the galaxy is mainly old and metal-poor, with an extended horizontal branch (HB) and a population of variable stars (see e.g., Saviane et al., 1996; Bernard et al., 2009). The structural analysis by Saviane et al. (1996) showed a highly flattened system ($e \sim 0.5$) with a surface density profile well-described by an exponential fit. The recovery of the full star formation history (SFH) from deep HST/ACS observations reaching the oldest main sequence turn-off by Monelli et al. (2010) showed that Tucana formed the majority of its stars more than 9 Gyr ago. It experienced a strong initial period of star formation (SF) starting very early on (∼13 Gyr ago). Tucana harbors at least two stellar sub-populations based on observed splitting of the HB, double red giant branch (RGB) bump, and the luminosity-period properties of the RR-Lyrae, which imply that this system experienced at least two early phases of SF in a short period of time. Using the same HST/ACS dataset, Savino et al. (2019) refined the HB analysis, showing that Tucana experienced two initial episodes of sustained SF followed by a third less intense, but more prolonged one, ending between 6 and 8 Gyr ago. The spatial analysis of the same dataset indicates the presence of a population age gradient inside $\sim 4\,R_e$ (Monelli et al., 2010; Hidalgo et al., 2013; Savino et al., 2019).

The first spectroscopic study of individual stars in the Tucana dSph was conducted by Fraternali et al. (2009), with the VLT/FORS2 instrument obtaining a relatively small sample of ∼20 RGB probable member stars. They reported the systemic velocity and velocity dispersion values ($\bar{v}_{\rm hel} = 194.0 \pm 4.3$ km s^{-1} and $\sigma_{\rm v} = 15.8^{+4.1}_{-3.1}$ km s^{-1}) for the galaxy, together with the presence of a maximum rotation signal of ∼16 km s^{-1}. They also determined a mean metallicity value of [Fe/H] $= -1.95 \pm 0.15$ dex with a dispersion of 0.32 ± 0.06 dex. The determination of the systemic velocity ruled out an association with a nearby HI cloud, confirming that Tucana is devoid of neutral gas (down to a HI mass of $1.5 \times 10^4\,M_\odot$), and in addition it is moving away from the LG barycenter (Fraternali et al., 2009). If bound, Tucana has not reached its apocenter yet. It is indeed possible that a past interaction between Tucana and the MW happened around 10 Gyr ago (roughly coinciding with the major drop in its SF; Sales et al., 2007; Fraternali et al., 2009; Teyssier et al., 2012).

A new spectroscopic study of Tucana's RGB stars has recently been conducted by Gregory et al. (2019) using VLT/FLAMES data. Their sample of

probable members is slightly larger than that of Fraternali et al. (2009), but covers a much more extended spatial area (up to $\sim 10\,R_{\rm e} \sim 2\,R_{\rm tidal}$). Their velocity dispersion value ($\sigma_{\rm v} = 14.4^{+2.8}_{-2.3}$ km s^{-1}) obtained for 36 probable members is similar to that of Fraternali et al. (2009), although their systemic velocity shows a significant offset ($\bar{v}_{\rm hel} = 216.7^{+2.9}_{-2.8}$ km s^{-1}); they also detect a velocity gradient of $k = 7.6^{+4.2}_{-4.3}$ km s^{-1} arcmin^{-1} along the optical major axis. Performing a dynamical modeling of Tucana's kinematic properties based on the FLAMES/GIRAFFE l.o.s. velocities of the probable members, the authors found a massive dark matter halo with a high central density. The implied dark matter halo mass profile is much denser than the other dwarfs of the LG, making Tucana the first exception of the too-big-to-fail problem (see e.g., Boylan-Kolchin et al., 2012). In fact, the pure N-body simulations in the framework of Λ cold dark matter (Λ-CDM) predict that the dwarf galaxies of the LG should live in denser halos than those inferred from observations. The fact that Tucana is found to reside in such a massive halo in agreement with Λ-CDM predictions seems to indicate that, during its evolution, it has been able to maintain its initial distribution of dark matter, independently of the internal and environmental mechanisms that have driven its evolution.

Motivated by the unique internal kinematics of Tucana and the importance of isolated dwarfs in disentangling evolutionary processes, in this study we present results from a new investigation of the kinematic and chemical properties of the stellar component of the Tucana dSph. We analyzed a new dataset of multi-object spectroscopic observations of 50 individual RGB stars taken with the VLT/FORS2 instrument targeting the near-IR wavelength region of the Ca II triplet (CaT) lines. To understand how systematics may influence the key results of our study, we further re-reduced the original datasets presented in Fraternali et al. (2009) and Gregory et al. (2019) and performed a combined analysis together with our own data. In this work, we present an in-depth and homogeneous analysis of all currently available spectroscopic data for the Tucana dSph.

The chapter is structured as follows: in Sect. 3.2, we present the data acquisition and reduction processes for all the datasets analyzed in this work. Section 3.3 is dedicated to the determination of the l.o.s. velocity and metallicity measurements. In Sect. 3.4, we describe the criteria applied to select likely member stars in the different datasets we present here. Section 3.5 shows the results from the kinematic analysis, presenting the determination of the galaxy systemic velocity and velocity dispersion, along with the search for a possible rotation signal and the implication for the dark matter halo properties of Tucana. In Sect. 3.6, we describe the determination of metallicities ([Fe/H]) and

TABLE 3.1— Parameters adopted for the Tucana dwarf galaxy.

Parameter	Units	Value	Ref.
$\alpha_{\rm J2000}$		$22^h41^m49.6^s$	(1)
$\delta_{\rm J2000}$		$-64°25'10''$	(1)
$\epsilon^{(a)}$		0.48 ± 0.03	(2)
P.A.	deg	97 ± 2	(2)
$R_{\rm core}$	arcmin (pc)	0.7 ± 0.1 (181 ± 28)	(2)
$R_{\rm tidal}$	arcmin (pc)	3.7 ± 0.5 (955 ± 139)	(2)
$R_{\rm e}$	arcmin (pc)	0.8 ± 0.1 (206 ± 28)	(2)
$L_{\rm V}$	$10^5 M_\odot$	5.5 ± 1.5	(2)
$I_{\rm TRGB}$		20.7 ± 0.15	(2)
E(B-V)		0.031	(3)
$D_\odot$	kpc	887 ± 49	(3)
$\overline{v}_{\rm hel}$	$\rm km\,s^{-1}$	180 ± 1.3	(4)
$\sigma_{\rm v}$	$\rm km\,s^{-1}$	$6.2^{+1.6}_{-1.3}$	(4)
[Fe/H]	dex	-1.58	(4)
$\sigma_{\rm [Fe/H]}$	dex	0.39	(4)

Notes. The table lists: the coordinates of the galaxy's optical center; the stellar ellipticity and position angle; the core, tidal and half-light geometric radii; the stellar luminosity in V-band; the tip of the red giant branch magnitude in I-band; the average reddening; the heliocentric distance; the parameters obtained in this work, i.e., the systemic velocity, the velocity dispersion, the median metallicity, and the intrinsic metallicity scatter. $^{(a)}\epsilon = 1 - b/a$.
References: (1) Lavery & Mighell (1992); (2) Saviane et al. (1996); (3) Bernard et al. (2009); (4) this work.

the subsequent chemical analysis. Finally, Sect. 3.7 is dedicated to our summary and conclusions, while in the appendices we report the detailed comparison between the measurements obtained for our dataset with those reported in the literature, along with supplementary material from the kinematic analysis.

The parameters adopted for the Tucana dSph are summarized in Table 3.1.

3.2 Data acquisition and reduction processes

The analysis we present in this work required combining data obtained with different instruments and observational set-ups. Here, we provide details about the data acquisition and reduction processes we followed.

3.2.1 The P91-FORS2 dataset

The primary dataset analyzed in this work was obtained with the FORS2 instrument mounted at the UT1 (Antu) of the Very Large Telescope (VLT) at the ESO Paranal observatory. Observations were taken in service mode over several nights between July 2013 and July 2014 as part of the ESO program 091.B-0251, PI: M. Zoccali (see Table 3.2). The instrument was used in multi-object spectroscopic mode (MXU), which allows the observer to employ exchangeable masks with custom-cut slits. We used pre-imaging FORS2 photometry taken in Johnson V- and I-band, to allocate slits to stars with colors and magnitudes compatible with Tucana's RGB. Slits that would otherwise have remained empty (five of them) were allocated to random targets in the same magnitude range. We selected 50 objects distributed over two overlapping masks of 27 slits each; the observation of four objects was repeated on purpose for internal accuracy measurements. Therefore, the selected targets covered an area up to the nominal King tidal radius of Tucana ($R_{\rm tidal} = 3.7'$), as can be seen in Fig. 3.1.

The adopted instrumental set-up and observing strategy were the same as in the previous chapter (see also Kacharov et al., 2017), so we only report the essentials here. We used the 1028z+29 holographic grism together with the OG590+32 order separation filter in order to cover the wavelength range between 7700 and 9500Å. Slits had spatial sizes of $1'' \times 10''$ ($8''$ in some cases to avoid overlaps) in the first mask (Tuc0) and of $1'' \times 8''$ ($7''$ for overlaps) in the second one (Tuc1). This led to a binned spectral dispersion of 0.84 Å pxl^{-1} and a resolving power of $R = \lambda_{\rm cen}/\Delta\lambda \sim 2600$ at $\lambda_{\rm cen} = 8600$Å (equivalent to a velocity resolution of 28 km s^{-1} pxl^{-1}). Ten identical observing blocks (OBs[1]) were taken for each pointing in order to reach the necessary S/N for velocity and metallicity measurements. In Table 3.2, we report a complete observing log.

The data were provided by ESO as individual OB-datasets within the FORS2 standard delivery plan. We adopted the same data-reduction process as in Ch. 2, based on IRAF routines and custom-made python scripts. Briefly, our pipeline was developed to organize and reduce each OB-dataset independently. After making bias and flat-field corrections on the two-dimensional (2D) multi-object scientific and lamp-calibration frames, these were also cleaned from cosmic rays and bad rows. The 2D images are corrected for distortions in the spatial direction by rectifying their slit traces in order to cut them into individual 2D

[1]The observations are organized by ESO in blocks taking into account the time to actually spend on the object, including foreseen overheads. Data are later delivered as OB-datasets which include the scientific exposures related to the individual OBs together with the associated acquisition and standard calibration frames (biases, arc lamp, dome flat fields).

spectra. The arc-lamp spectra are then used to find the wavelength solution to calibrate the scientific exposures, with a typical RMS accuracy of 0.05Å. The wavelength calibration also has the important effect of rectifying the sky lines, which had initially been curved by the instrument disperser, helping to reduce the residuals during the sky-subtraction part. The rectified wavelength-calibrated 2D individual scientific exposures were finally background subtracted, optimally extracted into 1D spectra and normalized by fitting the stellar continuum. The median S/N around the CaT for the individual exposures was ~ 8 Å^{-1}.

We then followed the approach already presented in Ch. 2 to stack the repeated individual exposures together for each target. To do so, we needed to account for possible zero-point displacements in the wavelength calibration, small slit-centering shifts, and the different dates of observation. The calculated wavelength calibration off-sets roughly varied between 5 and 25 km s^{-1} with an average error of 2 km s^{-1}. Slit-centering shifts ranged between $\pm 0.1 - 9.5$ km s^{-1} with errors of $\pm 1 - 5$ km s^{-1}. After applying the heliocentric correction, the above shifts were applied to the individual spectra. Repeated exposures then were averaged together, weighting them with their associated σ-spectra given by the extraction procedure. Final error-spectra were obtained accordingly. The median S/N around the CaT for the stacked spectra is $\sim$ 27 Å^{-1} (see also Table B.1 for the properties of each individual observed star).

3.2.2 A new reduction for the Fraternali et al. (2009) FORS2 dataset

Fraternali et al. (2009, hereinafter, F09) presented l.o.s. velocities and metallicities for 23 individual stars with magnitudes and colors compatible with Tucana's RGB (of which 17 were classified as members) from an earlier FORS2 MXU dataset (ESO program 69.B-0305(B), PI: E. Tolstoy). We wished to use this catalog to increase our sample size; however, a comparison with the l.o.s. velocities and metallicities between the targets in common (3) with the F09 catalog showed significant systematic shifts in both quantities (see Appendix 3.A.3 for details). For the sake of homogeneity, we therefore reduced the F09 dataset again following the same procedure as adopted for the P91 sample. Hereinafter, we refer to this additional sample as the P69 FORS2 dataset.

The instrumental set-up of the P69 program was similar to the one we adopted for our observations, with the difference being that the size of each slit was of $1.2'' \times 8''$, which translates into a slightly lower spectral resolution (≈ 30 km s^{-1} pxl^{-1}). A total of 45 initial targets were assigned to an equivalent number of slits packed into a single pointing centered on Tucana. The total

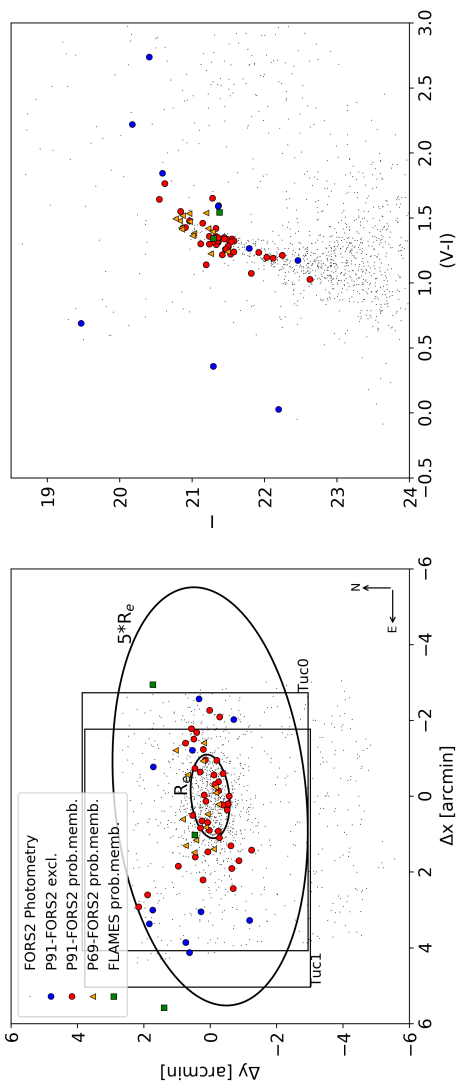

FIGURE 3.1— Spatial distribution (left) and color-magnitude diagram (right) of stars along the line of sight to the Tucana dSph. Black points represent the objects classified as stars in the FORS2 photometric data (see main text); red and blue dots indicate the P91-FORS2 MXU targets classified as probable members (i.e., with $P > 0.05$) and non-members, respectively. Yellow triangles and green squares represent the probable member stars from the P69-FORS2 and FLAMES datasets, respectively, which were added to the P91-FORS2 and analyzed through the text. The two observed FORS2 pointings are represented as large squares, while the ellipses denote the galaxy half-light radius and the spatial extension of the dataset (i.e., up to $5 \times R_e \sim R_{\rm tidal}$). We note that the photometric data are not corrected for reddening.

TABLE 3.2— Observing log of the P91 VLT/FORS2 MXU observations of RGB targets along the line of sight to the Tucana dSph.

Field	Position (R.A., Dec) (J2000)	Date / Time (UT)	Exp. (sec)	Airmass	Seeing (arcsec)	Grade$^{(\star)}$	Slits
Tuc0	22:41:56 -64:24:43	2013-07-30 / 04:26	3400	1.44	0.78	B	27 (16+11)
		2013-08-01 / 04:46	3400	1.39	0.80	A	
		2013-08-01 / 05:44	3400	1.32	0.92	A	
		2013-08-01 / 06:42	3400	1.30	0.90	A	
		2013-08-05 / 06:04	3400	1.30	0.98	A	
		2013-08-05 / 07:02	3400	1.31	1.13	A	
		2013-08-13 / 03:49	3400	1.41	0.69	A	
		2013-08-13 / 04:47	3400	1.33	0.57	A	
		2013-08-28 / 03:18	3400	1.36	0.65	A	
		2013-08-30 / 03:43	3400	1.33	0.89	A	
Tuc1	22:42:04, -64:24:47	2013-09-05 / 02:07	3500	1.43	1.62	C$^{(a)}$	27 (20+7)
		2013-09-06 / 03:34	3500	1.31	0.77	A	
		2013-09-06 / 04:37	3500	1.30	0.89	A	
		2013-09-13 / 01:53	3500	1.40	1.49	C$^{(b)}$	
		2013-09-13 / 02:54	3500	1.32	1.45	B	
		2013-10-01 / 01:35	3500	1.33	0.68	A	
		2013-10-25 / 02:17	3500	1.33	1.04	B	
		2014-07-21 / 07:28	3500	1.30	0.92	A	
		2014-07-21 / 08:40	3500	1.33	1.05	A	
		2014-07-27 / 06:07	3500	1.32	0.70	A	
		2014-07-27 / 07:10	3500	1.30	0.60	A	
		2014-07-27 / 08:18	200	1.33	0.65	C$^{(c)}$	
		2014-07-29 / 05:14	3500	1.37	0.62	A	
Total							54

Notes. From left to right, column names indicate: the pointing field name; the field center coordinates; observing date and starting time of the scientific exposure; the exposure time in seconds; the starting airmass; the average DIMM seeing during the exposure in arcsec; the ESO OB fulfillment grades (a full description is reported in the notes below); the number of slits/observed objects per mask. For each field, the mask design remained identical in each OB. The total number of slits (54) is reported in the last row of the table.
$^{(\star)}$ ESO OB fulfillment Grades: A) Fully within constraints – OB completed; B) Mostly within constraints, some constraint is 10% violated – OB completed; C) Out of constraints – OB must be repeated: $^{(a)}$ seeing increased up to $\sim 1.2''$ at OB's end - FWHM of spectra $\sim 1.0''$; $^{(b)}$ seeing, FLI, and Moon distance out of constraints; $^{(c)}$ aborted after 200s because sky conditions changed to thin clouds.

exposure time of the observations was 5.2 hours.

The reduction of some slits, in particular the background subtraction step, turned out to be particularly problematic, since these targets were not well-centered along the slit spatial direction, but placed at their edges. This led to 15 extracted spectra with high sky residuals, which made them unreliable for l.o.s. velocity and metallicity estimates. In addition, these targets had magnitudes and colors outside the RGB of Tucana. Therefore, we excluded them from the sample, along with two further objects whose extracted spectra did not show any CaT lines.

The final P69 sample was reduced to 28 objects, with five more than the initially published F09 catalog. Once stacked together, reliable spectra had an S/N ~ 22 Å^{-1} (see also Table B.2 for the properties of each individual observed star).

Another issue was the lack of through-slit images in the provided data, although in F09 it is reported that the objects were well-centered in the spectral direction after visual inspection during the spectroscopic run. However, we took into account the error related to the slit centering by assuming that it is a tenth of a pixel (~ 3 km s^{-1}, which is the typical error found checking for the slit centering) and adding it in quadrature during the velocity estimation step.

As can be seen in Appendix 3.A.2, there is good agreement for the measurements of the stars in common between this dataset (the P69 FORS2) and the P91 FORS2 (and for those cases where there is disagreement, the source of it can be traced back).

3.2.3 The FLAMES dataset

Gregory et al. (2019, hereinafter, G19) recently presented an additional sample of l.o.s. velocities (not metallicities) for individual stars in the direction of Tucana, taken with the FLAMES/GIRAFFE instrument at the VLT, as part of the ESO program 095.B-0133(A), PI: M. Collins. The spectrograph was used in MEDUSA mode, meaning in multi-fiber configuration, which allows for the simultaneous observation of up to 132 separate targets (sky fibers included). The instrument field of view (FoV) has a 25 arcmin diameter, and each fiber has an aperture on the sky of 1.2 arcsec. The grating used was the LR8, centered on 8817 Å and covering the CaT wavelength region, yielding a spectral resolution of $R \sim 6500$.

The authors reported the detection of 36 probable member stars, out to very large distances from Tucana's center, approximately up to 10 half-light radii. Given the larger spatial region probed by these data with respect to the FORS2 P91 and P69 datasets (compare Fig. 3.1 of this work to Fig. 1 in

G19), it was interesting to explore whether the G19 catalog of l.o.s. velocities could be used together with our determinations from the P91 and P69 FORS2 data. The comparison of the six stars in common between the P91 and G19 samples yields a discrepancy of $\sim$30 km s^{-1} for five of the six stars and of about -150 km s^{-1} for the other object, which does not allow the direct combination of the measurements. The G19 paper also reports an offset of $\sim$23 km s^{-1} between their velocities and those in the F09 catalog. We note that the offset of $\sim$30 km s^{-1} is compatible with the 23 km s^{-1} offset between G19 and F09 and the $\sim$7 km s^{-1} offset we found when comparing our P91 velocities to the F09 catalog (see Appendix 3.A.3 for further details). Given the above information, we proceeded to perform our own reduction of the FLAMES/GIRAFFE data, the characteristics of which we briefly describe below.

The observations were taken on six nights spread between June and September 2015, using two different fiber setups covering the same area: the first one (Tuc-1) had a total of 7hrs of exposure time accumulated over seven OBs, and the second setup (Tuc-2) got 6hrs of exposure time taken within six OBs, of which one was repeated twice. Each OB consisted of 3×1200sec exposures. The total number of individual targets was 164. The first setup had 14 fibers, and the second had 15 fibers allocated to empty sky regions distributed over the entire FoV. Only very few targets are spatially found inside the tidal radius of Tucana ($\sim$30 targets), with the others scattered over an area much larger than the nominal extension of this galaxy. In fact, the two pointings are off-centered by $\sim 9'$ from the optical center of Tucana.

The FLAMES data were downloaded from the science portal of the ESO archive as already processed spectra, meaning pre-reduced, wavelength-calibrated, extracted, and corrected to the barycentric velocity, but with no sky subtraction applied. For each OB, ESO delivers spectra stacked at the OB-level for the science targets and several auxiliary data, including the individual scientific exposures within an OB for both scientific targets and sky fibers [2]. The only remaining steps were to perform the sky subtraction, combine the spectra with repeated exposures, and, finally, calculate the radial velocities.

We first verified the quality of the wavelength calibration by cross-correlating the sky lines of the scientific exposures with a template sky spectrum, which was placed at the rest frame and obtained with a similar observational setup (Battaglia et al., 2011) [3]. However, the delivered spectra are shifted to the

[2] See `http://www.eso.org/observing/dfo/quality/PHOENIX/GIRAFFE/processing.html` for details.

[3] We further checked the wavelength calibration of the template spectrum itself using a high-resolution atlas of sky emission lines taken with the VLT/UVES instrument (Hanuschik, 2003), degraded to the spectral resolution of the template spectrum. The cross-correlation

heliocentric frame, including the sky lines, thus we had to remove this correction first. We then performed the cross-correlation for each spectrum of each OB dataset using the IRAF *fxcor* task, obtaining median offsets around 0.6 $\mathrm{km\,s^{-1}}$ with a global scatter of 0.7 $\mathrm{km\,s^{-1}}$. Therefore, the uncertainty related to the wavelength calibration resulted well below those from the velocity measurement (as shown later).

For the sky subtraction, we used the ESO *skycorr* tool (Noll et al., 2014). The idea behind this code is to adopt a physically motivated group scaling of the sky emission lines with respect to a reference sky spectrum according to their expected variability and given the date of the observations. We created the reference sky spectrum by first median combining the spectra of the fibers allocated to sky within the individual sub-exposures of each OB, and then by median combining the results for the individual sub-exposures. The optimized line groups in the reference sky spectrum are scaled to fit the emission lines in the science spectra and finally subtracted together with the sky continuum. Error spectra are also an output of the code. We used default input parameter while running *skycorr*. This method yielded satisfactory results for the majority of stars, particularly for spectra with low S/N.

The sky-subtracted science spectra were then normalized using a Chebyshev polynomial of order 3, together with their error spectra. Finally, repeated exposure of individual targets (including those the Tuc-1 and Tuc-2 set-ups have in common) were stacked together using a weighted average, with their error spectra combined accordingly. The typical S/N was ~ 11 $\mathrm{Å^{-1}}$, although in some cases it was as low as ~ 2 $\mathrm{Å^{-1}}$ (see also Table B.3 for the properties of each individual observed star).

The average S/N measured in our reduction of the FLAMES/GIRAFFE spectra is in good agreement with the S/N obtained from the GIRAFFE Exposure Time Calculator (ETC) considering typical values from the observed dataset: we used a black body template of $T_{\rm eff} = 4500$ K, an I-band magnitude of 21, an airmass of 1.2, a moon illumination fraction of 0.2, a seeing of $1.0''$, an object-fiber displacement of $0.3''$and a total exposure time of 10 hours (36000 sec). With this setting we obtained a calculated S/N of $15\,\mathrm{Å^{-1}}$, close to our typical S/N value.

3.2.4 Photometric data

Photometric data were used for all of the three datasets (FORS2 P91 and P69, and FLAMES/GIRAFFE) to exclude those objects whose magnitude and color

between these two spectra showed no significant wavelength shift.

were not compatible with being stars on Tucana's RGB (see Sect. 3.4), and for the FORS2 datasets to determine metallicities from the equivalent width of the CaT lines using calibrations from the literature (see Sect. 3.3).

We used the pre-imaging FORS2 photometric catalog introduced in Sect.3.2.1 to associate V- and I-band magnitudes to the target stars in the P91 and P69 spectroscopic datasets. The photometric catalog was astrometrized and the instrumental magnitudes were calibrated with the publicly available catalog from Holtzman et al. (2006) obtained with the Wide Field and Planetary Camera 2 of the Hubble Space Telescope (HST/WFPC2) being used as a reference. We used the aperture-photometry catalog provided in Johnson's $UBVRI$-system to actually find the astrometric solution of the FORS2 catalog and to perform the photometric calibration using the suite of codes *CataXcorr* and *CataComb*, kindly provided to us by P. Montegriffo and M. Bellazzini (INAF-OAS).

The case of the FLAMES dataset, on the other hand, was different. Since we did not have a photometric catalog covering an area as wide as that of the spectroscopic targets, we instead used the publicly available photometry of individual point sources from the first data release of the Dark Energy Survey (DES-DR1, Abbott et al., 2018). We found a match for 154 out of 164 spectroscopic targets, considering a tolerance radius of 1 arcsec. To be conservative, we did not exclude the targets that did not have a match in the DES-DR1 photometry from the photometric selection. The DES-DR1 *griz*-photometry needed then to be converted first to the SDSS *griz*-system[4] and finally to Johnson's system (see Jordi et al., 2005). The FLAMES data showed magnitudes as high as $V \sim 23$, which was also the limit of the DES-DR1 catalog, and, consequently, some targets had relatively large associated magnitude errors ($\delta_{\rm mag} \sim 0.2$).

3.3 Line-of-sight velocity and metallicity measurements

The determination of l.o.s. velocities and metallicities ([Fe/H]) from the stacked spectra was done in the same way as in Ch. 2. While we were able to measure both l.o.s. velocities and metallicity for the FORS2 P91 and P69 data, only l.o.s. velocities could be determined for FLAMES/GIRAFFE data, due to the low S/N ratio of those spectra.

Line-of-sight velocities were obtained using the *fxcor* task by cross-correlating with a synthetic spectrum resembling a low-metallicity RGB star convolved at the same spectral resolution of the dataset under consideration. For FORS2 we used the same template as in Ch. 2, and cross-correlated in the wavelength range $8400 - 8700$Å. For the FLAMES dataset we used a template from Zoccali et al.

[4] `https://des.ncsa.illinois.edu/releases/dr1/dr1-faq`

(2014), that is a synthetic spectrum of a star with $T_{\rm eff} = 4750$ K, $\log(g) = 2.5$ and [Fe/H] $= -1.3$ dex. In this case, we used the region around the two reddest lines of the CaT for the cross-correlation, since the first line often suffered from high residuals left by the subtraction of a sky emission line. This was not necessary for the FORS2 spectra, which suffer less from this problem due to their higher S/N.

In the following, we only keep objects whose stacked FORS2 and FLAMES spectra have a S/N$\gtrsim 10$ Å^{-1}, since this is the limit where the velocity errors provided by *fxcor* task appear reliable (see tests in Appendix 3.A.1). Average velocity errors for the FORS2 (FLAMES) spectra were found to be $\sim$7 km s^{-1} ($\sim$9 km s^{-1}).

As can be seen from the histogram in the right panel Fig. 3.2, the three datasets show a clear peak in the l.o.s. velocities around 180 km s^{-1}, where we roughly expect to find the members of Tucana. The FLAMES dataset presents a higher fraction of contaminants due to the large area covered by the observations. With our homogeneous analysis, we show a clear detection of the stars with velocities compatible with Tucana in all three datasets and no significant offsets, unlike what we found in direct comparison with our velocity measurements and those published in F09 and G19, as shown in the left panel of Fig. 3.2. We refer the reader to Appendix 3.A.3 and Sect. 3.5.2 for a detailed comparison with the studies taken from literature.

To estimate the [Fe/H] values, we adopted the Starkenburg et al. (2010) relation, which is a function of the equivalent widths (EWs) of the two reddest CaT lines, and of the $(V - V_{\rm HB})$ term, where $V_{\rm HB}$ is the mean magnitude of the galaxy's horizontal branch (HB). We obtained the EWs from the continuum-normalized stacked spectra by fitting a Voigt profile over a window of 15 Å around the CaT lines of interest, and using the corresponding error-spectra as the flux uncertainty at each pixel in the fitting process. The errors on the EWs were then calculated from the covariance matrix of the fitting parameters. For the $V_{\rm HB}$, we adopted the value of 25.32 from Bernard et al. (2009). Uncertainties on the [Fe/H] values were obtained by propagating the errors on the EWs, accordingly. Typical [Fe/H] errors were found to be around $0.15 - 0.25$ dex.

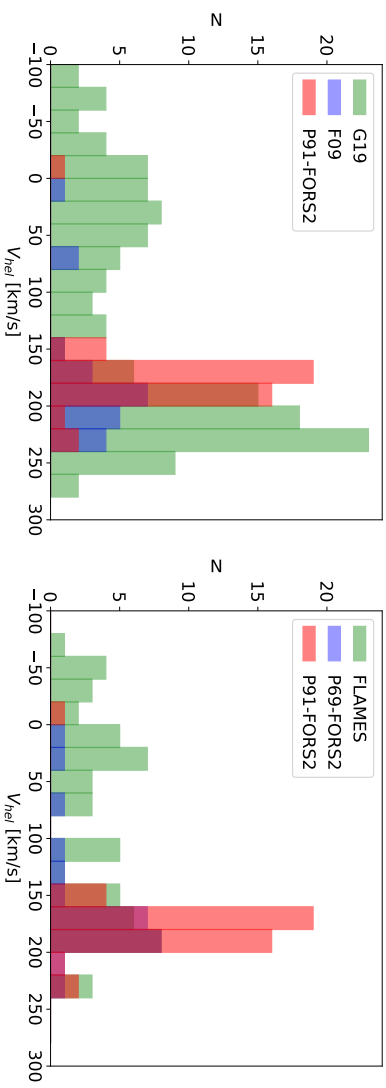

FIGURE 3.2— Histogram of l.o.s. velocity measurements from the analyzed datasets. *Left:* comparing the velocities from the P91-FORS2 dataset with those from literature, i.e. Fraternali et al. (2009) and Gregory et al. (2019). *Right:* same comparison using instead the velocity measurements from our reduction of the P69-FORS2 and FLAMES datasets. Note that, in the left panel, the peaks of the histograms fall at different velocities, while in the right panel, where the datasets shown were analyzed homogeneously, these differences are absent.

3.4 Membership & kinematic analysis

Before proceeding with the analysis of Tucana's kinematic and chemical properties, we needed to identify the stars that are probable members of Tucana and weed out possible contaminants (foreground MW stars and background galaxies). We followed the same steps for the membership selection in all the catalogs we analyzed.

We first selected targets located approximately along the RGB of Tucana, making our selection by magnitude and color. We used a set of isochrones (Girardi et al., 2000; Bressan et al., 2012) with age $t_{\rm age} = 12.6$ Gyr and [Fe/H] ~ -2.3 dex, and age $t_{\rm age} = 8$ Gyr and [Fe/H] ~ -0.4 dex to fix the blue and red color limits on the color-magnitude diagram (CMD). This color range was chosen to broadly cover the expected range of metallicities and stellar ages obtained from the SFH analysis of Tucana (Monelli et al., 2010; Savino et al., 2019). For the FLAMES dataset, due to the larger errors in the associated photometric dataset, we broadened the blue and red color limits applied to the FORS2 case by 0.2 mags. We further excluded the targets with spectra that showed high sky-residuals (and with S/N values < 10 Å^{-1}, as previously discussed) from all catalogs. Our P91 sample targets reduced from 50 to 43, the P69 objects reduced from 28 to 23, and the FLAMES one went from 164 to 58.

Given that the target selection of the three datasets was carried out completely independently, and might therefore include different biases, we proceeded by determining memberships and kinematic parameters by first considering our P91 FORS2 dataset on its own, a second time by combining it with the P69 sample, and, finally, while considering all the three sets. When we found common targets among the combined catalogs, we first kept those from the FORS2 datasets, with a higher priority for those of P91. Therefore, the combined FORS2 dataset has 63 targets, while including the FLAMES data gave a total of 109.

We then continued by assigning a membership probability to the individual targets in each considered dataset, applying a method based on the expectation maximization technique outlined in Walker et al. (2009c), but with the few modifications introduced by Cicuéndez et al. (2018). Briefly speaking, this approach makes it possible to carry out a Bayesian analysis to obtain the kinematic parameters of interest while assigning a probability of membership $P_{\rm M_i}$ to each i-star by maximizing the following log-likelihood equation:

$$\ln L = \Sigma_i P_{\rm M_i} \ln \left[P_{\rm mem}\, P_{\rm rad} \right] + \Sigma_i (1 - P_{\rm M_i}) \ln \left[P_{\rm non}\, (1 - P_{\rm rad}) \right], \qquad (3.1)$$

where $P_{\rm mem}$ is the target's probability distribution depending on its l.o.s. velocity, $P_{\rm rad}$ and $P_{\rm non}$ are the prior probabilities related to the surface density

profile of the galaxy and the presence of possible contaminants, respectively, while $P_{\mathrm{M_i}}$ is defined as:

$$P_{M_i} = \frac{P_{\mathrm{mem}}\, P_{\mathrm{rad}}}{P_{\mathrm{mem}}\, P_{\mathrm{rad}} + P_{\mathrm{non}}\, (1 - P_{\mathrm{rad}}).} \tag{3.2}$$

Both equations were adapted from Eqs. (3) and (4) of Walker et al. (2009c), respectively.

We run the Bayesian analysis using the *MultiNest* code (Feroz et al., 2009; Buchner et al., 2014), a multimodal nested sampling algorithm, in order to obtain the kinematic parameters and the membership probabilities all at once similarly to Cicuéndez et al. (2018). A further output of this code is the Bayesian evidence, which gives us the possibility to compare different kinematic models according to their statistical significance.

The spatial prior probability as a function of radius $P_{\mathrm{rad}}(R_i)$ accounts for the fact that we are more likely to observe a member star near the galaxy's center than in its outer regions. To this aim, we assumed a decreasing surface-number density profile, which is the sum of an exponential function and a uniform background. The parameters of the profile were obtained from a VLT/VIMOS photometric dataset centered on Tucana, which was kindly provided by G. Beccari (ESO) and M. Bellazzini (INAF-OAS). This photometry was preferred to the FORS2 pre-imaging and the DES-DR1 photometry used for the CMD-selection since it is much deeper (almost 3 magnitudes in I-band), although it extends up to the tidal radius. To obtain the best-fitting structural parameters we applied a Bayesian Markov chain Monte Carlo (MCMC) analysis following the density profile of the RGB stars, as was done in Cicuéndez et al. (2018), while accounting for contamination. The assumed profile proved to be a good representation of the observed surface-number density profile for Tucana, and the best-fitting structural parameters showed in Table 3.3 resulted perfectly compatible with those reported by Saviane et al. (1996)[5].

The prior probability of contamination by foreground stars P_{non} was based on the Besançon model (Robin et al., 2003). The generated distribution of l.o.s. velocities was well-fit by a Gaussian profile ($\bar{v}_{\mathrm{Bes}} = 57$ km s^{-1}; $\sigma_{\mathrm{Bes}} = 99$ km s^{-1}). The contamination model was generated in the direction of Tucana over an area equivalent to a FLAMES/GIRAFFE pointing selecting stars over the range of colors and magnitudes described above.

The l.o.s. velocity distribution of the probable member stars $P_{\mathrm{mem}}(v_{\mathrm{i}})$ was assumed to be Gaussian, as in Ch. 2, and accounted for the different kinematic

[5]These authors also performed an exponential fit to the RGB density profile, which, however, was obtained from a shallower photometry covering approximately the same area as that of VLT/VIMOS.

TABLE 3.3— Structural parameters from MCMC analysis fitting an exponential density profile to the RGB population selected in the VLT/VIMOS photometry. We report the value of the central density, the coordinates of the optical center, the scale parameters projected along the optical major axis, the position angle of the optical major axis, the ellipticity and the density of constant contamination.

Parameter	Units	Value
σ_0	stars arcmin^{-2}	475^{+32}_{-30}
(α_0, δ_0)	deg	340.4589 ± 0.0006, -64.4198 ± 0.0004
r_0	arcmin	0.72 ± 0.03
P.A.	deg	95.6 ± 1.9
ϵ		0.46 ± 0.02
σ_c	stars arcmin^{-2}	1.1 ± 0.2

models according to the following rotational term: $v_{\rm rot}(R_i)\cos(\theta - \theta_i)$, with R_i being the angular distance from the galaxy's center, θ_i the position angle (measured from north to east) of the i-th target star, θ the position angle of the kinematic major axis (i.e., the direction of the velocity gradient, perpendicular to the axis of rotation), while $v_{\rm rot}(R_i)$ is the modeled rotational velocity term. We fit and compared three kinematic models: a dispersion-only model (i.e., with the velocity rotation term set to zero), a model with its rotational velocity linearly increasing with its radius ($v_{\rm rot}(R_i) = k\,R_i$) and a flat one ($v_{\rm rot}(R_i) = v_{\rm c} = $ constant).

The free kinematic parameters were as follows: the systemic velocity $\bar{v}_{\rm hel}$ and velocity dispersion $\sigma_{\rm v}$ common to the three models, the position angle θ of the kinematic major axis, the velocity gradient k of the linear rotation model, and the constant rotational velocity v_c of the flat model. In our definition, the position angle θ varies between 0° and 180°, which means that a rotation signal (either expressed as k or $v_{\rm c}$) that has a negative sign implies a receding velocity on the west side of the galaxy (and would be equivalent to a positive gradient adding 180° to θ). The model evidences, Z, were combined through the Bayes factor, $B_{1,2} = Z_1/Z_2$, where the subscripts indicate a given model. To quantify the statistical significance of one model with respect to another, we made use of the Jeffreys scale, based on the natural logarithm of the Bayes factor: positive values of $(0-1), (1-2.5), (2.5-5), (5+)$ correspond to inconclusive, weak, moderate, and strong evidence favoring one model over the other (Ch. 2; but also Wheeler et al., 2017). In our case, we had the following Bayes factors: $\ln B_{\rm lin,flat}$, comparing the evidences of the two rotational models, and $\ln B_{\rm rot,disp}$, between the evidences of the best rotational model (choosing the one that has the largest Z) and that of the dispersion-only one.

We used the following priors for the kinematic parameters: $-50 < (\bar{v}_{\rm hel} - v_g)\,[{\rm km\,s^{-1}}] < 50$, where v_g is the initial mean value of the velocity distribution, $0 < \sigma_{\rm v}\,[{\rm km\,s^{-1}}] < 50$, $-50 < k\,[{\rm km\,s^{-1}\,arcmin^{-1}}] < 50$, and $-50 < v_c\,[{\rm km\,s^{-1}}] < 50$. The prior over θ was set iteratively: we initially chose the prior range $0 < \theta < \pi$, ran the MultiNest code the first time in order to obtain the maximum value θ_m from the θ posterior distribution, and ran the MultiNest code again while updating the prior range to $-\pi/2 < \theta - \theta_m < +\pi/2$. This choice accounted for the limit case of θ near 0 or π.

Results of the recovered probability-weighted kinematic parameters and evidences for the three analyzed datasets, together with the effective number of probable members (defined as $N_{\rm eff} \approx \Sigma_{\rm i} P_{\rm M_i}$) are reported in Table 3.4. The $P_{\rm M_i}$ finally assigned to each target were those obtained from the most significant kinematic model.

The P91 FORS2 dataset yields 39 effective members, while the inclusion of the P69 and FLAMES data adds about 15 more effective members. These numbers already double the member stars reported by F09 (17) and G19 (36, although when accounting for their probability of membership they reduce to $\sim$ 20 effective members). We shall note that for each analyzed dataset, the effective number of members resulted to be approximately the same for each kinematic model. In all cases, the systemic velocity is stable around 180 ${\rm km\,s^{-1}}$, while the velocity dispersion converges to 6 ${\rm km\,s^{-1}}$ for the dispersion-only model, which proved to be the most statistically significant one. Both the systemic velocity and velocity dispersion values are significantly lower than what has been reported in literature studies. We refer to Sect. 3.5 for the full discussion of the results from the kinematic analysis.

We should also note that the adopted method does not take into account the different selection functions of the various datasets that were independently built. Therefore, to test whether this introduced a bias in our results, we repeated the analysis, relaxing the assumption of an exponentially declining surface-number density profile for Tucana's stars, and simply required it to be monotonically decreasing (like in Walker et al., 2009c). No significant difference in the results was found.

3.5 Kinematic results

The analyses of the properties of the stellar component of Tucana carried out in the literature indicated a system with a relatively high l.o.s. velocity dispersion ($\sigma_v \sim 15$ ${\rm km\,s^{-1}}$) compared to other similarly luminous companions (see e.g., the compilation for LG dwarfs of Kirby et al., 2014 and Wheeler et al., 2017). The

TABLE 3.4— Parameters and evidences resulting from the probability-weighted Bayesian kinematic analysis for all the datasets analyzed in this work.

Sample	N_{in}	N_{eff}	Model	$\bar{v}_{hel}$ ($km\,s^{-1}$)	σ_v ($km\,s^{-1}$)	k ($km\,s^{-1}\,arcmin^{-1}$)	v_c ($km\,s^{-1}$)	θ (deg)	Bayes factor
P91	43	39	Linear	$178.9^{+1.4}_{-1.5}$	$6.2^{+1.9}_{-1.7}$	$-1.9^{+2.4}_{-5.1}$		5^{+40}_{-38}	$\ln B_{\rm lin,flat} = 0.4$
			Flat	$179.0^{+1.4}_{-1.3}$	$6.0^{+2.0}_{-1.6}$		$0.5^{+2.3}_{-2.1}$	164^{+50}_{-64}	$\ln B_{\rm rot,disp} = -2.6$
			No rotation	$179.0^{+1.3}_{-1.3}$	$5.7^{+1.7}_{-1.5}$				
P91+P69	63	53	Linear	$180.0^{+1.4}_{-1.4}$	$7.4^{+2.3}_{-1.7}$	$3.2^{+5.9}_{-2.9}$		173^{+23}_{-38}	$\ln B_{\rm lin,flat} = 0.6$
			Flat	$180.0^{+1.3}_{-1.4}$	$6.6^{+1.7}_{-1.3}$		$1.0^{+2.2}_{-2.0}$	152^{+34}_{-62}	$\ln B_{\rm rot,disp} = -2.3$
			No rotation	$180.0^{+1.3}_{-1.2}$	$6.4^{+1.6}_{-1.2}$				
All comb.	109	55	Linear	$180.2^{+1.5}_{-1.5}$	$8.4^{+2.2}_{-2.0}$	$6.3^{+4.5}_{-4.5}$		167^{+16}_{-26}	$\ln B_{\rm lin,flat} = 1.6$
			Flat	$179.9^{+1.3}_{-1.4}$	$7.0^{+1.9}_{-1.4}$		$1.5^{+2.2}_{-2.2}$	140^{+47}_{-61}	$\ln B_{\rm rot,disp} = -1.1$
			No rotation	$180.1^{+1.2}_{-1.3}$	$6.6^{+1.6}_{-1.2}$				

Notes. The reported values of the kinematic parameters represent the median of the corresponding marginalized posterior distributions, with 1-σ errors set as the confidence intervals around the central value enclosing 68% of each distributions.

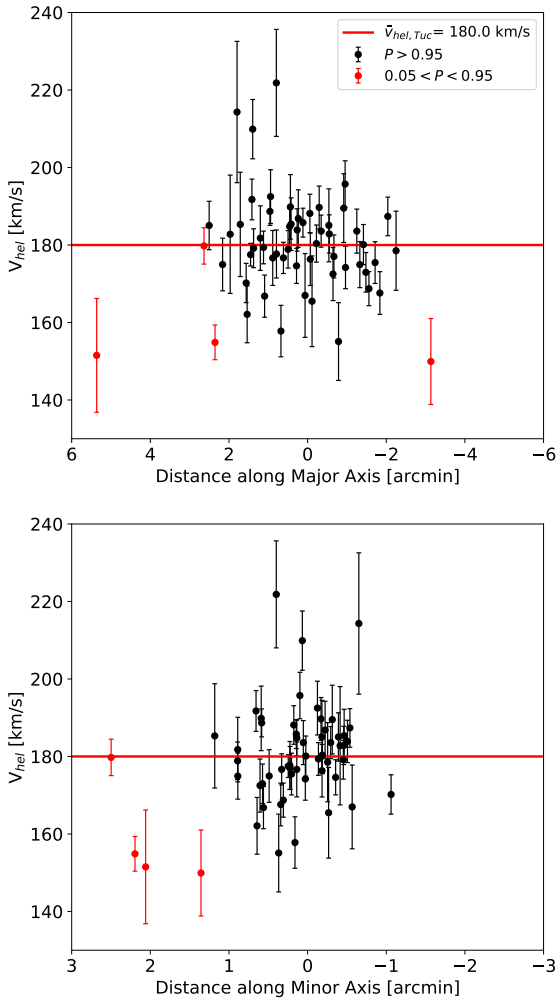

FIGURE 3.3— Line-of-sight velocity distributions of the stars from the combined FORS2 + FLAMES dataset, having membership probabilities $P > 0.95$ (in black) and $0.05 < P < 0.95$ (in red). The red solid line indicates the systemic velocity obtained from the kinematic analysis. *Left panel*: the distribution along the optical major axis; *right panel*: along the minor axis.

works of F09 and G19 also reported the tentative presence of a velocity gradient likely due to internal rotation, since perspective effects related to transverse motion are negligible at the distance of Tucana. However, in a Bayesian analysis of the rotational support of the stellar component of LG galaxies using data from the literature, Wheeler et al. (2017) found no significant evidences for rotation and a l.o.s. velocity dispersion as high as 21 $\mathrm{km\,s^{-1}}$ when analyzing the F09 catalog. Finally, there seems to be little agreement about the systemic velocity of Tucana among F09 and G19, showing an offset of ~ 20 $\mathrm{km\,s^{-1}}$ at more than 3-σ significance.

As shown in Table 3.4, our results are remarkably similar for all the cases we analyzed. When using the P91 FORS2 data alone, combining P91 and P69, or with all the datasets together, the systemic velocity and the velocity dispersion settled around $\sim$180 $\mathrm{km\,s^{-1}}$ and 6 $\mathrm{km\,s^{-1}}$, respectively. Furthermore, we found no significant evidence of rotation, with the dispersion-only model moderately favored in all of the cases. We note a slight increase in the velocity dispersion for the rotational models: this is caused by few targets acquiring a higher membership probability, due to the different fitted models. However, the effect is small, and all the velocity dispersion values we obtained are compatible within 1-σ.

We further performed a simpler analysis on the three datasets, considering only those targets with the highest membership probabilities (i.e., with $P_{\mathrm{M}} > 0.95$) looking for the kinematic parameters of a dispersion-only model, whose results confirmed those of the probability-weighted analysis. Performing the same test by adding those stars with a lower membership probability (i.e., with $0.05 < P_{\mathrm{M}} < 0.95$), would instead increase the velocity dispersion up to 8 $\mathrm{km\,s^{-1}}$, which is still within 1-σ of the previous results taking into account the error bars. We also note that these stars are found further away from the center of Tucana compared to the more probable members (see Fig. 3.3), but they are still inside the tidal radius of the galaxy. However, it is hard to discern whether the increase in the velocity dispersion seen when including stars with lower membership probability is caused by a radially increasing velocity-dispersion profile, or simply because (all or part of) these stars are contaminants. Considering those stars with a lower membership probability that have metallicity measurements, they seem to be preferentially metal-poor (see Fig.3.4). Therefore, it may also be that the increase in σ_v could be caused by the preferential inclusion of metal-poor stars with a hotter velocity dispersion than the more metal-rich stars (Tolstoy et al., 2004; Battaglia et al., 2006, 2008a, 2011; Amorisco & Evans, 2012a). We refer to Sect.3.6.2 for more details on this point.

We highlight the fact that underestimated (optimistic) or overestimated (pessimistic) velocity errors may impact on the measured velocity dispersion.

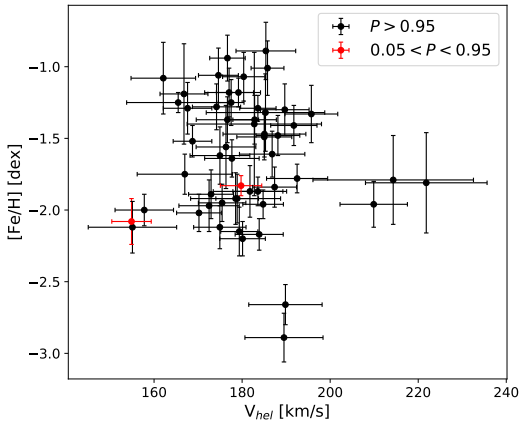

FIGURE 3.4— Metallicity versus heliocentric velocity for the observed target of the combined FORS2 dataset. Black dots represent the targets with $P > 0.95$, while red dots show those with $0.05 < P < 0.95$.

We refer the reader to Fig. 1 in Koposov et al. (2011) for an analysis of the impact of underestimated/overestimated velocity errors as a function of the ratio between the true error and the true velocity dispersion. However, as reported in Appendix 3.A.1, we conducted several consistency tests where we show that the velocity errors are well-determined.

Therefore, our results for Tucana point to a value for the velocity dispersion which is very unlikely to exceed 10 $\mathrm{km\,s^{-1}}$. We assume $\sigma_{\mathrm{v}} = 6.2^{+1.6}_{-1.3}$ $\mathrm{km\,s^{-1}}$as our reference value, averaging between the results of the dispersion-only model from the analyzed datasets.

3.5.1 MultiNest mock tests

Although we have found that the rotation signal in our catalog is not statistically significant, we conducted a series of mock tests in order to explore which rotational properties can be detected according to the characteristics of our data. To this aim, we followed the approach already introduced in Ch. 2: we produced mock catalogs of l.o.s. velocities assuming the same number, spatial position, velocity distribution, and velocity uncertainties of the observed data. Our base catalog was the combined FORS2 P91 + P69 + FLAMES

dataset after applying a $P_{\rm M} > 0.05$ cut; the inclusion of less probable members was a compromise to have the highest number of targets (57) within the largest spatial area. To each target we assigned a mock velocity $v_{\rm mock}$ randomly extracted from a Gaussian distribution centered on zero and of standard deviation equal to the assumed velocity dispersion, fixed at $\sigma_{\rm v,mock} = 6$ km s^{-1}. This value of $\sigma_{\rm v,mock}$ was set according to the converging results from the probability-weighted analysis of our datasets. We further added a linear rotational component $v_{\rm rot,mock}$ projected on the kinematic major axis, such that $v_{\rm rot,mock}/\sigma_{\rm v,mock} = n = 1.5, 1.0, 0.75, 0.5, 0.25, 0$ at the half-light radius. These correspond to velocity gradients of $k = 11.2, 7.5, 5.6, 3.7, 1.9, 0$ km s^{-1} arcmin^{-1}, which we simulated at three different position angles, starting from the P.A. of the optical semi-major axis (97°) and then adding 45 and 90 degrees (optical semi-minor axis). We chose an underlying linear rotation component since it resulted in higher evidence compared to a flat rotation model when analyzing our data. Each case was simulated $N = 1000$ times, in which we run our Bayesian kinematic analysis fitting just the linear rotation and the dispersion-only models in order to recover the related parameters and evidences. Results are shown in Table 3.5.

Results from the tests indicate that the linear rotation would be spotted with high significance for velocity gradient values ≥ 5.6 km s^{-1} arcmin^{-1} aligned with the projected optical major axis. If the underlying rotation is instead milder, for example with velocity gradients ≤ 3.7 km s^{-1} arcmin^{-1}, the recovered evidences for rotation are weak, inconclusive, or favoring the dispersion-only model, as we move through decreasing values of k and through different position angles. In any case, it is evident that if Tucana has a weak rotation signal (i.e., $k \leq 3.7$ km s^{-1} arcmin^{-1}), with the data we had, we could not detect it with high significance, particularly if it is not aligned with the optical major axis. If instead Tucana has a velocity gradient as reported in F09 and G19, meaning with a value close to $k = 5.6$ km s^{-1} arcmin^{-1} along the major axis, with our data we would have detected it with high significance, but this was not the case. Therefore, it seems that if rotation is actually present in Tucana, it is probably at a level of $v_{\rm rot}/\sigma_{\rm v} \lesssim 0.5$, and to detect it with high significance a better sampling would be needed, in particular at radii around $3 \lesssim R/R_e \lesssim 5$. We note that these results are conservative: in fact, if we had considered an input velocity dispersion as high as 10 km s^{-1}, the linear rotation signal would have been even more difficult to detect.

TABLE 3.5— Mock results for the P91+P69+FLAMES ($P > 0.05$) catalog using an input linear rotation model. The first two columns represent the input parameters of the rotation model. In all cases, the input systemic velocity V_{sys} and velocity dispersion σ_v were fixed to 0 and 6 km s^{-1}, respectively. The middle columns are the recovered parameter fitting a linear rotation model and a dispersion-only one, respectively. The last column is the Bayes factor accounting for the evidences of the two models.

k (km/s/′)	θ_k (°)	V_{sys} (km/s)	σ_v (km/s)	k (km/s/′)	θ_k (°)	V_{sys} (km/s)	σ_v (km/s)	$\ln B_{rot,disp}$
11.2	97	$0.03^{+1.26}_{-1.22}$	$6.08^{+1.11}_{-1.26}$	$11.40^{+0.88}_{-0.77}$	$96.83^{+9.17}_{-9.18}$	$2.69^{+1.22}_{-1.25}$	$16.56^{+1.33}_{-1.17}$	$34.06^{+5.43}_{-4.78}$
	142	$0.00^{+1.18}_{-1.27}$	$6.03^{+1.17}_{-1.18}$	$11.10^{+1.61}_{-1.58}$	$141.36^{+6.05}_{-6.81}$	$0.20^{+1.11}_{-1.27}$	$12.05^{+1.30}_{-1.24}$	$19.67^{+5.36}_{-4.55}$
	187	$-0.07^{+1.24}_{-1.29}$	$6.12^{+1.14}_{-1.36}$	$10.84^{+2.01}_{-1.80}$	$187.55^{+5.55}_{-4.70}$	$-2.36^{+1.16}_{-1.23}$	$9.70^{+1.21}_{-1.21}$	$9.92^{+4.49}_{-3.97}$
7.5	97	$0.08^{+1.17}_{-1.28}$	$6.00^{+1.11}_{-1.39}$	$7.73^{+0.84}_{-0.87}$	$96.03^{+12.62}_{-13.37}$	$1.76^{+1.09}_{-1.28}$	$11.63^{+1.19}_{-1.26}$	$19.11^{+4.84}_{-4.55}$
	142	$0.00^{+1.08}_{-1.13}$	$5.97^{+1.17}_{-1.26}$	$7.35^{+1.75}_{-1.57}$	$141.11^{+9.21}_{-12.74}$	$0.06^{+1.13}_{-1.03}$	$9.06^{+1.18}_{-1.28}$	$9.26^{+4.43}_{-4.02}$
	187	$-0.11^{+1.12}_{-1.18}$	$5.98^{+1.21}_{-1.26}$	$7.01^{+1.92}_{-1.91}$	$187.18^{+8.22}_{-7.34}$	$-1.55^{+1.06}_{-1.11}$	$7.85^{+1.16}_{-1.24}$	$3.12^{+3.56}_{-2.90}$
5.6	97	$0.01^{+1.16}_{-1.21}$	$6.10^{+1.24}_{-1.23}$	$5.94^{+0.91}_{-0.95}$	$96.35^{+16.68}_{-17.46}$	$1.19^{+1.15}_{-1.10}$	$9.59^{+1.23}_{-1.31}$	$10.85^{+4.75}_{-3.87}$
	142	$-0.03^{+1.20}_{-1.22}$	$6.01^{+1.24}_{-1.24}$	$5.46^{+1.47}_{-1.54}$	$139.47^{+11.33}_{-11.20}$	$0.04^{+1.26}_{-1.24}$	$7.88^{+1.10}_{-1.20}$	$4.41^{+3.54}_{-3.29}$
	187	$-0.17^{+1.25}_{-1.25}$	$6.10^{+1.26}_{-1.25}$	$5.03^{+1.94}_{-2.05}$	$188.44^{+12.05}_{-10.14}$	$-1.19^{+1.14}_{-1.18}$	$7.18^{+1.23}_{-1.25}$	$0.41^{+3.92}_{-3.30}$
3.7	97	$0.04^{+1.17}_{-1.21}$	$6.07^{+1.12}_{-1.28}$	$4.08^{+0.95}_{-0.92}$	$94.80^{+25.01}_{-23.97}$	$0.81^{+1.07}_{-1.13}$	$7.67^{+1.20}_{-1.15}$	$3.85^{+3.42}_{-3.13}$
	142	$-0.10^{+1.26}_{-1.18}$	$6.03^{+1.16}_{-1.23}$	$3.50^{+1.46}_{-1.27}$	$139.67^{+17.43}_{-27.83}$	$0.01^{+1.17}_{-1.05}$	$6.88^{+1.27}_{-1.29}$	$0.15^{+3.04}_{-1.99}$
	187	$-0.13^{+1.13}_{-1.23}$	$6.00^{+1.17}_{-1.19}$	$2.87^{+2.10}_{-1.58}$	$188.08^{+18.70}_{-15.21}$	$-0.73^{+1.06}_{-1.17}$	$6.55^{+1.21}_{-1.21}$	$-1.68^{+1.24}_{-1.24}$
1.9	97	$0.07^{+1.12}_{-1.23}$	$6.10^{+1.06}_{-1.31}$	$2.25^{+1.11}_{-1.06}$	$97.21^{+45.31}_{-50.07}$	$0.47^{+1.06}_{-1.21}$	$6.56^{+1.18}_{-1.24}$	$-1.40^{+2.48}_{-1.46}$
	142	$-0.08^{+1.13}_{-1.10}$	$6.00^{+1.14}_{-1.28}$	$1.63^{+1.47}_{-1.23}$	$152.44^{+26.47}_{-46.04}$	$-0.04^{+1.08}_{-1.13}$	$6.21^{+1.17}_{-1.14}$	$-2.41^{+1.53}_{-0.79}$
	187	$-0.05^{+1.09}_{-1.14}$	$6.01^{+1.10}_{-1.35}$	$1.26^{+1.74}_{-1.13}$	$183.09^{+31.00}_{-27.01}$	$-0.32^{+1.05}_{-1.11}$	$6.16^{+1.11}_{-1.17}$	$-2.81^{+1.42}_{-0.52}$
0.0	97	$0.01^{+1.10}_{-1.16}$	$5.97^{+1.19}_{-1.17}$	$0.17^{+1.18}_{-1.48}$	$146.72^{+30.94}_{-116.54}$	$0.01^{+1.07}_{-1.12}$	$6.03^{+1.15}_{-0.28}$	$-3.13^{+0.80}_{-0.28}$
	142	$-0.02^{+1.09}_{-1.18}$	$5.97^{+1.06}_{-1.24}$	$-0.18^{+1.52}_{-1.24}$	$168.49^{+29.45}_{-48.65}$	$-0.03^{+1.05}_{-1.16}$	$6.02^{+1.12}_{-1.16}$	$-3.09^{+0.89}_{-0.33}$
	187	$0.01^{+1.20}_{-1.20}$	$5.91^{+1.16}_{-1.24}$	$-0.04^{+1.38}_{-1.34}$	$176.81^{+42.76}_{-30.81}$	$0.02^{+1.14}_{-1.20}$	$5.98^{+1.16}_{-1.27}$	$-3.11^{+0.85}_{-0.31}$

3.5.2 Comparison with other works

In Appendix 3.A.3, we perform a comparative analysis of the velocity measurements for the individual stars derived in this work and those in F09 and G19. Here, we focus instead on the comparison of the recovered velocity parameters from the kinematic analyses of the different works.

Firstly, we ran our code on the F09 velocity measurements for member stars, and the same for G19, in order to see if we were able to recover their results. Considering a dispersion-only model, we found a 1-σ agreement between the recovered velocity parameters and those reported by these authors. Therefore, our procedure does not introduce a bias, and we can directly compare with the reported values in F09 and G19.

We found an offset of $\sim$ 15 (35) km s^{-1} for the systemic velocity between the values reported by F09 (G19) and by us – $\bar{v}_{\rm hel,F09} = 194.0 \pm 4.3$ km s^{-1} and $\bar{v}_{\rm hel,G19} = 216.7^{+2.9}_{-2.8}$ km s^{-1}. These offsets are somewhat higher but still compatible with those reported in Appendix 3.A.3, so we refer the reader to that section for an analysis of the possible causes. We stress that if we analyze our reduction of the P69 and the FLAMES data on their own, we obtain systemic velocities compatible at the 1-σ level with our value of $\sim$180 km s^{-1}; therefore, the differences encountered appear to be related to the treatment of the datasets. On the other hand, the velocity dispersion values (without accounting for the presence of possible gradients) reported by F09 and G19 – $\sigma_{\rm v,F09} = 15.8^{+4.1}_{-3.1}$ km s^{-1} and $\sigma_{\rm v,G19} = 14.4^{+2.8}_{-2.3}$ km s^{-1}, differ from our reference $\sigma_{\rm v}$ value almost at the 3-σ level.

If we were to analyze our reduction of the P69 FORS2 dataset alone, we would obtain 17 effective members out of 23 input targets, showing a velocity dispersion value of $\sigma_{\rm v,P69} = 11.1^{+3.7}_{-2.7}$ km s^{-1}, associated with a highly significant rotation signal. We noticed, however, that this gradient is driven by just two targets that have a very low membership probability when analyzing the combined FORS2 dataset. If we excluded them, the velocity dispersion would drop to $\sim$8 km s^{-1} and the velocity gradient basically disappears. Therefore, it seems here that the low-number statistics strongly limit the conclusions we could get on the kinematic status of Tucana via the P69 dataset on its own.

The comparison with G19 results are even more puzzling. If we were to apply the same exercises as for the P69 dataset, analyzing the FLAMES data on their own, we would obtain 11 effective members out of 58 targets, which, however, could not resolve the σ_v value. This is probably due to the combination of a small number of effective members and the fact that the average velocity error of stars with a high probability of membership ($\delta_{\rm v} \sim 6$ km s^{-1}) is comparable to the σ_v value we find in our main kinematic analysis.

Furthermore, we want to underline that we found several differences when comparing our velocity measurements to those of G19, as described in Appendix 3.A.3. We suspect that the way the data were actually sky subtracted has led to an excess of stars with velocities around 220 $\mathrm{km\,s^{-1}}$ in the G19 work, probably due to a combination of sky-line residuals and low S/N, which would have created fake CaT features.

3.5.3 Implications for Tucana's dark matter halo properties

As previously discussed, the analysis of the internal kinematic properties of Tucana yields consistent results across the combination of datasets. Our best value for the velocity dispersion of $\sigma_\mathrm{v} = 6.2^{+1.6}_{-1.3}$ $\mathrm{km\,s^{-1}}$ is significantly lower ($\sim$3-σ) than what was reported in the literature by both F09 and G19 (see also the discussion in the previous section), but closer now to the values observed for other similarly luminous dwarf galaxies of the Local Group (see e.g. Kirby et al., 2014; Revaz & Jablonka, 2018).

We use the Wolf et al. (2010) mass-estimator, valid for dispersion-supported spherical systems, to calculate Tucana's dynamical mass inside the half-light radius, $M_{1/2} = 3G^{-1}\sigma_\mathrm{v}^2 r_{1/2} \approx 4G^{-1}\sigma_\mathrm{v}^2 R_\mathrm{e}$, where G is the gravitational constant and $r_{1/2}$ is the 3D de-projected half-light radius, which can be approximated to $4/3R_\mathrm{e}$. Using the values from Table 3.1 and substituting for σ_v, we obtain $M_{1/2} = 0.7^{+0.4}_{-0.3} \times 10^7 M_\odot$, which corresponds to a mass-to-light ratio within the half-light radius of $M_{1/2}/L_V = 13^{+8}_{-7}\, M_\odot/L_\odot$, assuming a luminosity of $L_V = 5.5 \pm 1.5 \times 10^5\, L_\odot$ (adapted from Saviane et al., 1996).

Using instead the velocity dispersion values from F09 and G19, applying the Wolf et al. (2010) mass-estimator we would obtain $M_{1/2,\mathrm{F09}} = 4.8^{+2.6}_{-2.0} \times 10^7 M_\odot$ and $M_{1/2,\mathrm{G19}} = 3.9^{+1.6}_{-1.4} \times 10^7 M_\odot$ respectively, which are more than four time as large as our own best estimation of Tucana's mass.

Our measurements for velocity dispersion and dynamical mass of Tucana provide a new perspective to the discussion found in the literature. If instead of $M_{1/2}$ we use the value of the circular velocity $V_\mathrm{circ}(r_{1/2}) = \sqrt{3}\sigma_\mathrm{v}$, we obtain a value of 11^{+3}_{-2} $\mathrm{km\,s^{-1}}$ for Tucana, assuming our reference value for σ_v. This $V_\mathrm{circ}(r_{1/2})$ is comparable to those of other similarly luminous dwarfs like Carina, Sextans, and Leo II, as it is possible to see from Fig. 10 in G19, but also from Fig. 1 in Boylan-Kolchin et al. (2012). From this last reference, we find that Tucana should live in a Navarro-Frank-White (NFW) dark matter halo with a maximum circular velocity $V_\mathrm{max} \leq 24$ $\mathrm{km\,s^{-1}}$, as is the case for many dSphs of the LG. Therefore, Tucana is no exception to the too-big-to-fail problem, as claimed in G19. Furthermore, according to the halo mass concentration relation of Dutton & Macciò (2014), higher values of the maximum circular

velocity means higher central dark-matter concentrations. This would imply that Tucana does not reside in a very centrally dense halo, as was also predicted by G19.

We refer to Sect. 5.2.2 for a more extensive discussion on the too-big-to-fail problem in the contest of LG dwarf galaxies.

3.6 Chemical analysis

The analysis of the [Fe/H] values of the FORS2 combined dataset led to the following results: considering the values with $P_{\rm M} > 0.95$, we obtained median [Fe/H]$= -1.58$ dex, $\sigma_{\rm MAD} = 0.47$ dex, $\sigma_{\rm intrinsic} = 0.39$ dex; while adding the stars with $0.05 < P < 0.95$ we instead obtained a median of [Fe/H]$= -1.61$ dex, $\sigma_{\rm MAD} = 0.48$ dex, $\sigma_{\rm intrinsic} = 0.39$ dex. Therefore, Tucana is a metal-poor system with a significant spread in metallicity. The median [Fe/H] value measured for the likely members is in very good agreement with the integrated quantity derived from Tucana's SFH: $\langle$[Fe/H]$\rangle = -1.52 \pm 0.07$ dex (Monelli et al., 2010). In addition, our average [Fe/H] value falls within the rms scatter of the stellar luminosity-metallicity relation for LG dwarf galaxies reported by Kirby et al. (2013b), while the intrinsic scatter agrees well with the values of other similarly luminous dwarf galaxies (Leaman et al., 2013).

The distribution of the [Fe/H] values as a function of the elliptical radius is shown in Fig. 3.5. The significant scatter in metallicity toward the inner part of the galaxy is evident. In addition, there is a bimodality in the metallicity histogram suggesting the presence of two subpopulations. This can be related to the results obtained from deep photometric data (Monelli et al., 2010), where it was shown that the splitting observed in the HB, in the RGB bump, and in the properties of the RR-Lyrae stars, imply that Tucana has been able to produce a second generation of metal-rich stars thanks to the self-enrichment from the first stars in a very short period of star formation (~ 1 Gyr). In a more recent study, Savino et al. (2019) reanalyzed the photometric data from Monelli et al. (2010), by studying the main-sequence turn off and the HB of Tucana. They were able to obtain an SFH with a finer temporal resolution, showing that Tucana actually experienced two early phases of star formation (SF), followed by a third one ending between 6 and 8 Gyr ago, with the two initial episodes being the most intensive. According to the age-metallicity relation recovered by Savino et al. (2019), our [Fe/H] measurements could be related to the intermediate-old and intermediate-young age populations of the two last episodes of SF. This would explain the bimodality we observed in the metallicity histogram, while our most metal-poor stars could be related to the oldest episode of SF. However,

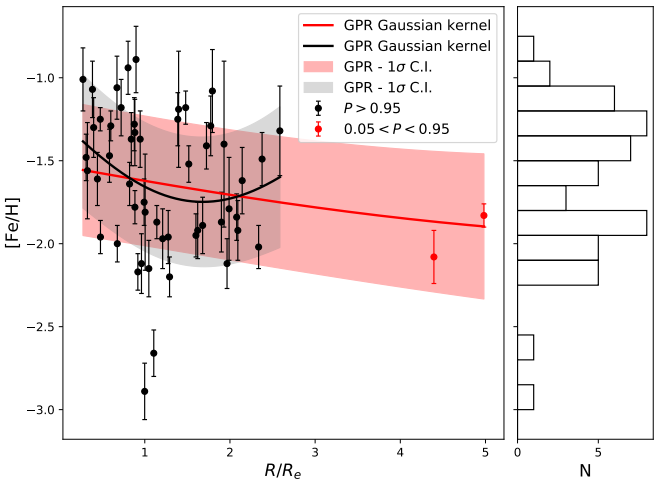

FIGURE 3.5— [Fe/H] as a function of the elliptical radius scaled with R_e for Tucana's probable member stars from the FORS2 combined dataset. Black dots represent the targets with membership probabilities $P > 0.95$, while the red dots show those with $0.05 < P < 0.95$. The black solid line represents the result of a Gaussian process regression analysis using a Gaussian kernel and taking into account an intrinsic scatter; the gray band indicates the corresponding 1-σ confidence interval. The solid red line and the red band indicate the same, but using all targets with $P > 0.05$. The histogram on the right side represents the metallicity distribution of the stars with $P > 0.95$.

despite the relatively high intensity of this SF period, we found very few stars with [Fe/H]< -2.25 dex. This is probably related to the fact that, for lower metallicity stars, due to weaker lines, a higher S/N is needed in order to get similar accuracy in [Fe/H] measurements.

3.6.1 Looking for a metallicity gradient

Observations have shown that in many LG dwarf galaxies the young and metal-rich stars are more spatially concentrated than the old and metal-poor ones that display a more extended spatial distribution. Their overall radial distribution produces a decreasing metallicity gradient, e.g., Fornax (Battaglia et al., 2006; Leaman et al., 2013), Phoenix (Kacharov et al., 2017), which could eventually

reach a plateau on the outside, e.g., Sculptor (Tolstoy et al., 2004), VV 124 (Kirby et al., 2013a), Cetus (Ch. 2). These results have also been reproduced by simulations (e.g., Schroyen et al., 2013; Revaz & Jablonka, 2018), which have shown that the shape of these gradients strongly depends on the combination of the stellar mass, SFH, and dynamical history of the system under consideration, although their strength could be influenced by merger events (Benítez-Llambay et al., 2016) or environmental effects such as tidal stripping (Sales et al., 2010).

Therefore, we investigated the presence of a metallicity gradient as a function of radius, first focusing on the stars with $P > 0.95$, which extended up to $\sim 3\,R_e$ (see Fig. 3.5). Performing an error-weighted linear least-square fit to the data, we obtained the value $m = \frac{\mathrm{d[Fe/H]}}{\mathrm{d}R} = -0.16 \pm 0.09$ dex arcmin^{-1} ($= -0.6 \pm 0.4$ dex kpc^{-1} $= -0.13 \pm 0.07$ dex R_e^{-1}, using the values reported in Table 3.1 for the conversions). We also performed a Gaussian process regression (GPR) analysis, where we used a Gaussian kernel together with a noise component to account for the intrinsic metallicity scatter. The GPR has the advantage of being a kernel-based non-parametric probabilistic method that makes it possible to compute empirical confidence intervals. Since we are looking for a smooth function, it performs better than a least-square fit in finding the general trend in the data. In our case, we confirmed the decreasing trend, although the 1-σ confidence limits proved quite large due to the high intrinsic scatter of the data, making the presence of a metallicity gradient within $\sim 3R_e$ dubious.

We further checked this result by performing a simple simulation, similarly to what was done in Sect. 2.6 for Cetus. We assumed a double Gaussian metallicity distribution with parameters roughly fitting the observed one, but no spatial variation ($\mu_{[Fe/H],1} = -2.0$ dex, $\sigma_{[Fe/H],1} = 0.2$ dex, $\mu_{[Fe/H],2} = -1.3$ dex, $\sigma_{[Fe/H],2} = 0.2$ dex, assuming the same fraction of stars in the two Gaussians). We then randomly extracted [Fe/H] values at the radial positions of our data. We further reshuffled the [Fe/H] values according to the observed errors, and, finally, we performed a linear least-square fit looking for a spatial metallicity gradient. We repeated this process 1000 times. The obtained average gradient was compatible with zero, with the associated scatter large enough to include within 1-σ the observed value of m. Therefore, with the data we had, the observed gradient within $R < 3\,R_e$ is not statistically significant.

Adding the stars with $0.05 < P < 0.95$ would extend the spatial coverage up to $R \sim 6R_e$, thanks to the two outermost targets, but would lead to an even milder gradient: $m = -0.07 \pm 0.04$ dex arcmin^{-1} ($= -0.28 \pm 0.16$ dex kpc^{-1} $= -0.06 \pm 0.03$ dex R_e^{-1}), by performing a linear least-square fit. The presence of a metallicity gradient in Tucana is expected from studies of deep-photometric data (Hidalgo et al., 2013; Savino et al., 2019). However it is probable that

we are mainly targeting stars belonging to the more recent episodes of SF, whose populations share similar spatial extensions (see e.g., Fig. 11b in Savino et al., 2019). Therefore, the presence of a metallicity gradient in Tucana is very tentative, and we would need a better sampling, in particular, of the metal-poor component, around $3 \lesssim R/R_e \lesssim 5$ to put our results on firmer ground.

We compared Tucana's metallicity gradient (or rather the lack thereof) with those of some MW satellites with similar luminosities ($L_V \lesssim 5^5 L_\odot$) and short SFHs, for example, Draco (Aparicio et al., 2001), Ursa Minor (Carrera et al., 2002), and Sextans (Bettinelli et al., 2018). All of them formed the majority of their stars more than 10 Gyr ago within a short period of SF, which in some cases may have lasted no more than 1 Gyr (i.e., Sextans). It has been shown that such short SFHs may lead to mild metallicity gradients in these systems (Marcolini et al., 2008; Kirby et al., 2011; Revaz & Jablonka, 2018). Indeed, both Draco and Ursa Minor show mild gradients with values of -0.05 dex R_e^{-1} and -0.03 dex R_e^{-1}, as reported by Schroyen et al. (2013) and Kirby et al. (2011), respectively[6]. Sextans, on the other hand, seems to have a stronger gradient of -0.24 dex R_e^{-1}, as reported by Schroyen et al. (2013) using the Battaglia et al. (2011) spectroscopic dataset. However, this value is somewhat overestimated since recent studies of the structural properties of Sextans (Roderick et al., 2016; Cicuéndez et al., 2018) show that this system is less extended than what was previously reported in the literature. Using the half-light radius value from Cicuéndez et al. (2018), we find a lower gradient of -0.18 dex R_e^{-1}, which is still far from the other dwarf's values and probably related to an early merger event that could have steepened its metallicity gradient (see Cicuéndez & Battaglia, 2018, but also Benítez-Llambay et al., 2016). If the case of Tucana is similar to those of Draco and Ursa Minor, as it seems, we would expect it to host an equally mild metallicity gradient, but it would take a better sampling of the spatial extension of the metal-poor component in Tucana to confirm it.

Please, refer to Sect. 5.2.3 for a detailed discussion on the metallicity properties of LG dwarf galaxies.

[6]We revised Draco's gradient using the more recent and spatially extended dataset of Walker et al. (2015): we performed a broad membership selection like in Walker et al. (2015) (see their Fig. 10) and then refined it by cross-correlating with the *Gaia*-DR2 catalog, selecting those targets co-moving with Draco. We found a value of -0.09 ± 0.02 dex R_e^{-1} from the linear least-square fit, in fair agreement with the previous one.

TABLE 3.6— Parameters from the Bayesian kinematic analysis of the metal-rich (MR) and metal-poor (MP) sub-samples defined in Sect.3.6.2.

	$P > 0.95$		$P > 0.05$	
Sample	N	$\sigma_{\rm v}$ ($\rm km\,s^{-1}$)	N	$\sigma_{\rm v}$ ($\rm km\,s^{-1}$)
MR	26	$6.0^{+1.9}_{-1.6}$	27	$5.9^{+1.9}_{-1.6}$
MP	26	$9.0^{+2.8}_{-2.4}$	27	$10.9^{+2.6}_{-2.2}$

3.6.2 Searching for two chemo-kinematically-distinct populations

Although we have not spotted a clear metallicity gradient in Tucana, the bimodality found in the metallicity distribution, may indicate the presence of two sub-populations which differ not only in their chemical properties, but also in their kinematics. Some of the dSphs satellites of the MW, such as Sculptor, Fornax, Carina, and Sextans, show such features where the metal-rich (usually more spatially concentrated) sub-population has colder kinematics than the metal-poor (and more extended) one (e.g., Tolstoy et al., 2004; Battaglia et al., 2006, 2008a, 2011; Koch et al., 2008; Amorisco & Evans, 2012a). Determining the chemo-kinematic properties of dSphs is of great interest, not only to better understand their evolutionary path, but also to get an insight into their dark matter properties (e.g., Battaglia et al., 2008a; Walker & Peñarrubia, 2011; Amorisco & Evans, 2012b; Strigari et al., 2018).

In the case of Tucana, we first analyzed the combined FORS2 dataset with the $P > 0.95$ cut applied (see Fig. 3.4). We took the median [Fe/H] value of -1.58 dex to split our sample into metal-rich (MR) and a metal-poor (MP) sub-samples. We then ran our code to obtain the kinematic parameters of both samples (see Sect.3.5). Using the dispersion-only model, we found $\sigma_{\rm v,MR} = 6.0^{+1.9}_{-1.6}$ $\rm km\,s^{-1}$ and $\sigma_{\rm v,MP} = 9.0^{+2.8}_{-2.4}$ $\rm km\,s^{-1}$, which are 1-σ from each other. Including instead the $0.05 < P < 0.95$ data, we obtained: $\sigma_{\rm v,MR} = 5.9^{+1.9}_{-1.6}$ $\rm km\,s^{-1}$ and $\sigma_{\rm v,MP} = 10.9^{+2.6}_{-2.2}$ $\rm km\,s^{-1}$, which are instead $\sim$2-σ from each other (see Table 3.6).

Therefore, there is weak evidence of two chemo-kinematically distinct sub-populations in Tucana. Additional data, in particular including external parts of the galaxy are necessary to reach firm conclusions, regarding the presence of a metallicity gradient as well as the possible distinct chemo-kinematic populations.

3.7 Summary and conclusions

In this chapter, we present results regarding the internal kinematic and metallicity properties of the Tucana dwarf spheroidal galaxy, based on the analysis of multi-object spectroscopic samples of individual RGB stars.

This analysis is based on a novel set of 50 individual objects collected with the VLT/FORS2 instrument in MXU mode in P91, complemented by a re-reduction and reanalysis of two datasets from the literature, namely the VLT/FORS2-MXU dataset presented in Fraternali et al. (2009, F09) and the VLT/FLAMES-GIRAFFE one by Gregory et al. (2019, G19). Applying a probabilistic membership approach, we find 39 effective members in our P91 sample, which doubles the number of Tucana's member stars found in F09 and G19.

A full re-reduction and analysis of the data presented in the literature was carried out because it became clear that the published catalogs could not be directly combined with the l.o.s. velocities we derived for the P91 sample: there are significant differences between the values of the systemic velocity reported in those studies with respect to that we derived from the P91 dataset ($\sim$195 $\mathrm{km\,s^{-1}}$ for F09, $\sim$215 $\mathrm{km\,s^{-1}}$ for G19, while $\sim$180 $\mathrm{km\,s^{-1}}$ in our case); and the comparison of the individual l.o.s. velocities for the stars in common were supporting the presence of shifts with respect to F09, but were not sufficient to fully quantify whether that was the only source of difference, or if it was even more unfavorable for the comparison with G19.

Following our homogeneous data reduction, we find an excellent agreement between velocity measurements of the three datasets both for stars in common (Fig. 3.6 top row panels) as well as for systemic velocity, which is stable around 180 $\mathrm{km\,s^{-1}}$ for the three datasets (see Fig.3.2, right panel, and Table 3.4). We proceeded to analyze the P91 dataset alone and also in combination with our treatment of the P69 and FLAMES data. The resulting values of the intrinsic l.o.s. velocity dispersion are consistently around 6 $\mathrm{km\,s^{-1}}$ when considering the three combinations of datasets (P91, P91+P69, all the three combined) and the highly probable members (probability of membership $P_{\mathrm{M}} > 0.95$); when including lower probability members, the velocity dispersion increases, but it is unlikely that σ_{v} is higher than 10 $\mathrm{km\,s^{-1}}$. Therefore, our analysis leads to the conclusion that the l.o.s. velocity dispersion of Tucana's stellar component is much lower than the values reported by F09 and G19 – $\sigma_{\mathrm{v,F09}} = 15.8^{+4.1}_{-3.1}$ $\mathrm{km\,s^{-1}}$ and $\sigma_{\mathrm{v,G19}} = 14.4^{+2.8}_{-2.3}$ $\mathrm{km\,s^{-1}}$.

Furthermore, we find no significant signs of internal rotation. Mock tests suggest that if Tucana had had a maximum rotational velocity of $\sim$10-15 $\mathrm{km\,s^{-1}}$ along the projected major axis (as previously reported in literature) with the data available to us, we should have detected it with high significance. On

the other hand, lower levels of rotation are not completely ruled out, but a larger sample would be needed to quantify their presence. Nevertheless, it seems improbable that Tucana is a fast rotator ($v_{\rm rot}/\sigma_{\rm v} \gtrsim 1$).

Assuming an average $\sigma_{\rm v} = 6.2^{+1.6}_{-1.3}\,{\rm km\,s^{-1}}$for our data, we obtain a dynamical mass within the half-light radius of $M_{1/2} = 0.7^{+0.4}_{-0.3} \times 10^7 M_{\odot}$. This translates into a circular velocity at the half-light radius of $V_{\rm circ}(r_{1/2}) = 11^{+3}_{-2}\,{\rm km\,s^{-1}}$, which implies that, if Tucana inhabits a NFW dark matter halo, it should have a similar density to those of other MW dSphs (Boylan-Kolchin et al., 2012). Therefore, Tucana is not an exception to the too-big-to-fail problem and not "a massive failure", as it had gained fame for being.

The analysis of Tucana's chemical properties was only carried out on the combined P91 and P69 FORS2 data, due to their higher S/N. We establish that the galaxy is mainly metal-poor with a significant scatter in metallicity (having a median [Fe/H] $= -1.58$ dex, $\sigma_{\rm MAD} = 0.47$ dex and $\sigma_{\rm intrinsic} = 0.39$ dex when considering only highly likely members, and median [Fe/H] $= -1.61$ dex, $\sigma_{\rm MAD} = 0.48$ dex, and $\sigma_{\rm intrinsic} = 0.39$ dex when including the less likely members). The derived values agree very well with SFH studies (Monelli et al., 2010; Savino et al., 2019). In addition, the average [Fe/H] falls between the rms scatter of the stellar luminosity-metallicity relation for LG dwarf galaxies (Kirby et al., 2013b).

Looking at the distribution of the [Fe/H] values as a function of radius, we find a mild metallicity gradient. However, the size and spatial distribution of the current datasets do not lead to a statistically significant detection. The presence of a gradient in Tucana would be expected from the age gradients inferred from deep photometric studies (Hidalgo et al., 2013; Savino et al., 2019), but also from both observations and simulations of similarly luminous dwarfs (see e.g., Leaman et al., 2013; Schroyen et al., 2013; Revaz & Jablonka, 2018), which indeed host mild metallicity gradients. Therefore, the presence of an underling gradient in Tucana is not excluded, but it would need a better sampling of the metal-poor component in Tucana (particularly at $R \gtrsim 3R_e$) to confirm it. Finally, we find a hint of the presence of multiple stellar populations with distinct chemo-kinematical properties, although in this case, the addition of new data would also help to put this result on firmer ground.

Authorship

This chapter is based on the published work of Taibi et al. (2020), where several authors has been involved. My contribution has been of the most relevant, from data reduction to the analysis and final writing of the manuscript.

3.A Appendix – consistency checks and comparisons

3.A.1 Consistency checks

We performed consistency checks in order to unveil the presence of possible systematic errors in our velocity determinations using *fxcor*, or other issues. For all the datasets analyzed, we searched for systematics by shifting the template spectrum at several velocities (from -50 km s^{-1} to 500 km s^{-1} at step of 50 km s^{-1}) and cross-correlating them with the templates themselves at rest, through the full wavelength range of data, and also only around the CaT. We did not find any significant systematic shift introduced by the cross-correlation procedure as a function of the velocity shift nor the cross-correlation range.

We also verified that the random errors were well-treated by the *fxcor* task and if they led to reliable velocity errors. In this case, we performed a Monte Carlo analysis, randomly adding the error-spectra from targets having measured S/N of 10, 15, 20, 25, and 30 Å^{-1} for the FORS2 datasets, and of 5, 10, 20, 50, and 100 Å^{-1} for the FLAMES one, to the shifted templates of the previous step. We performed 250 realizations for each case and found that the procedure tends to produce velocity errors that are underestimated with respect to the velocity scatter from the individual Monte Carlo runs for S/N lower than 10 Å^{-1}, for both datasets. Therefore, we take these values as the limit S/N above which we will trust the velocity error estimations. At this S/N, the velocity errors were found to be $\sim \pm 10$ km s^{-1} in both cases.

We further checked the choice of using the two reddest lines of the CaT for the cross-correlation measurements of the FLAMES dataset (see previous section), creating two more catalogs of velocity estimations using both the entire CaT range and the two bluest lines. Cross-correlating between catalogs and selecting those targets with an S/N $>$ 10 Å^{-1}, which reduced our sample to 76 objects out of 164, we found very good agreement, excluding eight targets that had velocity measurement differences more than 3-σ from each other. We visually checked the corresponding spectra for these targets and found that for the outliers the first and/or third line of the CaT resulted affected by sky residuals or were hidden by noise, while in general, the central line resulted more clearly visible. For fiber 118, the opposite happened, and we considered the measurement obtained using the full CaT range for this case.

Considering once again the velocities from targets having an S/N $>$ 10 Å^{-1}, we looked for cases were the cross-correlation procedure did not get a velocity solution, finding only two cases (fibers 18 and 55). Their visual inspection did not show obvious CaT lines, and we thus decided to discard these two targets.

Finally, we checked the internal accuracy of our P91 FORS2 dataset by

inspecting the four targets in common between the two pointings. Of these, three had reliable measurements of velocity and metallicity that were compatible within 1-σ, while the other one did not have reliable measurements. In fact, it did not show a visible CaT, and its I-magnitude and color were also not compatible with the RGB of Tucana (see also Sect.3.4). We then decided to discard this target from the sample and to average the measurements from the other three targets together.

We further excluded two more targets from the P91 FORS2 dataset since their measurements were not reliable due to high residuals in their spectra: these are slit 14, chip-2 of Tuc0 field, and slit 17, chip-1 of Tuc1. The high residuals in these two spectra were due to the stellar trace falling on a bad CCD-row and a poor sky-subtraction that could not be improved, respectively.

3.A.2 Comparison between measurements of different datasets obtained with our reduction

We compared the measurements obtained from the P91 dataset with those from our reduction of the P69 and FLAMES datasets, using the targets they had in common. This was an important step to ensure we could combine the velocity catalogs.

The P91 and P69 FORS2 datasets have five targets in common with measured velocities and metallicities, while the FLAMES dataset has seven targets in common (four taking those with S/N > 10 Å^{-1}) with the P91 FORS2 dataset and 18 (15) with the P69 one (see the top row of Fig. 3.6 for the velocity comparison).

The agreement between these common targets is excellent, mostly within 1-σ, except for three targets in common between the FLAMES dataset and the P69 FORS2 one (marked as object 1, 2 and 3 in the top row of Fig. 3.6) with velocities over 3-σ from each other. Of these targets, two are in common with the P91 FORS2 dataset (objects 1 and 3), which are in good agreement with the FLAMES measurements (Fig. 3.6 top row, central panel), but not with those of the P69 FORS2 dataset (Fig. 3.6 top row, right panel). We then found that the problem may reside with the measurements from the P69 FORS2 catalog. Therefore, we inspected these outliers, namely slits 9 and 10 of chip-1 and slit 13 of chip-2 (respectively object 1, 2, and 3 in the cited figures), finding that slits 9 and 13 have particularly noisy sky-line residuals around the first two CaT lines that may have compromised their measurements, while the spectrum of slit 10 was clean. However, this target was marked as a double star and with slit mis-centering problems in F09. We then decided to exclude these values from the P69 FORS2 catalog, but to maintain them in the P91

FORS2 and FLAMES datasets. In conclusion, after a homogeneous analysis, the measurements for stars in common, which were taken during several epochs as well as with different instruments and spectral resolution in the case of FORS2 and FLAMES, are found to be in very good agreement.

3.A.3 Comparison with other works

Comparison with F09: The l.o.s. velocity and metallicity distributions of the P91 and F09 datasets show a difference of $\sim$ 10 $\mathrm{km\,s^{-1}}$ and $\sim$ 0.25 dex in the mean values, respectively. We investigated whether clear offsets could be found by comparing the measurements of the targets in common between the two studies. There are only three such stars, for which the metallicities agree at the 1-σ level, but the l.o.s. velocities differ at 3-σ level for two stars, and 1.5-σ for the other one, respectively. The stars discrepant at the 3-σ level were slits 9 and 13 of chip-1 and -2, respectively (targets 7 and 18 in F09), whose P91 spectra do not show any particular issue.

Since we could not pinpoint the sources of these differences in the line-of-sight velocities, we decided to re-reduce and reanalyze the F09 FORS2 dataset, so as to be homogeneous with the treatment of the P91 data.

The comparison of the l.o.s. velocities and metallicities derived from our reduction of the P69 FORS2 dataset and those published by F09 showed average offsets of 7 $\mathrm{km\,s^{-1}}$ and 0.2 dex in the velocity and metallicity measurements, of the same signs and comparable to those previously found between the targets in common between the P91 FORS2 dataset and the F09 catalog (see Fig. 3.6 bottom row, left panel for the velocity comparison). It is unclear what leads to the measured difference in velocity. For the metallicities, the [Fe/H]-CaT EW calibration in F09 is equivalent to that used here in the metallicity and magnitude regime of Tucana's stars, and the 0.1 mag difference in the adopted V_{HB} value does not have a significant impact on the final [Fe/H] values. The main source of difference is likely to reside in how the EWs were calculated: in F09, Gaussian profiles were used to fit the CaT lines, while we adopt Voigt profiles. We checked that if we were to adopt Gaussian profiles, we would obtain lower metallicities of a difference comparable to the systematic shift we previously found. We want to stress, however, that the Voigt profiles represent a better fit to the CaT lines, in particular along the line wings (see e.g., Starkenburg et al., 2010).

Comparison with G19: We compared our own reduced datasets with the full catalog of observed targets by G19. There was not a good agreement in all cases. The P91 FORS2 dataset was the one with the lowest number of common targets (6), which showed mainly a systematic offset of $\sim 30\ \mathrm{km\,s^{-1}}$. One target,

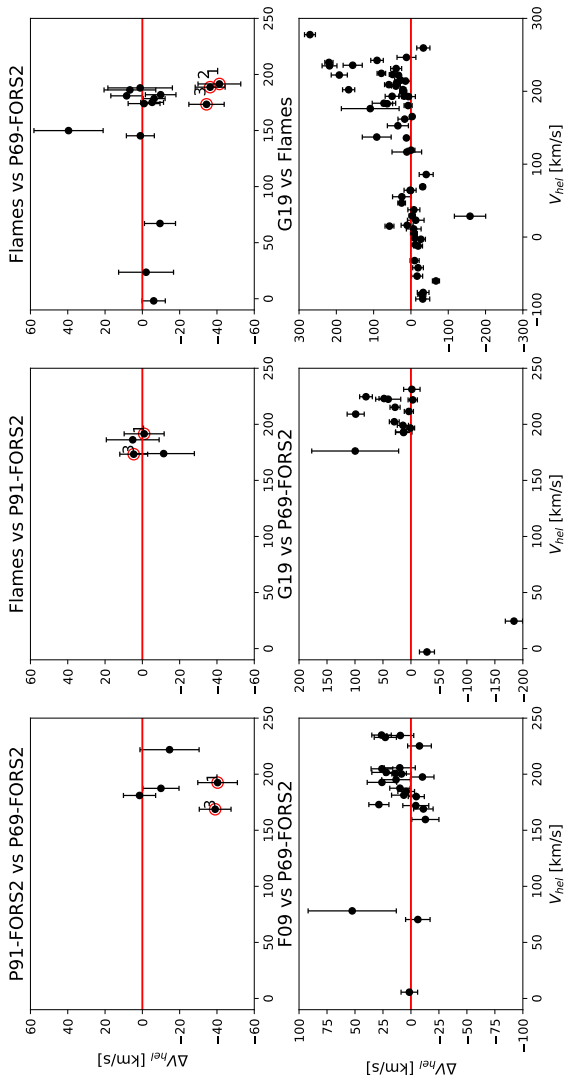

FIGURE 3.6— Velocity comparison for common targets between datasets – v_{hel} vs. Δv_{hel}. *Top:* between the datasets from our internal reduction – *left:* the FORS2 datasets; *center:* Flames vs. P91-FORS2; *right:* Flames vs. P69-FORS2. Red circles indicate the problematic targets highlighted in the main text. *Bottom:* between our datasets and those from the literature – *left:* F09 vs. P69-FORS2; *central:* G19 vs. P69-FORS2; *right:* G19 vs. Flames.

however, showed a velocity difference of $\sim 130\,\mathrm{km\,s^{-1}}$. We visually checked for it in our dataset (target 13 of chip-1 in Tuc0), finding a clean, high S/N spectrum, with no features that could have biased the velocity measurement.

The P69 FORS2 dataset proved to have 16 targets in common with G19 (see Fig. 3.6 bottom row, central panel). While for a few targets there is good agreement, overall, there is a large scatter in the distribution of velocity differences with one significant outlier (target 1 of chip-2). An inspection of its corresponding spectrum in the P69 data showed the CaT lines shifted with respect to the rest frame by $\sim 200\,\mathrm{km\,s^{-1}}$, compatible with what we found in the cross-correlation measurements, but significantly different from the $\sim 25 \pm 14$ $\mathrm{km\,s^{-1}}$ reported by G19.

The comparison between the velocities we derived from our treatment of the FLAMES dataset was even more puzzling, considering that the values obtained come from the same sample. As can be seen from the bottom-right panel of Fig. 3.6, there is a significant scatter among the 59 targets in common (we compared only those measurements from our dataset with a, $\mathrm{S/N} > 10\ \mathrm{\AA^{-1}}$), in particular at high velocities ($> 100\,\mathrm{km\,s^{-1}}$), and there might even be a dependence as a function of velocity between the two datasets. We also confirmed that these problems remain when considering only those targets marked as likely members of G19.

A systemic velocity for Tucana around 200 $\mathrm{km\,s^{-1}}$was found by G19. At $v_{\mathrm{hel,G19}} \sim 200\,\mathrm{km\,s^{-1}}$, the comparison in Fig. 3.6 (bottom row, right panel) gives velocities around $170 - 190\,\mathrm{km\,s^{-1}}$ for our FLAMES measurements of the same stars (i.e., velocities close to the systemic velocity we find for Tucana), as well as values between $0 - 50\,\mathrm{km\,s^{-1}}$, so, typical of foreground stars. Our suspicion is that the G19 catalog contains an excess of stars with velocities around $200\,\mathrm{km\,s^{-1}}$.

We investigate this possibility in two ways: by comparing the radial distribution of the G19 members with that obtained from photometric observations of Tucana's stars (test A) and comparing the G19 l.o.s. velocity distribution for the stars they considered as nonmembers with the expectations from a Galactic foreground model (test B). In both cases, we took into account the displacement of the FLAMES pointings from the center of Tucana.

Test A: We looked at the normalized cumulative radial distribution of G19's member stars, and compared it to that obtained from the observed surface density profile of Tucana that we measured from the VLT/VIMOS photometric catalog introduced in Sect.3.4. Although the VLT/VIMOS catalog does not cover the entire area of the FLAMES pointings, it was sufficient for following the surface-density profile of the RGB stars of Tucana up to its nominal tidal radius.

We found that the number of G19's member stars in the outer parts of Tucana, up to where VLT/VIMOS photometry extends, tends to be overestimated with respect to that expected from the photometry for Tucana's RGB stars in the same area. It could, however, be argued that the FLAMES/GIRAFFE fiber set-up might imprint a different distribution than that expected from the photometry. Therefore, we performed the following "Test B", which is instead free from this possible issue.

Test B: We now concentrate on the l.o.s. velocity distribution of the stars marked as nonmembers in G19, which should only contain Galactic contaminants: this distribution shows two clear peaks in the velocity histogram, one around 0 $\mathrm{km\,s^{-1}}$, and, unexpectedly, the other at ~ 200 $\mathrm{km\,s^{-1}}$ (G19, Fig. 6). Making the reasonable assumption that the nonmembers are mainly foreground Galactic contaminants, we compared their velocity distribution with that obtained from the Besançon model (Robin et al., 2003) generated in the direction of Tucana over an area equivalent to that of a FLAMES-GIRAFFE pointing, and by opting for the Besançon model stars to have similar positions on the CMD as on the FLAMES targets. The velocity distribution of the Besançon model stars showed just a single peak around 0 $\mathrm{km\,s^{-1}}$, with a smooth decline towards negative and positive velocities, with a tail extending to 300 $\mathrm{km\,s^{-1}}$. We checked if the peak at ~ 200 $\mathrm{km\,s^{-1}}$ for G19's nonmembers could be explained from the distribution expected from the Galactic model. We randomly chose, from the synthetic dataset, a number of stars equal to that of the G19 nonmembers, and, over 1000 trials, calculated the number of objects extracted from the Besançon model that would have velocities > 150 $\mathrm{km\,s^{-1}}$: we never got a number of contaminants as high as that of G19's nonmembers over the same velocity range. This indicates that the number of stars with velocities ~ 200 $\mathrm{km\,s^{-1}}$ in the G19 catalog of nonmembers could likely be overestimated. Performing the same exercise for our FLAMES targets that proved to be nonmembers (i.e., with $P < 0.05$) considering the targets with velocities > 120 $\mathrm{km\,s^{-1}}$ (accounting for the observed shift between the datasets), we found that the observed number of nonmembers is within the 87% (1.5-σ) of the distribution obtained for the contaminants.

We speculate that this excess of velocities around $\sim$200 $\mathrm{km\,s^{-1}}$ in the G19 dataset can be attributed to a sky subtraction problem around the CaT region. In fact, the sky-lines at 8504Å and 8548Å, which are around the first and second lines of the CaT, if badly subtracted could lead to strong absorption residuals. These features, in a low-S/N regime and during the cross-correlation procedure, could be mistaken for the first two CaT lines shifted at ~ 200 $\mathrm{km\,s^{-1}}$, so around the value of the systemic velocity reported for Tucana by G19.

4

An aMUSEing view of the isolated dwarf irregular galaxy IC 1613

ABSTRACT

Aims. To understand the internal mechanisms that shape the evolution of a dwarf galaxy, analysing its kinematic and chemical properties according to the ages and spatial distribution of its stars.

Methods. We analysed a new spectroscopic dataset taken with the integral-field-unit MUSE instrument mounted on the Very Large Telescope (VLT), capable of combining high spatial resolution to a wide spectral coverage ($\lambda\lambda 4750 - 9300$ Å) with a resolving power of $R = 1500 - 3000$, obtaining a large dataset of ~ 2000 extracted sources. The quality of the sample allowed us to perform the spectral classification and determination of radial velocities for more than 800 stars. At the same time we were able to obtain metallicities from the Ca II triplet lines for a selected subsample of red giant branch stars.

Results. The kinematic analysis led to a systemic velocity of $\bar{v}_{\rm sys} = -234.0 \pm 0.6$ km s^{-1} and to a velocity dispersion of $\sigma_{\rm v} = 11.3 \pm 0.5$ km s^{-1}, both in agreement with literature values. We also found with high statistical significance a linear rotation signal along the optical major axis of the galaxy. Stars follow the velocity field of the neutral HI component, although they start to decouple from the gas motion around the half-light radius. The chemical analysis led to a median [Fe/H] $= -1.07$ dex and an intrinsic scatter of 0.18 dex. The average [Fe/H] resulted slightly higher than literature values, but within the rms scatter of the stellar luminosity-metallicity relation. We found no signs of a radial metallicity gradient, compatible with results from other similarly luminous dwarf galaxies.

4.1 Introduction

IC 1613 is a Local Group (LG) dwarf irregular galaxy (dIrr) found in isolation. First discovered by Wolf (1906), it was recognised soon afterwards as an extragalactic object by Baade (1935, as reviewed by Sandage, 1971), who first determined its distance using Cepheid variable stars. Since then, several other measurements of its distance have been made using different indicators, including RR-Lyrae variable stars and the tip of the red giant branch (RGB). A compilation of all distance values in the literature (including their own) was reported by Bernard et al. (2010), who obtained a statistical average value of $(m - M)_0 = 24.400 \pm 0.014$, or 759 ± 5 kpc.

The large distance places IC 1613 far beyond the virial radius of both the Milky Way (MW) and M31 (McConnachie, 2012). However, it could probably be dynamically associated with the latter, although no signs of recent interaction appear, like signs of tidal disturbances. Interestingly, (Buck et al., 2019) assign to IC 1613 a high probability of being a backsplash galaxy of M31. Its low-luminosity, with an absolute magnitude of $M_V = -15.2$, corresponds to a stellar mass of $M_* \sim 10^8\ M_\odot$, similar to that of other LG dIrrs, like NGC 6822 and WLM (McConnachie, 2012).

The star formation history (SFH) and stellar content of IC 1613 have been studied in detail over the years (see e.g. Cole et al., 1999; Skillman et al., 2003; Bernard et al., 2007; Skillman et al., 2014). Based on deep Hubble Space Telescope (HST) Advance Camera for Survey (ACS) imaging, and after a review of archival HST data, Skillman et al. (2014) concluded that the SFH of IC 1613 has been constant throughout its life, with no evidence of an early dominant episode of star formation[1]. The chemical enrichment was linearly increasing through time, with average metallicities ranging from [Fe/H] ~ -2.0 dex to -0.8 dex. Stars were formed at an average rate of $\psi(t) = 0.081 \pm 0.001\ M_\odot \mathrm{yr}^{-1}$.

The structural properties of IC 1613 has been determined by studying the spatial distribution of stellar tracers in different evolutionary phases (see e.g. Albert et al., 2000; Borissova et al., 2000; Bernard et al., 2007; Garcia et al., 2009; Sibbons et al., 2015; McQuinn et al., 2017). In general, it was found that the young stars are more centrally concentrated than the intermediate-age and old stars, a common feature with many other dwarfs (see Pucha et al., 2019, and references therein). Recently, however, Pucha et al. (2019) using deep and wide Subaru/Hyper-SuprimeCam observations of IC 1613, showed that its young main sequence stars, along with the RGB and ancient horizontal branch

[1]The HST/ACS field analysed by Skillman et al. (2014), roughly located at the half-light radius of the galaxy, was considered as representative of the global SFH of IC 1613. The comparison with archival HST observations located at different radii supported this assumption.

(HB) stars, all extend to the outskirts of the galaxy, up to $\sim$ 24 arcmin (i.e. ~ 4 effective radii R_e). In particular, the young stars are found well beyond the currently active star forming regions (within $\sim 1.5R_e$), although with a much lower density compared to the intermediate and old age companions. They also showed a steeper radial density profile in the inner regions than in the outer ones, in contrast to the RGB and HB stars. This seems to imply a different formation channel between the younger (e.g. from gas pushed outward through stellar feedback) and older stars (probably via accretion) in the galaxy's outskirts.

As other dIrrs, IC 1613 contains an extended component of neutral hydrogen (HI) gas, with a clumpy distribution on the inside, but showing regular contours at larger radii (see van den Bergh, 2000, and references therein). In particular, the HI distribution is rich of shells and voids around the currently active star forming regions, where also the ionized gas is distributed (e.g. Lozinskaya et al., 2003; Silich et al., 2006; Moiseev & Lozinskaya, 2012). The HI kinematics shows a linearly increasing rotation curve with a $v_{\rm max} \sim 20$ km s^{-1} (Lake & Skillman, 1989; Oh et al., 2015). This value, however, probably represents a lower limit due to the fact that the inclination angle is poorly constrained for this galaxy, being almost face-on (Oh et al., 2015, but also Read et al., 2016). The mass modelling made by Oh et al. (2015) gave a total mass for the HI component of $M_{\rm HI} \sim 6 \times 10^7 M_\odot$, and a dynamical mass of $M_{\rm dyn} \sim 3 \times 10^8 M_\odot$, obtained up to a distance of ~ 3 kpc.

The chemical abundance of the interstellar medium has been obtained spectroscopically from the central HII regions resulting in a measurement of $12 + \log({\rm O/H}) = 7.73 \pm 0.04$ dex (Bresolin et al., 2007, but see also Lee et al., 2003 and Tautvaišienė et al., 2007). This value corresponds to an iron abundance of [Fe/H] $= -0.96$ dex, assuming [O/Fe] $= 0$ and a solar oxygen abundance of $12 + \log({\rm O/H}) = 8.69$ dex (Asplund et al., 2009). The first spectroscopic measurements of stars in IC 1613 were obtained from some of the brightest ones, that is, from 9 early B-type young supergiants (Bresolin et al., 2007) and 3 evolved M-type supergiants (Tautvaišienė et al., 2007). Both studies obtained compatible metallicity values, $12+\log({\rm O/H}) = 7.90\pm0.08$ dex the former study, while [Fe/H] $= -0.67 \pm 0.09$ dex the latter, recently confirmed by Berger et al. (2018) studying 21 young BA-type supergiant stars. Interestingly, these authors found a bi-modal metallicity distribution, that seems to be correlated to the spatial distribution of both gas and young stars. Furthermore, there are evidences from the youngest stellar population and evolved red supergiants of IC 1613 that the present-day [α/Fe] ratio could be sub-solar (i.e. ~ -0.1 dex, Tautvaišienė et al., 2007 and Garcia et al., 2014).

The spectroscopic analysis of a sample of 125 RGB stars in IC 1613 led to the measurement of an average metallicity of [Fe/H] $= -1.19 \pm 0.01$ dex (Kirby

et al., 2013b), in agreement with the fact that older stars are in general more metal-poor than the younger ones, and with the age-metallicity relation found by Skillman et al. (2014). On the same sample, Kirby et al. (2014) conducted a kinematic analysis which led to a systemic velocity of -231.6 ± 1.2 km s^{-1}, in agreement with values from the HI component (Lake & Skillman, 1989; Oh et al., 2015), and a velocity dispersion of $10.8^{+1.0}_{-0.9}$ km s^{-1}. They did not found signs of internal stellar rotation, later confirmed also by Wheeler et al. (2017) who re-analysed the Kirby's dataset. This is not surprising considering that the spatial distribution of this dataset is along the optical minor axis of the galaxy, while in general it is expected that the stellar rotation follows that of the gas, which in this case rotates roughly along the optical major axis (Oh et al., 2015). The dynamical mass at the half-light radius reported by Kirby et al. (2014) was of $M_{1/2} = 1.1 \pm 0.2 \times 10^8 M_\odot$.

Finally, thanks to the low values of both foreground and internal reddening along the line-of-sight (McConnachie, 2012), IC 1613 is an ideal laboratory to compare the observed properties of its diverse stellar content.

In this chapter we present a study of the stellar kinematic and chemical properties of IC 1613. We analysed a new set of spectroscopic data taken with the integral-field-unit MUSE instrument mounted on the Very Large Telescope (VLT). Taking advantage of the unique capabilities of this instrument, capable of combining high spatial resolution with wide spectral coverage, we were able to perform a kinematic analysis as a function of stellar age and to provide metallicites for the largest spectroscopic sample of RGB stars obtained to date for this galaxy.

The chapter is structured as follows: in Sect. 4.2 we give details on the data acquisition and reduction processes we conducted. Section 4.3 is dedicated to spectral classification and radial velocity determination. In Sect. 4.4 we report details on the determination of likely member stars and their subsequent kinematic analysis. Section 4.5 shows results of the chemical analysis of the RGB stars. Finally, Sect. 4.6 is dedicated to the summary and perspectives of future work, while in the appendices are reported details on the sanity checks conducted on the spectral-fitting codes used during our analysis.

The parameters adopted for IC 1613 throughout the text are summarized in Table 4.1.

TABLE 4.1— Parameters adopted for IC 1613 throughout the text.

Parameter	Units	Value	Ref.
$\alpha_{\rm J2000}$		$01^h04^m47.8^s$	(1)
$\delta_{\rm J2000}$		$+02°07'04''$	(1)
$\epsilon^{(a)}$		0.11 ± 0.03	(1)
P.A.	deg	50 ± 2	(1)
$R_{\rm e}$	arcmin (kpc)	6.8 ± 0.3 (1.50 ± 0.07)	(1)
$L_{\rm V}$	$10^6 M_\odot$	100 ± 15	(1)
$D_\odot$	kpc	759 ± 5	(2)
E(B-V)		0.025	(2)
$\bar{v}_{\rm sys}$	$\rm km\,s^{-1}$	-234 ± 0.6	(3)
$\sigma_{\rm v}$	$\rm km\,s^{-1}$	11.3 ± 0.5	(3)
[Fe/H]	dex	-1.07	(3)
$\sigma_{\rm [Fe/H]}$	dex	0.18	(3)
Conversion	$\rm pc\,arcmin^{-1}$	221	

Notes. The table lists: the coordinates of the galaxy's optical centre; the ellipticity; the position angle; the effective radius; the stellar luminosity in V-band; the heliocentric distance; the average reddening along the line-of-sight; the chemo-kinematic parameters obtained in this work, i.e., the systemic velocity, the velocity dispersion, the median metallicity, and the intrinsic metallicity scatter. $^{(a)}\epsilon = 1 - b/a$.
References. (1) McConnachie (2012); (2) Bernard et al. (2010); (3) this work.

4.2 Observations and Data Reduction

The data were acquired with VLT/MUSE (Bacon et al., 2010) in service mode, between August and December 2016, under ESO programme 097.B-0373 (PI: Battaglia). MUSE is an integral field spectrograph with a spatial sampling of 0.2 arcsec and a spectral resolution varying between $R = 1500 - 3000$ along its wavelength coverage. We used the nominal mode of MUSE which covers the wavelength range $4750 - 9300$ Å. We observed 3 fields (hereafter F1, F2, F3, moving outward from the centre; see Fig. 4.1 for their location) approximately along the projected semi-major axis of IC 1613, on the West side of the galaxy. We purposely avoided regions of on-going star formation.

Each field was observed with 11000 s on source, split in 5×2200 s exposures, obtained by rotating the position angle of the spectrograph by 90° with respect to the previous exposure. No separate sky field was acquired since the stellar component of IC 1613 is resolved in the magnitude range we are interested in, and the sky contribution is taken care of during the de-blending and extraction of the spectra phase of the data reduction (see Sect. 4.2.1).

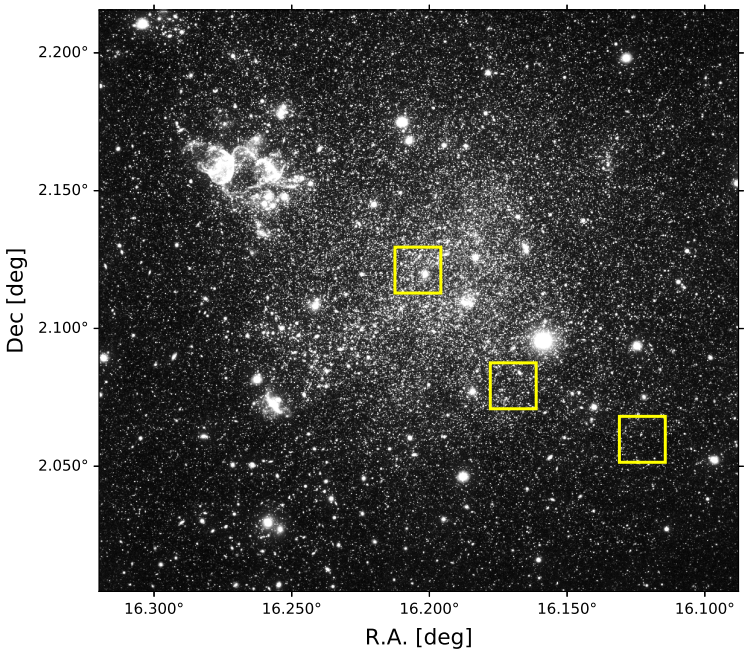

FIGURE 4.1— Finding chart showing the location of the 3 MUSE fields, marked as yellow boxes, overlaid over a wide-field image of IC1613 (Credit: ESO - VST/Omegacam Local Group Survey). North is up, East to the left.

The data were acquired in dark time, clear sky, with a request for a seeing in V-band at zenith $\leq$ 0.9 arcsec, fulfilled for all but one exposure of F1 (for which it deviated within 10% from the request).

4.2.1 Data Reduction and Source Extraction

The data reduction and source extraction steps were carried out by the proposal Co-I S. Kamann (Liverpool John Moores University). All data were reduced using version 1.6 of the official MUSE pipeline (Weilbacher et al., 2012). The basic steps of the reduction cascade (bias subtraction, slice tracing, wavelength calibration, and basic science processing) were performed using the de-

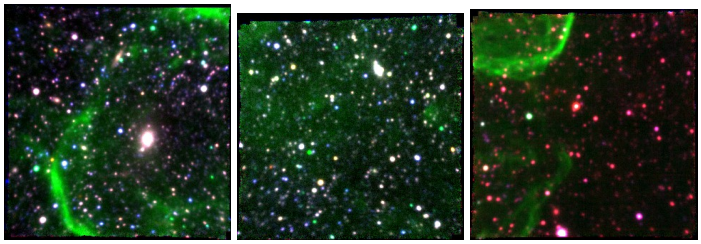

FIGURE 4.2— Rendering of combined V-, H_α and I-band MUSE images for F1, F2 and F3. The limits are chosen to encompass 98%, 98% and 99.5% of the pixel values and are plotted on a linear scale.

fault settings[2]. This resulted in 24 pixel tables (one per spectrograph) for each individual exposure. When combined the pixel tables for each exposure, the flux calibration was also applied using standard stars observed during the same nights. Further, sky emission lines were subtracted using appropriate LSF profiles created from the same arc frames used for the wavelength calibration and the default line list provided with the MUSE pipeline. The intensity of the sky lines was determined directly from the science data which contained sufficiently large patches of (almost) blank sky for this purpose. The sky emission line were further used to quantify the goodness of the wavelength calibration, which had an average accuracy of 0.03 Å, or 1.5 $\mathrm{km\,s^{-1}}$. We note that while the extraction described below does also perform a sky subtraction, we found that performing an additional sky subtraction during the data reduction does improve the results if the exposure times are long (typically more than a few minutes). The final step of the data reduction was the combination of all individual exposures obtained for a pointing. To this aim, the data were corrected for the small astrometric wobbles introduced when moving the de-rotator before running the combination recipe. The individual exposures were weighted according to their estimated seeing in the combination process. The end products of the data reduction were three data cubes, one for each field. Each cube has a dimension of approximately $300 \times 300 \times 3680$ pixels.

The PampelMuse software described in Kamann et al. (2013) was used to extract the stellar spectra from the reduced data cubes. To run PampelMuse, an input catalogue of source positions and an estimate of their initial magnitudes is required. Ideally, such a catalogue would be obtained from imaging data with a

[2]This also implied correcting for the radial velocity of the observer with reference to the barycentre of the Solar System.

higher spatial resolution than the MUSE data. A database of stellar photometry of Local Group dwarf galaxies, including IC 1613, obtained with the Hubble Space Telescope (HST) using the Wide Field Planetary Camera 2 (WFPC2) is publicly available (Holtzman et al., 2006). However, such data only match the central and outermost pointing, but not the one at intermediate radii. Since the MUSE data are only moderately crowded, the input catalogues were directly created from the data-cubes instead, while using the HST/WFPC2 catalogues for their subsequent calibration (see Sect. 4.2.2). To this aim, we produced *V*-, *R*- and *I*-band mock-images (see Fig. 4.2 for a RGB rendering) and extracted photometric catalogues using the DAOPHOT code (Stetson 1987)[3].

The raw version of these source catalogues (i.e. without astrometric solution or photometric calibration applied) were used as input to PampelMuse, which needs only an approximate estimate of the initial magnitude of the sources for deblending the spectra. Using these catalogues, PampelMuse first locates the positions of the stars in the data cubes as a function of wavelength. Then, it tries to recover the PSF of each observation under the assumption that the PSF can be approximated as an analytical Moffat profile. The parameters of the Moffat profile are allowed to vary with wavelength, e.g. to account for the characteristic decrease of the seeing with increasing wavelength. During this PSF-optimisation step, the code also refines the coordinates of all sources in a data cube. Afterwards, the wavelength dependencies of the source positions and the PSF parameters are modelled as low-order polynomials. This is done to suppress small scale variations of the parameters caused by the limited S/N of the data. Finally, PampelMuse performs a simultaneous PSF fit to all sources in each layer of a data cube in order to obtain the final spectra. During the last step, any unresolved component in the data is handled by including a background in the fit which is recomputed at fixed spatial offsets. As IC 1613 contains gaseous emission that varies on rather small spatial scales, well visible in Fig. 4.2, the background component was recomputed every 40 spaxels. Examples of extracted, sky-subtracted spectra are shown in Figs. 4.11 and 4.12.

PampelMUSE returned for each extracted spectrum their associated flux uncertainty per pixel. In addition, it also stored an S/N value calculated around their central wavelength (hereinafter S/N_C). However, since our sources covers

[3]The photometric catalogues were obtained as in Gallart et al. (1996): the DAOPHOT's FIND routine was used to search through the image for star-like objects exceeding the local background noise by at least 3-σ; using the PHOTOMETRY routine, crude aperture photometry and local sky values were derived for the detected objects; the point-spread function (PSF) was obtained using within 20 and 30 stars per image using a quadratically varying Gaussian function; finally ALLSTAR was ran to obtain PSF-fitted magnitudes for stars in each frame.

a wide spectral range (see Sect. 4.3.1), we calculated two further S/N indicators: one around 5500 Å (S/N_{550}), and the other on the continuum around the CaT lines (S/N_{CaT}). In this way, we had a more accurate picture of the quality of our spectra, depending on the spectral type of a given star.

4.2.2 Calibration of the photometric catalogues

The catalogues obtained from the MUSE data-cubes proved to be a valuable resource for our analysis, as they contain the spatial and photometric information of all the extracted sources. However, they needed to be astrometrized and photometrically calibrated. For these purposes, we used the publicly available HST/WFPC2 catalogues from Holtzman et al. (2006), which matched the F1 and F3 fields, and a proprietary Subaru/SuprimeCam[4] one for the F2 field.

We want to note that the field-of-view (FoV) of the Subaru catalogue ($34' \times 27'$) is wide enough to cover all the three MUSE fields at once. However, it lacked an astrometric solution at first, and it suffered of severe crowding toward the galaxy's centre, where F1 is placed. The HST catalogues, on the other hand, did not suffer from any of these problems and we used them as a baseline during the astrometric and photometric calibration processes.

The astrometric solution and photometric calibration were obtained using the suite of codes *CataXcorr* and *CataComb* kindly provided to us by P. Montegriffo and M. Bellazzini (INAF-OAS).

We downloaded the PSF-extracted HST catalogues with transformed magnitudes in the Johnson's system [5]. The covered photometric bands were V- and I-, with the addition of the B-band for the central HST pointing. The Subaru catalogue covered instead the Johnson's B- and V- bands. These were deep photometric catalogues, reaching down to the horizontal branch (at $V \sim 25$), which means that they cover a much wider photometric range than that of our MUSE data. Before proceeding, we performed a pre-cleaning, selecting all sources marked as stellar in the HST catalogues, while retaining those targets in the Subaru catalogue having DAOPHOT parameters: sharpness (SHARP) between -0.5 and 0.5, and a goodness-of-fit (CHI) < 1.

We started with the astrometrization of the Subaru catalogue. Due to its large FoV compared to that of the HST catalogues, we first performed a pre-astrometrization using the stars in common with a PanSTARRS catalogue (Chambers et al., 2016) generated within the FoV of the Subaru one[6]. We

[4]Kindly provided to us by M. Monelli (IAC).

[5]Catalogues can be found at `http://astronomy.nmsu.edu/holtz/archival/ic1613/html/ic1613.html`

[6]The PanSTARRS catalogue was shallower that the Subaru one, reaching only a magnitude

then used the external HST field catalogue to refine the astrometric solution, improving its accuracy to better than 0.05″.

The photometric bands of the MUSE catalogues we were interested in calibrating were V- and I-. Therefore, to make the calibration of the F2 field possible, we had to infer the Subaru I-band using the common targets with the central HST catalogue (which covered the B-band). We applied the following linear equation: $I_{\rm HST} - V_{\rm HST} = c_I\,(B_{\rm HST} - V_{\rm HST}) + ZP_I$. We obtained a colour term $c_I = -0.99$ and a zero-point $ZP_I = -0.08$, which allowed to calculate the $I_{\rm Sub}$ magnitudes, whose agreement with the $I_{\rm HST}$ of the common targets was good, showing a MAD scatter of 0.08 mags. However, comparing the $(V-I)$ colours of the common sources, we found a difference of ~ 0.2 mags, for those having $(V-I)_{\rm Sub} < 0.4$ mags. This implied the introduction of a colour bias for the probable main sequence stars of the F2 field, as can be appreciated in Fig. 4.3, whose calibration was based on the Subaru catalogue. Nevertheless, as we have seen from the HST catalogues, the large majority of IC1613's main sequence stars have $(V-I) \lesssim 0.4$. Therefore, this bias did not affect our subsequent kinematic analysis of this stellar population (see Sect. 4.4.2).

Finally, we used the mentioned catalogues to astrometrize and photometrically calibrate the corresponding MUSE fields – the HST ones with the F1 and F3 fields, while the Subaru one with the F2 field. For the photometric calibration of the MUSE pointings using the reference catalogues, we applied the following equations: $V_{\rm MUSE} - V_{\rm ref} = c_V\,(V_{\rm ref} - I_{\rm ref}) + ZP_V$, and $I_{\rm MUSE} - I_{\rm ref} = c_I\,(V_{\rm ref} - I_{\rm ref}) + ZP_I$. The accuracy of the astrometric and photometric solutions resulted on average around 0.08″and 0.05 mags, respectively.

The MUSE catalogues were then cleaned up in order to exclude those sources which are clearly non-stellar. We selected all those targets with the sharpness parameter between −0.5 and 0.5, and the goodness-of-fit (CHI) < 1. We further excluded all those targets having magnitudes in just one band, which in general were low S/N targets identified only in the I-band. The total extracted sources reduced then from 2293 to 2053.

In F1, F2, F3, we obtain about 65, 40, 10 sources with $S/N_{550} \geq 20$, and about 200, 120, 45 sources with $S/N_{\rm CaT} \geq 10$ (see Fig. 4.3). We note that, for this galaxy, the dust reddening and extinction along the line-of-sight are negligible, with average values: $A_V = 0.067$ and $A_I = 0.038$ (Schlafly & Finkbeiner, 2011). Therefore, we did not account for their contribution in our analysis or when reporting magnitudes and colours along the text.

lower the tip of the RGB (at $I \sim 21$).

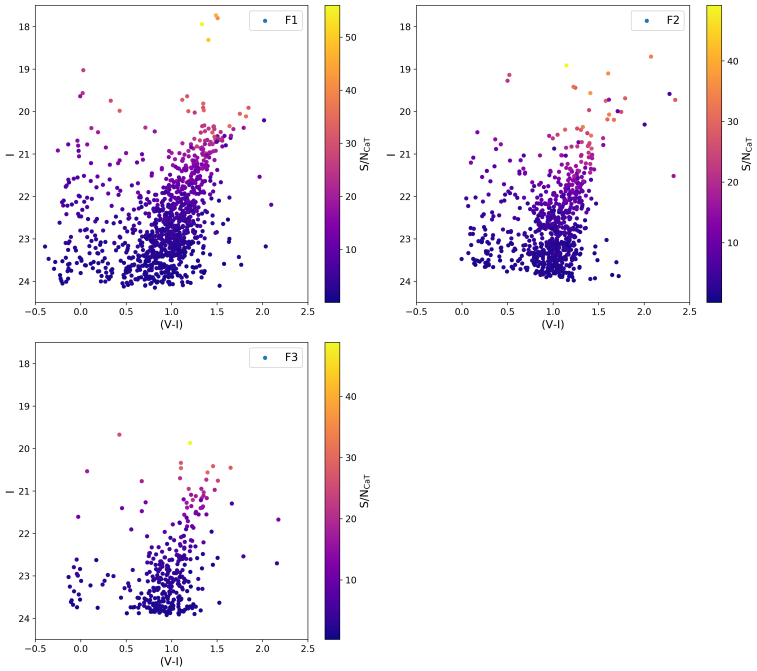

FIGURE 4.3— Colour-magnitude diagrams from MUSE images of the 3 fields, moving from the centre towards the outer regions from left to right; the filled circles represent the sources for which spectra have been extracted and they are colour-coded by their S/N around the CaT.

4.3 Spectral types and radial velocity determination

We performed a combined analysis using the spectral fitting codes ULySS (Koleva et al., 2009) and RVSPECFIT (Koposov et al., 2011; Li et al., 2019) to determine, respectively, the spectral type and radial velocity of our sources.

4.3.1 Spectral classification with ULySS

The spectral type classification was carried out with the same approach as in Roth et al. (2018); we refer the reader to this article for full details. A linear combination of up to 10 templates from the MIUSCAT stellar spectral library[7] (Vazdekis et al., 2012) was fitted to the observed spectra using the ULySS[8] code (Koleva et al., 2009). Since we are using ULySS to fit a spectrum with a linear combination of non-linear components, multiplied by a polynomial continuum, it is capable of identifying unresolved blended stars. In our case, no blends are found, not even in the central field. This is mostly expected, given the density of sources visible in Fig. 4.2, which was constructed from the MUSE data-cubes.

We stored the information of the 3 spectral types having the largest weights in the best-fit. Occasionally, the fit returns implausible mixes of spectral types. The apparent magnitude obtained by shifting the absolute magnitude in R-band of the stars in the MIUSCAT library to the distance of IC 1613 (distance modulus $(m-M)_0 = 24.40$, from Bernard et al., 2010), provided a way to weed out these clearly erroneous fits as they would lead to apparent magnitudes well below the detection limit of the MUSE data.

The ULySS spectral analysis was done for all those sources having a $S/N_K > 2$. Main outputs of the code were the best fitting spectral type, together with the associated spectral parameters ($T_{\rm eff}$, $\log(g)$ and [Fe/H]) and radial velocity. We verified by eye the ULySS outcomes, assigning several quality flags to each analysed object. We evaluated the quality of the input spectrum (QSP), the quality of the spectral fitting (QFT), the plausibility of the output radial velocity (PVR) and the plausibility of the spectral type classification (PCL); flags were reported as integer numbers ranging from one to four, with the lower value meaning a useless measure, while the higher value implying an excellent fit.

In this work, we used ULySS exclusively for spectral classification purposes, while we left the radial velocity determination part to the RVSPECFIT code. This

[7] The MIUSCAT stellar spectral library fills in the gap between the MILES (Sánchez-Blázquez et al., 2006) and the near-IR CaT library of Cenarro et al. (2001), using the Indo-U.S. (Valdes et al., 2004); it also extends the wavelength coverage slightly blue-ward of MILES and red-ward of the CaT library. MIUSCAT has been recently replaced by E-MILES (Vazdekis et al., 2016).

[8] `http://ulyss.univ-lyon1.fr`

TABLE 4.2— Spectral type classification from inspection of ULySS outcomes, with PCL flag between 3 and 4 obtained on the clean sample described in Sect. 4.2.2. Carbon and hot emission-line stars (labelled in the table as *C-star* and *Blue-em*, respectively)were identified by eye and analysed separately.

Sp. Type	$T_{\rm eff}$ (K)	N
M	$2400 - 3700$	5
K	$3700 - 5200$	506
G	$5200 - 6000$	53
F	$6000 - 7500$	46
A	$7500 - 10000$	57
B	$10000 - 30000$	97
O	> 30000	13
Blue-em	> 10000	30
C-star	< 3500	14
Total		821

was mainly because the velocity errors returned by ULySS were largely overestimated, not following a clear trend with source's brightness or S/N, while at the lowest S/N (i.e. $\lesssim 10$) we found that the returned radial velocities could be shifted up to 20 $\mathrm{km\,s^{-1}}$. We want to stress that the overestimated errors problem could be alleviated by setting ULySS in a single-template fitting-mode. The RVSPECFIT code, instead, was specifically optimized for radial velocity recover. It did not suffer of the aforementioned problems, as we verified in Appx. 4.A.1, and was our preferred routine for the radial velocity determinations. For further details on the comparison between ULySS and RVSPECFIT, please refer to Appx. 4.A.2.

In Table 4.2, we report results from the spectral classification obtained on the clean sample described in Sect. 4.2.2 for sources marked with a PCL flag between three and four (which implies an accuracy on the effective temperatures better than 500 K).

The visual inspection during the spectral classification also allowed us to identify other contaminants which were not removed during the previous photometric selection (Sect. 4.2.2): they were mainly background galaxies (comprising high-z emitters) and low S/N targets highly polluted by emission lines from the diffused ionized gas.

We also visually identified the carbon and hot emission-line stars which were missed out by ULySS due to the lack of adequate stellar templates, so to analyse them separately (see Sect. 4.3.3). In the future, we aim at exploring

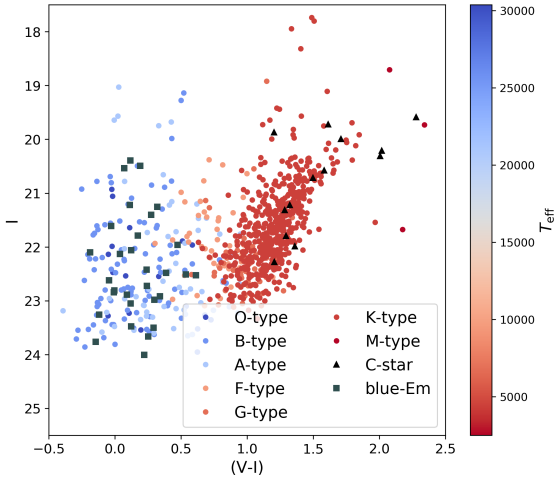

FIGURE 4.4— Colour-magnitude diagram for data selected with PCL-flag between 3 and 4 from the clean sample described in Sect. 4.2.2. Filled circles are colour-coded according to their effective temperature $T_{\rm eff}$; black triangles indicate the identified C-stars, while the grey squares mark the blue-emission line stars.

unsupervised machine learning techniques as an alternative method to fully automatize the spectral classification.

Looking at Table 4.2, the large majority of sources resulted to be K-type giants, with an almost constant representation in the other types, except for the M and O stars being a minority. In particular, among the M stars only one was found to be a giant, while the other four were likely MW-foreground dwarfs. We also report the presence of other two likely MW-contaminants classified as KV and GV stars.

The low number of O-stars can be related to several causes. Some of the low-S/N B-stars could potentially be O-stars. In fact, their luminosity in the visible is lower than that of the B- and A-types. They also tend to be born and evolve in the so-called OB-associations, whose internal extinction is not negligible (see e.g. Garcia et al., 2009). Another reason is that we are not including the hot emission-line stars with a compatible temperature. In fact, 25 of them have $T_{\rm eff}$ of 30000 K. This is, however, a value assigned ad-hoc due to the lack of suitable models for the hottest stars. The sparse coverage of the MIUSCAT library at the

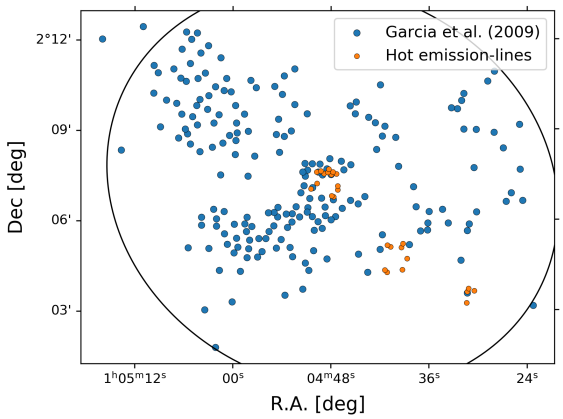

FIGURE 4.5— Spatial distribution of the hot emission-line stars (orange filled circles), compared to that of the OB-associations (blue filled circles) reported by Garcia et al. (2009). The black ellipse denotes the galaxy half-light radius.

highest effective temperatures, that is for $T_{\rm eff} > 10000$ K, is indeed a limiting factor for the spectral classification of the O-stars. Nevertheless, the spatial distribution of the hot emission-line stars shown in Fig. 4.5, seems to follow that of the OB-associations reported by Garcia et al. (2009). This confirms at least the goodness of our initial classification for many of them as very hot stars.

We are currently working on a dedicated analysis of the hottest stars using the FASTWIND stellar atmosphere code (Puls et al., 2005), optimized for the study of luminous blue stars ranging from A- to O-type. This will allow us to obtain reliable stellar parameters ($T_{\rm eff}$, $\log(g)$, [Fe/H])c for the bluest, and youngest, stars in our sample.

Looking at the coolest stars identified in our sample, the high number of C-stars compared to that of the only found M-giant would render the C/M ratio much greater than one, which is unexpected for IC 1613. In fact, literature works report an average value of C/M$\sim$ 0.5 (see e.g. Chun et al., 2015; Sibbons et al., 2015, based on wide-area *JHK*-photometric surveys). There could be several reasons of why our C/M value is significantly overestimated. In this regard, by cross-correlating with the published catalogues of Chun et al. (2015) and Sibbons et al. (2015), who have examined stars brighter than the tip of the RGB, we found among the common targets that several stars we classified as

K-giants would have been M-type instead. This would add 14 more M-stars, assuming as correct the identification reported by these authors. At the same time, we found a match for five of the brightest C-stars, confirming our initial classification. Of the remaining C-star candidates in our sample, we report an uncertain spectral classification for four of them due to their relatively high magnitudes, $I \sim 22$, and low S/N, ~ 10. It is important to notice that both C- and M-stars are thermally-pulsing AGBs (TP-AGB) which could show long-period variability (from 100 to 700 days) with brightness excursions of several magnitudes (see e.g. Menzies et al., 2015). Hence, it is not unlikely to detect them down to $I \sim 22$. We leave, however, to a future variability study their final identification.

Therefore, assuming to have 10 bona-fide C-stars and 15 M-types, this would bring our C/M close to 0.6, in very good agreement with the literature values. We want to stress, however, that we count in the future to improve the identification process of the C- and M-type stars in our sample. This would help us not only to determine a spectroscopic C/M ratio, but also to explore its spatial variation. The C/M ratio, in fact, is informative about the chemical evolution of the AGB stars, which are an intermediate age ($1-10$ Gyr) stellar population (Cioni et al., 2006; Cioni, 2009; Sibbons et al., 2015), which can be directly compared to that of the RGB stars.

4.3.2 Velocity determination with RVSPECFIT

The determination of line-of-sight velocities was carried out using the template-fitting code RVSPECFIT (v.0.0.1) developed by S. Koposov[9], which has been recently used in Li et al. (2019). The routine performs a direct pixel fitting to the observed spectra using interpolated spectral templates generated from the PHOENIX-2.0 library of high-resolution synthetic spectra Husser et al. (2013)[10]. The library covers a wide range in wavelength, going from 500 Å to 5.5 μm, and stellar parameters: $2300 < T_{\rm eff}\,({\rm K}) < 15000$, $0.0 < \log(g)\,({\rm dex}) < +6.0$, $-4.0 < [{\rm Fe/H}]\,({\rm dex}) < +1.0$ and $-0.2 < [\alpha/{\rm M}]\,({\rm dex}) < +1.2$. However, it is currently not optimized for very hot star. The spectral-fitting makes use of templates generated from a fine, uniform grid of spectral parameters obtained by interpolating the original PHOENIX grid, after restricting the wavelength range to that of the MUSE spectra and decreasing the spectral resolution accordingly. This step is performed only once before the spectral-fitting procedure. Afterwards, the RVSPECFIT code performs a final interpolation when generating the best-fitting template for each observed spectrum, obtained on the basis of a

[9] https://github.com/segasai/rvspecfit
[10] http://phoenix.astro.physik.uni-goettingen.de/

χ^2-minimization procedure. The code does not require spectrum normalization and can deal with non flux-calibrated spectra. However, it is mandatory to provide an error spectrum associated to the input flux. Together with the radial velocity, RVSPECFIT also returns estimations of the spectral parameters, $T_{\rm eff}$, $\log(g)$, [Fe/H] and [α/M], together with their estimated errors. Quality-check indicators are returned too: the skewness and kurtosis of the probability distribution from the velocity estimation, and the chi-squared value of the spectral fit. For further details on RVSPECFIT we refer the reader to Li et al. (2019), but see also Koposov et al. (2011).

We ran RVSPECFIT on all those targets having $S/N > 2$ (in all the S/N indicators), which reduced our clean sample to 1455 input sources. We initially fixed [α/M] = 0, in order to reduce the grid parameters to be fitted, and limited the velocity grid to $|v_{\rm rad}| < 1000$ km s^{-1}. We also verified on a smaller sample of spectra the impact of allowing [α/M] to vary: for the great majority of cases we did not find any noticeable difference in the recovered velocities. Therefore, we stuck to the initial choice, which also allowed a faster calculation.

The goodness of the recovered parameters was quantified in a series of tests, whose details are given in Appx. 4.A.1. Here we report the essentials. Primarily, we found that the velocity errors returned by RVSPECFIT were underestimated by a factor of 1.4, because the flux uncertainty associated to the input spectra was also underestimated by the same factor. This was systematically observed in all spectra, independently of their spectral type or measured S/N. We needed, therefore, to apply this correction to all the velocity error measurements. Among the recovered radial velocities, instead we found some unreliable values near the velocity grid borders, though with a high associated error. This was the case with some of the lowest S/N objects.

The recovery of spectral parameters was, on the other hand, particularly limited. From a series of mock tests (see details in Appx. 4.A.1), we verified that their associated errors were largely underestimated compared to the scatter of the recovered measurements. We would like to stress, however, that the optimal use we made of RVSPECFIT was the recovery of radial velocities. We count in the future to improve the recovery of spectral parameters and the determination of reliable error-bars by applying a Markov Chain Monte Carlo (MCMC) estimation in a similar fashion as shown in Li et al. (2019). One of the code outputs is indeed the calculated χ^2, which could be used as part of the input likelihood for the MCMC estimation.

In general, we needed to further clean our sample from the more uncertain velocity measurements. The quality-check parameters returned by RVSPECFIT then helped us to further clean our sample: we retained all those targets having |skewness| < 0.5. which means requiring that the probability distribution

from the velocity estimations were fairly symmetrical. We further removed those targets with $\delta_v > 20$ km s^{-1}, ensuring the exclusion of highly uncertain measurements without the need of finding an optimal cut in S/N, which would necessarily have to take into account the spectral type of our sources. With these conditions applied, our sample reduced then to 838 sources. The mean velocity error was of $\delta_v \sim 10$ km s^{-1}, while the mean S/N$_C$ resulted around 10.

4.3.3 Carbon and hot-emission-line stars

The velocity determination for the carbon and hot emission-line stars identified during the spectral classification (see Sect. 4.3.1) was performed separately, since the spectral library used by RVSPECFIT is not optimized for the analysis of C- and emission-line stars. For the C-stars we obtained radial velocities with ULySS using stellar templates from the X-Shooter library of carbon stars (Gonneau et al., 2016). On the other hand, velocities for the hot emission-line stars were obtained performing a Gaussian fit to the H_α and (when available) H_β emission lines, assuming velocity errors as a fraction (one-tenth) of the average full-width-at-half-maximum. Since these errors were adopted ad-hoc to represent the goodness of fit to the emission lines, while those returned by ULySS for the C-stars were probably overestimated (see Appx. 4.A.2), we used these stars to perform only a qualitative analysis, looking for their mean velocity and spatial distribution, compared also to other stellar populations in the main sample. Therefore, we retained all those stars with a plausible velocity determination (i.e. with a PVR-flag > 3), which implied 9 selected C-stars (4 in both F1 and F2, and 1 in F3) with an $S/N_{CaT} \sim 15$, and 26 hot emission-line stars (14, 8 and 4 in fields F1, F2 and F3, respectively) having average $S/N_{550} \sim 20$.

4.4 Kinematic analysis

To proceed with the kinematic analysis, we first needed to identify the possible contaminants left in our sample. We had already removed many of them during the spectral classification process, with the rest expected to be foreground stars. We used then the method outlined in Ch. 3, which allows to perform a Bayesian kinematic analysis while assigning membership probabilities P_{M_i} to the single targets. This approach is based on the expectation maximization technique presented in Walker et al. (2009c).

The P_{M_i} values depend on the l.o.s. velocities of the single targets, but also on the prior information based on their radial distances from the galaxy's centre and on the expected l.o.s. velocity distribution of the possible contaminants. The spatial prior takes into account that the probability of membership is higher

the closer to the galaxy's centre. In this case, we simply required that our targets should follow a monotonically decreasing radial density profile applying an isotonic regression model, with no assumptions about its functional form[11]. On the other hand, we used the Besançon model of Galactic foreground stars (Robin et al., 2003) to obtain the expected l.o.s. velocity distribution of the contaminants. We generated a catalogue along IC1613's field-of-view over an area up to its half-light radius, covering the range of colours and magnitudes of our targets. In this way the velocity distribution resulted well sampled and representative of the spatial area around the MUSE pointings. We approximated it as the sum of two Gaussian profiles (with means $\bar{v}_{\rm Bes,1} = 3\ {\rm km\,s^{-1}}$, $\bar{v}_{\rm Bes,2} = -68$ ${\rm km\,s^{-1}}$, and standard deviations $\sigma_{\rm Bes,1} = 26\ {\rm km\,s^{-1}}$, $\sigma_{\rm Bes,2} = 97\ {\rm km\,s^{-1}}$, with an amplitude ratio of $k_1/k_2 \sim 1.45$). According to this model, considering the small area covered by the MUSE pointings and the spanned range of magnitudes and colours, we expect to find in total less than 10 foreground contaminants, in the velocity range between $-400\ {\rm km\,s^{-1}}$ and $200\ {\rm km\,s^{-1}}$.

The Bayesian analysis allowed us to explore different kinematic models. In our case, we compared a model with the rotational term linearly increasing with radius, and one with no rotation included. The rotational term took the following form: $k\,R_i\cos(\theta - \theta_i)$, where k is the velocity gradient, (R_i, θ_i) are the angular distance from the galaxy's centre and position angle (P. A.) of the i-target, and θ is the P. A. of the kinematic major axis. The particular spatial distribution of the MUSE pointings and the limited area they covered, prevented us to from finding θ. Therefore, we forced θ to be the P. A. of either the optical ($\theta_{\rm opt} = 50$ deg, McConnachie, 2012) and gaseous ($\theta_{\rm gas} = 73.7$ deg, Oh et al., 2015) components. The free parameters to be fitted were then the systemic velocity $\bar{v}_{\rm syst}$, the velocity dispersion $\sigma_{\rm v}$ common to both models, and the linear gradient k. We assumed the following prior ranges: $-50 < (\bar{v}_{\rm syst} - v_{\rm glx})[{\rm km\,s^{-1}}] < 50$, where $v_{\rm glx}$ is the mean value of the input velocity distribution, $0 < \sigma_{\rm v}[{\rm km\,s^{-1}}] < 50$, $-10 < k[{\rm km\,s^{-1}\,arcmin^{-1}}] < 10$. The analysis also returned the model evidence Z which resulted useful for comparing the statistical significance of one model against another through the use of the Bayes factor $\ln(B_{1,2}) = \ln(Z_1/Z_2)$. We obtained the kinematic parameters and the membership probabilities using the MultiNest code (Feroz et al., 2009; Buchner et al., 2014), a multi-modal nested sampling algorithm.

Results of the probability-weighted analysis are reported in Table 4.3. Of the initial 838 targets, 823 resulted with a $P_{\rm M_i} > 0.95$. We found rotation to be strongly favoured against a dispersion-only model, although we cannot discern with high confidence which of the linear rotation models with different

[11] https://scikit-learn.org/stable/modules/isotonic.html

TABLE 4.3— Parameters and evidences resulting from the probability-weighted Bayesian kinematic analysis.

N_{in}	N_P	Model	$\bar{v}_{sys}$ ($km\,s^{-1}$)	σ_v ($km\,s^{-1}$)	k ($km\,s^{-1}\,arcmin^{-1}$)	Bayes factor
		Linear-optic	-234.0 ± 0.6	11.3 ± 0.5	1.2 ± 0.2	$\ln B_{opt,HI} = 1.2$
838	823	Linear-HI	-234.1 ± 0.6	11.3 ± 0.5	1.3 ± 0.3	$\ln B_{rot,disp} = 8.5$
		No rotation	-235.7 ± 0.5	11.7 ± 0.5		

Notes. The reported values of the kinematic parameters represent the median of the corresponding marginalized posterior distributions, with 1-σ errors set as the confidence intervals around the central value enclosing 68% of each distributions.

kinematic P. A. is to be preferred. Nevertheless, it seems that a rotation signal is clearly detected along the optical major axis, where the MUSE pointings are distributed, with a median value of 1.2 ± 0.2 $km\,s^{-1}\,arcmin^{-1}$. The systemic velocity of the rotational models settled around -234 $km\,s^{-1}$, while the velocity dispersion resulted of 11.3 ± 0.5 $km\,s^{-1}$. These values are within $\sim$1-σ from those previously published by Kirby et al. (2014). On the other hand, Wheeler et al. (2017) analysing the data from Kirby et al. (2014) reported a rotation value which resulted largely unconstrained. We recall that the spatial distribution of these data is along the optical minor axis, while our sample is distributed in the perpendicular direction, where we do detect a clear rotation signal. Therefore, this is the first time that stellar rotation is detected with high significance in IC 1613.

On a closer inspection, the posterior distribution of the velocity gradient k resulted to be positively correlated to that of the systemic velocity parameter, as shown in Fig. 4.6, in a way that a higher value of k would suppose a higher $\bar{v}_{sys}$ too. This was somewhat expected, since our sample is distributed only along one side of the optical major axis, which prevents to disentangle the two parameters. One way to break the correlation would be to fix $\bar{v}_{sys}$ to an independent value, for example to that of the gas, and explore the posterior distribution of the velocity gradient. We could then directly compare the stellar and HI kinematics.

Indeed, the analysis of the HI component (Oh et al., 2015) led to a systemic velocity of -232.2 ± 2.2 $km\,s^{-1}$, within 1-σ from our value, and a linear rotational velocity (corrected for the inclination $i = 48°$) of ~ 2 $km\,s^{-1}\,arcmin^{-1}$ along the HI kinematic major axis. This is comparable to our best value of the rotation gradient, which increases to $\sim$ 1.6 $km\,s^{-1}\,arcmin^{-1}$ assuming the inclination value of the gas. We note, however, the limitations of this comparison: the HI inclination value reported by Oh et al. (2015) is poorly constrained, being this

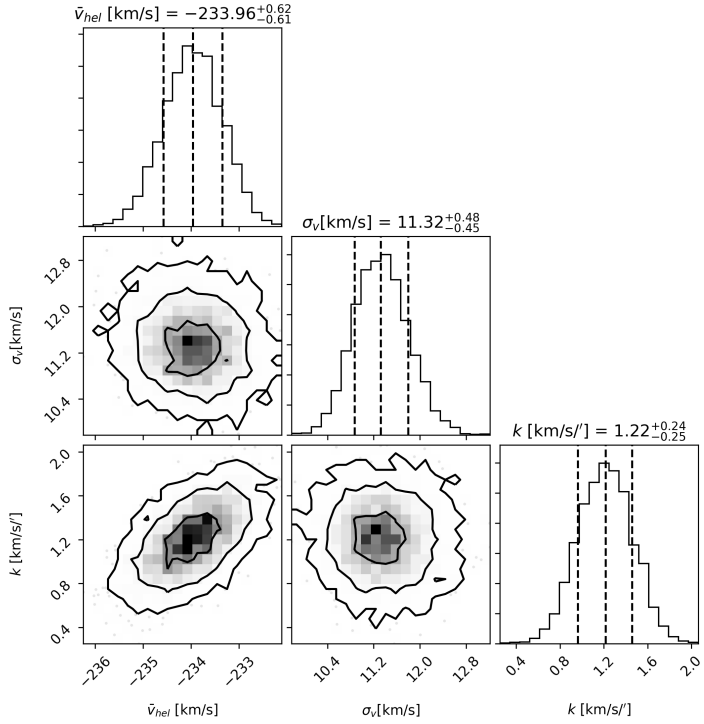

FIGURE 4.6— MultiNest 2D and marginalized posterior probability distributions for the parameters assuming a linear rotational model with the kinematic P. A. aligned with that of the optical major axis. Dashed lines in the histograms indicate the 16th, 50th and 84th percentiles. Contours are shown at 1-, 2-, and 3-σ level.

galaxy almost face-on (see also (Read et al., 2016)), while the stars do not have to share the same inclination of the gas. Furthermore, the gas centre and P. A. values used by Oh et al. (2015) do not exactly coincide with the optical ones that we adopted. For a more detailed comparison, we refer to the next session, where we explored the kinematic properties of each pointing and the variation of radial velocities with radius by fixing the centre and P. A. values to those of the HI component. In the direct comparison between stars and gas, we corrected for the inclination only when explicitly stated, assuming the HI value for both components.

The best-fitting results of our probability-weighted kinematic analysis imply a $v_{\rm rot}/\sigma_{\rm v} \sim 0.6$ at the average radius of F3 (which is approximately equal to $R_{\rm e}$). Our result is slightly lower than that of a similarly luminous galaxy, such as WLM: $v_{\rm rot}/\sigma_{\rm v} \sim 1$ inside $R_{\rm e}$ (Leaman et al., 2012). It is also not so far from that of the HI component, which shows a $v_{\rm rot}/\sigma_{\rm v} \sim 1.5$, within the same radius (not accounting for the HI inclination value, Oh et al., 2015).

We continued our analysis by further selecting those sources with a $P_{\rm M_i} > 0.95$, creating a high-fidelity sample to use as a basis for exploring the kinematic properties of different sub-samples, without the need to re-obtain the membership probabilities.

We verified that the inclusion of the carbon and hot emission-line stars would not have changed the results obtained. Nevertheless, we kept them separated from the final sample.

4.4.1 Kinematic properties along each pointing

We looked at the kinematic properties of each pointing in order to verify the variation of radial velocities with radius, but also to search for a spatial variation of the velocity dispersion, because the models adopted in the previous section allow only for a constant value.

We divided our high-fidelity sample in three sub-samples, one for each pointing, and ran the kinematic analysis applying a dispersion-only model. Results are reported in Table 4.4. It is evident how the systemic velocity relative to each field changes toward lower values moving outward from the galaxy's centre. This is also visible by looking at the radial velocity distributions per field, as shown in Fig. 4.7. In particular, if we assume $\bar{v}_{\rm sys,F2} \approx \bar{v}_{\rm sys,F3}$, the velocity difference between the central field and the external ones is of ~ 5 km s^{-1}. This is in agreement with the observed velocity gradient ($k \sim 1$ km s^{-1} arcmin^{-1}), considering that the distance between F1 and F3 is of ~ 5 arcmin. Furthermore, the systemic velocity of the central field (F1), which lies close to the optical galaxy's centre, is in agreement with that obtained in the previous section for the entire

TABLE 4.4— Results from the Bayesian kinematic analysis performed for each pointing applying a dispersion-only model. The values of the kinematic parameters and their units are reported in the same way as in Table 4.3.

Sample	N	$\bar{v}_{\rm sys}$	$\sigma_{\rm v}$
F1	437	$-233.6^{+0.7}_{-0.7}$	$11.5^{+0.6}_{-0.6}$
F2	303	$-239.4^{+0.7}_{-0.7}$	$8.6^{+0.7}_{-0.6}$
F3	83	$-237.3^{+1.4}_{-1.4}$	$9.4^{+1.5}_{-1.3}$

sample when applying the best-fitting linear rotation model. However, the fact that F2 and F3 showed approximately the same velocity could also imply that the rotation signal start to flatten for $R > 4$ arcmin.

In order to further investigate this effect, we performed an additional kinematic analysis on the full sample. We fixed the galaxy's centre, P. A., and systemic velocity values to those of the gas, as they are reported in Oh et al., 2015. This allowed us not only to directly compare the rotation signals from gas and stars, but also to reduce the free parameters to be fitted. In this way, we could apply a more realistic model, along with the usual linear rotation one, based on a radially-varying pseudo-isothermal sphere: $v_{\rm rot} = v_0 \sqrt{1 - R_0/R} \arctan(R/R_0)$, where R is the angular distance from the galaxy's centre, while v_0 and R_0 are the velocity and radial scale parameters, respectively (see also Wheeler et al., 2017). The velocity gradient k obtained for the linear rotation model was of 1.6 ± 0.2 km s^{-1} arcmin^{-1}, a little higher from what found before, but not surprising since this parameter is positively correlated with the systemic velocity, as shown in Fig. 4.6. Accounting for the galaxy's inclination, this value equals that of the gas of ~ 2 km s^{-1} arcmin^{-1} . On the other hand, the v_0 and R_0 scale parameters of the pseudo-isothermal model were found to be highly correlated, with output values of $13.4^{+5.3}_{-3.0}$ km s^{-1} and $2.9^{+2.3}_{-1.3}$ arcmin, respectively. The pseudo-isothermal model resulted also with a higher significance compared to the linear rotation one. Indeed, it seems to provide a better fit to the data, as shown in Fig. 4.8. However, we have too few spatial points to break the scale parameters degeneracy, and have a better constrain on the actual flattening of the rotation curve. We recall that the only available spectroscopic dataset that we could use to improve the spatial sampling is that published by Kirby et al. (2014) which, unluckily, is mainly distributed along the optical minor axis of the galaxy providing, as already shown by Wheeler et al. (2017), a poor constrain to the rotation signal.

The flattening of the rotation curve for $R \gtrsim 0.5\ R_{\rm e}$ is probably an effect of the asymmetric drifts. In fact, the random motion of the stars has the effect

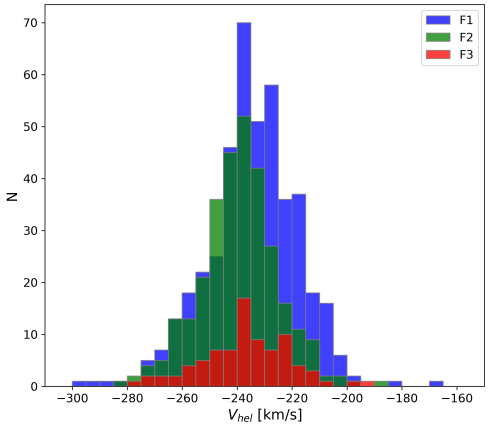

FIGURE 4.7— Histogram of the radial velocity measurements from the probable members ($P_{\mathrm{M_i}} > 0.95$) divided per pointing.

of lowering the rotation signal. This effect is greater when the rotational and dispersion components are comparable. Correcting the average velocities of the single fields for the asymmetric drift[12], we obtained indeed a circular velocity comparable to that of the gas. We note that the asymmetric drift correction of the gas component resulted negligible inside R_e (Oh et al., 2015). Our result is similar to what observed in WLM (Leaman et al., 2012), although both its gas and stars rotate at a higher rate than those of IC 1613.

We further notice a decrease in the velocity dispersion profile moving outward along the fields (see Fig. 4.8). In particular, $\sigma_{\mathrm{v,F1}}$ is in agreement with that obtained for the whole sample, while we recovered lower values for the F2 and F3 fields at almost 3- and 2-σ level, respectively. This is something similar to what was spotted for WLM by Leaman et al. (2012), although their σ_{v} started to decrease at $R > R_{\mathrm{e}}$.

On the other hand, the velocity dispersion profile of the gas starts around

[12]We followed the formalism of Read et al., 2016, using their Eqs. 9 and 12. Although their analysis focused on the HI component, for our purposes the same reasoning could be applied to the stellar field.

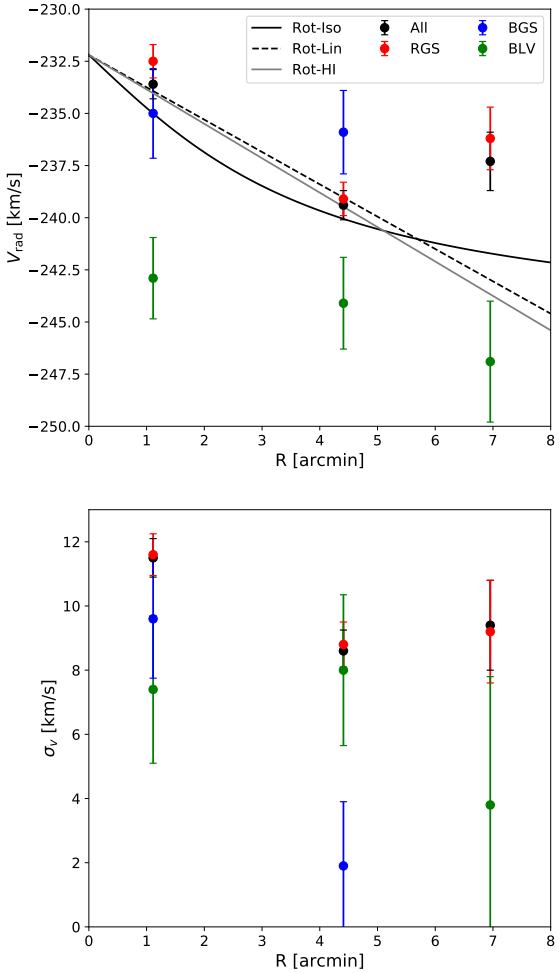

FIGURE 4.8— *Top:* average radial velocity per pointing and spectral type. Black circles represent the total values per pointing, while coloured circles indicate average values obtained from the sub-samples of red giant stars (in red), main sequence stars (in blue), and blue-loop and variable stars (in green). The black lines represent, respectively, the rotation curves obtained applying a pseudo-isothermal (solid line) and a linear rotation model (dashed line). The grey solid line indicates the observed linear rotation curves of the HI component (not corrected for galaxy's inclination) as reported in Oh et al. (2015). *Bottom:* velocity dispersion values per pointing and spectral type, following the same colour-coding of the left panel.

$\sim$ 5 km s^{-1} near the galaxy's centre to then rise up to $\sim$ 9 km s^{-1} at $R \sim 0.5\ R_{\rm e}$ arcmin, that is around the position of F2, to finally decrease and stabilize again around $\sim$ 5 km s^{-1} for $R \gtrsim R_{\rm e}$ arcmin (Oh et al., 2015). It is probable that the lower HI density due to the presence of a central shell-like gas structure could have had an impact on the gas kinematics, and hence on the velocity dispersion profile, inside $R \lesssim 0.5\ R_{\rm e}$ arcmin (see Moiseev & Lozinskaya, 2012; Stilp et al., 2013). The HI velocity dispersion is indeed correlated to the gas surface mass density, which regulates the amount of local turbulence. We will further investigate in the future if this could be related to the higher velocity dispersion measured from the stars in F1.

Having obtained the circular velocities per pointing by correcting for the asymmetric drift, we could calculate then the rotationally derived mass within the extension of our data. We used the equation $M_c(R) = V_c^2 R/G$, where G is the gravitational constant, R the considered radius and V_c the circular velocity obtained at that radius. We are interested in the enclosed mass within the 3D de-projected half-light radius $r_{1/2} \simeq (4/3)R_{\rm e}$. This allows us to make a direct comparison with mass estimates made at the same radius for dispersion supported systems. While our data extend out to $R_{\rm e}$, we assume that around F3 both the rotation and dispersion profile are rather flat. Therefore, we use the $v_{\rm rot,F3}$ and $\sigma_{\rm v,F3}$ values to calculate the circular velocity at $r_{1/2}$, obtaining a value of 15 ± 2 km s^{-1}. We note that this value takes into account the galaxy's inclination, assumed to be equal to the Oh et al. (2015) value. The rotationally derived mass resulted then $M_c(r_{1/2}) = 1.0 \pm 0.3 \times 10^8 M_\odot$. The corresponding mass-to-light ratio within the half-light radius was $M_c(r_{1/2})/L_V = 1.1 \pm 0.3\ M_\odot/L_\odot$.

For comparison, we calculated also the dispersion-based value for the dynamical mass. To this end, we used the Wolf et al. (2010) mass-estimator, that is $M_{1/2} = 3G^{-1}\sigma_{\rm v}^2 r_{1/2} \approx 4G^{-1}\sigma_{\rm v}^2 R_{\rm e}$, where again G is the gravitational constant and $r_{1/2} \simeq (4/3)R_{\rm e}$. We note that this mass estimator is valid as long as the system is spherically symmetric, without rotation and with a flat radial velocity dispersion profile. To some degree, these conditions are violated for IC 1613. However, the system has a low ellipticity, the stellar rotation signal is quite low ($V_{\rm rot}/\sigma_{\rm v} \sim 0.5$), while the velocity dispersion profile appears to be flat for $R > 0.5\ R_e$ and it should not be significantly affected by rotation within the effective radius. Taking these considerations into account, we obtained a dynamical mass of $M_{1/2} = 1.1 \pm 0.2 \times 10^8 M_\odot$, in very good agreement with the previous results, but also with the value reported by Kirby et al. (2014).

TABLE 4.5— Results from the Bayesian kinematic analysis performed for each sub-sample applying the linear-rotation and dispersion-only models. The values of the kinematic parameters and their units are reported in the same way as in Table 4.3.

Sample	N	$\bar{v}_{\rm sys}$	$\sigma_{\rm v}$	k	$\ln B_{\rm rot,disp}$
RGS	706	$-233.5^{+0.6}_{-0.6}$	$10.6^{+0.5}_{-0.4}$	$1.2^{+0.2}_{-0.2}$	7.4
		$-235.3^{+0.6}_{-0.5}$	$10.9^{+0.5}_{-0.5}$		
BGS	50	$-234.5^{+1.8}_{-1.8}$	$8.0^{+1.7}_{-1.4}$	$0.2^{+1.1}_{-1.2}$	-1.8
		$-234.5^{+1.7}_{-1.7}$	$7.9^{+1.6}_{-1.3}$		
BLV	67	$-242.9^{+1.6}_{-1.6}$	$6.6^{+1.6}_{-1.3}$	$0.7^{+0.6}_{-0.6}$	-1.9
		$-244.0^{+1.3}_{-1.3}$	$6.8^{+1.5}_{-1.3}$		

4.4.2 Kinematic properties as a function of stellar type

We continued by dividing our high-fidelity sample into several sub-samples based on the observed feature of the CMD. Indeed, as show in Fig 4.3, our dataset consists of several stellar populations of different ages. We explore here the possibility that these populations show also different kinematic properties.

In order to select the red giant stars (RGS) in our sample, or namely those belonging to the RGB and AGB with stellar ages $1 < t_{\rm age} < 13$ Gyr, we defined a limit following the linear relation $I > -9.5 \times (V - I) + 29.5$. This limit was able to separate stars with $T_{\rm eff}$ lower than ∼6000 K, as we verified with those objects having high quality measurements (i.e. PCL-flag of 3 and 4). The young main sequence stars (BGS) of $t_{\rm age} < 0.1$ Gyr, instead, were selected assuming a $(V - I) < 0.4$, which separated them not only from the RGS, but also from the bright blue-loop and variable stars (BLV), having $0.1 < t_{\rm age} < 1$ Gyr. In fact, the CMD region roughly between $0.4 \lesssim (V - I) \lesssim 0.8$ delimits the instability strip for IC 1613 (Bernard et al., 2010). These variable stars have a fast moving photosphere, which could bias the spectroscopic velocity determination. On the full sample, they are a minority of stars and their contribution is averaged out. However, they could be an important fraction of the stars with a $(V - I) \lesssim 0.8$. Therefore we analysed these three separate groups of stars, selected following the above photometric limits[13].

We ran the kinematic analysis applying both the dispersion-only model and the linear rotation one (fixing $\theta_{\rm kin} = \theta_{\rm opt}$). Results are reported in Table 4.5. The RGS sub-sample values were compatible at 1-σ level with those of the probability-weighted analysis, with also the rotation model being strongly favoured. This was somehow expected, being this sub-sample a large fraction of

[13]Photometric limits and stellar ages for the different selected populations were defined following the synthetic CMD reported in Aparicio & Gallart, 2004.

the original one. Same conclusions were reached while analysing the RGS per field, as also shown in Fig. 4.8.

The BGS, instead, did not show significant signs of rotation, with the systemic velocity being within 1-σ from that of the RGS sub-sample. The velocity dispersion value instead resulted lower at the 2-σ level. This is consistent with the fact that hot stars are too young to be dynamically relaxed like the RGS (see e.g. Leaman et al., 2012). What is more, the found value of $\sigma_{\rm v,BGS} = 7.9^{+1.6}_{-1.3}$ km s^{-1} is well in agreement with that measured from the HI gas, $\sigma_{\rm v,HI} = 7 \pm 2$ km s^{-1} (Oh et al., 2015) (where the error represents the boundaries of the dispersion profile). The absence of rotation could be explained by the lack of BGS in the F3 field (see Fig. 4.8). By adding to this sub-sample the hot-emission line stars, which we recall were excluded from the main analysis due to overestimated velocity errors, we recovered that the average velocity per field followed that of the RGS. Therefore, the youngest stars are probably rotating at the same pace as the older ones. We could not obtain, instead, a velocity dispersion profile for the BGS, due to $\sigma_{\rm v}$ resulting not resolved in F2, the lack of BGS in F3, and the inability to use the hot emission-line stars for this purpose.

The analysis of the BLV, on the other hand, led to significantly different results than those obtained for RGS and BGS. As shown in Table 4.5, the resulting systemic velocity was ~ 10 km s^{-1} lower than that of these sub-samples at the 3-σ level, while the velocity dispersion resulted lower at respectively the $\sim$ 3- and 1-σ level. The BLVs also showed no significant signs of rotation and the average velocity for each pointing was systematically lower than the rest of stars of almost ~ 10 km s^{-1}, as shown in Fig. 4.8.

It is likely that the BLV sample consists mainly of variable stars, in particular classical Cepheids. They are young ($t_{\rm age} < 0.5$ Gyr) supergiant stars, which vary their brightness by almost 1 magnitude with a period of variability between $-0.5 \lesssim \log(P)$ [days] $\lesssim 2$ (see e.g. Proxauf et al., 2018, and references therein). As showed in Udalski et al. (2001) and Bernard et al. (2010), they are the dominant type of variable stars in the bright part (i.e. with $V < 24$ mags) of IC 1613's instability strip. In particular, a substantial fraction of them have a short-period variability (i.e. with $\log(P) < 0.5$ days, Bernard et al., 2010). Classic Cepheids also show variations in radial velocities, so that when they become brighter their surface gains radial velocity towards us, only to lose it when they become dimmer. This process shows a typical excursion of $\sim \pm 30$ km s^{-1} around the stellar average velocity (see e.g. Proxauf et al., 2018, but also Carroll & Ostlie, 2006).

If we were to observe these stars preferentially when they are brighter or dimmer, we would be introducing a bias in the velocity determination. How-

ever, while observing a group of them, their periods would all show different phases. This implies that in a given observing run we would have some stars with positive velocity offsets, while others showing negative shifts, in a way that on average this contributions would cancel each other out. We verified this conclusion performing a simple simulation where we generated a sample of 70 variable stars with periods of 2.5 days and phases added at random. Variability profiles followed a sawtooth function with velocity amplitudes of ± 30 km s^{-1}. We measured the velocity values choosing a random moment on a temporal baseline of 15 days, finding that their average tended to zero (assumed as the systemic velocity of the mock stars). The results we achieved were still valid even if the generated stars followed a distribution of periods, with also different velocity amplitudes. We verified that this also applies when simulating repeated observations. We recall that our spectra were extracted from data-cubes obtained by stacking five individual exposures per pointing. Therefore, we can exclude in principle the relation of the velocity shift with a preferential sampling of the variability curve of the observed stars.

We warn instead on the difference of measuring radial velocities from hydrogen or metallic lines in variable stars, especially for Cepheids (see e.g. Vinko et al., 1998). This difference is greater (up to 50 km s^{-1}) the longer the variability period, while it is lower ($\lesssim 20$ km s^{-1}) for those with shorter periods (i.e. $P < 10$ days). Since the probable Cepheids in our sample are expected to be mainly short-period variables, this could be a possible reason to explain the observed velocity shift. We note that in the mock tests reported in Sect. 4.A.1 we did not find any bias introduced by RVSPECFIT while obtaining radial velocities from templates compatible with this kind of stars (assuming a typical $T_{\rm eff} \sim 6500$ K), neither in the low S/N regime (i.e. < 10). However, this only confirms the goodness of RVSPECFIT in correctly recovering the input velocity. We did no tests using actual variable star models, which could show instead biased measurements. We plan to further investigate this aspect in the future. Furthermore, we also count to perform a variability study on our sample, analysing the photometric data and extracted spectra obtained from the single exposures data-cubes, using also ancillary photometric data, like the Subaru/Suprimecam catalogue presented in Sect. 4.2.2, to aid the identification of variable stars in our MUSE fields.

About the C- and blue emission-line stars, a simple analysis of their velocity distribution showed an average velocity of -236.0 ± 4.5 km s^{-1} and -238.8 ± 1.3 km s^{-1}, respectively. They also showed a considerable scatter (measured as standard deviation) of 13.0 km s^{-1} and 6.5 km s^{-1} . These values are qualitatively in good agreement with those obtained from the Bayesian analysis of the main sample when applying the dispersion-only model. In particular, the

scatter of the hot emission-line stars is in agreement with the $\sigma_{\rm v}$ found for the BGS. The average velocities per field of the C- and blue emission-line stars agree within the errors with those obtained for the entire sample, and in particular with those of the BGS and RGS.

Therefore, it appears that the different type of stars in our sample (excluded the BLV for previously explained reasons), all show a similar kinematic behaviour. In particular, the young stars (BGS together with the hot-emission line stars), appears to rotate at the same pace as the older ones (i.e. the RGS and C-stars). The velocity dispersion, instead, increases on average with the stellar age (i.e. $\sigma_{\rm v,BGS} < \sigma_{\rm v,RGS}$). This is qualitatively similar to what found by Leaman et al. (2012) for WLM. We count in the future to provide stellar ages for our sample, which will allow us to have a finer sampling of $\sigma_{\rm v}$ as a function of time, and to be informative on the processes that dynamically heat the stars in IC 1613.

4.5 Chemical analysis of the RGB stars

We performed the chemical analysis only on a sub-sample of likely RGB stars, since the metallicity estimation using RVSPECFIT for the whole sample resulted to be largely unreliable (see Sect. 4.A.1).

We made use of the Starkenburg et al. (2010) calibration to estimate [Fe/H] values directly from the observed CaT lines in each selected spectrum. As shown in Kacharov et al. (2017), this calibration can be safely applied to data of spectral resolution as low as $R \sim 2600$, comparable to that of our MUSE spectra around the CaT lines. The Starkenburg's calibration combines the equivalent widths (EWs) of the two reddest Ca II lines with the $(V - V_{\rm HB})$ term, where V is the visual magnitude of the selected star and $V_{\rm HB}$ that of the horizontal branch. The EWs were obtained by fitting a Voigt profile over a 15Å window around the selected Ca II lines, weighting at each pixel for the flux uncertainty stored in the error spectrum. The EWs uncertainties were then calculated from the covariance matrix of the fitted Voigt parameters. We adopted a $V_{\rm HB}$ value of 24.91 (Bernard et al., 2010). Final uncertainties for the metallicity values were obtained by error propagation of the EW's uncertainties. We verified that the input magnitude's errors does not have a significant impact on the final [Fe/H] uncertainties.

The sub-sample to be analysed was obtained using the empirical limit defined in Sect. 4.4.2, which helped to separate the likely RGB stars from the main sequence ones. We verified the goodness of this selection using a set of isochrones (Bressan et al. 2012) with $Z = 0.0001$ ([Fe/H]~ -2.3 dex) and $t_{\rm age} > 1$ Gyr,

TABLE 4.6— Results from the chemical analysis. Columns are the considered sample, its size N, its median metallicity together with its scaled median absolute deviation and intrinsic scatter.

Sample	N	[Fe/H]	$\sigma_{\rm MAD}$	$\sigma_{\rm intrinsic}$
Tot	288	−1.07	0.28	0.18
F1	159	−1.04	0.28	0.16
F2	98	−1.10	0.31	0.22
F3	31	−1.16	0.27	–

which traced the lower range of metallicities and stellar ages for the RGB stars as obtained from the SFH analysis of IC 1613 (Skillman et al., 2014).

We further selected all those stars having $S/N_{CaT} > 10$, which allowed us to obtain uncertainties on the EWs to better than 20%. This also helped to remove any blue loop stars that might be present at the higher magnitudes, where they merge with the RGB. The sub-sample resulted with 296 selected sources.

We note that a fraction of stars in our sub-sample are probably AGB stars, brighter on average, for which the calibration method can be applied anyway, since it does not introduce a significant systematic bias compared to RGB stars (see discussion in Pont et al., 2004).

The uncertainties obtained in the EW measurements resulted to be about 0.5 Å, while the average [Fe/H] error was ~ 0.4 dex. However, few targets (8) had metallicity values with $\delta_{\rm [Fe/H]} > 0.8$ dex, which were excluded from the subsequent analysis.

From the analysis of the metallicity values we obtained median [Fe/H] = −1.07 dex, $\sigma_{\rm MAD} = 0.28$ dex and $\sigma_{\rm intrinsic} = 0.18$ dex. These values are in good agreement with those reported by Kirby et al. (2013b): median [Fe/H] = −1.22 dex and $\sigma_{\rm MAD} = 0.23$ dex, also obtained targeting the RGB stars of the galaxy. The small deviations we found can be attributed to the different spectral resolution of their data and technique to obtain the metallicity values (namely by directly fitting the available Fe lines). We also note the different spatial distribution of the Kirby et al. (2013b) data, mainly distributed along the minor axis of the galaxy, which could hint to the presence of slightly different enriched mediums.

We further analysed our sample considering each pointing separately. We found that the median [Fe/H] value tends to decrease from the central to the outer field, while the scatter $\sigma_{\rm MAD}$ tends to stay constant, as reported in Table 4.6. Looking at the metallicity distribution per field, as shown in Fig. 4.9, it is evident the decrease of metal-rich stars from F1 to F3 fields. However, it is

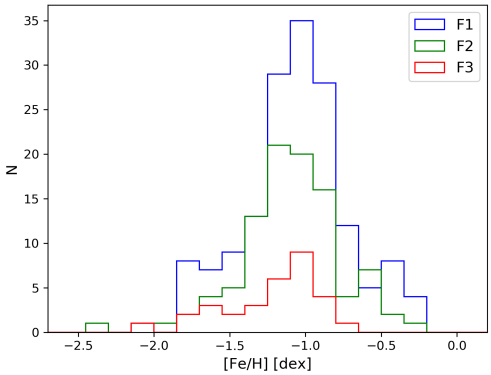

FIGURE 4.9— Histograms of the metallicity values for each pointing.

also true that F2 and, in particular, F3 contain fewer stars than F1. Therefore, we ran a two-dimensional two-sided Kolmogorov-Smirnov test to verify if the field samples are drawn from the same parent distribution. We stress that they are three independent samples. We compared separately F2 and F3 against F1, which is the largest sample and the one with the widest range of metallicities. We found that F1 and F2 are likely drawn from the same distribution, with a p-value of 0.45, with the same result for F3 as well, despite the lower p-value of 0.09. Therefore, an actual lack of metal-rich stars in the most external field seems unlikely. This is consistent with the fact that IC 1613 has constantly been forming stars in a spatially homogeneous way (see Skillman et al., 2014), at least up to R_e, which is also how far our data extends.

The variation of the metallicity distribution is also visible when plotted against the spatial radial direction, as shown in Fig. 4.10. We investigated then the presence of a radial metallicity gradient performing first an error-weighted linear least-square fit to the data, obtaining a value of $m = \frac{\mathrm{d[Fe/H]}}{\mathrm{d}R} = -0.02 \pm 0.01$ dex arcmin^{-1} ($= -0.08 \pm 0.05$ dex kpc^{-1} $= -0.12 \pm 0.08$ dex R_e^{-1}). The resulting gradient is very mild and consistent with a lack thereof, which is compatible with what has been observed in other dIrr (see e.g. Leaman et al., 2013).

We ran also a Gaussian process regression (GPR) analysis using a Gaussian kernel together with a noise component to account for the intrinsic metallicity

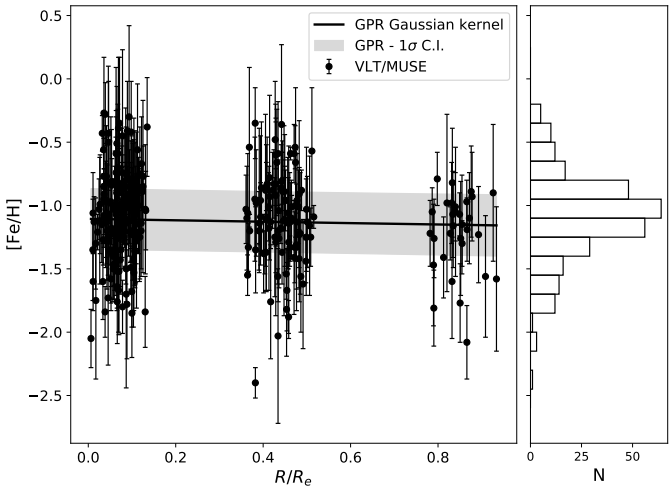

FIGURE 4.10— [Fe/H] values as a function of the elliptical radius scaled with R_e, represented as black dots. The black solid line represents the result of a Gaussian process regression analysis using a Gaussian kernel and taking into account an intrinsic scatter; the grey band indicates the corresponding 1-σ confidence interval. The histogram on the right side represents the metallicity distribution of the sample stars.

scatter of the data. From Fig. 4.10 it is evident that the result is compatible within 1-σ with a null trend. This means that the bulk of the data, having [Fe/H] values ~ -1.0 dex, does not show a significant spatial variation.

4.6 Summary and future work

In this chapter, we present results from the chemo-kinematic analysis of the stellar component of the isolated dwarf irregular galaxy IC 1613.

The analysis was based on a new set of spectroscopic data collected with the VLT/MUSE instrument. We obtained a large dataset of ~ 2000 extracted sources, from which we separated the stellar objects for their subsequent spectral classification and analysis.

The quality of the dataset allowed for a fairly accurate spectral classification (i.e. with $T_{\rm eff}$ determined to better than 500 K) of 824 stars. We found a major

component of K-type stars, together with representatives from all the other types (from O- to M-). We also identified a sample of hot emission-line stars, along with one of carbon-stars.

For all types, except for the C-stars and hot emission-line stars, the determination of radial velocities was made with a pixel-to-pixel analysis which led to obtain accurate measurements (i.e. with $\delta_{\rm v} < 20$ km s^{-1} and abs(skewness) < 0.5) for 838 objects. We performed on this sample a probability-weighted analysis that allowed us to explore different kinematic models. The identified 823 probable members (i.e. having $P_M > 0.95$) showed a significant linear rotation signal along the optical major axis of the galaxy. This is the first time that a stellar rotation signal is confirmed with high significance for this galaxy. Stars follow the velocity field found for the neutral HI component, as reported in Oh et al. (2015), although they appear to rotate at a lower pace than the gas. The systemic velocity of $\bar{v}_{\rm sys} = -234.0 \pm 0.6$ km s^{-1} was in agreement with literature values, as well the velocity dispersion value of $\sigma_{\rm v} = 11.3 \pm 0.5$ km s^{-1}.

We further analysed the probable members looking at the kinematic properties of each individual field and for different stellar type selections. The individual fields analysis confirmed the presence of a rotation signal, which is decoupled from that of the gas due to the effects of the asymmetric drift. The dynamical mass obtained from the circular velocity resulted in agreement with literature values (Kirby et al., 2014; Oh et al., 2015). The radial velocity dispersion profile showed instead a decreasing trend that appear to flatten moving outward.

The kinematic analysis of the different selected stellar populations showed in general a coherent picture with the analysis of the main sample. However, we found that the selected sub-sample of blue-loop and variable stars showed radial velocities which were systematically lower than those of the other selections. We attributed this discrepancy to the fact of sampling mainly variable stars, in particular classical Cepheids, an issue that we will better explore in the future.

The chemical analysis was conducted only on the sub-sample of red giant stars exploiting the wavelength region of the Ca II triplet lines. We obtained a median [Fe/H] $= -1.07$ dex, with scatter values of $\sigma_{\rm MAD} = 0.28$ dex and $\sigma_{\rm intrinsic} = 0.18$ dex. The galaxy resulted then slightly metal-richer than what previously reported by Kirby et al. (2013b). Nevertheless, the average [Fe/H] is well within the rms scatter of the stellar luminosity-metallicity relation found for the LG dwarf galaxies by the same authors. The spatial distribution of the [Fe/H] values showed no significant signs of a radial metallicity gradient, compatible with results from other dIrrs (Leaman et al., 2013). We count in the future to add the information on the metallicity of the bluest, and therefore youngest, stars of our sample to better explore the eventual presence of a radial [Fe/H] gradient.

Through the text we left open many points that would need in future a dedicated effort to be carried out. We resume here the main points:

- through a collaboration with researchers at the Leibniz-Institute for Astrophysics in Potsdam (Germany), is being carried out a dedicated analysis of the massive stars in our sample using the FASTWIND stellar atmosphere code (Puls et al., 2005), that will allow us to obtain reliable stellar parameters and radial velocities from their spectra.
- We count to improve the identification process of the C- and M-type stars in our sample, and therefore to constrain the spectroscopic C/M ratio. This will tell us more on the chemical properties of the intermediate-age stellar population of IC 1613.
- We intend to conduct a variability analysis on our data, in order to confirm the probable presence of Cepheid stars, but also to find other sources of stellar variability associated to this galaxy.
- The RGB are the largest representatives in our sample, for which we also obtained metallicity values. By combining the spectroscopic and photometric information, we aim to get stellar ages with an accuracy to better than 50% in order to get a finer sampling of the velocity dispersion profile as a function of time.
- From a more technical point of view, we aim at exploring unsupervised machine learning techniques as an alternative method to fully automatize the spectral classification. Furthermore, we count to improve the quality of the recovered spectral parameters with RVSPECFIT by providing credible confidence limits through Bayesian analysis.

One of the great advantages of studying resolved stellar populations with MUSE is the possibility to obtain spectra from all the detectable sources in its field of view. This implies, for a galaxy like IC 1613, to potentially obtain a large amount of information not only from stars at different evolutionary stages, but also from the ionized interstellar medium, and even from background galaxies and foreground contaminants. For these reasons we further aim:

- to analyse the ionized gas medium using available emission lines, like H_α or oxygen nebular ones. In this way, we will provide a velocity field for the gas to directly compare with that available from the stars. We will also get an insight on the kinematics of the shell-like gas structure visible in field F1 and compare it with that of the youngest stars.

- To connect the spectroscopic information derived in this work with that of future *Gaia* data releases, and obtain the first determination of the systemic proper motion of this galaxy. With the current data release (*Gaia*-DR2) in fact a sufficiently accurate measure could not be obtained.

Authorship

The work presented in this chapter is part of an ongoing project that actively involves several researchers from different institutions. My contribution has focused in the calibration of photometric catalogues; the interpretation of spectral classification; the determination of radial velocity measurements using a novel software and subsequent kinematic analysis; the determination of metallicity values for a sub-sample of stars and subsequent chemical analysis.

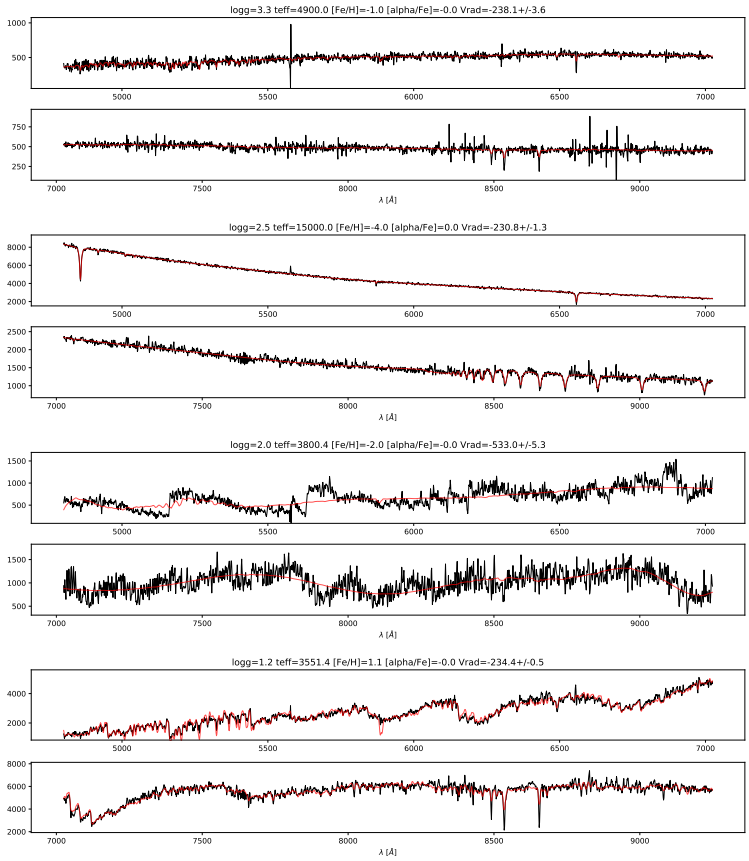

FIGURE 4.11— Example of sky-subtracted, wavelength calibrated, extracted spectra from our dataset. In red the best-fitting templates provided by RVSPECFIT, with the output spectral parameters ($\log(g)$, $T_{\rm eff}$, [Fe/H], [α/Fe], $V_{\rm rad}$) indicated in the labels. From top to bottom examples of: an RGB star; a main sequence star; a C-star; an M-star.

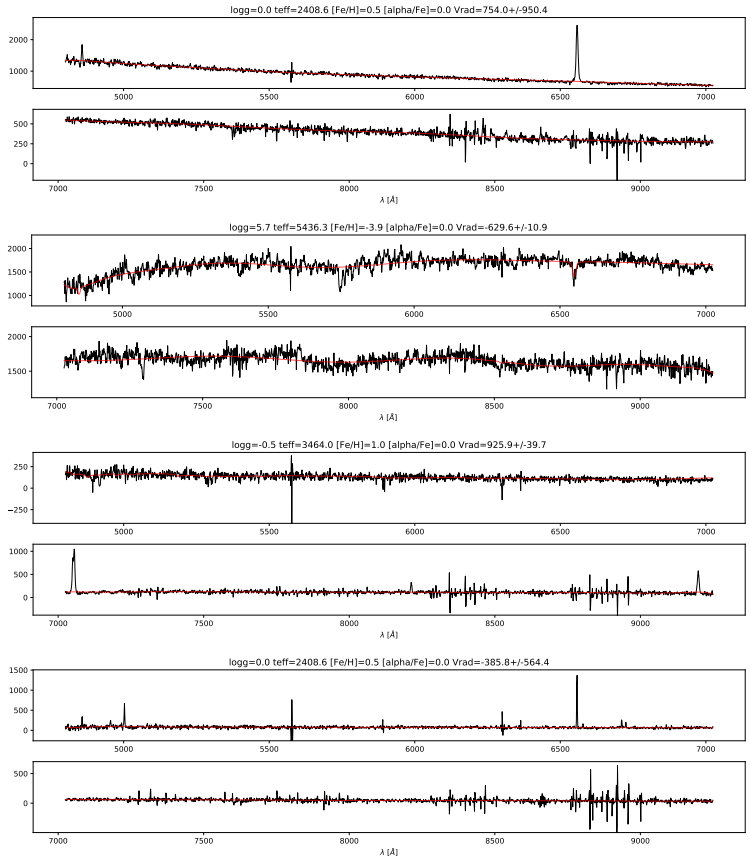

FIGURE 4.12— Example of sky-subtracted, wavelength calibrated, extracted spectra from our dataset. In red the best-fitting templates provided by RVSPECFIT, with the output spectral parameters ($\log(g)$, $T_{\rm eff}$, [Fe/H], [α/Fe], $V_{\rm rad}$) indicated in the labels. From top to bottom examples of: an hot-emission-line star; a background galaxy; a blend with an high redshift emitting-galaxy; an example of ionized gas in IC 1613.

4.A Appendix – Consistency checks

4.A.1 Check RVSPECFIT performance

We checked the performance of RVSPECFIT on the radial velocity determination. We first verified how reliable are the velocity errors returned by the code. To this end, we performed a Monte Carlo analysis adding Poisson noise to a template chosen from the PHOENIX library, having the same wavelength range and spectral resolution of our MUSE spectra. The template we used matches a typical red giant star – $T_{\rm eff}$ = 4000 K, $\log(g) = +1.0$ and [Fe/H] = −1.5 dex; since we wanted to verify the general performance of the code, we chose a template according to the main stellar population of our sample. We produced 250 realizations at S/N_{CaT} of 2.5, 5, 7.5, 10, 15, 25 and 50 pxl^{-1}. The recovered velocity errors from the mock spectra compared well to the velocity scatter in all cases, even at $S/N_{CaT} = 2.5$ pxl^{-1} where, however, the uncertainties resulted to be large ($\delta_{\rm v} \sim 25$ km s^{-1}).

To test for possible systematic velocity shifts we ran the code on several noiseless templates from the PHOENIX library of giant stars at different $T_{\rm eff}$ (from 2500 K to 15000 K) at fixed [Fe/H] = −1.5 dex. Templates were shifted at several radial velocities, from −50 km s^{-1} to 500 km s^{-1} at step of 50 km s^{-1}. We obtained that RVSPECFIT correctly recovers the assigned radial velocities, although it struggles with the cooler stars with 2500 K $< T_{\rm eff} <$ 5000 K. Up to $T_{\rm eff}$ = 3000 K, the problem was related to the spectral fit being seldom good to deliver an accurate velocity, while for higher temperatures we recovered small systematic shifts of $\sim +2.5$ km s^{-1} at $T_{\rm eff}$ = 3500 K, decreasing to $\sim +1.0$ km s^{-1} at $T_{\rm eff}$ = 5000 K.

We have checked which is the lower limit in $T_{\rm eff}$ expected from the $(V-I)$ colours of the targets in our sample, using the empirical calibration for red giant stars from Alonso et al. (1999), valid in the colour range of $0.8 < (V-I) < 2.2$ and mostly metallicity independent. We found a value of $\sim$ 4000 K, which kept us out from the problematic regime for velocity determinations.

The Monte Carlo tests described above gave us an overview about the general behaviour of RVSPECFIT. However, in these tests we generated the mock spectra using an ideal Poisson noise that did not take into account for the higher flux uncertainty found in the observed spectra around the sky emission lines, nor where a cosmic ray had randomly hit. In addition, we found that the flux uncertainty stored with the observed spectra was underestimated by an average factor of 1.4 with respect to the measured noise on the observed flux. This was systematically found in all spectra, independently of their spectral type or S/N. We attribute this effect to an improper error propagation during the

sky subtraction and spectral extraction steps. Therefore, being the error spectrum a mandatory input of RVSPECFIT, we explored its impact on the velocity measurements returned by the code.

We considered first the spectrum of an observed red giant star – ID-59 from F1, $T_{\rm eff} \sim 5000$ K and $\log(g) \sim 3$ dex according to RVSPECFIT, and as it could be roughly guessed by its position on the CMD. The measured $S/N_{\rm CaT}$ was of ~ 5. We took the associated model spectrum fitted by RVSPECFIT to perform several Monte Carlo tests. In each of them, we added a random value in every pixel of the model spectrum. The random value was extracted from a Gaussian distribution of standard deviation equal to a given flux uncertainty in that pixel. We then analysed the generated mock spectrum with RVSPECFIT and repeated the entire process for 250 times. We did three tests of this kind.

T1, the flux uncertainty used to generate the mock spectra was equal to the observed one; this same uncertainty was used as the associated error spectrum of the so generated mock spectra.

T2, the flux uncertainty to generate the mock spectra was the observed one multiplied by 1.4; the same scaled uncertainty was assumed as mock error spectrum.

T3, the flux uncertainty was the observed one multiplied by 1.4, while the not scaled flux uncertainty was assumed as mock error spectrum. Results are reported in Table 4.7.

In all tests, the recovered radial velocities agreed on average with the input one, while the velocity scatter resulted in agreement with the average velocity error only in T1 and T2. In T3, the median velocity error resulted to be underestimated with respect to the velocity scatter by a factor of ∼1.4, the same multiplicative value used during the noise-adding step while creating the mock spectra. We repeated the T3 test with other two observed red giant stars from F1 at $S/N_{\rm CaT}$ of ~ 10 and 15, obtaining the same results.

Therefore, in order to obtain reliable results we repeated the T3 test considering also other intervals of effective temperature. This allowed us not only to verify the conclusions reached in the previous tests, but also to test the general behaviour of RVSPECFIT analysing stars of different spectral types. In Sect. 4.4.2, we investigated in fact how the kinematic properties of IC 1613 change according to different stellar populations. Specifically, we found that stars selected having observed colours between $0.4 \lesssim (V-I) \lesssim 0.7$ showed velocities which were on average significantly discrepant (by ~ 10 km s^{-1}) with respect to those of the parent sample. Therefore, we repeated the T3 test with three giant stars selected from this sub-sample having $S/N_{\rm CaT} \sim 25, 15$ and 10. Stars were selected to have a best fitting template with $T_{\rm eff} \sim 6500$ K, which is a typical temperature in this colour range. We wanted to verify in particular that

RVSPECFIT was not introducing any bias when recovering the radial velocities. As shown in Table 4.7, we well recovered the input parameters.

We further repeated the T3 test with several hot stars, selected to have $(V - I) < 0.4$. We chose two intervals of compatible effective temperatures, $T_{\rm eff} \sim 10000$ K and ~ 15000 K, with $S/N_{550} \sim 30 - 50$ and $\sim 10 - 15$. In this case, stars were selected also from field F2, to verify consistency between the results from different fields. A further motivation in this case was to verify the introduction of any bias by RVSPECFIT due to the paucity of spectral lines to be fitted. Again, we reached to the same conclusions as before.

Therefore, results from the T3 tests indicate that if the flux uncertainty is underestimated by a constant factor, in this case 1.4, the same value is recovered for the velocity errors too. We needed to apply then this correction to the velocity errors returned by RVSPECFIT for the observed spectra. Furthermore, we verified the ability of RVSPECFIT to recover the input radial velocities without introducing any bias, independently of the spectral type or S/N.

The T3 tests also gave us an insight on the quality of the spectral parameters returned by RVSPECFIT. In general, we found that the associated errors were largely underestimated, often by an order of magnitude, compared to the measurements scatter. Focusing on the latter values, we found that $T_{\rm eff}$ and $\log(g)$ could be recovered with an accuracy < 500 K and < 1 dex, respectively, for stars with an input $T_{\rm eff} \leq 6500$ K and $S/N_{\rm CaT} \gtrsim 10$. On the other hand, for stars with an input $T_{\rm eff} \geq 10000$ K and $S/N_{550} \gtrsim 10$, we got an accuracy < 2000 K and < 1 dex. Furthermore, the procedure tends to introduce a systematic offset of ~ 200 K in the recovered effective temperatures. We double checked the goodness of $T_{\rm eff}$ determinations by comparing the RVSPECFIT measurements for the observed spectra with those obtained applying, when possible, the Alonso's empirical relation described above. We found a linear agreement with the RVSPECFIT values which resulted, however, systematically higher of ~ 200 K, as spotted in the mock tests. The recovered metallicities [Fe/H], instead, showed high scatters ($\gtrsim 0.5$ dex) at any input values of effective temperature and S/N, resulting then not informative. We further verified these results by comparing them with the metallicities obtained for the red giant stars from the CaT lines, without finding any significant agreement.

The mock tests we performed were informative of the general behaviour of RVSPECFIT. However, they were computationally expensive and limited to few selected cases. In order to provide reliable confidence limits for the recovered spectral parameters, we count in the future to improve our procedure by applying a Bayesian method in a similar fashion as done in Li et al. (2019).

TABLE 4.7— Results from the Monte Carlo tests. Columns are: the ID of the star; the measured radial velocity with the uncorrected error; the S/N obtained from the continuum around the CaT lines for $T_{\rm eff} \leq 6500$ K, or around 5500 Å otherwise; the effective temperature measured by RVSPECFIT; the type of test done; the median S/N of the mock spectra obtained in the same way as the observed one; the median of the mock radial velocities; the scaled median absolute deviation (MAD) of the mock radial velocities; the median of the mock velocity errors, with the MAD within parenthesis; the mean and standard deviation of the difference between the mock velocities and the measured one, scaled for the mock velocity errors.

ID	$V_{\rm rad,o}$	S/N	$T_{\rm eff}$	Test	$S/N_{\rm m}$	$\mu(V_{\rm rad})$	$\sigma(V_{\rm rad})$	$\mu(\delta_{V_{\rm rad}})$	$\frac{(V_{\rm rad}-V_{\rm rad,o})}{\delta_{V_{\rm rad}}}$
	km s^{-1}	pxl^{-1}	K		pxl^{-1}	km s^{-1}	km s^{-1}	km s^{-1}	
F1-59	-256.6 ± 7.8	5.6	5000	T1	8.9	-255.8	8.6	8.6 (0.7)	0.08, 0.95
				T2	6.3	-256.1	13.5	12.2 (1.3)	0.01, 1.09
				T3	6.4	-256.1	11.5	8.6 (1.0)	0.01, 1.49
F1-72	-235.2 ± 5.7	10.4	5000	T3	9.2	-235.6	9.5	6.1 (0.4)	0.14, 1.44
F1-73	-253.5 ± 3.7	14.9	5000	T3	14.8	-253.0	5.9	4.3 (0.2)	0.17, 1.46
F1-1015	-242.2 ± 1.6	24.0	6500	T3	22.0	-242.1	3.1	2.2 (0.1)	0.01, 1.48
F1-1202	-245.1 ± 2.7	15.0	6500	T3	15.0	-245.6	4.8	3.4 (0.1)	-0.11, 1.45
F1-502	-241.7 ± 7.7	8.0	6500	T3	8.0	-240.9	13.6	8.1 (1.0)	0.0, 1.59
F1-156	-238.3 ± 4.5	30.6	10000	T3	27.0	-238.6	6.2	4.8 (0.2)	-0.17, 1.32
F1-1260	-237.4 ± 11.0	10.0	10000	T3	12.0	-237.8	19.2	13.0 (1.5)	0.04, 1.32
F2-1413	-235.5 ± 3.2	33.0	10000	T3	30.0	-235.1	4.9	3.6 (0.1)	0.01, 1.37
F2-1528	-262.2 ± 10.3	9.5	10000	T3	10.0	-260.7	14.2	10.1 (1.0)	0.09, 1.40
F1-1449	-226.6 ± 4.0	50.0	15000	T3	47.0	-226.6	5.8	4.0 (0.1)	-0.07, 1.54
F1-1331	-246.1 ± 10.3	15.0	15000	T3	17.0	-246.5	17.0	10.6 (1.4)	0.01, 1.50
F2-1000	-238.5 ± 2.9	52.0	15000	T3	50.0	-238.4	4.5	3.2 (0.1)	0.05, 1.44
F2-1519	-234.7 ± 10.8	16.1	15000	T3	17.0	-236.5	16.6	11.6 (1.0)	-0.16, 1.44

4.A.2 RVSPECFIT vs. ULySS

In our analysis, we used RVSPECFIT and ULySS in a complementary way: the former for radial velocity measurements, while the latter for spectral classification. However, since both codes provide similar outputs, we compared their performances in recovering the radial velocity and $T_{\rm eff}$ from the observed spectra.

We considered all those targets which passed the photometric selection (see Sect. 4.2.2) having measurements from both RVSPECFIT and ULySS, further selecting those with PVR and PCL flags between 2 and 4, and abs(skewness) $<$ 0.5, for a sub-sample of 922 objects.

The radial velocity errors for the ULySS measurements were obtained from Monte Carlo simulations using several templates of giant stars at different intervals of temperature and S/N. We made this choice because the formal errors returned by ULySS were generally overestimated, without following any clear trend with the S/N or spectral type. For the Monte Carlo simulations we chose seven templates from the MIUSCAT library (see Sect.4.3.1), with $T_{\rm eff}$ ranging from 3500 K to 20000 K. The simulations were performed by adding Poisson noise to each template to obtain simulated spectra at increasing S/N intervals, with values ranging from 4 to 30. We repeated each process 100 times. For each template, the recovered velocity scatter as a function of S/N was fitted by an exponential law. The ULySS measurements were then divided into effective temperature bins according to the templates considered, and the velocity errors assigned using the corresponding exponential fit.

First we compared the velocity differences for pair measurements obtained with the ULySS and RVSPECFIT codes. We found that $\sim$ 75% of the measured velocities are in agreement within the combined uncertainties, obtained as $\sqrt{\delta^2_{\rm rad,rvsp} + \delta^2_{\rm rad,ULySS}}$. The comparison is shown in Fig. 4.13 where for clarity we reported only those measurements with a combined error < 30 km s^{-1}. Nevertheless, the difference between the ULySS and RVSPECFIT measurements shown an average positive shift of ~ 5 km s^{-1}. What is more, the higher shifts were observed for those objects with a S/N$_{\rm K} < 10$. This was somehow expected for the UlySS measurements, since the Monte Carlo tests showed average velocity shifts of up to 20 km s^{-1} for templates with effective temperatures of $\sim$ 4500 K and greater than $\sim$ 10000 K having simulated $S/N < 10$. On the other hand, we have already showed in Sect. 4.A.1 the capacity of RVSPECFIT to correctly recover radial velocities even at the lowest S/N. This is a very important point because most of the stars in our dataset are in a low S/N regime ($\lesssim 10$), where RVSPECFIT showed its strength in the recovery of radial velocities.

The comparison of effective temperatures was instead merely qualitative,

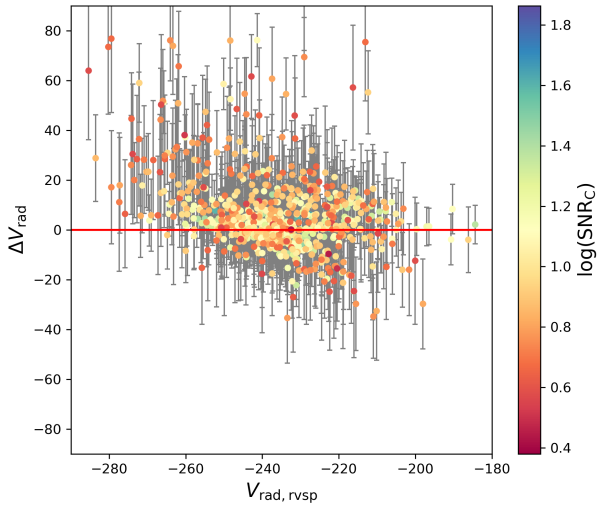

FIGURE 4.13— Velocity differences for pair measurements obtained with the RVSPECFIT and ULySS codes. The solid red line represents the zero velocity offset. Filled circles are colour-coded according to their S/N_C, while the grey error-bars indicate the combined uncertainty, that is $\sqrt{\delta^2_{\rm rad,rvsp} + \delta^2_{\rm rad,ULySS}}$.

since the values returned by RVSPECFIT had associated errors which were largely underestimated (see previous section). In the ULySS case, instead, for each spectrum the stored temperature value is that of the best fitting template, which was chosen by eye among the most likely templates. This procedure had an accuracy of up to ~ 500 K, for a quality PCL-flag between 3 and 4.

The comparison worked well for values < 10000 K, since the PHOENIX library used by RVSPECFIT is not optimized for very hot stars. In general, ULySS returned $T_{\rm eff}$ which were $\sim$500 K lower than those of RVSPECFIT.We have previously found that RVSPECFIT tend to return temperatures which are somewhat overestimated.

5

Kinematic, chemical and mass properties of Local Group dwarf galaxies

Part of the material included in this chapter has been published in:

Hermosa Muñoz, L.; Taibi, S.; Battaglia, G.; Iorio, G.; Rejkuba, M.; Leaman, R.; Cole, A.; Irwin, M.; Jablonka, P.; Kacharov, N.; McConnachie, A.; Starkenburg, E.; Tolstoy, E., 2020, A&A, 634, A10.

ABSTRACT

In this chapter we present results from a comparison of the properties of Local Group dwarf galaxies, along with the chemo-kinematic analysis of the isolated dwarf galaxy in Aquarius.

In the comparative analysis of LG dwarf galaxies we focus on their internal kinematic and radial metallicity properties. The kinematic results for the sample of galaxies analysed in this thesis (i.e. Cetus, Tucana, IC 1613 and Aquarius) add to those of other LG systems having similar physical properties. In particular, the internal $v_{\rm rot}/\sigma_{\rm v}$ of Cetus and Tucana is similar to that of satellite dwarfs, challenging tidal stirring models on the formation of dSphs.

The dynamical mass estimation of our sample shows how they add to the other LG dwarf galaxies residing in dark matter halos less massive than expected. The too-big-to-fail problem then persists, regardless of the environment in which these systems reside.

Finally, we show the results of a homogeneous analysis aimed at finding radial variations in metallicity measurements from LG dwarf galaxies. Several of the analysed systems show mild metallicity gradients, independently of their environmental status. In general, the brightest systems show a lower dispersion in their values than those with a lower luminosity. The role of the environment seems limited, while the steepest slopes may be associated to past mergers.

Before delving into the comparison, we present results of the Aquarius analysis that show how its stellar motion is found to counter-rotate with respect to that of the HI component, being the first time that such effect is observed at this luminosity. The average metallicity obtained from the chemical analysis is normal for a system of this stellar mass; there are hints of a radial metallicity gradient and of two chemo-kinematically distinct stellar populations.

5.1 The Aquarius dwarf galaxy

In the first part of this chapter we present results from the analysis of the Aquarius dwarf galaxy, already published in Hermosa Muñoz, L.; Taibi, S.; et al. (2020). My contribution to the Aquarius work has been very relevant, since I provided tools for the data-reduction and chemo-kinematic analysis. In particular I performed a series of mock tests aimed at exploring the reliability of the kinematic parameters obtained from our dataset. I report here the essential details of the analysis, focusing in particular on the part of the mock tests. For a detailed discussion of all steps, please refer to the full article of Hermosa Muñoz et al. (2020).

5.1.1 Introduction

The Aquarius dwarf galaxy (also known as DDO 210) is located at the periphery of the Local Group (LG), at ~ 1 Mpc from both the Milky Way (MW) and M31 (based on measurements of the tip of the RGB, Lee et al., 1999; McConnachie et al., 2005, and variable stars, Ordoñez & Sarajedini, 2016). Only two galaxies are known to be within 500 kpc of it (i.e. SagDIG and NGC 6822, see Cole et al., 2014). Its free-fall time-scale into the MW or M31 is approximately equal to a Hubble time (McConnachie et al., 2006; McConnachie, 2012). Therefore, Aquarius is found in extreme isolation and has likely never interacted with the MW or M31 during its lifetime.

In literature, this system has been referred to both as a dwarf transition (dTr, e.g. Mateo, 1998; McConnachie et al., 2006) and a dwarf irregular galaxy (dIrr Cole et al., 2014, although they recognized its transition properties). In fact, it shows a higher stellar to gas mass fraction than other dTrs, such as Phoenix or Pegasus (see McConnachie, 2012). It also shows a clear UV surface brightness profile (Lee et al., 1999) similar to systems classified as dIrrs. However, there is a lack of active star forming regions, despite the presence of young stars formed in the last few hundreds Myr. Its star formation history (SFH) has indeed decreased during the last 2 Gyrs, being almost null at the moment, after reaching a peak between 6 and 8 Gyrs ago (Cole et al., 2014). The difficulty to assign a clear morphological type to this galaxy reflects the importance of referring to dwarf galaxies on the basis of their physical properties. This is also true for galaxies of the same morphological type, which can show very different evolutionary pathways (Gallart et al., 2015).

The stellar component of Aquarius presents a well-defined position angle and an ellipticity that varies with radius, becoming more circular in the outer parts (McConnachie et al., 2006). The surface density of the overall stellar

population is well described by an exponential profile, which matches also the spatial distribution of the intermediate-old age component (i.e. RGB and red clump stars). The younger stars on the other hand (i.e. of main sequence and blue-loops) present a different spatial profile, implying that the recent history of star formation occurred in a spatially more concentrated region than in earlier epochs (McConnachie et al., 2006). The young stars are also shifted few arcminutes to the east with respect to the optical centre, and coincident with a small cavity in the HI profile, as indicated by McConnachie et al. (2006).

Only two spectroscopic studies (Kirby et al., 2014, 2017) have investigated the properties of the stellar component. From the individual analysis of ~ 25 RGB stars, Kirby et al. (2017) found a dark-matter-dominated system, with no significant signs of internal rotation. The average metallicity resulted typical for a dwarf galaxy with the luminosity of Aquarius.

The properties of the neutral gas have been well determined over time, showing that the HI morphology differs from that of the stars, as the HI distribution is predominantly spherical, while the stellar one is much more elliptical (e.g. Young et al., 2003; Begum & Chengalur, 2004; McConnachie et al., 2006). Both Young et al. (2003) and Begum & Chengalur (2004) reported a small velocity gradient in the HI gas, as recently confirmed by Iorio et al. (2017), who measured a maximum circular velocity of ~ 16 km s^{-1} along a P.A. $= 77$ deg.

Here we present results from our analysis of a spectroscopic sample of individual red giant branch (RGB) stars, observed in the region of the near-IR Ca II triplet (CaT) lines. The adopted parameters for Aquarius used in this chapter are summarized in Table 5.1.

5.1.2 Observations, data reduction and measurements

Observations were taken as part of the ESO Program 091.B-0331 (PI: G. Battaglia) using the FORS2 instrument at UT-1 of the Very Large Telescope (VLT) in mask-exchange multi-slit (MXU) mode. Targets were selected to be likely RGB stars belonging to Aquarius using the Subaru/SuprimeCam photometric data in the Johnson-Cousins V- and I-band of McConnachie et al. (2006). Slits that would have remained otherwise empty were assigned to random objects. Pre-imaging exposures taken with the same instrument were used to ensure precise slit allocations. We selected 53 individual objects distributed over two masks, with two of them observed in both masks. Mask slits were designed to be 1 arcsec wide by 8 arcsec long (for two slits their length was reduced to 6 arcsec to avoid overlap with adjacent slits). For each mask were taken 10 exposures for a total observing time of 25 h. On average the airmass was around 1.1 with the seeing about 0.9 arcsec for one mask and 1.1 arcsec for the other. The instru-

TABLE 5.1— Parameters adopted for the Aquarius (DDO 210) dwarf galaxy.

Parameter	Units	Value	Ref.
$\alpha_{\rm J2000}$		$20^h46^m51.8^s$	(1)
$\delta_{\rm J2000}$		$-12°50'53''$	(1)
$\epsilon^{(a)}$		0.5 ± 0.1	(1)
P.A.$_*$	deg	99 ± 1	(1)
$R_{\rm e}$	arcmin	1.10 ± 0.03	(2)
$M_{\rm V}$		-10.6 ± 0.3	(1)
$D_\odot$	kpc	1072 ± 39	(1)
$E(B-V)$		0.045	(3)
P.A.$_{\rm HI}$	deg	77.3 ± 15.2	(4)
$\bar{v}_{\rm hel}$	$\rm km\,s^{-1}$	-142.2 ± 1.8	(5)
$\sigma_{\rm v}$	$\rm km\,s^{-1}$	$10.3^{+1.6}_{-1.3}$	(5)
k	$\rm km\,s^{-1}\,arcmin^{-1}$	$-5.0^{+1.6}_{-1.9}$	(5)
P.A.$_{\rm rot}$	deg	139^{+17}_{-27}	(5)
[Fe/H]	dex	-1.59 ± 0.05	(5)
$\sigma_{\rm [Fe/H]}$	dex	0.25	(5)

Notes. The table lists: the coordinates of the galaxy's optical centre; the stellar ellipticity and position angle; the geometric effective radius; the stellar absolute magnitude in V-band; the distance modulus and heliocentric distance; the average reddening along the line-of-sight; the HI position angle; the parameters obtained in this work: the systemic velocity, the velocity dispersion, the velocity gradient, the kinematic position angle, the median metallicity, and the intrinsic metallicity scatter. $^{(a)}\epsilon = 1 - b/a$.
References. (1) McConnachie (2012); (2) McConnachie et al. (2006); (3) Schlafly & Finkbeiner (2011); (4) Iorio et al. (2017); (5) this work.

mental set-up and observation strategy adopted were the same as those already described in detail in Ch. 2 and 3 for the FORS2-MXU data of Cetus and Tucana. Similarly, we followed the same procedure for the data reduction, as well as for the determination of the line of sight (l.o.s.) velocities and metallicities.

In Fig. 5.1 the spatial distribution of the observed targets is shown, together with their position on the colour-magnitude diagram.

The wavelength corrections ranged from $\pm1.2 - 16.9$ $\rm km\,s^{-1}$ with errors $\pm0.7-2.9$ $\rm km\,s^{-1}$. The slit correction instead ranged between $\pm0.15-8.5$ $\rm km\,s^{-1}$ with errors $\pm0.4 - 4.2$ $\rm km\,s^{-1}$.

The heliocentric velocities $v_{\rm hel}$ and equivalent widths (EWs) of the CaT lines were measured on the stacked spectra, obtained from a weighted sum of the individual exposures. The median S/N measured in the continuum regions around the CaT lines was of 25 $\rm pxl^{-1}$.

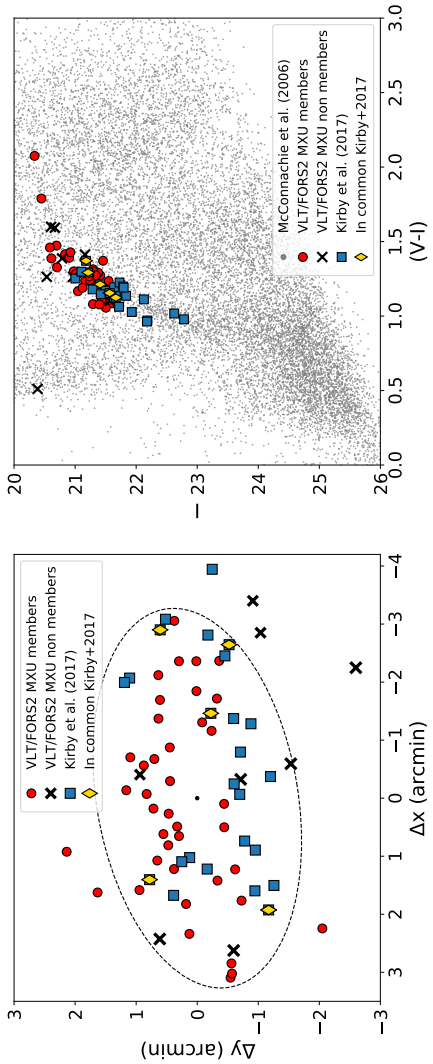

FIGURE 5.1— Spatial distribution (left) of the targets projected onto the tangent-plane and colour-magnitude diagram of the stars along the line-of-sight to Aquarius (right). The red circles represent the stars observed with VLT/FORS2-MXU and classified as Aquarius members, blue squares show the sample of member stars from Kirby et al. (2017), yellow diamonds are the stars in common between these two studies, and black crosses correspond to the VLT/FORS2-MXU RGB stars that have been classified as probable non-members of the galaxy. On the left panel, the ellipse has a semi-major axis equal to 3 times the effective radius of the galaxy, with a position angle of 99° and ellipticity of 0.5 (see Table 5.1). The black dot represents the galactic centre. On the right panel, grey points represent the objects classified with high confidence as stars in the Subaru/SuprimeCam photometric data ($34' \times 27'$) of McConnachie et al. (2006). Magnitudes have been corrected for extinction adopting the $E(B-V)$ value from Table 5.1, along with the reddening law $A_V = 3.1 \times E(B-V)$.

The heliocentric velocities were obtained by performing a cross correlation around the CaT line with the synthetic spectrum of a red giant star, as done for Cetus and Tucana in Ch. 2 and 3. In the same way, metallicities were obtained by applying the Starkenburg et al. (2010) relation, assuming for the visual magnitude of the horizontal branch a value of $V_{\rm HB} = 25.45 \pm 0.20$ (Cole et al., 2014). The velocity and [Fe/H] values of the two stars observed repeatedly with the two masks were in agreement within the errors in both cases. Therefore their measurements were combined using a weighted average. The median error in the velocity and [Fe/H] measurements obtained from the stacked spectra resulted of 4.8 $\rm km\,s^{-1}$ and 0.13 dex, respectively.

Before proceeding with the determination of the kinematic and chemical properties of Aquarius, we removed the eventual contaminants in our sample following a two steps procedure. First, we excluded one target based on its photometric properties (i.e. colour and magnitude), which were not compatible with those of the RGB stars at the distance of Aquarius. Second, we performed a selection based on the kinematic properties of the observed stars. We retained those targets that fulfilled the condition $|v_{\rm hel} - v_{\rm bulk}| < 3\,{\rm MAD}(v_{\rm hel} - v_{\rm bulk})$, where $v_{\rm bulk}$ is the expected bulk velocity at the position of each given star, calculated by applying a Bayesian analysis that solved iteratively for the systemic velocity of the system, its velocity dispersion and the best-fitting model for the internal kinematic (see details in Sect. 5.1.3). The estimation of these parameters was an iterative process, fitting the data until convergence. These steps reduced our dataset to 45 probable-member stars.

5.1.3 Kinematic analysis

For a full discussion on the internal kinematics of Aquarius, we refer to Hermosa Muñoz et al. (2020). Here we report on the most exciting result, that is to say the detection of a misaligned rotation between the stellar and gas components.

From Fig. 5.2, it is clear already the presence of a mild velocity gradient for the stellar component along the optical major axis. In order to confirm this finding and obtain an estimation of the kinematic parameters, we performed a Bayesian analysis following the same methodology described in Ch. 2. The corresponding results are presented in Table 5.2. We compared three different kinematic models, two taking into account rotation, either changing linearly with the radius or constant, and a dispersion-only model. The free parameters were: the systemic velocity and velocity dispersion common to the three models ($\rm v_{hel}$ and $\sigma_{\rm v}$, respectively); the position angle (θ) of the kinematic major axis for the rotation models; and the rotational term expressed either as a velocity gradient (k) for the linear model, or as a constant value for the flat model (v_c).

TABLE 5.2— Parameters and evidences resulting from the application of the Bayesian analysis to the whole FORS2/MXU sample of members, as well as divided in metal-rich (MR) and metal-poor (MP) samples.

Sample	Method	$v_{\rm hel}$ ($\mathrm{km\,s^{-1}}$)	$\sigma_{\rm v}$ ($\mathrm{km\,s^{-1}}$)	k ($\mathrm{km\,s^{-1}\,arcmin^{-1}}$)	$v_{\rm c}$ ($\mathrm{km\,s^{-1}}$)	θ (°)	Bayes factor
All	Linear rotation	$-142.2^{+1.8}_{-1.8}$	$10.3^{+1.6}_{-1.3}$	$-5.0^{+1.6}_{-1.9}$		139^{+17}_{-27}	$\ln B_{\rm lin,flat} = 1.7$
	Flat rotation	$-142.4^{+2.0}_{-2.0}$	$11.2^{+1.6}_{-1.4}$		$-7.1^{+2.9}_{-3.0}$	137^{+22}_{-30}	$\ln B_{\rm rot,disp} = 1.6$
	Dispersion-only	$-141.5^{+1.9}_{-2.1}$	$12.0^{+1.7}_{-1.5}$				
MR	Linear rotation	$-141.1^{+2.0}_{-2.1}$	$8.2^{+2.0}_{-1.6}$	$-3.7^{+1.9}_{-2.1}$		87^{+53}_{-49}	$\ln B_{\rm lin,flat} = 0.5$
	Flat rotation	$-140.6^{+2.2}_{-2.2}$	$8.7^{+2.1}_{-1.7}$		$-4.3^{+3.4}_{-3.1}$	76^{+49}_{-44}	$\ln B_{\rm rot,disp} = -1.8$
	Dispersion-only	$-140.9^{+2.1}_{-2.1}$	$9.1^{+2.1}_{-1.6}$				
MP	Linear rotation	$-142.9^{+3.3}_{-3.2}$	$13.1^{+2.9}_{-2.2}$	$-5.8^{+2.5}_{-2.7}$		145^{+21}_{-32}	$\ln B_{\rm lin,flat} = -0.8$
	Flat rotation	$-144.6^{+3.3}_{-3.2}$	$12.9^{+2.9}_{-2.2}$		$-14.5^{+6.3}_{-6.1}$	157^{+15}_{-22}	$\ln B_{\rm rot,disp} = 0.6$
	Dispersion-only	$-142.3^{+3.7}_{-3.6}$	$15.4^{+3.2}_{-2.5}$				

Notes. The reported values of the kinematic parameters represent the median of the corresponding marginalized posterior distributions, with 1-σ errors set as the confidence intervals around the central value enclosing 68% of each distributions.

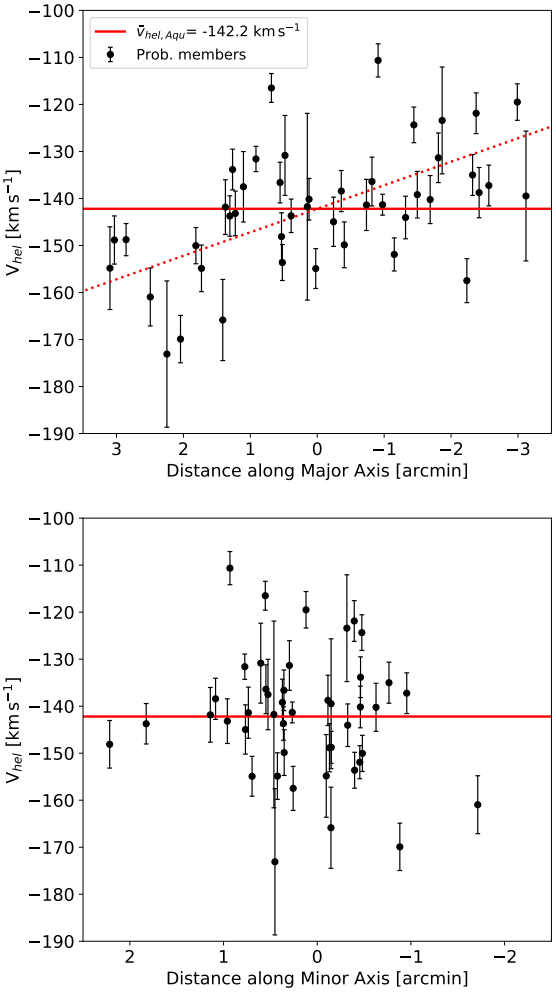

FIGURE 5.2— Line-of-sight velocity distributions of the probable-member stars. The red solid and dashed lines indicate respectively the systemic velocity and velocity gradient obtained for the linear rotation model from the kinematic analysis. *Left panel*: distribution along the optical major axis; *right panel*: along the minor axis.

We used the returned model evidence Z to compare the statistical significance of one model compared to the other in terms of the natural logarithm of the Bayes factor $\ln B_{1,2} = \ln Z_1/Z_2$. In our case we considered the Bayes factor comparing the two rotation models ($\ln B_{\rm lin,flat}$) and that between the best rotation model and the dispersion-only one ($\ln B_{\rm rot,disp}$).

We found that the linear rotation model was weakly favoured both with respect to the constant rotation model ($\ln B_{\rm lin,flat}$=1.7) and with respect to the dispersion-only model ($\ln B_{\rm rot,disp}$=1.6). The systemic velocity, dispersion and velocity gradient derived with this approach were, respectively, $\bar{v}_{\rm hel} = -142.2^{+1.8}_{-1.8}$ km s^{-1}, $\sigma_{\rm v} = 10.3^{+1.6}_{-1.3}$ km s^{-1} and $k = -5.0^{+1.6}_{-1.9}$ km s^{-1} arcmin^{-1} (-16^{+5}_{-6} km s^{-1} kpc^{-1}). The best-fitting position angle of the kinematic major axis was $\theta = 139^{+17}_{-27}$ deg, shifted with respect to that of the galaxy optical major-axis by 40 deg, although consistent with it at the 1.5-σ level. In our definition, a negative velocity gradient with θ between 0° and 180° implies a receding velocity on the West side (and would be equivalent to a positive gradient with $\theta = \theta + 180°$). Therefore, there are evidences of a mild stellar rotation in this system. Considering that our data extend on average out to ~ 2.5 arcmin, that is almost twice the half-light radius, this would imply a $v_{\rm rot}/\sigma_{\rm v} \sim 1.2 \pm 0.4$, at that radius. We note that Aquarius is an isolated galaxy with a small angular extension on the sky, thus it is very unlikely that the detected velocity gradient is due to tidal disturbances or to the projection effects of the three-dimensional movement of the galaxy through the line of sight.

Our results for the systemic velocity and velocity dispersion are within 1-σ from those obtained by Kirby et al. (2017) analysing 25 RGB probable-member stars. However, they did not find signs of internal rotation, being only able to place a 95% confidence limit of a constant rotational velocity < 9 km s^{-1}. We confirmed their results by applying our Bayesian analysis, showing that the presence of rotation cannot be proven conclusively from the Kirby et al. (2017) sample. These findings are also compatible with the work of Wheeler et al. (2017) analysing an older dataset from Kirby et al. (2014): although they reported for Aquarius a $v_{\rm rot}/\sigma_{\rm v} \sim 2$, this value suffered of large errors and the Bayesian evidence of rotation resulted inconclusive.

Analysing the kinematic properties of the HI component, Iorio et al. (2017) found a weak velocity gradient of $\sim$5 km s^{-1} out to a radius of 1.5 arcmin, similar to the rotational velocity we obtained at approximately the same radius. However, the HI kinematic major-axis has a P.A. of 77.3 ± 15.2 deg, that means the gas is receding on the East side. Therefore, the stellar kinematics we examined is significantly misaligned compared to that of the HI. This effect has been already observed in NGC 6822 (Demers et al., 2006) and systems outside the

LG. However, this would be the first time that a misaligned rotation between two different components of a galaxy is measured down to the luminosity of Aquarius.

Mock tests

We performed a series of tests on mock catalogues in order to understand what type of rotational properties can be detected given the characteristics of the datasets in hand. To this aim, we produced sets of mock l.o.s. velocities at the same position as the spectroscopically observed stars, which we analysed like the actual data. These were extracted from a Gaussian distribution centred on zero and of standard deviation equal to the assumed velocity dispersion, adding to each value its corresponding velocity uncertainty, also assumed to be Gaussian. We further added a projected rotational component obtained from the model under consideration (linear or flat), having $v_{\rm rot,mock}/\sigma_{\rm mock} = n = 1.5, 1.0, 0.75, 0.5, 0.25, 0$ at twice the half-light radius (see Table 5.1); the velocity dispersion $\sigma_{\rm mock}$ was fixed to $10\,{\rm km\,s^{-1}}$ for all cases. The simulated linear rotation models correspond to velocity gradients $k = 6.8, 4.5, 3.4, 2.3, 1.1$ and 0 ${\rm km\,s^{-1}\,arcmin^{-1}}$, while the constant rotation models had rotational velocities $v_{\rm c} = 15, 10, 7.5, 5.0, 2.5$ and 0 ${\rm km\,s^{-1}}$. All the cases were simulated for three different position angles which correspond to the P.A. of the projected semi-major axis of the stars (99°), then adding 45 and 90 degrees (semi-minor axis). Each single case was simulated N = 1000 times. The mock tests were run both on the FORS2-MXU and the Kirby et al. (2017) samples.

Results indicate that rotation can be detected with at least a weak positive evidence when along the optical major axis of the galaxy for $n \geq 0.75$ for the FORS2 dataset and $n \geq 1$ for the Kirby et al. (2017) sample. Both datasets have a similar sensitivity to the direction of rotation and model type in terms of ranking, with the FORS2 sample yielding larger evidences for a given model, and therefore a better capability to detect rotation at a given n. The datasets under consideration are not sensitive to small levels of rotation ($n \leq 0.5$ for FORS2, $n \leq 0.75$ for K17), since these return either inconclusive or even weak evidences disfavouring the presence of rotation. In the dispersion-only case ($n = 0$) both samples favour this model over the two that include rotation, demonstrating that there is no bias towards the rotational models.

We recall that the observed value of the rotation support for the FORS2 dataset was of $v_{\rm rot}/\sigma_{\rm v} \sim 1.2 \pm 0.4$ along a kinematic axis with P.A. ~ 140 deg, while the Bayes factors resulted in $\ln B_{\rm lin,flat} = 1.7$ and $\ln B_{\rm rot,disp} = 1.6$. These values are compatible with results from mock tests simulating a linear rotation model with $n = 1.5$ along the minor axis or at intermediate P.A., with $n = 1$

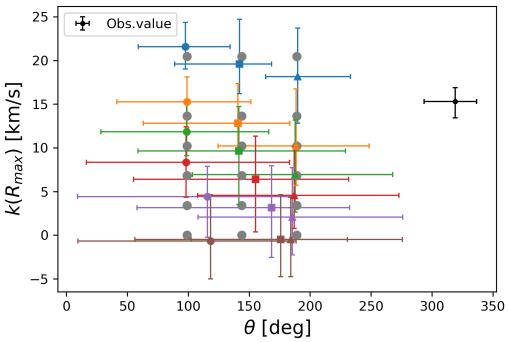

FIGURE 5.3— Rotation velocity at $R_{\rm max} = 3'$ vs. kinematic position angle recovered from the mock tests on the FORS2 dataset simulating a linear rotation model. Grey circles represent input values, while coloured circles, squares and triangles represent recovered values at different simulated kinematic P.A.; colours from blue to brown represent decreasing values of n, while the error bars are the 99% confidence interval (C.I.); in black the observed value from our data-set with error bars at 68% C.I.

along the intermediate axis or the major axis, or with $n = 0.75$ along the major axis.

From the mock tests we also extracted the information on how well the kinematic major axis P.A. and the rotational velocity at a given radius are recovered for the various n (see Fig. 5.3). The initial values are always retrieved within the 99% confidence interval (C.I.), with a small bias towards underestimating the rotation signal when the kinematic major axis is along the optical minor axis. Also in terms of amplitude of the rotational velocity, the favourite models would be those with $n \geq 0.75$.

However, when comparing with the velocity gradient and kinematic major axis P.A. obtained for the observed FORS2 dataset, we found that they are beyond the 99% C.I. of that retrieved for models with kinematics similar to that exhibited by the HI gas (see Fig. 5.3), indicating that the misalignment/counter-rotation between the stellar and gas components is not due to number statistics, spatial coverage and measurement errors of our FORS2 data.

It has been noted in the literature that the P.A. determination of both optical and gas components is somewhat uncertain, and it could be compatible with the P.A. we measured for the kinematic major axis (see McConnachie et al., 2006;

Iorio et al., 2017). However, even assuming that stars and gas share the same P.A., they clearly rotate in opposite directions, with the former receding on the West side, while the latter on the East side of Aquarius. We quantified that the velocity difference between these two components is approximately of $5\,\mathrm{km\,s^{-1}}$ along the HI P.A. and reaches $\sim 10\,\mathrm{km\,s^{-1}}$ close to the East and North-West edges of the HI disc.

Iorio et al. (2017) found signs of a possible inflow/outflow of gas in Aquarius, as an extended region of HI emission along the minor axis not connected with the rotating HI disc. Furthermore, McConnachie et al. (2006) suggested a recent gas accretion event as a possible reason for the young stellar population found slightly off-centred. We postulate then that in general the kinematics of the HI component in Aquarius might be dominated by recently accreted gas, while the RGB stars, which according to their SFH are likely to be dominated by ~ 8 Gyr old stars (Cole et al., 2014), are tracing the kinematic properties as they were imprinted a much longer time ago along a different kinematic axis.

Dynamical mass estimation

We used the rotational velocity obtained from the stars to calculate the corresponding circular velocity and, therefore, estimate the dynamical mass of Aquarius. In order to do so, we applied first the asymmetric drift correction to the stellar motion since, as in the case of gas, random motions are suppressing the rotation curve, especially at smaller radii. We are interested into calculate the dynamical mass inside the half-light radius. The circular velocity value was obtained following the same procedure described in Ch. 4 for IC 1613. We note that we did not correct the rotational velocity for the inclination factor $\sin i$, but assuming that this value is similar to that of the gas (i.e. $\sin i_{\mathrm{HI}} \sim 0.9$, Iorio et al., 2017), this correction would be rather small. Therefore, we obtained a circular velocity of $V_{\mathrm{c}}(r_{1/2}) = 17 \pm 2\ \mathrm{km\,s^{-1}}$, where $r_{1/2}$ is the 3D de-projected half-light radius. The associated rotationally derived mass is then $M_{\mathrm{c}}(r_{1/2}) = V_{\mathrm{c}}^2 r_{1/2}/G = 31 \pm 7 \times 10^6 M_{\odot}$. This value is in very good agreement with that we would derive applying the Wolf et al. (2010) formula, that is $M_{1/2} = 34^{+11}_{-9} \times 10^6 M_{\odot}$. If we express this value in terms of circular velocity, assuming to have only random motions, it would be $V_{\mathrm{c}}(r_{1/2}) = \sqrt{3}\sigma_{\mathrm{v}} = 18^{+3}_{-2}\ \mathrm{km\,s^{-1}}$. This shows how the kinematics inside the half-light radius is actually dominated by the velocity dispersion. The mass-to-light ratio is then $M_{1/2}/L_V \sim 20 \pm 5$, assuming a visual luminosity of $L_V = 1.5 \pm 0.1 \times 10^6 L_{\odot}$ (adapted from McConnachie, 2012), which implies that Aquarius is a dark matter dominated system.

We refer to the second part of this chapter for a discussion on the dynamical

masses derived for the LG dwarf galaxies and their implications in a cosmological context.

5.1.4 Metallicity properties

From the metallicity analysis of the Aquarius FORS2 data we obtained a median value of $[\mathrm{Fe/H}] = -1.59 \pm 0.05$ dex. This is compatible with the average value of -1.50 ± 0.06 dex reported by Kirby et al. (2017), and in full agreement with the luminosity-metallicity relation for Local Group dwarf galaxies. We further measured a metallicity spread of $\sigma_{\mathrm{MAD}} = 0.30$ dex, while the intrinsic dispersion, taking into account the measurements errors and assuming a Gaussian metallicity distribution function, resulted $\sigma_{\mathrm{intr}} = 0.25$ dex. This value is in agreement with the intrinsic dispersion measured for other LG dwarf galaxies of similar luminosity (Leaman et al., 2013).

The metallicity radial variation was analysed as done in the previous chapters, using a Gaussian process regression (GPR). We recall that the GPR is a non-parametric analysis, it does not depend on a fixed boxcar like for example the running median, and the output has a probabilistic meaning. We used a Gaussian kernel together with a noise component to take into account the intrinsic scatter of the data. Results are shown in Fig. 5.4, where we plot the variation of [Fe/H] as a function of the elliptical radius. The presence of a very mild negative metallicity gradient can be appreciated. We confirmed this results by also running a median fit to the data.

Since the GP analysis returns a trend similar to a linear relation, we performed a simple Bayesian linear regression, including an intrinsic scatter term, to estimate the significance of the metallicity gradient. The resulting cumulative posterior distribution of the slope of the metallicity gradient indicated that the possibility of not having a gradient is within 96% ($\sim$1.75-σ). So, while there are indications of a gradient, with this data-set we cannot exclude a flat trend within 2-σ.

The possible presence of a metallicity gradient has led us to look for subpopulations with different chemo-kinematic properties. We divided our data-set into a metal-rich (MR) and a metal-poor (MP) sample based on the median [Fe/H] value of the entire set (22 and 23 stars, respectively). We performed then a Bayesian maximum likelihood analysis (as done in Sect. 5.1.3) on both samples; the resulting parameters and evidences are reported in Table 5.2. We can see, independently from the fitted kinematic model, that the velocity dispersion values for the two samples are at $\sim$2-σ from each other. This tentative result of a spatially concentrated metal-rich population with a lower velocity dispersion compared to a spatially extended metal-poor one with a higher dis-

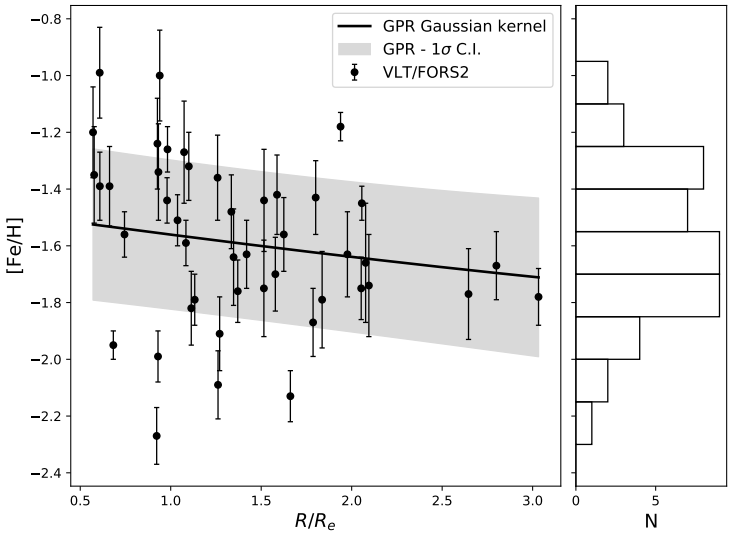

FIGURE 5.4— [Fe/H] as a function of the elliptical radius for Aquarius probable member stars. Error-bars show the uncertainties on the [Fe/H] measurements for the individual stars. The black solid line represents the result of a Gaussian process regression analysis using a Gaussian kernel and taking into account an intrinsic scatter; the grey band indicates the corresponding 1-σ confidence interval. The histogram on the right side represents the metallicity distribution of the probable members.

persion value, is similar to our findings for Cetus and Tucana (see Ch. 2 and 3), but also to what has already been found with a higher significance in several other dwarf galaxies of the LG (e.g. Tolstoy et al., 2004; Battaglia et al., 2006, 2008b; Amorisco & Evans, 2012b; Breddels & Helmi, 2014).

5.2 Chemo-kinematic properties of Local Group dwarf galaxies

Throughout this thesis we have presented results on the analysis of the isolated dwarf galaxies Cetus, Tucana, IC 1613 and Aquarius. They have different luminosities, SFHs and morphological types. Here we compare their retrieved

chemo-kinematic properties with those of the other LG dwarf galaxies, both isolated or satellites of the MW and M31.

5.2.1 Comparison of the kinematic properties

The kinematic analysis of the Cetus and Tucana dSphs showed that they are dispersion supported systems with no significant signs of internal rotation. This is in agreement with results for other dSphs that are satellites of either the MW or M31, as showed by the comprehensive analysis of Wheeler et al. (2017). In this work authors showed that in general dSphs have low rotation-to-dispersion ratios of $v_{\rm rot}/\sigma_{\rm v} < 0.5$ (measured at 90% of the extent of the data). A notable exception is the case of Andromeda II, one of M31's satellites, with a $v_{\rm rot}/\sigma_{\rm v} \sim 1.5$ showing, however, an unusual prolate rotation, probably the product of a recent merger (see Amorisco et al., 2014; Lokas et al., 2014; Fouquet et al., 2017). This is similar to the case of Phoenix, an isolated dTr, for which our collaborators also found evidences of prolate rotation with a comparable $v_{\rm rot}/\sigma_{\rm v} \sim 1.5$ (see Kacharov et al., 2017).

On the other hand, our study of the gas-rich IC 1613 and Aquarius dwarfs showed the presence of internal rotation in both cases, with $v_{\rm rot}/\sigma_{\rm v} \sim 0.5 - 1$ at one and two half-light radii, respectively. Thanks to our analysis, we have increased the statistical evidence for rotation in both systems over previous works (Kirby et al., 2014, 2017). They add to other dTrs/dIrrs for which values of $0.5 \lesssim v_{\rm rot}/\sigma_{\rm v} \lesssim 2$ have been observed with high significance (see Wheeler et al., 2017).

These results place strict limits on evolutionary models and, in particular, on the internal kinematics of dwarf galaxies progenitors. The lack of rotation in Cetus and Tucana, which spent most of their lifetimes in isolation, while in the past they may have interacted just once with the MW or M31 (based on their l.o.s. systemic velocity, see Lewis et al., 2007; Fraternali et al., 2009), is of particular importance for tidal stirring models. In this scenario, a gas-rich and rotation-supported progenitor (i.e. having $v_{\rm rot}/\sigma_{\rm v} \sim 3$) is expected to lose mass and angular momentum, and turn into a dSph through tidal and ram-pressure stripping aided by heating due to the ionizing UV-cosmic background (see Mayer, 2010, review). These models require special accretion conditions and orbital times together with a specific range of pericentric distances from the host-galaxy to allow the progenitor dwarf galaxy to achieve a complete transformation into a dSph, as shown in Kazantzidis et al. (2011). However, none of the simulations ran by Kazantzidis et al. (2011) achieved a complete transformation in a single pericentric passage, neither when the combined effects of ram-pressure stripping and stellar feedback driven by supernova winds is taken

into account (Kazantzidis et al., 2017). The presence of a shallow (or cored) dark matter density profile could instead increase the probability of transformation into a dSph-type object, though systems are required to evolve in low eccentricity and/or large pericentric distance orbits to survive the tidal interaction, and may still be left with internal rotation and high flattening residuals (i.e. $v_{\rm rot}(r_{1/2})/\sigma_{\rm v} \sim 0.6$ and $e \sim 0.5$, see Kazantzidis et al., 2013).

Although it is hard to test the hypothesis of a cored profile in Cetus and Tucana due to the limited size of our datasets, we already shown during the kinematic analysis that if rotation is actually present in these systems it would be at a level of $v_{\rm rot}(r_{1/2})/\sigma_{\rm v} < 0.5$, despite their high ellipticity (i.e. $e \sim 0.5$). Furthermore, Cetus and Tucana are devoid of neutral gas (at least down to a HI mass of $1.5 \times 10^4 M_{\odot}$ for the latter), and move on very radial orbits with respect to the LG's barycentre, being, if bound, close to their apocentre (Lewis et al., 2007; Fraternali et al., 2009). Therefore, it is hard to explain the evolution of Cetus and Tucana, and their apparently complete transformation into dSphs, according to current tidal stirring models. We note that our results only partly limit the role of the environment in shaping the evolution of these systems, but rather question the initial hypothesis of tidal stirring models on the kinematic status of dwarf galaxy progenitors.

In this regard, we note that another prediction of tidal stirring models is that at greater distances from MW or M31, dwarf galaxies should show higher rotation support ratios (Kazantzidis et al., 2011). Thanks to our analysis of IC 1613 and Aquarius, we confirm instead the conclusions made by Wheeler et al. (2017) for which even the isolated dwarfs of the LG (with a luminosity $L_V < 10^8 L_{\odot}$) have kinematics largely dominated by random motions (i.e. with $0.5 \lesssim v_{\rm rot}/\sigma_{\rm v} \lesssim 2$). In fact, adding our results to those of Wheeler et al. (2017), it does not appear a clear correlation of $v_{\rm rot}/\sigma_{\rm v}$ with distance from the closest host-galaxy (see in particular their Fig. 3). This is in contrast with the initial hypothesis of tidal stirring models that progenitors dwarfs are fast-rotating flat-systems whose properties should resemble those of the present-day dIrr population. Wheeler et al. (2017) concluded then that progenitor dwarfs may be instead rather thick and only mildly rotation-supported.

While the Wheeler et al. analysis was done examining RGB stars of all ages, Leaman et al. (2017) provided an in-depth analysis about the velocity dispersion profile as function of stellar age for a sub-sample of LG's galaxies. They showed that the higher velocity dispersion values observed for the older stars are related to the fact that they were born from a turbulent interstellar medium, which decreased its velocity dispersion over time due to gas exhaustion. Systems in the mass range of dwarf galaxies are also affected by internal scattering that increase their $\sigma_{\rm v}$ at all ages.

While future high-resolution cosmological simulations of the LG will help to shed a light on the above conclusions, from an observational point of view it would be important to better constrain the stellar rotation signal for those systems in which this detection resulted more uncertain. This is particularly true for those MW's satellites that have been reported hosting mild velocity gradients, like Carina, Fornax, Sextans and Sculptor (Battaglia et al., 2008a; Walker et al., 2008; Battaglia et al., 2011). These values are in part affected by perspective effects due to the streaming motion of these systems around the MW (see discussion in the review of Battaglia et al., 2013). We postpone the analysis to a future work that uses Gaia-DR2 data to pinpoint the effect of perspective motion in classical MW's satellites.

5.2.2 Comparison of the dynamical mass estimation

We continue comparing the dynamical mass estimation made for our sample, or equivalently their calculated circular velocities, to those of other LG dwarf galaxies.

In Fig. 5.5 (bottom panel), we show the position of LG dwarf galaxies on the $V_{\rm circ} - r_{1/2}$ plane using the compilation of Kirby et al. (2014), with our updated values for Cetus, Tucana, IC 1613 and Aquarius. Navarro-Frank-White (NFW) halos sampled from the halo mass concentration relation of Dutton & Macciò (2014) are also shown, colour-coded by $V_{\rm max}$. The NFW circular velocity curves are generated for 300 mock halos, which are uniformly sampled in virial mass between $8.5 \leq \log M_{\rm vir} \leq 11$, and follow the redshift zero halo mass concentration relation from Dutton & Macciò (2014) with scatter of $\sigma_{\rm lnc} = 0.25$. These halos are shown in Fig. 5.5 (top panel), colour-coded by their $V_{\rm max}$.

In Fig. 5.6, to be comprehensive, we further reproduced plots where the mock halos are colour-coded by concentration, or virial mass. In the top panel, the LG dwarf galaxies are colour-coded according to their stellar mass; a probable correlation is visible between the circular velocity and the stellar mass. In the bottom panel, observed dwarf galaxies with virial masses estimated from dynamical modelling (Leaman et al., 2012; Read & Erkal, 2019) are also colour-coded, illustrating the tension between predicted and observed density profiles.

We stress how the reported value for Aquarius and IC 1613 are only lower limits due to their unknown stellar inclination angle. While this correction would be rather small for Aquarius, assuming that the inclination angle is equal to that of the HI component, for IC 1613 this correction instead would be significant, considering that it's a galaxy placed almost face-on. If we assume an $i = 15$ deg (as discussed in Read et al., 2016), the circular velocity of IC 1613 would increase to $V_{\rm c} \sim 25\,{\rm km\,s^{-1}}$, closer to similarly massive dwarf galaxies (see

Fig. 5.6, bottom panel).

In general, it is evident how the circular velocities from our sample add to those of the other dwarfs of similar stellar mass (see Fig. 5.6, bottom panel), which appear to reside in dark matter halos with lower $V_{\rm max}$ (or concentration c) than predicted. This is the so-called "too-big-to-fail" problem (see e.g. Boylan-Kolchin et al., 2012). In fact, pure N-body cosmological simulations in the framework of Λ cold dark matter (Λ-CDM) predict that the dwarf galaxies of the LG should live in denser halos than those inferred from observations. In particular, this means that dwarf galaxies with stellar masses between $10^5 \lesssim M_*/M_\odot \lesssim 10^8$ should live in dark-matter halos with $V_{\rm max} > 30$ km s^{-1}, while their observed circular velocities point to $V_{\rm max} < 30$ km s^{-1}. The generic observation is that dwarf galaxies in this stellar mass range have inferred central halo masses $\sim 50\%$ smaller than those predicted by dark matter only simulations (see the review of Bullock & Boylan-Kolchin, 2017, and references therein).

Advanced numerical hydrodynamic simulations taking into account the effect of stellar feedback have shown that the formation of cored profiles in many dwarf galaxies (specifically for those having $M_* \approx 10^6 M_\odot$) could potentially solve the too-big-to-fail problem, while for less massive systems environmental effects (i.e. tidal and ram-pressure stripping, disk shocking) have been invoked (Bullock & Boylan-Kolchin, 2017, but also Zolotov et al., 2012; Arraki et al., 2014; Brooks & Zolotov, 2014; Brook & Di Cintio, 2015; Wetzel et al., 2016; Sawala et al., 2016; Dutton et al., 2016; Fattahi et al., 2018; Buck et al., 2019). However, these effects do not fully account for the fact that also the isolated low-mass dwarf galaxies (like Tucana and Aquarius) add to the too-big-to-fail problem. Furthermore, recipes for stellar feedback depend on several adopted parameters, which may vary among different simulations. Clearly, future computational efforts need to be invested into exploring this low-mass galactic regime (i.e. $M_* < 10^6 M_\odot$).

5.2.3 Comparison of the metallicity properties

It is known that the average metal content of a galaxy correlates with its stellar luminosity (see Kirby et al., 2013b, and references therein). Local Group dwarf galaxies follow a linear relation in the stellar luminosity-metallicity plane, and the isolated systems studied in this work, as shown in Fig. 5.7, are not an exception. Their average metallicities fall within the scatter of the relation, except for Cetus which is found, however, at < 2-σ. We note that our metallicities were calculated applying the CaT calibration method, while those of Kirby et al. (2013b) showed in Fig. 5.7 were obtained by direct fitting of the Fe I absorption lines. The fact that our reported [Fe/H] values are close to those expected for their luminosity, shows how eventual variations in the [Ca/Fe] ratio, inherent to

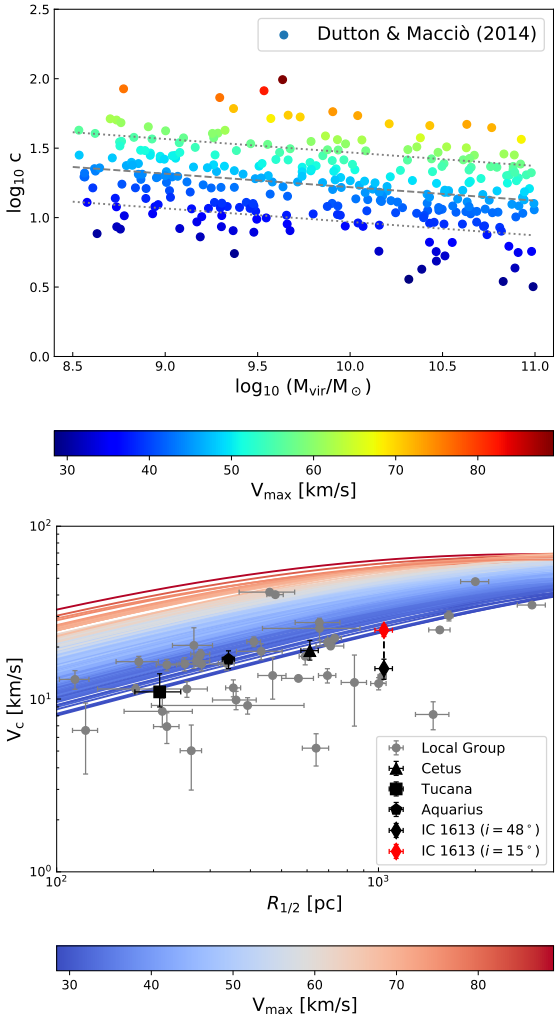

FIGURE 5.5— Top panel: distribution of NFW halos in virial mass − concentration plane used to construct circular velocity profiles in the bottom panel and Fig. 5.6. Halos are colour-coded by $V_{\rm max}$. Bottom panel: circular velocity at half-light radius (under assumption of flat $\sigma_{\rm v}$ profile, isotropy, and sphericity) for Local Group galaxies from Kirby et al. (2014) and the isolated dwarfs of our sample. Circular velocity profiles for NFW halos are shown colour-coded by $V_{\rm max}$. Local Group galaxies are shown as grey filled circles. Cetus, Tucana, Aquarius and IC 1613 are marked as black triangle, square, pentagon and diamond, respectively; they occupy locations comparable to other dwarfs of similar stellar mass (see also Fig. 5.6). For IC 1613, the $V_{\rm c}$ value is also reported assuming the inclination value from Read et al. (2016), marked with a red diamond.

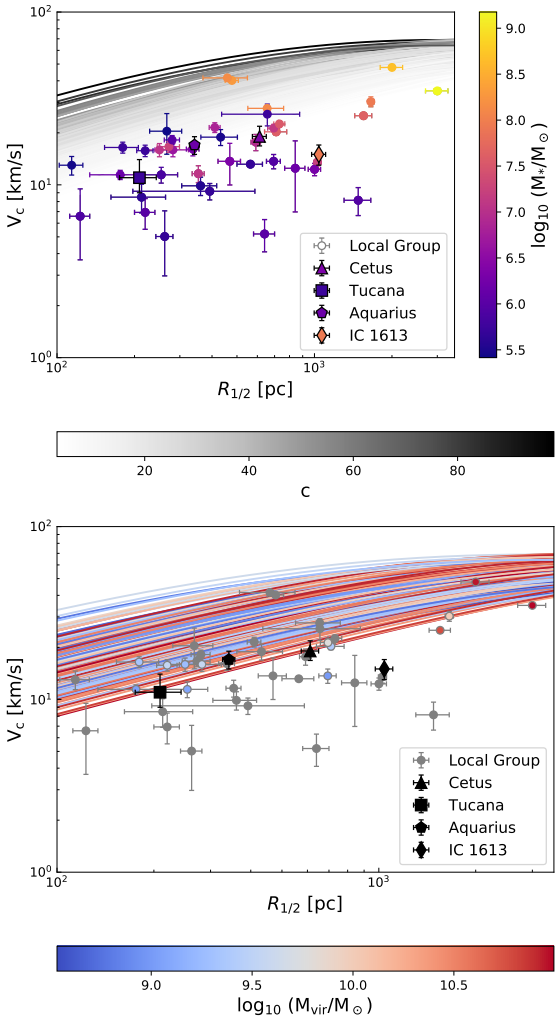

FIGURE 5.6— Same as Fig. 5.5, but with halo circular velocity profiles colour-coded by concentration (top) and virial mass (bottom). Top panel: the Local Group dwarf galaxies are colour-coded according to their stellar mass; a probable correlation is visible between the circular velocity and the stellar mass. Bottom panel: the colour-coded dots that follow the same colour schema as the halo virial mass profiles are Local Group dwarf galaxies for which virial masses were obtained from dynamical modelling (Leaman et al., 2012; Read & Erkal, 2019).

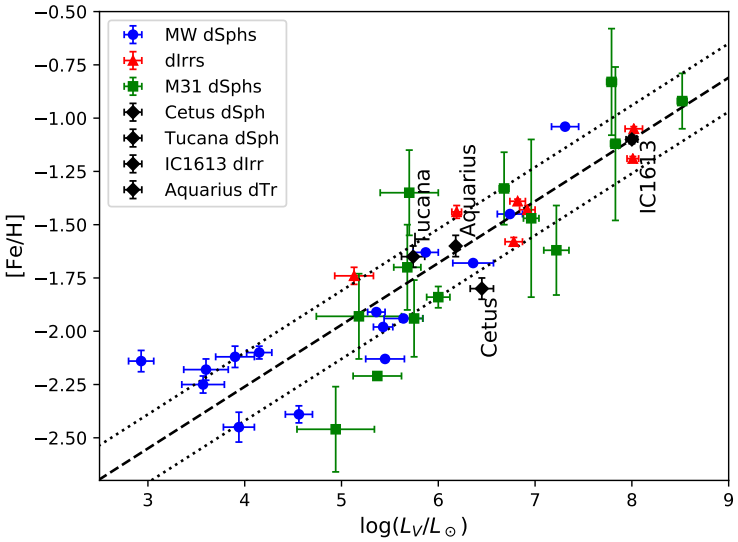

FIGURE 5.7— Stellar luminosity-metallicity relation for Local Group dwarf galaxies. Blue circles represent Milky Way dSph satellites; green squares are M31's dSph satellites; green diamonds are isolated dIrrs; all values as reported by Kirby et al. (2013b). Black diamonds indicate the position of Cetus, Tucana, IC 1613 and Aquarius based on the average [Fe/H] derived in this work. The dashed line is the least-square fit calculated by Kirby et al. (2013b) for the dIrrs and MW's dSphs, while the dotted lines show the rms about the linear fit.

our calibration method, do not move our measurements far from the relation, considering the scatter around it.

For each of the systems analysed in this thesis, we have explored the spatial variation of their [Fe/H] measurements. To summarize, we found a marginally significant metallicity gradient only in the case of Cetus, while the other systems showed milder values, consistent with a lack thereof. It is true, however, that for Tucana and Aquarius we would benefit in the future of larger spectroscopic datasets to increase in particular our number statistics in the outskirts of these systems (i.e. for $R \gtrsim 3\,R_{\rm e}$) where we expect to find mainly metal-poor stars. If we were to confirm the presence of a metallicity gradient in these isolated systems, we would further support the hypothesis that this is an intrinsic char-

acteristic of LG dwarf galaxies, as has been observed in Phoenix (Kacharov et al., 2017) and VV 124 (Kirby et al., 2013a), and not the main product of interactions with a large host, such as the MW or M31.

Numerical hydrodynamic simulations and theoretical works have shown that for an isolated dwarf galaxy factors like its star formation history, mass, angular momentum, and specific accretion events, are expected to contribute to producing a radial metallicity gradient (e.g. Marcolini et al., 2008; Schroyen et al., 2013; Benítez-Llambay et al., 2016; Revaz & Jablonka, 2018). For satellite galaxies, it is possible that tidal stripping effects could affect the strength of such gradients (see Sales et al., 2010).

In this context, we compared our results with those obtained from publicly available spectroscopic catalogues of red giant stars in LG dwarf galaxies. We made sure to analyse systems with more than 50 individual measurements. We used metallicity values from the compilation of MW's satellite and isolated dwarf galaxies of (Kirby et al., 2013b), except for Draco (Walker et al., 2015), Fornax (Battaglia et al., 2006), Sculptor (Battaglia & Starkenburg, 2012, applying the membership defined in Iorio et al., 2019), Sextans (Cicuéndez et al., 2018), and the systems we have analysed in this thesis (i.e. Cetus, IC 1613 and Aquarius). We further included Carina (Koch et al., 2006), VV 124 (Kirby et al., 2013a), Leo A (Kirby et al., 2017), WLM (Leaman et al., 2013), and Phoenix (Kacharov et al., 2017). For the Andromeda's satellites we only included M32, NGC 205, NGC 185, NGC 147, Andromeda VII, Andromeda II (Ho et al., 2015), together with Andromeda VII (Kirby et al., 2020). For homogeneity, the celestial coordinates, distances, luminosities (as visual absolute magnitudes), morphological types, and structural parameters of all the considered systems were taken from McConnachie (2012).

We applied the membership criteria established in each of the works cited above. Only for Draco we performed a broad membership selection like in Walker et al. (2015, see their Fig. 10) and then refined it by cross-correlating with the *Gaia*-DR2 catalogue, selecting those targets co-moving with Draco.

We then examined the radial variation of the metallicity values as a function of the elliptical radius. To this end, we performed a homogeneous analysis applying the Gaussian process regression (GPR) method, used in previous chapters, to all selected datasets. We recall that the analysis returns a smooth function with an associated error-bar that takes into account the intrinsic scatter of the data. From the GPR analysis we saved two parameters: the maximum metallicity gradient and the metallicity difference. Both parameters were calculated on the returned smooth function. The first was obtained by performing a linear fit between the initial value and the minimum (if present) of the GPR curve. The second is simply the difference between these two points.

We scaled the recovered metallicity gradients by the half-light radius R_e. We note that this is a possible normalization, while other works in the literature have reported values normalized, for example, to the King's core radius R_{core} (e.g. Leaman et al., 2013). We are also aware about the possible bias introduced by using structural parameters that has not been obtained from homogeneous photometric data: for example, the half-light radius for the brightest dwarfs in our sample were adapted by McConnachie (2012) from the isophotal radius R_{25} obtained in B-band photometry, which preferentially traces the young stellar population, while structural parameters for the early-type dwarfs are generally obtained from the older populations. Since the young stellar population is typically less spatially extended, the effective radii for the brightest dwarfs could be underestimated, which implies that the corresponding metallicity gradients could be overestimated. As shown below, this is a minor issue for the brightest dwarfs, due to their shallow metallicity gradients.

We further stress that, although we used the same method for all systems, metallicities were obtained in different ways depending on the considered study, namely by direct fit of the available Fe I absorption lines (works of Kirby et al.), by full spectral-fitting using synthetic spectra (Walker et al., 2015), or applying the CaT calibration method (all the others). We have already discussed the validity of the CaT method applied to dwarf galaxies (see Ch. 1). Being an empirical method, different calibrations has been proposed in literature and the selected datasets are not homogeneous in this sense. However, differences between calibration methods are rather small and mostly limited to systematic shifts, in the range $-2.5 < [Fe/H] < -0.5$ where most of dwarf galaxies measurements are distributed (see e.g. discussion in Battaglia et al., 2008b). Since we are interested in analysing the radial variation and internal differences of the metallicity measurements in the selected dwarf galaxies, we do not expect the different calibration methods to be a significant issue. Furthermore, we have showed in the case of Aquarius a general agreement with the work of Kirby and collaborators comparing [Fe/H] measurements of common targets (see details in Hermosa Muñoz et al., 2020). Regarding the Draco dataset of Walker et al., the same authors showed a general agreement with previous measurements taken by Kirby et al. (2013b). The same conclusions were reached by Ho et al. (2015), comparing common measurements with Kirby et al. (2011). Therefore, we continued with our analysis bearing in mind that differences between quoted values shall be attributed only marginally to the different [Fe/H] methods applied.

In Fig. 5.8 (top panel) is shown the result of the GPR analysis on the whole sample of dwarf galaxies. It is already visible how the majority of analysed systems show a declining radial metallicity trend, while others show almost flat profiles. For comparison, we also show results from the same analysis ran in

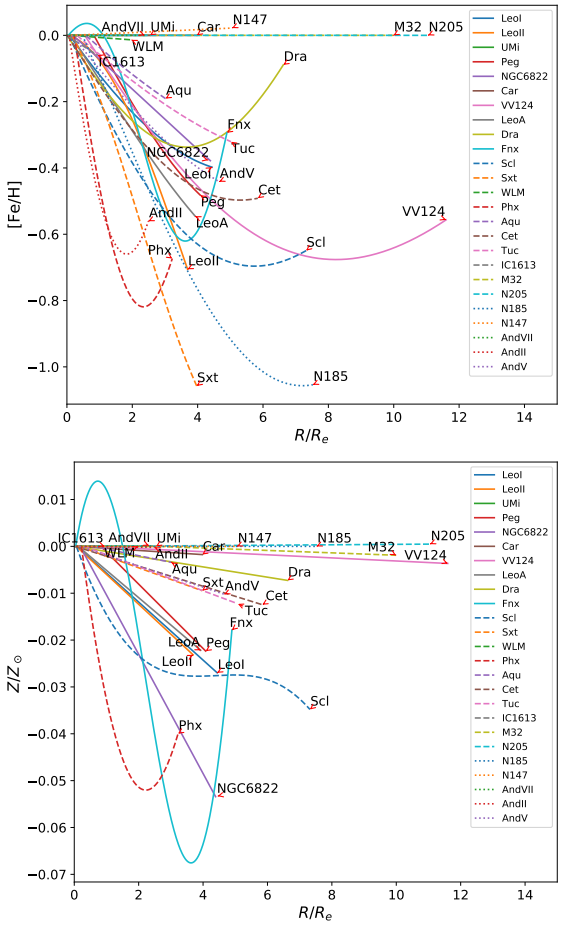

FIGURE 5.8— Results from the Gaussian process regression analysis using a Gaussian kernel and taking into account the intrinsic scatter of the analysed systems. Each dwarf galaxy has a unique combination of colour and line-style. Radial profiles are normalized to their central metallicity value. *Top panel:* using [Fe/H] metallicity values. *Bottom panel:* using values in terms of the linear metal fraction $Z/Z_\odot$.

terms of the linear metal fraction $Z/Z_{\odot}$. From the bottom panel of Fig. 5.8, we see how many systems still show a decreasing trend, despite some notable exceptions: for example, And II, which shows the strongest gradient in [Fe/H], here has a much shallower value; quite the opposite happens for NGC 6822. We attribute this discrepancy to the change of scale, from logarithmic to linear, which exaggerate the errors associated to metal-richer values, leading to these unexpected results. In this case we just want to draw attention to the differences that could arise by moving the analysis onto the linear metallicity scale. From here on, for continuity with other studies reported in the literature, we focus on the results obtained using the logarithmic metallicity scale.

We continue then by showing how the derived metallicity parameters (maximum gradient and difference) compare to other measured quantities for the considered sample of dwarf galaxies.

Figure 5.9 shows the absolute visual magnitude of the considered dwarfs as a function of the calculated metallicity gradient (top panel) and metallicity difference (bottom panel), colour-coded according to being found in isolation or as satellites of the MW or M31. In Fig. 5.10 instead we show the same plots, but colour-coded depending on whether they had a fast star formation history or a slow one, following the definition of Gallart et al. (2015) (see also Ch. 1).

It is visible from the top panel of both figures how the most luminous dwarfs (i.e. $M_V < -14$) show shallow gradients, with 5/7 objects having values compatible with a flat trend within the errors. From $M_V \gtrsim -13$ systems start to show a large scatter. In particular, those dwarfs of medium luminosity (i.e. $-13.5 < M_V < -10$) show a smaller scatter, with 8/10 objects tightly packed around $\frac{\mathrm{d[Fe/H]}}{\mathrm{dR_e}} \sim -0.1$ dex R_e^{-1}. Looking at the bottom panel of these figures, it is evident how in general the most luminous systems tend to have lower metallicity difference values, compared to the least luminous ones. This is in agreement with what shown in the upper panels of the same figures, that the dispersion in the metallicity gradient values increases as the luminosity (or stellar mass) decreases.

From Fig. 5.9 it is evident that this luminosity trend does not strongly correlate with the environment of the analysed systems, since there are no clear differences between satellite or isolated dwarfs, neither in terms of gradients nor of metallicity differences. This limits the role of the environment, intended as a prolonged interaction with a host-galaxy, as the lead actor in the formation of strong radial metallicity gradients in LG dwarf galaxies. We cannot exclude though that tidal effects may contribute in shaping the strength of metallicity gradients. In fact, satellites show a higher scatter both in the metallicity gradient and difference values with respect to the isolated dwarfs. Furthermore, 4/5

systems with the strongest gradients (i.e. $\frac{\mathrm{d[Fe/H]}}{\mathrm{dR_e}} < -0.2$ dex R_e^{-1}) are satellites. However, we must point out that And II, Phoenix, and probably Sextans, experienced a past merger event (see e.g. Amorisco et al., 2014; Kacharov et al., 2017; Cicuéndez & Battaglia, 2018; but also Benítez-Llambay et al., 2016, on the role of mergers in the outside-in formation of dSphs). We recall how the case of And II is remarkably similar to that of Phoenix (Kacharov et al., 2017): both systems show very pronounced gradients and a peculiar prolate rotation, although they live in different environments.

To further investigate the role of the environment, we also checked if the calculated quantities for the MW's satellites correlate with their first infall time or their orbit eccentricity. These parameters should be informative on the combined action of tidal and ram-pressure stripping. Referring to the works of Fillingham et al. (2019) and Miyoshi & Chiba (2020)[1], in both cases we did not find a clear trend within the quoted quantities. We further looked at the quenching time provided by Fillingham et al. for the MW's satellites, defined as the difference between the first infall time and the time at which 90% of the stars were formed (i.e. t_{90}), again finding no clear correlation. This reinforce our previous conclusions on the limited role of tidal and ram-pressure stripping as the main cause of the formation of metallicity gradients.

To better understand the relation between SFH duration and the strength of metallicity gradients, we compared our measurements with the t_{90} parameter, that indicates the look-back time at which each dwarf galaxy formed 90% of its total stellar mass. We used in this case the compilation of Weisz et al. (2015), except for those dwarfs analysed by Albers et al. (2019). It appears from Fig. 5.11 that the observed trend in the analysed systems tentatively correlates with the duration of their star formation histories. The brightest dwarfs, for which we measured metallicity gradients mainly consistent with zero, are those with the most sustained and continuous periods of star formation (Weisz et al., 2014; Gallart et al., 2015; Albers et al., 2019); NGC 147, 185, 205, 6822, IC 1613 and WLM also show clear evidences of internal rotation, with $v_{\mathrm{rot}}/\sigma_{\mathrm{v}} \gtrsim 0.5$ (see Leaman et al., 2013; Wheeler et al., 2017; this work). This is in agreement with results from hydrodynamic simulations of isolated dwarfs ran in a cosmological contest, like those of Schroyen et al. (2013) and Revaz & Jablonka (2018). These authors showed how the combination of a continuous SFH and rotation support in the brightest dwarfs help the spatial stellar mixing and prevent the formation of strong metallicity gradients.

[1]Both works exploit *Gaia*-DR2 data, although they differ into modelling the MW-like potential. The former study used the Phat ELVIS suite of high-resolution, cosmological, zoom-in simulations, while the latter performed an analytical modelling of a time-varying gravitational potential.

The least luminous dwarfs are those with the shortest SFHs, having produced the majority of their stars during an initial period of star formation, with the only exception of Carina that have episodically formed stars through time (see Weisz et al., 2014; Gallart et al., 2015). In these systems, the short SFH combined to dynamical heating by internal feedback should prevent the formation of strong gradients; an early merger event, however, could lead to the formation of a relatively strong and long-standing gradient (Revaz & Jablonka, 2018; but see also Benítez-Llambay et al., 2016). Indeed, this is in agreement with the large scatter we observe for the metallicity properties of the faintest dwarfs.

The medium luminosity dwarfs have instead a variety of SFHs: short, but in general more extended than the least luminous dwarfs, for And II, Cetus, Sculptor and VV 124 (Jacobs et al., 2011; Gallart et al., 2015); delayed for Aquarius and Leo A (Cole et al., 2014); extended and only recently stopped for Leo I and Fornax (Gallart et al., 2015). An extended SFH is expected to reinforce the metallicity gradient (Revaz & Jablonka, 2018) and indeed dwarf galaxies in this luminosity range, as seen in Fig. 5.10, show a smaller scatter around ~ 0.1 dex R_e^{-1}.

As shown in Fig. 5.11, it is visible from the top panel how systems with a prolonged SFH show a lower scatter than those that stopped to form stars early-on. Combined with the above results, it appears how systems of large luminosity seem to have more similar strengths of their metallicity gradients, while at lower luminosity there is a larger variety of values. In general, the role of the environment seems limited, although we cannot exclude that effects such as tidal and ram-pressure stripping may have an impact in shaping the strengths of metallicity gradients. What seems clear instead is the role of past mergers in steepening the observed gradients.

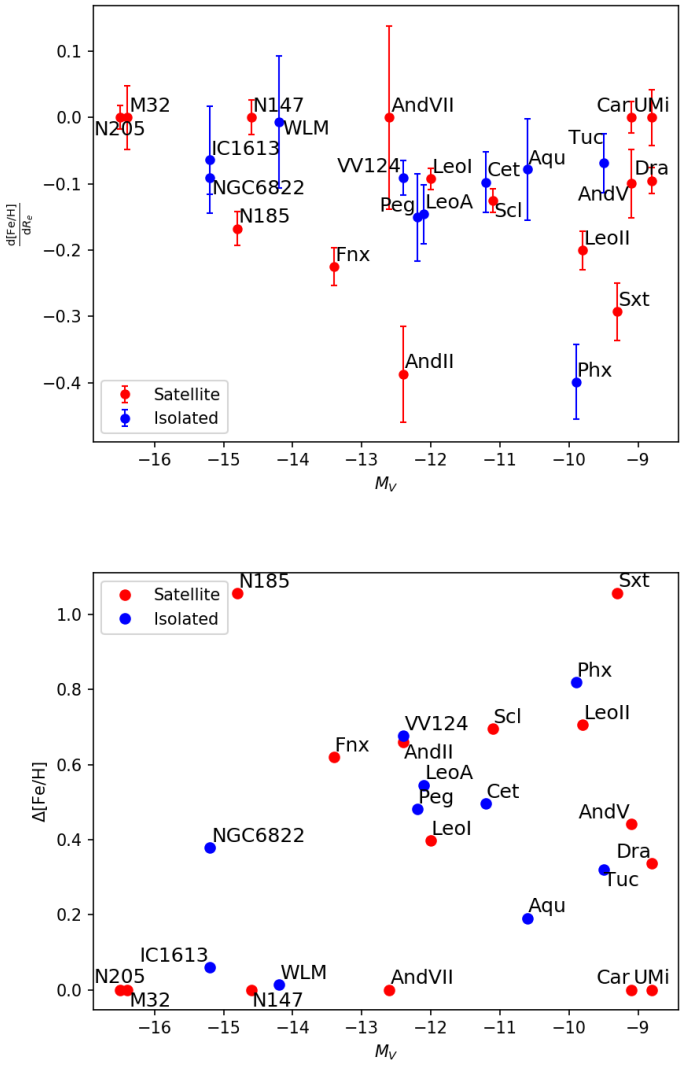

FIGURE 5.9— *Top:* Absolute visual magnitude vs. maximum metallicity gradient. Dwarfs are colour-coded depending on whether they are MW's satellites (red circles) or isolated dwarfs (blue circles). *Bottom*: same as above but as a function of the maximum metallicity difference.

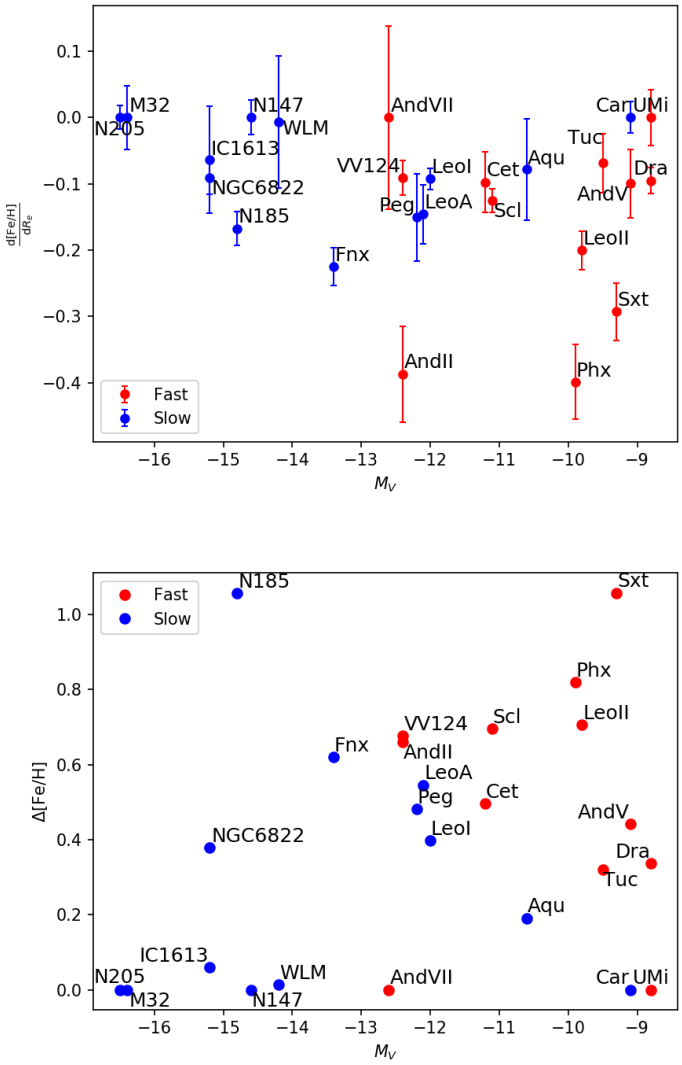

FIGURE 5.10— *Top:* Absolute visual magnitude vs. metallicity difference. Dwarfs are colour-coded depending on whether they had a fast star formation history (red circles) or a slow one (blue circles), according to the definition of Gallart et al. (2015). *Bottom*: same as above but as a function of the maximum metallicity difference.

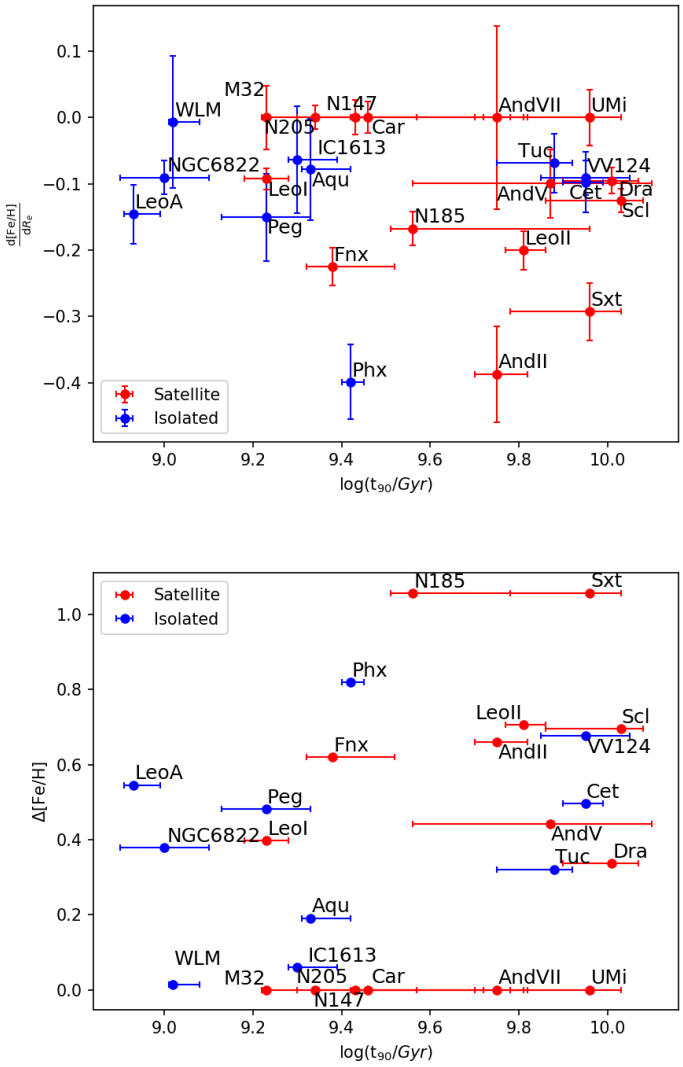

FIGURE 5.11— Look-back time at which each dwarf galaxy formed 90% of its total stellar mass vs. its maximum metallicity gradient (top) or its metallicity difference (bottom). Colour-coding as for the previous two figures.

5.3 Conclusions

In this chapter we present results from the chemo-kinematic analysis of the isolated dwarf galaxy in Aquarius, along with a comparative analysis of the properties of Local Group dwarf galaxies.

The analysis of Aquarius led to the identification of 45 probable-member stars, which doubles the available samples in the literature. While the systemic velocity and velocity dispersion resulted in agreement with past measures, we also find evidences of a linear rotation signal implying a $v_{\rm rot}/\sigma_{\rm v} \sim 1$ at twice the half-light radius. What is more, the detected velocity gradient is of comparable magnitude as that of the HI gas, but the rotation signals from the two components point in opposite directions. This is the first time that a misaligned rotation is detected down to the luminosity of Aquarius. In the LG, a similar phenomenon has been detected only for the brighter NGC 6822 (Demers et al., 2006). The metallicity properties are normal for a galaxy as luminous as Aquarius, while we detect the tentative presence of a radial metallicity gradient and of two chemo-kinematically distinct sub-populations that would need, however, further data to be confirmed.

The comparison of the kinematic properties of LG dwarf galaxies shows how Cetus and Tucana add to other dSphs for which have been reported no significant signs of internal rotation, make it difficult for tidal stirring models to explain their evolution and current kinematic status. We further show how the internal kinematics of IC 1613 and Aquarius is similar to that of other isolated gas-rich dwarf galaxies with $0.5 \lesssim v_{\rm rot}/\sigma_{\rm v} \lesssim 2$. This reinforce the conclusions of Wheeler et al. (2017), which found no fast rotators (i.e. $v_{\rm rot}/\sigma_{\rm v} \sim 3$) among the isolated dwarfs of the LG, proposing that the progenitor dwarfs should have been rather thick and only mildly rotation-supported (see also Leaman et al., 2017).

The dynamical mass estimation for the isolated systems analysed in this thesis show how they add to the population of LG dwarf galaxies (both isolated and satellites) that appear to reside in dark matter halos with lower maximum circular velocities (or central concentration) than predicted. This is the so-called too-big-to-fail-problem (e.g. Boylan-Kolchin et al., 2012). Our findings reinforce the conclusions of Kirby et al. (2014) that this is a common issue among LG dwarf galaxies, independently of the environment in which they reside.

The comparison of metallicity properties among LG dwarf galaxies focuses on the results of an homogeneous analysis we made, looking for a radial variation in their metallicity measurements. We found that the formation of mild metallicity gradients is common among the considered systems, despite the large error bars found in some cases, and it seems independent from their environ-

mental status. In particular, it appears how systems of large luminosity, which also had a prolonged star formation history, have metallicity gradients of similar strengths, while at lower luminosity the variety of values, but also of SFHs, is larger. In general, the environment role seems limited, although we cannot exclude it may have an impact in shaping the strengths of metallicity gradients. On the other hand, those systems showing the steepest gradients may had suffered of past mergers.

Authorship

The first part of this chapter is based on the published work of Hermosa Muñoz et al. (2020), for which I have already stated my contribution in the first section. The second part of the chapter is dedicated to a new analysis that I have carried out to place the results of this thesis in the wider context of the Local Group systems.

6

Conclusions

In this thesis we have studied a sample of dwarf galaxies from the Local Group (LG) found in isolation. The systems examined were two early-types, Cetus and Tucana, and two late-types, IC 1613 and Aquarius. For each of them we analysed sizeable samples of stars from spectroscopic observations, obtaining accurate line-of-sight velocity and metallicity measurements from individual stars distributed over a wide-area. We were then able to determine the kinematic and chemical properties of these systems, together with their internal mass content. The obtained results were finally compared to those of the other LG dwarf galaxies.

6.1 Stellar chemo-kinematics of the Cetus dwarf spheroidal galaxy

In Chapter 2 we presented results from the analysis carried out on a spectroscopic dataset obtained with the Very Large Telescope (VLT) FORS2 instrument for 80 individual red giant branch (RGB) targets in the Cetus dSph, of which 54 resulted to be probable members.

The kinematic analysis showed that Cetus is a mainly pressure-supported system ($\bar{v}_{\rm hel} = -78.9^{+1.7}_{-1.6}$ km s^{-1}, $\sigma_{\rm v} = 11.0^{+1.6}_{-1.3}$ km s^{-1}) with no significant signs of internal stellar rotation. Our results were generally in agreement with those previously reported by Kirby et al. (2014), despite some differences in the obtained values, for which we were able to recover the source of discrepancy. In addition, extensive mock tests showed that the exclusion of a significant rotation

signal inside the half-light radius is robust, indicating that the presence of an eventual rotational component would be weak and not capable of producing the observed galaxy ellipticity.

The dynamical mass estimation showed that Cetus is a dark matter dominated system, with a mass-to-light ratio of $M_{1/2}/L_V \sim 25\,M_\odot/L_\odot$ within the half-light radius. Our results add Cetus to the growing scatter in stellar-dark matter halo properties in low-mass galactic systems (e.g. Brook & Di Cintio, 2015; Buck et al., 2019).

Results from the chemical analysis showed that Cetus is a metal-poor system with a significant metallicity spread. We detected a radial [Fe/H] gradient (with a 2-σ significance) comparable to other systems of similar luminosity but inhabiting very different environments. We also reported the tentative presence of two chemo-kinematically distinct stellar populations.

The presence of a stellar population gradient was confirmed by our analysis of an ancillary deep photometric dataset obtained with the Subaru/SuprimeCam instrument. The same photometric data helped us to reveal the presence in the direction of Cetus of a foreground population that most likely belongs to the Sagittarius stream.

6.2 The Tucana dwarf spheroidal galaxy: not such a massive failure after all

Chapter 3 was devoted to the study of the Tucana dSph, based on the analysis of several spectroscopic samples of individual RGB stars. In particular, we homogeneously analysed a novel set of 50 individual RGB candidates collected during P91 with the VLT/FORS2 instrument, together with two re-reduced datasets from the literature, namely the VLT/FORS2 sample from Fraternali et al. (2009, F09) and the VLT/FLAMES one by Gregory et al. (2019, G19). The number of probable members from the P91 dataset alone doubled those reported by F09 and G19.

The complete re-reduction and analysis of the literature data was carried out because of the significant differences between the systemic velocity we derived for the P91 dataset and those reported by the previous studies, supported by the presence of shifts in the radial velocities of stars common to the sample. Following our homogeneous analysis, we found excellent agreement between velocity measurements from the three dataset, leading to a systemic velocity stable around 180 $\mathrm{km\,s^{-1}}$.

When considering high-probable members, either from the P91 dataset alone and as a combination with the other sets, the velocity dispersion of Tucana

was consistently around 6 $\mathrm{km\,s^{-1}}$. The inclusion of lower probability members increased the velocity dispersion value, but without exceeding the 10 $\mathrm{km\,s^{-1}}$. Therefore, the velocity dispersion of Tucana resulted significantly lower than what previously reported by F09 and G19 ($\sim 15\ \mathrm{km\,s^{-1}}$). In addition, we found no significant evidences for internal rotation, in contrast with results from F09 and G19 who reported a maximum rotational velocity of $\sim 10 - 15\ \mathrm{km\,s^{-1}}$. We conducted several mock tests, ruling out the presence of a rotation signal as high as that reported in literature. However, a lower level of rotation is still possible, although it seems improbable that Tucana is a fast rotator.

The new value of the velocity dispersion led to a dynamical mass $M_{1/2}$ much lower than what previously reported. This implies that Tucana is neither an exception to the too-big-to-fail problem, nor does it live in a very centrally dense dark-matter-halo, as claimed by G19.

The chemical analysis carried out on the FORS2 data showed that Tucana is mainly metal-poor with a significant scatter in [Fe/H]. We found hints of the presence of a radial metallicity gradients (although not statistically significant) and of two chemo-kinematically distinct stellar populations (with a 2-σ significance). The addition of new data, in particular outside the central region, could help to put these results on a firmer ground.

6.3 An aMUSEing view of the isolated dwarf irregular galaxy IC 1613

In Chapter 4 we presented results from the chemo-kinematic study of the IC 1613 dIrr. The analysis was based on a new spectroscopic dataset obtained from three VLT/MUSE pointings distributed along the optical major axis of the galaxy. We collected a large dataset of ~ 2000 extracted sources, selecting the stellar objects for their spectral classification and analysis.

We were able to perform a spectroscopic classification, with an accuracy on the effective temperature better than 500 K, for 824 stars. We found a major component of K-type stars, together with representatives from all the other types (from O- to M-). We also identified a sample of hot emission-line stars, along with one of carbon-stars, which were analysed separately.

The determination of radial velocities was made with a pixel-to-pixel analysis that led accurate measurements (i.e. $\delta_{\mathrm{v}} < 20\ \mathrm{km\,s^{-1}}$ and abs(skewness) < 0.5) for 838 objects. We performed on this sample a probability-weighted analysis exploring different kinematic models. The identified 823 probable member stars resulted to linearly rotate along the optical major axis. This is the first time that the stellar rotation signal is confirmed in this galaxy with great significance.

Stars resulted to follow the velocity field of the neutral HI component (Oh et al., 2015), although they appear to rotate at a lower pace than the gas. Both the systemic velocity and velocity dispersion resulted in agreement with literature values (e.g. Kirby et al., 2014).

The kinematic analysis of the individual fields confirmed the presence of stellar rotation, while the radial velocity dispersion profile showed a decreasing trend that flatten moving outward. On the other hand, the kinematics of different selected stellar populations, showed in general a coherent picture with the analysis of the main sample. However, we found that the selected sub-sample of blue-loop showed radial velocities which were systematically lower than those of the other selections, an issue that we will better explore in the future and might be related to the variable nature of (part of) these objects.

We performed the chemical analysis only on the selected sub-sample of RGB stars, exploiting the spectral region of the Ca II triplet lines. The average metallicity (-1.07 dex) resulted slightly higher than what previously found by Kirby et al. (2013b), but well within the rms scatter of the stellar luminosity-metallicity relation reported by the same authors. We also found no significant signs of a radial metallicity gradient, compatible with results from other dIrrs of similar luminosity (Leaman et al., 2013). We count in the future to explore the metallicity properties of the bluest, and hence youngest, stars in our sample.

6.4 Kinematic, chemical and mass properties of Local Group dwarf galaxies

In Chapter 5 we compared the kinematic and chemical properties, together with the mass determinations, obtained for our sample of isolated systems with those of the other dwarf galaxies of the Local Group.

Before to do so, we presented results of the chemo-kinematic study of the isolated Aquarius dwarf. The analysis was carried out on a VLT/FORS2 spectroscopic dataset, leading to the identification of 45 probable-member stars, which doubles the available samples in the literature. While both the systemic velocity and velocity dispersion were in agreement with past measures, Aquarius also showed a linear rotation signal that is counter-rotating with respect to that of the HI component. This is the first time that such effect is observed for a LG dwarf galaxy of this luminosity. The average metallicity obtained from the chemical analysis was normal for a system of this stellar mass. We detected hints of a radial metallicity gradient and of two chemo-kinematically distinct stellar populations that would need, however, further data to be confirmed.

The comparative kinematic analysis showed that the lack of significant in-

ternal rotation for Cetus and Tucana resembles the case of satellite dSphs, for which similar results have been reported, making it difficult for tidal stirring models to explain their evolution and current kinematic state. In addition, the internal kinematics of IC 1613 and Aquarius is similar to that of other isolated gas-rich dwarf galaxies with rotation-support between $0.5 \lesssim v_{\rm rot}/\sigma_{\rm v} \lesssim 2$. This reinforce the conclusions of Wheeler et al. (2017), which found no fast rotators (i.e. $v_{\rm rot}/\sigma_{\rm v} \sim 3$) among the isolated dwarfs of the LG, concluding that the progenitor of dwarf galaxies should have been rather thick and only mildly rotation-supported (see also Leaman et al., 2017).

The dynamical mass estimation carried out for our sample of isolated systems showed that they add to the other LG dwarf galaxies (both isolated and satellites) whose kinematic properties suggest that they reside in dark matter halos with circular maximum velocities (or central concentration) lower than expected in dark-matter-only simulations. Our findings reinforce the conclusions of Kirby et al. (2014) that this so-called too-big-to-fail-problem (e.g. Boylan-Kolchin et al., 2012) is a common issue among LG dwarf galaxies, independently of the environment in which they reside.

For the comparison of metallicity properties between LG dwarf galaxies, we performed a homogeneous analysis looking for a radial variation in their metallicity measurements. We found that the formation of mild metallicity gradients is common among the analysed systems, despite the large error bars found in some cases, and it seems independent from their environmental status. In particular, it appeared how systems of large luminosity, which also had a prolonged star formation history (SFH), were sharing metallicity gradients of similar strengths. At lower luminosities, instead, the variety of values was larger, reflecting also a variety of SFHs. In general, the environment role seemed to be limited, although we could not exclude it may have had an impact in shaping the strengths of metallicity gradients. On the other hand, those systems showing the steepest gradients were found in the literature to have probably experienced past merger/accretion events.

6.5 Future prospects

The goal of this thesis has been to increase our knowledge on the internal chemo-kinematic properties of a selected sample of isolated LG dwarf galaxies. Although with our analysis we have obtained several interesting results, some points have necessarily remained open and would deserve further attention in the future.

In particular, for Cetus and Tucana it would be interesting to increase con-

siderably (or at least double) the currently available spectroscopic samples, with more line-of-sight velocity and metallicity measurements of probable stellar members, especially to increase the number statistics outside their half-light radius. They would help to confirm the tentative presence of two stellar populations with distinct chemo-kinematic properties, which would allow to perform a detailed dynamical mass-modelling and study the central properties of their halo mass profile (see e.g. Battaglia et al., 2008a; Walker & Peñarrubia, 2011). On the other hand, the increase in metallicity values would definitely help to constraint the presence of a radial metallicity gradient. The use of a large field-of-view spectrograph, such as FLAMES or the future MOONS instrument on the VLT, would be particularly suitable in the case of Cetus, which is extended on the sky ($R_{\rm tidal} \sim 32$ arcmin).

The IC 1613 analysis we presented in Ch. 4 is just the tip of the iceberg of what could potentially be done with the available data. In Sect. 4.6 we have resumed some of the main open points that would need in the future a dedicated effort to be carried out. Among them we recall the analysis of the massive stars in our sample, which will allow us to obtain reliable stellar parameters and radial velocities from their spectra, and the automatic spectral classification via unsupervised machine-learning.

The study of Aquarius revealed the interesting presence of a misaligned rotation between stars and gas. It would be interesting to verify with the acquisition of new data if the young stellar population also shares such characteristic.

Finally, we count to compare our results on the radial metallicity properties of LG dwarf galaxies with those of high-resolution cosmological simulations that have made predictions on the chemical properties of such systems (e.g. Revaz & Jablonka, 2018).

The research field on dwarf galaxies is expanding rapidly and in the future it will benefit from the data collected with new large facilities and improved numerical simulations. At the moment, many questions are left unanswered. For example, the role of the environment (intended as the tidal and ram-pressure influence from a host-galaxy) is increasingly important in modern cosmological simulations of the LG that attempt to address the problems faced by Λ-CDM at the smallest scales. On the other hand, we have seen how observations of the internal chemo-kinematics of dwarf galaxies do not show significant systematic differences between isolated and satellite systems. To better understand the role of the environment, it will be crucial to improve our current knowledge of the isolated dwarf galaxies with the acquisition of new large datasets having a wide-area homogeneous coverage, and with the discovery of new systems.

The census of isolated dwarfs with stellar masses similar to that of Tucana (i.e. $M_\star \sim 10^5\, M_\odot$) is probably still incomplete (see Fattahi et al., 2020), while

uFds have not yet been discovered in the field. Current wide-area photometric surveys, like DES and Pan-STARRS, when completed will help us to constrain the number of expected faint systems in the field, whereas only with the use of a large telescope will be possible to obtain a complete census of them. The Vera C. Rubin observatory (formerly known as the Large Synoptic Survey Telescope, i.e. LSST) will dramatically improve our view of the Local Universe in terms of discovered faint systems. At the end of its survey, LSST stacked data will potentially provide a complete census (for the southern hemisphere) of dwarf galaxies down to a luminosity of $M_V = -4$ (i.e. $M_* \sim 10^3\, L_\odot$) within ~ 1 Mpc distance from the MW (Simon, 2019).

Most of the coming new systems will need a spectroscopic follow-up to confirm their galactic nature and characterize their internal properties. The closest systems to the MW will benefit from specific observations within future surveys, like WEAVE, 4MOST and DESI. Farther away systems will instead need dedicated observations which, depending on their luminosity and actual distance, will be achievable only with future 30-m class telescopes, like the Extremely Large Telescope of the European Southern Observatory. A great advance in the study of isolated systems of Tucana-like luminosity will also come from 10-m telescopes entirely dedicated to spectroscopic observations with high multiplexing capabilities, like the Mauna-Kea Spectroscopic Explorer.

Finally, the last data-release of *Gaia* will provide systemic proper motions even for bright systems outside the virial radius of the MW, such as IC 1613. Combined with the available spectroscopic information and the upcoming observations from the Hubble Space Telescope (PI: T. Sohn) of the systemic proper motions for many M31 satellites and isolated dwarfs (including Cetus and Tucana), we will be able to learn about the 3D motion of several LG systems, which will certainly help to know more on how our galactic neighbourhood has evolved.

All the aforementioned facilities and surveys will eventually help to advance on the most compelling question in this field (and probably in astrophysics) at present, that is, what is the nature of dark matter. We have seen how dwarf galaxies, thanks to their large mass-to-light ratios, are perfect laboratories for testing Λ-CDM predictions on the smallest galactic scales. Increasing our knowledge of the internal properties of isolated systems, particularly of the faintest ones, will give us the opportunity to learn what is the actual inner density profile of an undisturbed dark matter halo. Although observationally challenging, this discovery could potentially help to distinguish between different types of dark matter candidates, or open the way for a new physics.

Despite the uncertain nature of dark matter, the future of dwarf galaxies seems brighter than ever.

A

Appendix to Chapter 2

A.1 MultiNest mock tests - Output tables

In this section we report tables with the output values from MultiNest mock tests. There are six tables, depending on whether we created the input databases according to the solid-body or the flat rotation velocity law, and on which catalog (ours, K14, L07) we used to obtain the target spatial positions and error distribution information. In each table, input databases are indicated according to their n and θ values ($n = \{2, 1, 0.5, 0.25, 0\}$ and $\theta = \theta_C + \{0°, 45°, 90°\}$, where $\theta_C = 63°$). Note that we have simulated an additional case with $n = 0.75$ for input databases created according to the constant rotation law, in order to have a smoother transition between cases $n = 1$ and 0.5. This allowed to compensate for the fact that constant rotation resulted more difficult to detect with respect to solid-body rotation, as explained in Sect. X. We got similar result to the $n = 0.5$ cases created according to the solid-body rotation law, with strong to moderate evidences of rotation, depending on the axis of the input constant velocity.

TABLE A.1— Output results for catalogs created according to the solid-body rotation law (top table) or to the constant rotation law (bottom table), following our targets spatial positions and error distribution. Columns represent: n and θ input values; output parameters for the linear rotation model (systemic velocity, velocity dispersion, gradient and position angle); output parameters for the flat rotation model (systemic velocity, velocity dispersion, constant rotation velocity and position angle); output parameters for the dispersion-only model (systemic velocity and velocity dispersion); Bayes factor for the linear versus the flat rotation model; Bayes factor for the favored rotation model against the dispersion-only one.

n	θ (°)	V_{sys} (km/s)	σ_v (km/s)	k (km/s/')	θ_k (°)	V_{sys} (km/s)	σ_v (km/s)	V_c (km/s)	θ_{V_c} (°)	V_{sys} (km/s)	σ_v (km/s)	$\ln B_{lin/flat}$	$\ln B_{rot/disp}$
2	63	$10.30^{+0.20}_{-0.20}$	$7.39^{+0.49}_{-0.49}$	$63.49^{+2.42}_{-2.42}$	$4.46^{+2.62}_{-2.62}$	$18.45^{+1.44}_{-1.44}$	$19.01^{+1.45}_{-1.45}$	$80.22^{+10.74}_{-10.74}$	$7.70^{+2.77}_{-2.77}$	$19.70^{+0.46}_{-0.46}$	$28.61^{+4.31}_{-4.31}$	$51.61^{+7.26}_{-7.26}$	
	108	$9.78^{+1.35}_{-1.35}$	$7.40^{+0.34}_{-0.34}$	$108.57^{+3.71}_{-3.71}$	$5.06^{+2.85}_{-2.85}$	$19.82^{+0.13}_{-0.13}$	$19.50^{+0.37}_{-0.37}$	$119.24^{+8.01}_{-8.01}$	$6.45^{+2.81}_{-2.81}$	$19.90^{+0.07}_{-0.07}$	$77.48^{+8.16}_{-8.16}$	$108.90^{+8.60}_{-8.60}$	
	153	$10.31^{+1.42}_{-1.42}$	$7.43^{+0.33}_{-0.33}$	$153.24^{+3.78}_{-3.78}$	$1.76^{+2.86}_{-2.86}$	$19.86^{+0.10}_{-0.10}$	$19.49^{+0.38}_{-0.38}$	$147.64^{+7.67}_{-7.67}$	$1.03^{+2.81}_{-2.81}$	$19.91^{+0.05}_{-0.05}$	$87.62^{+8.56}_{-8.56}$	$116.09^{+10.96}_{-10.96}$	
1	63	$10.03^{+1.48}_{-1.48}$	$3.67^{+0.49}_{-0.49}$	$63.50^{+4.89}_{-4.89}$	$1.78^{+1.97}_{-1.97}$	$12.56^{+0.83}_{-0.83}$	$12.84^{+0.45}_{-0.45}$	$81.78^{+5.83}_{-5.83}$	$3.99^{+1.32}_{-1.32}$	$16.12^{+0.59}_{-0.59}$	$8.31^{+4.72}_{-4.72}$	$17.18^{+9.05}_{-9.05}$	
	108	$10.18^{+1.40}_{-1.40}$	$3.72^{+0.33}_{-0.33}$	$107.90^{+5.74}_{-5.74}$	$2.37^{+2.43}_{-2.43}$	$16.70^{+1.74}_{-1.74}$	$18.12^{+1.36}_{-1.36}$	$125.76^{+9.96}_{-9.96}$	$3.15^{+2.68}_{-2.68}$	$19.18^{+0.59}_{-0.59}$	$21.39^{+4.98}_{-4.98}$	$33.63^{+5.96}_{-5.96}$	
	153	$10.23^{+1.39}_{-1.39}$	$3.70^{+0.33}_{-0.33}$	$152.57^{+7.04}_{-7.04}$	$1.78^{+2.56}_{-2.56}$	$17.41^{+1.66}_{-1.66}$	$18.47^{+1.14}_{-1.14}$	$149.93^{+13.05}_{-13.05}$	$0.81^{+2.76}_{-2.76}$	$19.28^{+0.53}_{-0.53}$	$25.71^{+4.35}_{-4.35}$	$36.81^{+4.10}_{-4.10}$	
0.5	63	$9.82^{+1.39}_{-1.39}$	$1.77^{+0.49}_{-0.49}$	$63.13^{+9.49}_{-9.49}$	$1.09^{+4.74}_{-4.74}$	$10.56^{+1.97}_{-1.97}$	$6.27^{+2.20}_{-2.20}$	$77.75^{+28.22}_{-28.22}$	$2.00^{+4.76}_{-4.76}$	$11.70^{+1.29}_{-1.29}$	$1.50^{+2.21}_{-2.21}$	$3.59^{+3.01}_{-3.01}$	
	108	$10.07^{+1.39}_{-1.39}$	$1.91^{+0.33}_{-0.33}$	$106.72^{+11.40}_{-11.40}$	$1.64^{+1.85}_{-1.85}$	$11.97^{+1.38}_{-1.38}$	$10.87^{+3.07}_{-3.07}$	$128.99^{+13.37}_{-13.37}$	$2.15^{+2.01}_{-2.01}$	$13.72^{+1.72}_{-1.72}$	$6.55^{+2.75}_{-2.75}$	$10.84^{+5.20}_{-5.20}$	
	153	$10.19^{+1.38}_{-1.38}$	$1.88^{+0.33}_{-0.33}$	$153.36^{+13.31}_{-13.31}$	$1.00^{+1.88}_{-1.88}$	$12.16^{+1.61}_{-1.61}$	$12.37^{+3.21}_{-3.21}$	$153.87^{+10.81}_{-10.81}$	$0.41^{+2.04}_{-2.04}$	$13.85^{+1.75}_{-1.75}$	$7.27^{+3.69}_{-3.69}$	$11.52^{+6.05}_{-6.05}$	
0.25	63	$10.16^{+1.49}_{-1.49}$	$0.85^{+0.32}_{-0.32}$	$62.17^{+20.16}_{-20.16}$	$0.66^{+1.69}_{-1.69}$	$10.15^{+1.19}_{-1.19}$	$3.46^{+2.49}_{-2.49}$	$83.25^{+39.49}_{-39.49}$	$1.11^{+1.60}_{-1.60}$	$10.43^{+1.20}_{-1.20}$	$-0.84^{+0.81}_{-0.81}$	$-0.38^{+2.49}_{-2.49}$	
	108	$10.08^{+1.26}_{-1.26}$	$0.96^{+0.39}_{-0.39}$	$107.41^{+25.53}_{-25.53}$	$0.54^{+1.68}_{-1.68}$	$10.52^{+1.33}_{-1.33}$	$5.09^{+2.83}_{-2.83}$	$131.35^{+24.08}_{-24.08}$	$0.79^{+1.68}_{-1.68}$	$10.92^{+1.25}_{-1.25}$	$0.55^{+1.83}_{-1.83}$	$1.15^{+7.27}_{-7.27}$	
	153	$9.96^{+1.37}_{-1.37}$	$0.86^{+0.39}_{-0.39}$	$134.88^{+26.60}_{-26.60}$	$0.44^{+1.67}_{-1.67}$	$10.40^{+1.43}_{-1.43}$	$5.33^{+3.02}_{-3.02}$	$148.73^{+24.15}_{-24.15}$	$0.13^{+1.67}_{-1.67}$	$10.85^{+1.35}_{-1.35}$	$0.82^{+2.28}_{-2.28}$	$1.18^{+2.46}_{-2.46}$	
0	63	$10.06^{+1.47}_{-1.47}$	$-0.05^{+0.42}_{-0.42}$	$60.57^{+48.33}_{-48.33}$	$-0.20^{+1.67}_{-1.67}$	$10.11^{+1.33}_{-1.33}$	$0.58^{+2.48}_{-2.48}$	$118.00^{+0.83}_{-0.83}$	$-0.01^{+1.55}_{-1.55}$	$10.10^{+1.38}_{-1.38}$	$-1.21^{+0.44}_{-0.44}$	$-1.58^{+6.85}_{-6.85}$	
	108	$10.19^{+1.39}_{-1.39}$	$0.01^{+0.41}_{-0.41}$	$65.22^{+47.89}_{-47.89}$	$0.06^{+1.64}_{-1.64}$	$10.21^{+1.39}_{-1.39}$	$0.93^{+2.69}_{-2.69}$	$111.43^{+1.31}_{-1.31}$	$0.10^{+1.66}_{-1.66}$	$10.22^{+1.38}_{-1.38}$	$-1.13^{+0.60}_{-0.60}$	$-1.56^{+6.28}_{-6.28}$	
	153	$9.87^{+1.36}_{-1.36}$	$0.11^{+0.42}_{-0.41}$	$62.45^{+48.21}_{-48.85}$	$-0.03^{+1.58}_{-1.59}$	$9.97^{+1.36}_{-1.37}$	$0.74^{+2.47}_{-2.48}$	$96.89^{+1.86}_{-52.80}$	$0.10^{+1.56}_{-1.54}$	$9.99^{+1.33}_{-1.17}$	$-1.07^{+0.56}_{-0.44}$	$-1.62^{+6.62}_{-10.28}$	

n	θ (°)	V_{sys} (km/s)	σ_v (km/s)	k (km/s/')	θ_k (°)	V_{sys} (km/s)	σ_v (km/s)	V_c (km/s)	θ_{V_c} (°)	V_{sys} (km/s)	σ_v (km/s)	$\ln B_{lin/flat}$	$\ln B_{rot/disp}$
2	63	$0.03^{+2.18}_{-2.20}$	$14.13^{+1.49}_{-1.50}$	$3.96^{+0.07}_{-0.08}$	$54.16^{+5.87}_{-5.95}$	$-0.19^{+1.60}_{-1.61}$	$9.83^{+1.37}_{-1.39}$	$20.11^{+1.93}_{-1.92}$	$64.12^{+8.35}_{-8.29}$	$4.06^{+2.75}_{-2.74}$	$19.17^{+0.21}_{-0.20}$	$-11.12^{+2.22}_{-5.02}$	$23.12^{+5.93}_{-4.34}$
	108	$-0.70^{+2.14}_{-2.14}$	$13.79^{+1.49}_{-1.49}$	$74.48^{+6.39}_{-6.39}$	$0.18^{+1.65}_{-1.65}$	$10.12^{+1.39}_{-1.39}$	$20.05^{+2.36}_{-2.36}$	$106.73^{+7.72}_{-7.72}$	$18.20^{+1.80}_{-1.80}$	$19.07^{+0.19}_{-0.19}$	$-9.39^{+2.78}_{-2.78}$	$20.21^{+4.34}_{-4.34}$	
	153	$-1.18^{+2.03}_{-2.03}$	$12.87^{+1.65}_{-1.65}$	$149.33^{+20.20}_{-20.20}$	$0.20^{+1.64}_{-1.64}$	$10.10^{+1.39}_{-1.39}$	$20.37^{+2.04}_{-2.04}$	$154.16^{+5.42}_{-5.42}$	$-0.94^{+2.19}_{-2.19}$	$14.94^{+1.83}_{-1.83}$	$-6.23^{+4.03}_{-4.03}$	$12.48^{+4.21}_{-4.21}$	
1	63	$0.46^{+1.78}_{-1.78}$	$11.08^{+1.26}_{-1.26}$	$54.87^{+7.85}_{-7.85}$	$0.38^{+1.63}_{-1.63}$	$9.98^{+1.18}_{-1.18}$	$9.92^{+2.09}_{-2.09}$	$62.58^{+16.67}_{-16.67}$	$2.48^{+2.88}_{-2.89}$	$12.67^{+1.57}_{-1.57}$	$-2.12^{+2.69}_{-2.97}$	$6.35^{+3.68}_{-3.65}$	
	108	$-0.33^{+1.76}_{-1.76}$	$11.00^{+1.28}_{-1.28}$	$76.49^{+8.58}_{-8.58}$	$0.18^{+1.62}_{-1.62}$	$9.95^{+1.19}_{-1.19}$	$10.32^{+2.27}_{-2.27}$	$106.86^{+15.56}_{-15.56}$	$1.26^{+1.90}_{-1.90}$	$12.61^{+1.56}_{-1.56}$	$-1.79^{+2.51}_{-2.51}$	$5.71^{+4.68}_{-4.68}$	
	153	$-0.44^{+1.74}_{-1.74}$	$11.01^{+1.47}_{-1.47}$	$131.11^{+34.88}_{-34.88}$	$0.34^{+1.66}_{-1.66}$	$10.13^{+1.41}_{-1.41}$	$9.57^{+3.63}_{-3.63}$	$154.88^{+11.76}_{-11.76}$	$-0.39^{+1.76}_{-1.76}$	$11.47^{+1.56}_{-1.56}$	$0.10^{+1.74}_{-1.74}$	$1.51^{+9.10}_{-9.10}$	
0.75	63	$0.42^{+1.76}_{-1.76}$	$10.96^{+1.25}_{-1.25}$	$56.17^{+15.95}_{-15.95}$	$0.24^{+1.65}_{-1.65}$	$10.16^{+1.24}_{-1.24}$	$7.70^{+2.15}_{-2.15}$	$63.86^{+21.88}_{-21.88}$	$1.80^{+1.78}_{-1.78}$	$11.87^{+1.29}_{-1.29}$	$-1.16^{+2.29}_{-2.29}$	$2.46^{+5.23}_{-5.23}$	
	108	$-0.21^{+1.70}_{-1.70}$	$10.63^{+1.33}_{-1.33}$	$78.39^{+10.46}_{-10.46}$	$0.06^{+1.63}_{-1.63}$	$10.07^{+1.19}_{-1.19}$	$7.36^{+2.35}_{-2.35}$	$107.47^{+21.26}_{-21.26}$	$0.57^{+1.72}_{-1.72}$	$11.19^{+1.36}_{-1.36}$	$-0.61^{+2.28}_{-2.28}$	$1.82^{+6.28}_{-6.28}$	
	153	$-0.82^{+1.67}_{-1.67}$	$10.24^{+1.41}_{-1.41}$	$118.57^{+19.14}_{-19.14}$	$-0.33^{+1.62}_{-1.62}$	$10.11^{+1.39}_{-1.39}$	$6.29^{+2.92}_{-2.92}$	$150.79^{+18.26}_{-18.26}$	$-0.53^{+1.65}_{-1.65}$	$10.70^{+1.43}_{-1.43}$	$0.69^{+1.74}_{-1.74}$	$0.36^{+6.98}_{-6.98}$	
0.5	63	$0.14^{+1.74}_{-1.74}$	$10.44^{+1.24}_{-1.24}$	$54.74^{+9.32}_{-9.32}$	$0.11^{+1.62}_{-1.62}$	$10.16^{+1.22}_{-1.22}$	$5.80^{+2.36}_{-2.36}$	$58.91^{+28.46}_{-28.54}$	$1.02^{+1.68}_{-1.69}$	$11.00^{+1.26}_{-1.26}$	$-0.31^{+2.18}_{-2.32}$	$0.87^{+5.45}_{-5.47}$	
	108	$0.10^{+1.67}_{-1.67}$	$10.38^{+1.22}_{-1.22}$	$73.86^{+9.85}_{-9.85}$	$0.30^{+1.61}_{-1.61}$	$10.17^{+1.21}_{-1.21}$	$5.03^{+2.50}_{-2.50}$	$104.56^{+32.44}_{-32.44}$	$0.66^{+1.65}_{-1.65}$	$10.62^{+1.23}_{-1.23}$	$-0.01^{+2.23}_{-2.23}$	$-0.22^{+4.05}_{-4.05}$	
	153	$-0.59^{+1.65}_{-1.65}$	$10.35^{+1.40}_{-1.40}$	$84.87^{+14.38}_{-14.38}$	$-0.24^{+1.61}_{-1.61}$	$10.07^{+1.38}_{-1.38}$	$3.38^{+2.86}_{-2.86}$	$149.17^{+31.74}_{-31.74}$	$-0.42^{+1.60}_{-1.60}$	$10.37^{+1.38}_{-1.38}$	$0.17^{+6.99}_{-6.99}$	$-0.93^{+7.69}_{-7.69}$	
0.25	63	$0.16^{+1.64}_{-1.64}$	$10.08^{+1.37}_{-1.37}$	$61.63^{+9.28}_{-9.28}$	$0.04^{+1.63}_{-1.63}$	$10.00^{+1.39}_{-1.39}$	$2.61^{+2.42}_{-2.42}$	$67.88^{+38.80}_{-38.80}$	$0.31^{+1.62}_{-1.62}$	$10.23^{+1.39}_{-1.39}$	$-0.50^{+0.52}_{-0.52}$	$-1.53^{+7.37}_{-7.61}$	
	108	$0.32^{+1.62}_{-1.62}$	$10.04^{+1.19}_{-1.20}$	$64.26^{+6.77}_{-6.77}$	$0.33^{+1.60}_{-1.60}$	$9.91^{+1.20}_{-1.20}$	$2.62^{+2.55}_{-2.55}$	$109.65^{+9.84}_{-9.84}$	$0.45^{+1.57}_{-1.57}$	$10.11^{+1.18}_{-1.18}$	$-0.47^{+1.30}_{-1.30}$	$-1.50^{+7.60}_{-7.60}$	
	153	$-0.67^{+1.60}_{-1.61}$	$10.04^{+1.36}_{-1.19}$	$69.97^{+88.15}_{-50.12}$	$-0.48^{+1.61}_{-1.61}$	$9.90^{+1.36}_{-1.20}$	$2.11^{+2.66}_{-2.65}$	$127.60^{+43.92}_{-43.66}$	$-0.70^{+1.56}_{-1.56}$	$10.03^{+1.36}_{-1.18}$	$-0.49^{+0.62}_{-0.88}$	$-1.65^{+8.68}_{-6.51}$	

TABLE A.2— Output results for catalogs created according to the solid-body rotation law (top table) or to the constant rotation law (bottom table), following K14 spatial positions and error distribution. Columns as in Table A.1.

n	θ (°)	V_{sys} (km/s)	σ_v (km/s)	k (km/s/°)	θ_k (°)	V_{sys} (km/s)	σ_v (km/s)	V_c (km/s)	θ_{V_c} (°)	V_{sys} (km/s)	σ_v (km/s)	$\ln B_{tim,flat}$	$\ln B_{rot,disp}$
2	63	$0.07^{+1.07}_{-1.07}$	$9.82^{+0.87}_{-0.79}$	$7.52^{+0.33}_{-0.33}$	$63.17^{+4.14}_{-4.14}$	$-0.05^{+1.80}_{-1.80}$	$18.19^{+1.07}_{-1.07}$	$19.66^{+0.26}_{-0.26}$	$71.11^{+6.71}_{-6.71}$	$-1.31^{+1.95}_{-1.95}$	$19.87^{+0.10}_{-0.10}$	$60.78^{+7.13}_{-7.13}$	$125.08^{+8.07}_{-8.07}$
	108	$-0.20^{+1.06}_{-1.07}$	$9.80^{+0.88}_{-0.79}$	$7.38^{+0.37}_{-0.37}$	$107.44^{+4.16}_{-4.16}$	$0.15^{+1.76}_{-1.76}$	$17.78^{+1.17}_{-1.17}$	$19.57^{+0.32}_{-0.32}$	$94.28^{+6.76}_{-6.76}$	$-1.61^{+1.93}_{-1.93}$	$19.85^{+0.11}_{-0.11}$	$56.78^{+7.04}_{-7.04}$	$113.26^{+10.26}_{-8.96}$
	153	$-0.06^{+1.07}_{-1.07}$	$9.73^{+0.89}_{-0.78}$	$7.38^{+0.36}_{-0.37}$	$152.87^{+2.15}_{-2.01}$	$1.04^{+1.96}_{-1.96}$	$13.26^{+1.07}_{-0.97}$	$18.70^{+1.67}_{-1.67}$	$144.27^{+5.48}_{-5.48}$	$-0.71^{+1.77}_{-1.77}$	$17.90^{+1.67}_{-1.67}$	$28.26^{+8.39}_{-8.39}$	$54.71^{+9.38}_{-9.38}$
1	63	$-0.15^{+1.07}_{-1.07}$	$9.93^{+0.89}_{-0.79}$	$3.77^{+0.33}_{-0.33}$	$63.53^{+8.45}_{-8.45}$	$-0.03^{+1.27}_{-1.27}$	$12.05^{+1.01}_{-0.91}$	$14.13^{+1.56}_{-1.56}$	$68.02^{+9.21}_{-9.21}$	$-0.93^{+1.67}_{-1.67}$	$16.66^{+1.16}_{-1.16}$	$17.27^{+5.16}_{-5.16}$	$45.94^{+6.39}_{-6.39}$
	108	$0.04^{+1.06}_{-1.06}$	$9.71^{+0.86}_{-0.78}$	$3.74^{+0.37}_{-0.37}$	$108.29^{+7.82}_{-7.82}$	$0.54^{+1.26}_{-1.26}$	$11.91^{+1.00}_{-1.00}$	$13.87^{+1.65}_{-1.65}$	$99.85^{+8.83}_{-8.83}$	$-0.80^{+1.61}_{-1.61}$	$15.97^{+1.24}_{-1.24}$	$17.65^{+4.93}_{-4.93}$	$43.60^{+5.46}_{-5.46}$
	153	$0.20^{+1.08}_{-1.08}$	$9.97^{+0.88}_{-0.79}$	$3.66^{+0.35}_{-0.35}$	$152.43^{+5.84}_{-5.84}$	$0.84^{+1.42}_{-1.42}$	$10.90^{+0.84}_{-0.84}$	$10.53^{+2.04}_{-2.04}$	$145.37^{+8.21}_{-8.21}$	$-0.25^{+1.39}_{-1.39}$	$12.59^{+1.03}_{-1.03}$	$6.71^{+3.88}_{-3.88}$	$16.79^{+4.70}_{-4.70}$
0.5	63	$-0.11^{+1.06}_{-1.06}$	$9.84^{+0.79}_{-0.78}$	$1.94^{+0.33}_{-0.33}$	$63.53^{+15.70}_{-15.70}$	$0.02^{+1.13}_{-1.13}$	$10.32^{+0.81}_{-0.81}$	$7.18^{+1.62}_{-1.62}$	$69.80^{+19.00}_{-19.00}$	$-0.58^{+1.22}_{-1.22}$	$11.76^{+0.99}_{-0.99}$	$4.26^{+2.98}_{-2.98}$	$13.09^{+5.14}_{-5.14}$
	108	$-0.03^{+1.06}_{-1.06}$	$10.09^{+0.88}_{-0.78}$	$1.89^{+0.36}_{-0.36}$	$102.43^{+15.67}_{-15.67}$	$0.24^{+1.15}_{-1.15}$	$10.56^{+0.92}_{-0.92}$	$6.94^{+1.52}_{-1.52}$	$97.06^{+15.81}_{-15.81}$	$-0.51^{+1.25}_{-1.25}$	$11.95^{+0.99}_{-0.99}$	$4.35^{+3.78}_{-3.78}$	$12.05^{+5.89}_{-5.89}$
	153	$-0.05^{+1.07}_{-1.07}$	$9.89^{+0.89}_{-0.79}$	$1.73^{+0.39}_{-0.39}$	$151.66^{+10.21}_{-10.21}$	$0.22^{+1.11}_{-1.11}$	$10.18^{+0.80}_{-0.80}$	$4.88^{+1.97}_{-1.97}$	$143.57^{+16.62}_{-16.62}$	$-0.35^{+1.12}_{-1.12}$	$10.54^{+0.91}_{-0.91}$	$1.06^{+1.88}_{-1.06}$	$2.31^{+3.33}_{-2.16}$
0.25	63	$0.08^{+1.07}_{-1.07}$	$9.86^{+0.79}_{-0.79}$	$1.00^{+0.36}_{-0.36}$	$67.41^{+29.53}_{-29.53}$	$0.07^{+1.10}_{-1.10}$	$10.04^{+0.80}_{-0.80}$	$3.52^{+1.95}_{-1.95}$	$75.19^{+30.74}_{-30.74}$	$-0.20^{+1.10}_{-1.10}$	$10.42^{+0.81}_{-0.81}$	$0.37^{+1.39}_{-1.39}$	$1.49^{+2.62}_{-1.49}$
	108	$0.00^{+1.06}_{-1.06}$	$9.81^{+0.86}_{-0.78}$	$0.95^{+0.39}_{-0.39}$	$105.68^{+28.36}_{-28.36}$	$0.10^{+1.09}_{-1.09}$	$9.86^{+0.88}_{-0.88}$	$3.38^{+1.65}_{-1.65}$	$99.11^{+31.57}_{-31.57}$	$-0.19^{+1.10}_{-1.10}$	$10.17^{+0.89}_{-0.89}$	$0.36^{+1.83}_{-1.83}$	$1.26^{+3.01}_{-1.26}$
	153	$-0.13^{+1.05}_{-1.05}$	$9.78^{+0.87}_{-0.78}$	$0.66^{+0.36}_{-0.36}$	$150.20^{+26.11}_{-26.11}$	$0.00^{+1.09}_{-1.09}$	$9.82^{+0.88}_{-0.88}$	$2.20^{+1.88}_{-1.88}$	$139.01^{+33.35}_{-33.35}$	$-0.27^{+1.08}_{-1.08}$	$10.01^{+0.88}_{-0.88}$	$-0.50^{+1.05}_{-1.05}$	$-0.95^{+2.22}_{-2.22}$
0	63	$-0.14^{+1.05}_{-1.05}$	$9.78^{+0.89}_{-0.78}$	$0.15^{+0.40}_{-0.40}$	$113.24^{+36.03}_{-36.03}$	$-0.17^{+1.07}_{-1.07}$	$9.77^{+0.78}_{-0.78}$	$0.51^{+1.69}_{-1.69}$	$120.21^{+37.60}_{-37.60}$	$-0.17^{+1.05}_{-1.05}$	$9.76^{+0.77}_{-0.77}$	$-0.68^{+0.63}_{-0.63}$	$-1.98^{+1.07}_{-1.98}$
	108	$-0.21^{+1.06}_{-1.06}$	$9.80^{+0.78}_{-0.78}$	$0.15^{+0.47}_{-0.47}$	$107.47^{+44.08}_{-44.08}$	$-0.19^{+1.08}_{-1.08}$	$9.83^{+0.78}_{-0.78}$	$-0.31^{+1.68}_{-1.68}$	$104.21^{+49.65}_{-49.65}$	$-0.25^{+1.09}_{-1.09}$	$9.85^{+0.77}_{-0.77}$	$-0.70^{+0.54}_{-0.54}$	$-1.79^{+0.43}_{-0.43}$
	153	$0.16^{+1.06}_{-1.07}$	$9.88^{+0.86}_{-0.78}$	$-0.15^{+0.45}_{-0.44}$	$96.35^{+48.69}_{-48.69}$	$0.13^{+1.08}_{-1.08}$	$9.90^{+0.79}_{-0.79}$	$-0.55^{+1.70}_{-1.70}$	$98.83^{+51.63}_{-49.92}$	$0.15^{+1.06}_{-1.06}$	$9.86^{+0.85}_{-0.78}$	$-0.65^{+0.51}_{-0.51}$	$-1.93^{+0.39}_{-0.39}$

n	θ (°)	V_{sys} (km/s)	σ_v (km/s)	k (km/s/°)	θ_k (°)	V_{sys} (km/s)	σ_v (km/s)	V_c (km/s)	θ_{V_c} (°)	V_{sys} (km/s)	σ_v (km/s)	$\ln B_{tim,flat}$	$\ln B_{rot,disp}$
2	63	$-0.40^{+1.33}_{-1.33}$	$12.82^{+1.07}_{-0.96}$	$4.14^{+0.47}_{-0.44}$	$53.37^{+9.81}_{-8.75}$	$-0.04^{+1.09}_{-1.09}$	$9.91^{+0.88}_{-0.79}$	$20.28^{+1.35}_{-1.35}$	$62.21^{+5.53}_{-5.42}$	$-1.14^{+1.87}_{-1.87}$	$18.91^{+1.46}_{-1.32}$	$-20.55^{+4.89}_{-4.89}$	$59.09^{+7.82}_{-7.20}$
	108	$-1.58^{+1.33}_{-1.33}$	$12.87^{+1.07}_{-0.95}$	$3.84^{+0.50}_{-0.49}$	$111.16^{+9.27}_{-9.27}$	$-0.17^{+1.08}_{-1.08}$	$9.76^{+0.87}_{-0.79}$	$20.32^{+1.49}_{-1.49}$	$108.19^{+5.01}_{-5.01}$	$-2.33^{+1.80}_{-1.80}$	$18.33^{+1.42}_{-1.29}$	$-20.81^{+5.85}_{-5.85}$	$54.33^{+6.78}_{-6.78}$
	153	$-1.69^{+1.33}_{-1.33}$	$11.82^{+0.95}_{-0.89}$	$4.61^{+0.67}_{-0.62}$	$157.24^{+4.20}_{-4.20}$	$-0.14^{+1.07}_{-1.07}$	$9.74^{+0.87}_{-0.78}$	$19.73^{+1.54}_{-1.54}$	$153.19^{+3.76}_{-3.76}$	$-2.09^{+1.38}_{-1.38}$	$14.63^{+1.17}_{-1.05}$	$-11.40^{+4.26}_{-4.26}$	$32.41^{+7.16}_{-6.45}$
1	63	$0.09^{+1.13}_{-1.13}$	$10.69^{+0.89}_{-0.82}$	$2.08^{+0.42}_{-0.37}$	$52.79^{+14.19}_{-14.19}$	$0.29^{+1.09}_{-1.09}$	$9.80^{+0.79}_{-0.79}$	$10.14^{+1.36}_{-1.36}$	$63.77^{+10.03}_{-10.03}$	$-0.40^{+1.30}_{-1.30}$	$12.65^{+1.04}_{-0.94}$	$-4.27^{+3.58}_{-3.58}$	$18.53^{+4.34}_{-4.34}$
	108	$-0.85^{+1.14}_{-1.14}$	$10.62^{+0.93}_{-0.83}$	$1.91^{+0.42}_{-0.42}$	$111.09^{+15.33}_{-15.33}$	$-0.23^{+1.07}_{-1.07}$	$9.69^{+0.86}_{-0.78}$	$9.81^{+1.49}_{-1.49}$	$107.30^{+10.03}_{-10.03}$	$-1.35^{+1.29}_{-1.29}$	$12.39^{+1.02}_{-0.92}$	$-4.43^{+3.57}_{-3.57}$	$16.82^{+5.50}_{-4.77}$
	153	$-0.78^{+1.12}_{-1.12}$	$10.58^{+0.91}_{-0.82}$	$2.29^{+0.63}_{-0.57}$	$158.97^{+7.78}_{-7.78}$	$-0.03^{+1.10}_{-1.10}$	$10.05^{+0.88}_{-0.80}$	$9.71^{+1.94}_{-1.94}$	$153.42^{+7.70}_{-7.70}$	$-1.04^{+1.21}_{-1.21}$	$11.41^{+0.95}_{-0.86}$	$-2.13^{+3.14}_{-3.14}$	$7.75^{+4.60}_{-4.60}$
0.75	63	$-0.09^{+1.11}_{-1.11}$	$10.42^{+0.87}_{-0.82}$	$1.58^{+0.54}_{-0.54}$	$59.14^{+22.84}_{-22.84}$	$-0.02^{+1.14}_{-1.14}$	$9.90^{+0.89}_{-0.89}$	$7.85^{+1.97}_{-1.97}$	$63.25^{+14.64}_{-14.64}$	$-0.46^{+1.24}_{-1.24}$	$11.55^{+0.97}_{-0.87}$	$-1.23^{+2.62}_{-2.62}$	$10.25^{+4.87}_{-4.87}$
	108	$-0.83^{+1.10}_{-1.10}$	$10.16^{+0.89}_{-0.80}$	$1.45^{+0.50}_{-0.50}$	$108.35^{+19.69}_{-19.69}$	$-0.30^{+1.08}_{-1.08}$	$9.64^{+0.87}_{-0.78}$	$7.32^{+1.42}_{-1.42}$	$106.28^{+14.91}_{-14.91}$	$-1.23^{+1.13}_{-1.13}$	$11.18^{+0.86}_{-0.86}$	$-1.84^{+2.68}_{-2.68}$	$8.86^{+3.73}_{-3.73}$
	153	$-0.56^{+1.08}_{-1.08}$	$10.00^{+0.89}_{-0.81}$	$1.62^{+0.62}_{-0.57}$	$157.24^{+10.97}_{-10.97}$	$0.12^{+1.08}_{-1.08}$	$9.83^{+0.87}_{-0.78}$	$7.13^{+1.98}_{-1.98}$	$151.62^{+10.02}_{-10.02}$	$-0.75^{+1.13}_{-1.13}$	$10.65^{+0.90}_{-0.82}$	$-0.33^{+2.14}_{-2.14}$	$3.38^{+3.45}_{-3.38}$
0.5	63	$-0.30^{+1.07}_{-1.07}$	$9.90^{+0.81}_{-0.79}$	$1.03^{+0.54}_{-0.51}$	$62.73^{+31.47}_{-31.47}$	$-0.26^{+1.08}_{-1.08}$	$9.62^{+0.86}_{-0.78}$	$4.84^{+2.01}_{-2.01}$	$65.80^{+22.98}_{-22.98}$	$-0.54^{+1.13}_{-1.13}$	$10.33^{+0.93}_{-0.83}$	$-0.04^{+2.99}_{-2.99}$	$3.19^{+3.53}_{-3.19}$
	108	$-0.39^{+1.07}_{-1.07}$	$10.09^{+0.89}_{-0.80}$	$1.06^{+0.51}_{-0.51}$	$106.68^{+30.64}_{-30.64}$	$-0.15^{+1.09}_{-1.09}$	$9.93^{+0.79}_{-0.79}$	$5.18^{+1.49}_{-1.49}$	$104.52^{+22.07}_{-22.07}$	$-0.64^{+1.12}_{-1.12}$	$10.53^{+0.83}_{-0.83}$	$-0.37^{+2.25}_{-2.25}$	$3.02^{+3.01}_{-3.02}$
	153	$-0.54^{+1.07}_{-1.07}$	$9.93^{+0.88}_{-0.79}$	$0.95^{+0.66}_{-0.66}$	$155.26^{+18.46}_{-18.46}$	$-0.15^{+1.06}_{-1.06}$	$9.79^{+0.87}_{-0.78}$	$4.15^{+2.00}_{-2.00}$	$154.80^{+18.31}_{-18.31}$	$-0.70^{+1.10}_{-1.10}$	$10.24^{+0.89}_{-0.80}$	$0.28^{+1.20}_{-1.20}$	$0.27^{+2.76}_{-0.27}$
0.25	63	$0.18^{+1.07}_{-1.06}$	$9.91^{+0.89}_{-0.78}$	$0.59^{+0.43}_{-0.43}$	$62.58^{+42.94}_{-42.94}$	$0.22^{+1.08}_{-1.08}$	$9.88^{+0.87}_{-0.78}$	$2.60^{+1.91}_{-1.91}$	$74.74^{+48.99}_{-48.99}$	$0.01^{+1.08}_{-1.09}$	$10.06^{+0.89}_{-0.79}$	$-0.09^{+1.22}_{-0.09}$	$-0.69^{+2.73}_{-1.51}$
	108	$-0.34^{+1.06}_{-1.06}$	$9.99^{+0.79}_{-0.79}$	$0.53^{+0.45}_{-0.45}$	$118.05^{+45.41}_{-45.41}$	$-0.09^{+1.09}_{-1.09}$	$9.91^{+0.79}_{-0.79}$	$2.61^{+1.68}_{-1.68}$	$110.81^{+49.89}_{-49.89}$	$-0.42^{+1.09}_{-1.09}$	$10.08^{+0.80}_{-0.80}$	$-0.25^{+1.07}_{-0.25}$	$-1.05^{+2.13}_{-1.13}$
	153	$-0.35^{+1.06}_{-1.06}$	$9.85^{+0.87}_{-0.78}$	$0.43^{+0.51}_{-0.48}$	$148.44^{+39.82}_{-40.31}$	$-0.14^{+1.08}_{-1.08}$	$9.81^{+0.87}_{-0.79}$	$2.00^{+1.83}_{-1.83}$	$143.13^{+38.86}_{-38.86}$	$-0.40^{+1.06}_{-1.06}$	$10.04^{+0.87}_{-0.78}$	$-0.12^{+0.65}_{-0.65}$	$-1.64^{+2.28}_{-0.72}$

TABLE A.3— Output results for catalogs created according to the solid-body rotation law (top table) or to the constant rotation law (bottom table), following L07 spatial positions and error distribution. Columns as in Table A.1.

n	θ	V_{sys}	σ_v	k	θ_k	V_{sys}	σ_v	V_c	θ_{V_c}	V_{sys}	σ_v	$\ln B_{tm,flat}$	$\ln B_{cat,disp}$
	(°)	(km/s)	(km/s)	(km/s/′)	(°)	(km/s)	(km/s)	(km/s)	(°)	(km/s)	(km/s)		
2	63	$-0.27^{+1.04}_{-1.04}$	$10.35^{+1.02}_{-1.02}$	$7.39^{+0.92}_{-0.92}$	$63.89^{+10.78}_{-10.78}$	$0.52^{+2.40}_{-2.40}$	$15.26^{+1.87}_{-1.87}$	$18.68^{+0.97}_{-0.97}$	$79.07^{+11.91}_{-11.91}$	$-5.08^{+2.74}_{-2.74}$	$19.26^{+0.54}_{-0.54}$	$15.94^{+4.38}_{-4.38}$	$33.67^{+6.74}_{-6.74}$
	108	$-0.32^{+1.95}_{-1.95}$	$10.14^{+1.42}_{-1.42}$	$7.52^{+0.88}_{-0.88}$	$106.93^{+10.58}_{-10.58}$	$1.98^{+2.46}_{-2.46}$	$16.79^{+1.70}_{-1.70}$	$19.11^{+0.72}_{-0.72}$	$99.01^{+11.57}_{-11.57}$	$-3.54^{+2.76}_{-2.76}$	$19.58^{+0.91}_{-0.91}$	$22.13^{+4.08}_{-4.08}$	$44.49^{+6.84}_{-6.84}$
	153	$0.38^{+1.93}_{-1.93}$	$10.23^{+1.40}_{-1.40}$	$7.25^{+1.16}_{-1.16}$	$150.39^{+9.49}_{-9.49}$	$3.30^{+2.42}_{-2.42}$	$13.41^{+1.59}_{-1.59}$	$17.31^{+0.53}_{-0.53}$	$129.57^{+13.36}_{-13.36}$	$1.07^{+2.60}_{-2.60}$	$18.15^{+1.59}_{-1.59}$	$9.65^{+3.09}_{-3.09}$	$22.67^{+4.34}_{-4.34}$
	63	$-0.59^{+1.91}_{-1.91}$	$9.78^{+1.01}_{-1.01}$	$3.62^{+0.90}_{-0.90}$	$71.71^{+23.21}_{-23.21}$	$1.03^{+2.18}_{-2.18}$	$11.16^{+1.70}_{-1.70}$	$12.28^{+2.66}_{-2.66}$	$76.93^{+19.22}_{-19.22}$	$-3.23^{+2.60}_{-2.60}$	$14.40^{+1.81}_{-1.81}$	$3.84^{+2.08}_{-2.08}$	$11.43^{+4.36}_{-4.36}$
1	108	$0.05^{+1.94}_{-1.94}$	$10.05^{+1.48}_{-1.48}$	$4.04^{+0.70}_{-0.70}$	$103.79^{+20.69}_{-20.69}$	$2.16^{+2.24}_{-2.24}$	$11.86^{+1.49}_{-1.49}$	$13.96^{+2.49}_{-2.49}$	$96.32^{+16.96}_{-16.96}$	$-1.92^{+2.35}_{-2.35}$	$15.76^{+1.93}_{-1.93}$	$5.15^{+3.39}_{-3.39}$	$15.39^{+4.19}_{-4.19}$
	153	$-0.07^{+1.98}_{-1.98}$	$10.55^{+1.62}_{-1.62}$	$3.33^{+1.08}_{-1.08}$	$151.78^{+23.86}_{-23.86}$	$1.30^{+2.19}_{-2.19}$	$11.15^{+1.45}_{-1.45}$	$9.36^{+2.01}_{-2.01}$	$135.13^{+23.91}_{-23.91}$	$0.38^{+2.02}_{-2.02}$	$12.74^{+1.52}_{-1.52}$	$1.58^{+2.99}_{-2.99}$	$5.75^{+3.08}_{-3.08}$
	63	$-0.45^{+1.94}_{-1.94}$	$10.41^{+1.61}_{-1.61}$	$2.13^{+0.99}_{-0.99}$	$67.67^{+36.66}_{-36.66}$	$0.19^{+2.17}_{-2.17}$	$11.05^{+1.66}_{-1.66}$	$6.77^{+3.03}_{-3.03}$	$69.96^{+33.74}_{-33.74}$	$-1.64^{+2.04}_{-2.04}$	$11.93^{+1.68}_{-1.68}$	$0.75^{+1.99}_{-1.99}$	$2.28^{+3.30}_{-3.30}$
0.5	108	$-0.03^{+1.95}_{-1.95}$	$10.15^{+1.48}_{-1.48}$	$2.08^{+0.83}_{-0.83}$	$105.10^{+38.76}_{-38.76}$	$0.93^{+2.04}_{-2.04}$	$10.58^{+1.48}_{-1.48}$	$7.08^{+2.86}_{-2.86}$	$97.74^{+30.49}_{-30.49}$	$-0.88^{+1.89}_{-1.89}$	$11.72^{+1.46}_{-1.46}$	$0.51^{+1.99}_{-1.99}$	$2.92^{+3.07}_{-3.07}$
	153	$-0.35^{+1.87}_{-1.87}$	$9.95^{+1.39}_{-1.39}$	$1.53^{+0.74}_{-0.74}$	$152.37^{+40.14}_{-40.14}$	$0.35^{+2.00}_{-2.00}$	$10.13^{+1.41}_{-1.41}$	$5.14^{+3.05}_{-3.05}$	$134.21^{+39.53}_{-39.53}$	$-0.20^{+1.79}_{-1.79}$	$10.72^{+1.42}_{-1.42}$	$-0.14^{+1.98}_{-1.98}$	$0.40^{+3.44}_{-3.44}$
	63	$0.22^{+1.86}_{-1.86}$	$9.70^{+1.37}_{-1.37}$	$1.15^{+1.03}_{-1.03}$	$52.75^{+42.18}_{-42.18}$	$0.56^{+1.97}_{-1.97}$	$9.84^{+1.87}_{-1.87}$	$4.14^{+3.05}_{-3.05}$	$64.54^{+41.29}_{-41.29}$	$-0.65^{+1.71}_{-1.71}$	$10.03^{+1.53}_{-1.53}$	$-0.48^{+0.78}_{-0.78}$	$-0.62^{+3.38}_{-3.38}$
0.25	108	$-0.20^{+1.93}_{-1.93}$	$10.27^{+1.41}_{-1.41}$	$1.36^{+0.99}_{-0.99}$	$85.78^{+43.86}_{-43.86}$	$0.35^{+2.02}_{-2.02}$	$10.20^{+1.60}_{-1.60}$	$4.03^{+3.03}_{-3.03}$	$96.09^{+42.69}_{-42.69}$	$-0.71^{+1.89}_{-1.89}$	$10.72^{+1.39}_{-1.39}$	$-0.36^{+1.98}_{-1.98}$	$-0.00^{+3.67}_{-3.67}$
	153	$-0.08^{+1.91}_{-1.91}$	$10.34^{+1.43}_{-1.43}$	$0.66^{+1.09}_{-1.09}$	$130.96^{+45.67}_{-45.67}$	$0.12^{+2.02}_{-2.02}$	$10.33^{+1.42}_{-1.42}$	$2.46^{+3.39}_{-3.39}$	$92.82^{+45.84}_{-45.84}$	$-0.22^{+1.76}_{-1.76}$	$10.57^{+1.41}_{-1.41}$	$-0.52^{+0.99}_{-0.99}$	$-0.95^{+3.65}_{-3.65}$
	63	$0.27^{+1.80}_{-1.80}$	$9.62^{+1.34}_{-1.34}$	$-0.12^{+1.02}_{-1.02}$	$53.35^{+44.01}_{-44.01}$	$0.23^{+1.91}_{-1.91}$	$9.64^{+1.56}_{-1.56}$	$-0.01^{+3.08}_{-3.08}$	$63.54^{+47.70}_{-47.70}$	$0.17^{+1.68}_{-1.68}$	$9.66^{+1.33}_{-1.33}$	$-0.59^{+0.90}_{-0.90}$	$-1.41^{+3.82}_{-3.82}$
0	108	$0.09^{+1.85}_{-1.85}$	$10.20^{+1.36}_{-1.36}$	$0.05^{+0.99}_{-0.99}$	$86.01^{+45.49}_{-45.49}$	$-0.05^{+1.97}_{-1.97}$	$10.16^{+1.58}_{-1.58}$	$-0.04^{+3.11}_{-3.11}$	$71.75^{+48.86}_{-48.86}$	$-0.07^{+1.76}_{-1.76}$	$10.31^{+1.36}_{-1.36}$	$-0.59^{+0.36}_{-0.36}$	$-1.30^{+3.50}_{-3.50}$
	153	$-0.28^{+1.80}_{-1.80}$	$9.71^{+1.30}_{-1.30}$	$0.09^{+1.01}_{-1.01}$	$24.71^{+42.34}_{-42.34}$	$-0.16^{+1.91}_{-1.91}$	$9.72^{+1.39}_{-1.39}$	$-0.49^{+3.02}_{-3.02}$	$67.49^{+48.83}_{-48.83}$	$-0.09^{+1.68}_{-1.68}$	$9.75^{+1.35}_{-1.35}$	$-0.55^{+0.28}_{-0.28}$	$-1.43^{+3.29}_{-3.29}$

n	θ	V_{sys}	σ_v	k	θ_k	V_{sys}	σ_v	V_c	θ_{V_c}	V_{sys}	σ_v	$\ln B_{tm,flat}$	$\ln B_{cat,disp}$
	(°)	(km/s)	(km/s)	(km/s/′)	(°)	(km/s)	(km/s)	(km/s)	(°)	(km/s)	(km/s)		
2	63	$-3.44^{+2.37}_{-2.37}$	$12.57^{+1.78}_{-1.78}$	$4.54^{+1.28}_{-1.28}$	$59.54^{+20.86}_{-20.86}$	$0.47^{+2.11}_{-2.11}$	$10.33^{+1.59}_{-1.59}$	$20.45^{+2.79}_{-2.79}$	$63.85^{+10.11}_{-10.11}$	$-7.12^{+2.96}_{-2.96}$	$17.54^{+2.15}_{-2.15}$	$-3.81^{+3.82}_{-3.82}$	$17.73^{+4.53}_{-4.53}$
	108	$-4.13^{+2.20}_{-2.20}$	$12.93^{+1.76}_{-1.76}$	$4.61^{+0.89}_{-0.89}$	$117.36^{+18.83}_{-21.94}$	$-0.28^{+2.05}_{-2.05}$	$10.12^{+1.60}_{-1.60}$	$20.21^{+2.22}_{-2.22}$	$107.58^{+10.96}_{-11.91}$	$-5.46^{+2.73}_{-2.73}$	$18.55^{+2.25}_{-2.25}$	$-4.89^{+3.23}_{-3.23}$	$21.31^{+5.64}_{-5.64}$
	153	$-1.19^{+2.16}_{-2.16}$	$11.79^{+1.50}_{-1.50}$	$5.80^{+1.48}_{-1.48}$	$164.20^{+16.47}_{-16.47}$	$0.41^{+2.05}_{-2.05}$	$9.94^{+1.40}_{-1.40}$	$19.20^{+2.39}_{-2.39}$	$153.51^{+9.44}_{-9.44}$	$-0.45^{+2.29}_{-2.29}$	$15.09^{+1.23}_{-1.23}$	$-2.01^{+3.29}_{-3.29}$	$12.89^{+4.23}_{-4.23}$
	63	$-2.33^{+2.03}_{-2.03}$	$10.75^{+1.64}_{-1.64}$	$2.36^{+1.00}_{-1.00}$	$61.83^{+36.42}_{-36.42}$	$-0.47^{+2.09}_{-2.09}$	$10.34^{+1.62}_{-1.62}$	$9.81^{+2.91}_{-2.91}$	$64.25^{+22.93}_{-22.93}$	$-3.90^{+1.68}_{-1.68}$	$12.56^{+1.72}_{-1.72}$	$1.16^{+2.68}_{-2.68}$	$4.85^{+4.87}_{-4.87}$
1	108	$-1.96^{+2.05}_{-2.05}$	$11.39^{+1.46}_{-1.46}$	$2.38^{+0.88}_{-0.88}$	$105.73^{+33.73}_{-33.73}$	$-0.24^{+2.09}_{-2.09}$	$10.44^{+1.63}_{-1.63}$	$10.42^{+2.53}_{-2.53}$	$103.67^{+21.02}_{-20.94}$	$-2.71^{+2.03}_{-2.02}$	$12.90^{+1.74}_{-1.55}$	$0.10^{+2.59}_{-2.44}$	$5.53^{+3.69}_{-3.76}$
	153	$-0.01^{+1.97}_{-1.97}$	$10.62^{+1.44}_{-1.44}$	$2.35^{+1.28}_{-1.28}$	$162.19^{+8.59}_{-8.59}$	$0.33^{+2.03}_{-2.03}$	$10.05^{+1.40}_{-1.40}$	$9.34^{+3.13}_{-3.13}$	$149.88^{+22.72}_{-22.72}$	$0.41^{+1.89}_{-1.89}$	$11.57^{+1.46}_{-1.46}$	$2.69^{+2.87}_{-2.87}$	$1.75^{+4.48}_{-4.48}$
	63	$-1.66^{+1.99}_{-1.99}$	$10.71^{+1.64}_{-1.64}$	$1.85^{+1.16}_{-1.16}$	$47.68^{+30.59}_{-30.59}$	$-0.48^{+2.10}_{-2.10}$	$10.49^{+1.61}_{-1.61}$	$7.12^{+3.20}_{-3.20}$	$59.19^{+30.09}_{-30.09}$	$-2.90^{+1.86}_{-1.86}$	$11.39^{+1.65}_{-1.65}$	$1.42^{+2.05}_{-2.05}$	$1.75^{+4.58}_{-4.58}$
0.75	108	$-1.30^{+1.95}_{-1.95}$	$10.42^{+1.43}_{-1.43}$	$2.01^{+0.93}_{-0.93}$	$104.04^{+38.23}_{-38.23}$	$-0.02^{+2.09}_{-2.09}$	$10.08^{+1.42}_{-1.42}$	$8.22^{+3.51}_{-3.51}$	$105.57^{+25.26}_{-25.26}$	$-1.87^{+1.89}_{-1.89}$	$11.77^{+1.47}_{-1.47}$	$0.88^{+1.87}_{-1.87}$	$3.27^{+4.59}_{-4.59}$
	153	$-0.76^{+1.95}_{-1.95}$	$10.44^{+1.40}_{-1.40}$	$1.77^{+1.22}_{-1.22}$	$156.57^{+8.19}_{-8.19}$	$-0.32^{+2.05}_{-2.05}$	$10.29^{+1.41}_{-1.41}$	$6.88^{+3.91}_{-3.91}$	$149.72^{+13.14}_{-13.14}$	$-0.31^{+1.84}_{-1.84}$	$11.25^{+1.44}_{-1.44}$	$1.63^{+2.63}_{-2.63}$	$1.42^{+4.63}_{-4.63}$
	63	$-1.52^{+1.92}_{-1.92}$	$10.59^{+1.59}_{-1.59}$	$1.15^{+1.06}_{-1.06}$	$54.31^{+44.78}_{-44.78}$	$-0.80^{+2.04}_{-2.04}$	$10.42^{+1.59}_{-1.59}$	$5.01^{+3.91}_{-3.91}$	$66.02^{+40.91}_{-40.91}$	$-1.94^{+1.78}_{-1.78}$	$10.83^{+1.59}_{-1.59}$	$1.07^{+0.60}_{-0.60}$	$-0.10^{+4.86}_{-4.86}$
0.5	108	$-0.74^{+1.93}_{-1.93}$	$10.57^{+1.45}_{-1.45}$	$1.32^{+0.96}_{-0.96}$	$122.71^{+39.08}_{-39.08}$	$-0.10^{+2.03}_{-2.03}$	$10.42^{+1.62}_{-1.62}$	$5.97^{+3.94}_{-3.78}$	$109.59^{+34.72}_{-37.08}$	$-1.20^{+1.84}_{-1.84}$	$11.02^{+1.54}_{-1.42}$	$0.79^{+0.92}_{-0.92}$	$0.42^{+4.33}_{-4.33}$
	153	$-0.37^{+1.88}_{-1.89}$	$10.20^{+1.41}_{-1.41}$	$0.64^{+1.13}_{-1.13}$	$132.20^{+42.95}_{-42.95}$	$-0.21^{+1.97}_{-1.97}$	$10.22^{+1.40}_{-1.40}$	$3.86^{+3.28}_{-3.28}$	$136.71^{+42.10}_{-42.10}$	$-0.24^{+1.74}_{-1.74}$	$10.37^{+1.40}_{-1.40}$	$1.21^{+0.79}_{-0.79}$	$-0.31^{+4.86}_{-4.86}$
	63	$-0.80^{+1.89}_{-1.89}$	$10.37^{+1.59}_{-1.59}$	$0.49^{+1.08}_{-1.08}$	$41.89^{+42.86}_{-42.86}$	$-0.58^{+1.99}_{-1.99}$	$10.28^{+1.58}_{-1.58}$	$2.54^{+3.27}_{-3.27}$	$64.70^{+47.11}_{-47.11}$	$-1.07^{+1.75}_{-1.75}$	$10.40^{+1.56}_{-1.56}$	$0.19^{+0.45}_{-0.45}$	$-1.27^{+5.40}_{-5.40}$
0.25	108	$-0.18^{+1.87}_{-1.89}$	$10.21^{+1.59}_{-1.59}$	$0.58^{+0.97}_{-0.99}$	$75.43^{+46.13}_{-47.09}$	$0.24^{+2.00}_{-2.00}$	$10.15^{+1.41}_{-1.41}$	$2.82^{+3.04}_{-3.04}$	$101.18^{+48.34}_{-48.34}$	$-0.33^{+1.73}_{-1.73}$	$10.49^{+1.40}_{-1.40}$	$0.19^{+0.39}_{-0.99}$	$-1.16^{+5.54}_{-5.52}$
	153	$0.23^{+1.92}_{-1.92}$	$10.40^{+1.61}_{-1.61}$	$0.56^{+1.06}_{-1.06}$	$98.95^{+48.61}_{-48.61}$	$0.14^{+2.00}_{-2.00}$	$10.59^{+1.40}_{-1.40}$	$2.25^{+3.36}_{-3.36}$	$134.97^{+48.07}_{-48.07}$	$0.08^{+1.79}_{-1.79}$	$10.78^{+1.40}_{-1.40}$	$0.26^{+0.48}_{-0.48}$	$-1.24^{+5.40}_{-5.40}$

A.2 Target tables

TABLE A.4— Properties of the observed VLT/FORS2 targets in Cetus dSph. Column (1) field (Cen = 1, NE = 2, SE = 3, NW = 4); (2) slit aperture: numbers < 30 indicate observed targets from chip-1, otherwise from chip-2 – numbers counted from bottom to top of the CCD; (3) RA-Dec coordinated in J2000; (4) V band magnitude with error from Subaru/SuprimeCam photometric catalog (5) I band magnitude with error from Subaru/SuprimeCam photometric catalog (6) l.o.s. heliocentric velocity with velocity error; (6) metallicity with metallicity error; (8) S/N ratio in pxl^{-1}; (9) membership (Y= member; N= non-member). 3 stars had repeated measurements: targets 17, 20 and 21 from Cen field corresponding to targets 10, 8 and 6 from NE field, respectively; in this table we report the single measurements as well as the averaged values used during the analysis process.

Notes. Stars marked as nonmembers were excluded according to the following criteria (see Sect. 2.4 for full description): $^{(\star)}$ target excluded because without a reliable spectral extraction; $^{(a)}$ based on their magnitudes and colors: (†) target belong to the MSTO feature described in Sect. 2.8; $^{(b)}$ based on their kinematics: (‡) target excluded because without a reliable metallicity estimation; $^{(b)}$ based on the iterative kinematic selection.

F	S	R.A., Dec (J2000) (deg)	V	I	v_{hel} (km/s)	[Fe/H] (dex)	S/N (pxl^{-1})	M
1	1	6.53688, -11.04748	22.245 ± 0.007	21.004 ± 0.004	-82.9 ± 6.2	-1.83 ± 0.10	37.8	Y
1	2	6.54593, -11.06429	22.149 ± 0.006	20.803 ± 0.004	-91.2 ± 6.3	-1.47 ± 0.11	28.9	Y
1	3	6.53830, -11.03623	22.151 ± 0.006	20.768 ± 0.004	-77.4 ± 10.1	-1.28 ± 0.12	12.6	Y
1	4	6.54504, -11.04530	21.943 ± 0.005	20.711 ± 0.003	-77.8 ± 4.6	-1.96 ± 0.12	47.7	Y
1	5	6.54512, -11.03542	22.222 ± 0.007	21.063 ± 0.004	-75.7 ± 7.2	-2.12 ± 0.10	25.4	Y
1	6	6.54664, -11.03221	22.216 ± 0.007	20.967 ± 0.004	-69.4 ± 4.3	-1.58 ± 0.13	25.2	Y
1	7	6.55304, -11.04146	22.123 ± 0.006	20.820 ± 0.004	-78.1 ± 3.9	-1.23 ± 0.12	27.8	Y
1	8	6.55643, -11.04140	22.247 ± 0.007	21.126 ± 0.005	-76.8 ± 4.4	-1.86 ± 0.11	27.0	Y
1	9	6.56251, -11.04938	22.179 ± 0.006	20.992 ± 0.004	-85.6 ± 4.1	-0.96 ± 0.14	28.6	Y
1	10	6.56207, -11.03662	21.955 ± 0.006	20.788 ± 0.004	-76.9 ± 3.1	-1.63 ± 0.12	32.6	Y
1	11	6.56366, -11.03405	21.950 ± 0.005	20.772 ± 0.004	-78.3 ± 5.7	-1.91 ± 0.14	31.2	Y
1	12	6.56208, -11.02086	21.957 ± 0.006	20.688 ± 0.003	-91.4 ± 3.6	-1.71 ± 0.12	32.4	Y
1	13	6.57068, -11.03632	22.202 ± 0.007	21.095 ± 0.004	-61.3 ± 4.6	-2.03 ± 0.12	22.3	Y
1	14	6.56771, -11.02073	22.305 ± 0.007	21.121 ± 0.005	-88.8 ± 6.3	-1.72 ± 0.12	21.2	Y
1	15	6.57265, -11.02699	21.870 ± 0.005	20.593 ± 0.003	-84.5 ± 5.2	-1.83 ± 0.09	35.3	Y
1	16	6.59213, -11.06961	22.355 ± 0.007	21.136 ± 0.005	-82.7 ± 6.5	-1.49 ± 0.20	17.8	Y
	rep.	6.57904, -11.02699	22.357 ± 0.007	21.189 ± 0.005	-91.4 ± 3.3	-1.32 ± 0.13	...	Y
1	17				-91.2 ± 3.7	-1.29 ± 0.17	24.8	
2	10				-92.3 ± 7.3	-1.37 ± 0.19	22.1	
1	18	6.58434, -11.03270	22.010 ± 0.006	20.749 ± 0.004	-89.3 ± 4.0	-1.50 ± 0.12	30.7	Y
1	19	6.57914, -11.01265	22.298 ± 0.007	21.045 ± 0.004	-92.2 ± 4.7	-1.25 ± 0.15	25.3	Y
	rep.	6.58899, -11.02351	22.166 ± 0.006	20.962 ± 0.004	-83.9 ± 4.1	-2.16 ± 0.08	...	Y
1	20				-97.3 ± 5.6	-2.22 ± 0.11	30.6	
2	8				-69.1 ± 5.9	-2.07 ± 0.13	29.5	
	rep.	6.59423, -11.02139	22.313 ± 0.007	21.178 ± 0.005	-66.8 ± 3.8	-2.04 ± 0.10	...	Y
1	21				-74.3 ± 8.6	-2.07 ± 0.13	25.7	
2	6				-64.9 ± 4.4	-1.99 ± 0.18	20.8	
1	31	6.48997, -11.06058	22.688 ± 0.009	21.462 ± 0.006	-66.5 ± 4.2	-1.04 ± 0.27	19.3	Y
1	32	6.49335, -11.05962	22.486 ± 0.008	21.275 ± 0.005	-65.3 ± 4.1	-1.20 ± 0.20	22.6	Y
1	33	6.49151, -11.04743	22.167 ± 0.006	21.024 ± 0.004	-67.0 ± 5.1	-2.22 ± 0.13	26.7	Y

TABLE A.4— continued.

F	S	R.A., Dec (J2000) (deg)	V	I	v_{hel} (km/s)	[Fe/H] (dex)	S/N (pxl^{-1})	M
1	34	6.49907, -11.05631	22.303 ± 0.007	21.036 ± 0.004	-75.5 ± 4.0	-0.90 ± 0.17	27.4	Y
1	35	6.49919, -11.04752	22.148 ± 0.006	20.845 ± 0.004	-73.5 ± 4.0	-1.25 ± 0.12	29.2	Y
1	36	6.51416, -11.07648	22.178 ± 0.006	20.989 ± 0.004	-100.3 ± 7.0	-1.64 ± 0.15	22.5	Y
1	37	6.50501, -11.04473	22.180 ± 0.006	20.955 ± 0.004	-71.5 ± 6.2	-1.42 ± 0.16	27.3	Y
1	38	6.51469, -11.06296	22.036 ± 0.006	20.809 ± 0.004	-67.5 ± 5.8	-2.36 ± 0.08	30.2	Y
1	39	6.52432, -11.08034	22.346 ± 0.007	21.044 ± 0.004	-80.8 ± 5.0	-1.38 ± 0.19	20.5	Y
1	40	6.51815, -11.05490	22.298 ± 0.007	20.988 ± 0.004	-73.0 ± 4.4	-1.36 ± 0.13	26.5	Y
1	41	6.52159, -11.05413	22.075 ± 0.006	20.604 ± 0.003	-82.7 ± 4.4	-1.02 ± 0.13	33.5	Y
1	42	6.52743, -11.06280	21.996 ± 0.006	20.646 ± 0.003	-99.7 ± 4.2	-1.39 ± 0.12	38.9	Y
1	43	6.52120, -11.03572	22.072 ± 0.006	20.917 ± 0.004	-66.3 ± 5.9	-2.23 ± 0.09	29.9	Y
1	44	6.52532, -11.03752	22.430 ± 0.008	21.177 ± 0.005	-80.0 ± 4.1	-1.08 ± 0.14	28.4	Y
2	1	6.62692, -10.98979	22.306 ± 0.007	21.202 ± 0.005	-70.7 ± 5.3	-2.66 ± 0.14	32.2	Y
2	2	6.62047, -11.02169	22.151 ± 0.006	20.931 ± 0.004	-84.6 ± 4.6	-1.91 ± 0.12	29.5	Y
2	3	6.62018, -10.97139	21.940 ± 0.005	20.731 ± 0.004	-89.1 ± 5.5	-2.81 ± 0.15	43.1	Y
2	4	6.61073, -11.01024	21.893 ± 0.005	20.651 ± 0.003	-85.9 ± 3.2	-1.65 ± 0.09	33.0	Y
2	5	6.60175, -10.96567	22.197 ± 0.006	21.063 ± 0.004	-80.9 ± 5.6	-2.42 ± 0.12	28.3	Y
2	7	6.59280, -11.01003	22.057 ± 0.006	20.866 ± 0.004	-350.8 ± 7.1	/	34.1	N$^{(b)}$
2	9	6.58461, -11.01562	22.088 ± 0.006	20.793 ± 0.004	-73.8 ± 6.4	-1.39 ± 0.13	33.3	Y
2	11	6.57328, -11.01102	21.771 ± 0.005	20.59 ± 0.003	9.1 ± 5.9	/	41.4	N$^{(b)}$
2	31	6.66900, -10.97425	22.122 ± 0.006	20.865 ± 0.004	-74.6 ± 5.7	-1.42 ± 0.14	32.8	Y
2	32	6.66218, -11.014	22.076 ± 0.006	20.739 ± 0.004	/	/	4.3	N$^{(\star)}$
2	33	6.66026, -10.99978	22.132 ± 0.006	21.019 ± 0.004	-59.1 ± 5.1	-1.85 ± 0.12	31.9	Y
2	34	6.65242, -10.98151	22.167 ± 0.006	20.972 ± 0.004	-59.4 ± 6.5	-2.31 ± 0.13	33.0	Y
2	35	6.64503, -11.01836	22.279 ± 0.007	20.980 ± 0.004	-55.4 ± 11.6	-1.35 ± 0.11	24.5	Y
2	36	6.64520, -10.97766	21.880 ± 0.005	20.663 ± 0.003	-86.4 ± 4.7	-2.42 ± 0.09	40.0	Y
2	37	6.63863, -11.02350	22.152 ± 0.006	20.945 ± 0.004	-76.6 ± 5.7	-1.80 ± 0.15	21.8	Y
3	1	6.69005, -11.18939	22.491 ± 0.008	21.445 ± 0.006	-269.2 ± 8.6	/	14.3	N$^{(b)}$
3	2	6.67327, -11.16669	22.036 ± 0.006	21.113 ± 0.005	-113.1 ± 7.1	-1.87 ± 0.23	20.8	Y
3	3	6.67343, -11.15788	22.406 ± 0.007	20.663 ± 0.003	-15.3 ± 4.9	-1.79 ± 0.12	34.0	N$^{(c)}$
3	4	6.65313, -11.13756	21.444 ± 0.004	20.707 ± 0.003	-99.8 ± 59.9	/	17.0	N$^{(a)}$
3	5	6.70653, -11.16299	20.980 ± 0.003	20.571 ± 0.003	-7223.6 ± 99.9	/	7.5	N$^{(a)}$
3	6	6.66050, -11.13212	21.982 ± 0.006	21.386 ± 0.005	-70.3 ± 8.1	/	13.3	N$^{(a,\dagger)}$
3	7	6.71027, -11.15561	23.332 ± 0.015	20.956 ± 0.004	-3126.8 ± 25.1	/	16.5	N$^{(a)}$
3	8	6.67261, -11.12727	23.622 ± 0.019	21.285 ± 0.005	989.8 ± 33.3	/	10.6	N$^{(a)}$
3	9	6.67263, -11.12138	22.661 ± 0.009	21.524 ± 0.006	-46.3 ± 8.0	-2.00 ± 0.31	13.6	Y
3	10	6.70292, -11.12720	22.492 ± 0.008	21.370 ± 0.005	-125.5 ± 9.7	-1.67 ± 0.27	15.1	N$^{(c)}$
3	31	6.65333, -11.22907	23.345 ± 0.015	20.770 ± 0.004	-61.5 ± 8.4	/	23.5	N$^{(a)}$
3	32	6.65380, -11.22331	21.341 ± 0.004	20.080 ± 0.002	3713.0 ± 30.3	/	32.1	N$^{(a)}$
3	33	6.64821, -11.21443	22.561 ± 0.008	20.494 ± 0.003	-66.7 ± 5.7	-2.25 ± 0.09	32.4	Y
3	34	6.67011, -11.21540	22.163 ± 0.006	21.097 ± 0.004	-94.5 ± 6.9	-2.05 ± 0.25	17.2	Y
3	35	6.62680, -11.184	22.554 ± 0.008	21.334 ± 0.005	55.9 ± 10.1	/	13.6	N$^{(b)}$
3	36	6.63913, -11.18699	23.612 ± 0.019	20.930 ± 0.004	-31.4 ± 21.5	/	21.2	N$^{(a)}$
3	37	6.66534, -11.19491	22.161 ± 0.006	21.038 ± 0.004	91.6 ± 5.9	/	15.8	N$^{(b)}$
3	38	6.68470, -11.19680	22.382 ± 0.007	21.042 ± 0.004	-9.6 ± 6.8	-2.04 ± 0.26	18.4	N$^{(c)}$
4	1	6.37661, -10.93484	22.260 ± 0.007	21.107 ± 0.004	-80.6 ± 5.3	-1.70 ± 0.18	23.5	Y
4	2	6.34739, -10.91718	22.416 ± 0.008	20.589 ± 0.003	13.4 ± 3.5	/	25.7	N$^{(b)}$
4	3	6.35494, -10.90558	23.172 ± 0.014	20.975 ± 0.004	-9.1 ± 8.3	/	17.5	N$^{(a)}$
4	4	6.40200, -10.91746	22.498 ± 0.008	21.456 ± 0.006	-59.9 ± 19.4	-2.28 ± 0.30	8.0	Y
4	5	6.36032, -10.89001	23.304 ± 0.015	21.804 ± 0.007	33.7 ± 16.7	/	9.1	N$^{(b)}$
4	6	6.38581, -10.89334	23.582 ± 0.018	22.265 ± 0.010	-46.4 ± 19.1	/	6.3	N$^{(b,\ddagger)}$
4	7	6.34763, -10.8755	22.505 ± 0.008	21.262 ± 0.005	9.6 ± 13.9	/	11.7	N$^{(b)}$

TABLE A.4— continued.

F	S	R.A., Dec (J2000) (deg)	V	I	v_{hel} (km/s)	[Fe/H] (dex)	S/N (pxl^{-1})	M
4	31	6.31670, -10.96733	22.207 ± 0.007	20.696 ± 0.003	-7.9 ± 4.0	-1.76 ± 0.19	17.4	N$^{(c)}$
4	32	6.32031, -10.95838	22.132 ± 0.006	20.399 ± 0.003	6.1 ± 3.9	/	25.7	N$^{(b)}$
4	33	6.32984, -10.95438	22.490 ± 0.008	21.253 ± 0.005	-114.4 ± 8.3	-1.81 ± 0.29	15.9	Y
4	34	6.35298, -10.95691	22.658 ± 0.009	20.292 ± 0.003	3.6 ± 7.9	/	27.7	N$^{(b)}$
4	35	6.38168, -10.95799	23.458 ± 0.017	21.419 ± 0.006	-2426.4 ± 28.5	/	10.7	N$^{(a)}$

B

Appendix to Chapter 3

B.1 Targets tables

TABLE B.1— Properties of observed P91-FORS2 dataset in the Tucana dSph. Column (1) field Tuc0 and Tuc1; (2) slit aperture: numbers < 30 indicate observed targets from chip-1, otherwise from chip-2 – numbers counted from bottom to top of the CCD; (3) RA-Dec coordinated in J2000; (4) V band magnitude with error from VLT/FORS2 photometric catalog (5) I band magnitude with error from same catalog (6) l.o.s. heliocentric velocity with error; (6) metallicity with error; (8) S/N ratio in pxl^{-1} (the conversion factor to $\mathrm{\AA}^{-1}$ is 1.09);(9) probability of membership – the three columns indicate the probabilities obtained using the P91 dataset alone (P_1), combining with the P69 (P_2) and further adding the FLAMES data(P_3). Four stars had repeated measurements: targets 31, 32, 33, and 35 from Tuc0 field corresponding to targets 31, 32, 33, and 36 from Tuc1 field, respectively; in this table, we report the single measurements as well as the averaged values used during the analysis process.
Notes. In the P columns, stars marked as "Ph" are nonmembers, excluded according to their magnitudes and colors, or because they lack reliable measurements (see Sect. 3.4 for full description).

F	S	R.A., Dec (J2000) (deg)	V	I	v_{hel} ($\mathrm{km\,s^{-1}}$)	[Fe/H] (dex)	S/N ($\mathrm{pxl^{-1}}$)	P P_1	P_2	P_3
0	1	340.4913, -64.41896	22.79 ± 0.02	21.44 ± 0.04	176.6 ± 7.1	−1.37 ± 0.16	22.5	0.99	0.99	0.99
0	2	340.4834, -64.41816	22.75 ± 0.03	21.53 ± 0.04	157.8 ± 6.6	−2.00 ± 0.11	21.4	0.99	0.99	0.99
0	3	340.4762, -64.41057	22.33 ± 0.02	21.19 ± 0.04	189.8 ± 8.3	−2.66 ± 0.14	29.4	0.99	0.99	0.99
0	4	340.4645, -64.42837	22.69 ± 0.02	21.33 ± 0.04	183.9 ± 5.5	−2.17 ± 0.11	24.5	0.99	0.99	0.99
0	5	340.4565, -64.42895	22.88 ± 0.02	21.56 ± 0.03	167.0 ± 10.8	−1.75 ± 0.14	19.4	0.99	0.99	0.99
0	6	340.4511, -64.42363	22.19 ± 0.02	20.55 ± 0.03	165.5 ± 11.7	−1.25 ± 0.07	12.2	0.99	0.99	0.99
0	7	340.4421, -64.42360	22.29 ± 0.02	20.87 ± 0.03	183.6 ± 4.1	−1.29 ± 0.09	38.3	0.99	0.99	0.99
0	8	340.4334, -64.42592	22.81 ± 0.03	21.57 ± 0.03	182.8 ± 4.9	−1.37 ± 0.17	16.2	0.99	0.99	0.99
0	9	340.4283, -64.41176	22.72 ± 0.02	21.46 ± 0.04	155.1 ± 10.0	−2.12 ± 0.18	21.3	0.99	0.99	0.99
0	10	340.4199, -64.41700	22.83 ± 0.02	21.49 ± 0.04	174.2 ± 5.5	−1.28 ± 0.16	23.1	0.99	0.99	0.99

TABLE B.1— continued.

F	S	R.A., Dec (J2000) (deg)	V	I	v_{hel} (km s^{-1})	[Fe/H] (dex)	S/N (pxl^{-1})	P		
								P_1	P_2	P_3
0	11	340.4090, -64.41599	22.34 ± 0.02	20.91 ± 0.03	183.6 ± 5.7	−1.87 ± 0.10	36.3	0.99	0.99	0.99
0	12	340.3984, -64.41116	22.44 ± 0.02	20.96 ± 0.04	168.7 ± 4.4	−1.52 ± 0.11	29.0	0.99	0.99	0.99
0	13	340.3879, -64.41004	22.89 ± 0.02	21.55 ± 0.04	167.6 ± 5.5	−1.29 ± 0.18	20.7	0.99	0.99	0.99
0	14	340.3760, -64.42418	22.67 ± 0.02	21.36 ± 0.04	187.4 ± 5.0	−1.84 ± 0.14	26.6	0.99	0.99	0.99
0	15	340.3693, -64.41906	22.89 ± 0.02	21.82 ± 0.04	178.5 ± 10.2	−1.92 ± 0.18	18.8	0.99	0.99	0.99
0	16	340.3576, -64.41379	22.39 ± 0.02	20.17 ± 0.03	43.3 ± 5.8	−2.05 ± 0.05	54.0	Ph		
	rep.	340.6158, -64.40893	22.96 ± 0.02	21.36 ± 0.04	146.1 ± 7.0	−1.88 ± 0.12	27.0	0.02	0.02	0.03
0	31				147.5 ± 13.6	-1.81 ± 0.18	25.2			
1	31				145.6 ± 8.3	-1.94 ± 0.17	28.9			
	rep.	340.6056, -64.4071	21.65 ± 0.02	21.29 ± 0.03	/	/	24.3	Ph		
0	32				/	/	22.7			
1	32				/	/	25.9			
	rep.	340.5832, -64.43912	22.95 ± 0.02	21.36 ± 0.03	225.8 ± 4.4	−1.67 ± 0.09	26.5	0.00	0.00	0.00
0	33				221.8 ± 7.2	-1.75 ± 0.12	24.3			
1	33				228.3 ± 5.6	-1.55 ± 0.15	28.6			
0	34	340.5744, -64.41475	23.63 ± 0.03	22.46 ± 0.05	/	/	7.7	Ph		
	rep.	340.5692, -64.38342	22.39 ± 0.02	20.62 ± 0.03	179.8 ± 4.7	−1.83 ± 0.07	35.0	0.89	0.88	0.88
0	35				181.0 ± 6.4	-1.88 ± 0.11	32.5			
1	36				178.3 ± 6.9	-1.79 ± 0.09	37.5			
0	36	340.5508, -64.43098	22.78 ± 0.02	21.50 ± 0.04	185.0 ± 6.2	−1.49 ± 0.16	20.2	0.99	0.99	0.99
0	37	340.5418, -64.41572	23.23 ± 0.02	22.03 ± 0.05	175.0 ± 6.8	−1.62 ± 0.20	14.7	0.99	0.99	0.99
0	38	340.5302, -64.43026	23.65 ± 0.03	22.63 ± 0.08	182.8 ± 15.3	−1.40 ± 0.50	8.2	0.99	0.99	0.99
0	39	340.5278, -64.40337	23.15 ± 0.02	21.92 ± 0.04	185.3 ± 13.4	−1.32 ± 0.27	16.1	0.99	0.99	0.99
0	40	340.5186, -64.41192	22.90 ± 0.03	21.58 ± 0.05	162.1 ± 7.3	−1.08 ± 0.25	21.6	0.99	0.99	0.99
0	41	340.5072, -64.42974	22.39 ± 0.02	20.84 ± 0.03	179.2 ± 5.0	−1.18 ± 0.10	30.8	0.99	0.99	0.99
1	1	340.5224, -64.43385	23.46 ± 0.03	22.25 ± 0.07	214.3 ± 18.2	−1.79 ± 0.31	9.6	0.98	0.99	0.99
1	2	340.5116, -64.44016	22.67 ± 0.02	21.36 ± 0.05	170.2 ± 5.1	−2.02 ± 0.13	23.7	0.99	0.99	0.99
1	3	340.5134, -64.41830	22.78 ± 0.02	21.44 ± 0.05	177.5 ± 2.9	−1.25 ± 0.16	26.6	0.99	0.99	0.99
1	4	340.4990, -64.42399	22.63 ± 0.02	21.33 ± 0.03	179.4 ± 4.2	−2.15 ± 0.17	26.6	0.99	0.99	0.99
1	5	340.4922, -64.42342	22.63 ± 0.02	21.41 ± 0.04	192.5 ± 6.9	−1.78 ± 0.10	26.6	0.99	0.99	0.99
1	6	340.4890, -64.41446	23.31 ± 0.02	22.12 ± 0.06	221.8 ± 13.8	−1.81 ± 0.35	13.2	0.98	0.98	0.98
1	7	340.4818, -64.41523	22.75 ± 0.02	21.33 ± 0.04	176.7 ± 4.0	−0.94 ± 0.16	27.9	0.99	0.99	0.99
1	8	340.4706, -64.42798	22.86 ± 0.02	21.54 ± 0.05	185.4 ± 6.8	−0.89 ± 0.20	22.0	0.99	0.99	0.99
1	9	340.4658, -64.42591	22.78 ± 0.02	21.49 ± 0.03	174.6 ± 4.5	−1.06 ± 0.19	20.3	0.99	0.99	0.99
1	10	340.4619, -64.41730	22.60 ± 0.02	21.29 ± 0.03	185.8 ± 3.7	−1.01 ± 0.19	25.6	0.99	0.99	0.99
1	11	340.4553, -64.41642	22.42 ± 0.02	21.12 ± 0.03	188.1 ± 5.0	−1.48 ± 0.14	33.6	0.99	0.99	0.99
1	12	340.4446, -64.42166	22.73 ± 0.03	21.47 ± 0.03	189.7 ± 5.5	−1.30 ± 0.18	22.3	0.99	0.99	0.99
1	13	340.4351, -64.42136	22.59 ± 0.02	21.24 ± 0.03	185.1 ± 9.4	−1.47 ± 0.16	26.2	0.99	0.99	0.99
1	14	340.4321, -64.41439	22.61 ± 0.02	21.15 ± 0.03	177.0 ± 5.5	−1.18 ± 0.17	27.7	0.99	0.99	0.99
1	15	340.4200, -64.42276	22.53 ± 0.02	21.24 ± 0.04	189.5 ± 8.9	−2.89 ± 0.17	24.7	0.99	0.99	0.99
1	16	340.4267, -64.39091	22.43 ± 0.02	20.59 ± 0.03	-8.5 ± 4.1	−1.88 ± 0.10	48.0	0.00	0.00	0.00
1	17	340.4098, -64.41052	23.05 ± 0.02	21.79 ± 0.05	/	/	16.1	Ph		
1	18	340.4026, -64.40694	22.67 ± 0.02	21.35 ± 0.04	172.9 ± 5.1	−1.89 ± 0.17	25.9	0.99	0.99	0.99
1	19	340.3919, -64.41256	22.70 ± 0.02	21.36 ± 0.04	175.5 ± 5.4	−1.95 ± 0.13	23.7	0.99	0.99	0.99
1	20	340.3787, -64.43124	22.22 ± 0.02	22.19 ± 0.05	/	/	7.9	Ph		
1	34	340.5865, -64.38883	20.16 ± 0.01	19.47 ± 0.02	/	/	49.0	Ph		
1	35	340.5724, -64.39045	23.15 ± 0.03	20.41 ± 0.04	/	/	27.3	Ph		
1	37	340.5571, -64.38788	22.93 ± 0.02	21.28 ± 0.05	154.9 ± 4.5	−2.08 ± 0.16	29.1	0.06	0.07	0.08

TABLE B.2— Properties of observed P69-FORS2 dataset in the Tucana dSph. Column (1) slit aperture: numbers < 30 indicate observed targets from chip-1, otherwise from chip-2 – numbers counted from bottom to top of the CCD; (2) RA-Dec coordinated in J2000; (3) V band magnitude with error from VLT/FORS2 photometric catalog (4) I band magnitude with error from same catalog (5) l.o.s. heliocentric velocity with error; (6) metallicity with error; (7) S/N ratio in pxl^{-1} (the conversion factor to $Å^{-1}$ is 1.08); (8) probability of membership according to the best-fitting kinematic model – the three columns indicate the probabilities obtained using the P69 dataset alone (P_1), combining with the P91 (P_2) and further adding the FLAMES data(P_3).
Notes. In the P columns, stars marked as "Ph" are nonmembers, excluded according to their magnitudes and colors, or because their measurements proved to be unreliable (see Sect. 3.4 and Appendix 3.A for full description). $^{(a)}$ New with respect to Fraternali et al. (2009); $^{(b)}$ in common with the P91-FORS2 dataset.

Slit	R.A., Dec (J2000) (deg)	V	I	v_{hel} (km/s)	[Fe/H] (dex)	S/N (pxl^{-1})	P P_1	P_2	P_3
1	340.4472, -64.42209	22.44 ± 0.02	20.97 ± 0.02	180.4 ± 4.8	-1.07 ± 0.17	20.4	0.99	0.99	0.99
2	340.4532, -64.42234	22.48 ± 0.02	21.26 ± 0.02	176.3 ± 6.8	-1.56 ± 0.29	15.0	0.99	0.99	0.99
3	340.4586, -64.39465	22.22 ± 0.02	20.96 ± 0.02	144.2 ± 5.2	-1.52 ± 0.22	19.8	0.17	0.01	0.02
4	340.4647, -64.4236	22.64 ± 0.01	21.22 ± 0.01	186.8 ± 7.4	-1.61 ± 0.16	19.4	0.99	0.99	0.99
5$^{(a)}$	340.4698, -64.43846	23.26 ± 0.03	21.50 ± 0.05	130.4 ± 10.1	-1.37 ± 0.20	11.9	0.13	0.04	0.04
6	340.4748, -64.41809	22.39 ± 0.01	20.87 ± 0.01	184.8 ± 4.6	-1.96 ± 0.10	29.8	0.99	0.99	0.99
7	340.4799, -64.40572	22.28 ± 0.02	20.85 ± 0.02	178.9 ± 4.8	-1.92 ± 0.17	24.5	0.99	0.99	0.99
8	340.4881, -64.41732	22.73 ± 0.03	21.19 ± 0.03	177.7 ± 6.2	-1.64 ± 0.13	18.9	0.99	0.99	0.99
9$^{(b)}$	340.4920, -64.42341	22.61 ± 0.02	21.35 ± 0.02	232.8 ± 8.0	-1.28 ± 0.22	15.4	Ph		
10	340.4963, -64.41156	22.45 ± 0.02	21.01 ± 0.02	225.0 ± 7.2	-2.00 ± 0.18	19.8	Ph		
11	340.5012, -64.41237	22.73 ± 0.01	21.49 ± 0.01	166.8 ± 5.4	-1.19 ± 0.35	13.0	0.99	0.99	0.99
12	340.5069, -64.40718	22.28 ± 0.02	20.86 ± 0.02	181.8 ± 8.3	-1.87 ± 0.18	21.8	0.99	0.99	0.99
13	340.5105, -64.42116	22.31 ± 0.02	20.83 ± 0.02	209.9 ± 7.6	-1.96 ± 0.16	18.3	0.99	0.96	0.96
14	340.5140, -64.41146	22.49 ± 0.03	20.96 ± 0.02	191.7 ± 5.3	-1.41 ± 0.14	23.9	0.99	0.99	0.99
23$^{(b)}$	340.5695, -64.3833	22.41 ± 0.03	20.65 ± 0.04	179.5 ± 5.7	-1.95 ± 0.16	25.2	0.79		
24	340.5742, -64.37577	0.0 ± 0.0	0.0 ± 0.0	4.2 ± 4.8	/	32.8	0.00	0.00	0.00
25$^{(a,b)}$	340.5836, -64.43902	22.95 ± 0.02	21.46 ± 0.03	236.4 ± 14.1	-2.01 ± 0.26	17.4	0.63		
31	340.3294, -64.4244	21.78 ± 0.02	20.59 ± 0.02	208.6 ± 5.2	/	23.5	Ph		
33$^{(a)}$	340.3435, -64.39041	22.61 ± 0.02	21.33 ± 0.02	110.3 ± 14.9	-2.42 ± 0.28	14.6	0.00	0.00	0.00
35	340.3536, -64.41425	22.59 ± 0.02	21.0 ± 0.02	76.6 ± 7.3	-1.77 ± 0.15	21.4	0.00	0.00	0.00
39$^{(a,b)}$	340.3762, -64.4242	22.69 ± 0.02	21.38 ± 0.02	197.3 ± 8.3	-2.11 ± 0.21	12.9	0.99		
40	340.3820, -64.45349	0.0 ± 0.0	0.0 ± 0.0	25.6 ± 11.1	/	27.0	0.00	0.00	0.00
43$^{(b)}$	340.3973, -64.41121	22.45 ± 0.02	20.98 ± 0.02	207.8 ± 7.3	-1.14 ± 0.17	21.3	Ph		
44	340.4024, -64.41617	22.27 ± 0.02	20.77 ± 0.02	180.1 ± 5.2	-2.20 ± 0.12	25.7	0.99	0.99	0.99
45	340.4100, -64.40206	22.41 ± 0.02	21.03 ± 0.02	174.9 ± 5.9	-2.12 ± 0.15	21.3	0.99	0.99	0.99
46$^{(a)}$	340.4163, -64.40805	21.09 ± 0.01	20.36 ± 0.01	-160.6 ± 4.8	/	31.7	Ph		
47	340.4206, -64.41588	22.68 ± 0.02	21.28 ± 0.02	195.7 ± 6.0	-1.33 ± 0.20	14.7	0.99	0.99	0.99
49	340.4348, -64.40812	22.37 ± 0.03	21.01 ± 0.02	172.5 ± 6.8	-1.97 ± 0.18	24.3	0.99	0.99	0.99

TABLE B.3— Properties of observed FLAMES/GIRAFFE dataset in the Tucana dSph. Column (1) object-ID from fits header; (2) fiber-ID used through text; (3) RA-Dec coordinated in J2000; (4) V band magnitude transformed from DES photometric catalog (5) I band magnitude transformed from the same catalog (6) l.o.s. heliocentric velocity with error; (7) S/N ratio in pxl^{-1} (the conversion factor to $Å^{-1}$ is 2.24); (8) probability of membership according to the best-fitting kinematic model – the two columns indicate the probabilities obtained using the FLAMES dataset alone (P_1), and combining with the FORS2 data(P_2).
Notes. In the P columns, stars marked as "Ph" are non-members excluded according to their magnitudes and colors or because their measurements resulted to be not reliable or because having a S/N< $10Å^{-1}$ (see Sect. 3.4 and Appendix 3.A for full description).
[a] In common with the FORS2 datasets.

Object	Fiber	R.A., Dec (J2000) (deg)	V	I	v_{hel} (km/s)	S/N (pxl^{-1})	P P_1	P_2
44068	1	340.34104, -64.366778	22.976	20.486	19.7 ± 6.4	12.0	Ph	
58039	2	340.27637, -64.447250	23.368	22.183	/	0.8	Ph	
53427	3	340.38987, -64.422028	22.861	21.823	/	2.2	Ph	
49196	4	340.40287, -64.401111	23.340	22.133	/	3.4	Ph	
100020	5	340.32892, -64.424889	24.880	22.406	/	3.3	Ph	
51120	6	340.36892, -64.411639	22.996	21.890	160.6 ± 18.8	3.2	Ph	
100019	7	340.38075, -64.453639	20.716	19.920	23.6 ± 9.6	15.3	Ph	
39027	8	340.54671, -64.333556	22.992	21.378	79.6 ± 18.1	6.2	0.00	0.00
31104	9	340.34300, -64.279222	22.230	20.723	292.6 ± 16.6	9.4	0.00	0.00
27260	10	340.47533, -64.253083	22.898	21.565	39.3 ± 9.0	3.8	Ph	
37852	11	340.49483, -64.326306	23.199	21.657	7.0 ± 7.1	5.2	0.0	0.00
37244	12	340.42596, -64.322194	22.103	20.879	191.3 ± 14.3	7.8	0.0	0.00
45927	13	340.13696, -64.379889	22.964	21.509	451.9 ± 4.5	3.7	Ph	
44431	14	340.31504, -64.368972	22.904	21.351	-201.6 ± 13.2	4.9	Ph	
45504	15	340.21796, -64.376917	23.023	21.510	234.5 ± 13.8	5.4	0.00	0.00
40746	16	340.45733, -64.345333	22.190	21.000	230.3 ± 18.6	6.6	0.00	0.00
30380	17	340.29579, -64.274167	23.089	21.909	/	3.5	Ph	
34523	18	340.51400, -64.302361	22.602	21.179	/	5.3	Ph	
32778	19	340.45058, -64.290778	24.225	21.797	/	3.8	Ph	
32116	20	340.50783, -64.286083	22.204	20.595	32.4 ± 5.2	11.8	0.00	0.00
43472	21	340.44033, -64.363083	22.615	21.174	-38.7 ± 11.9	4.4	Ph	
39444	22	340.25721, -64.336389	22.121	20.730	126.7 ± 7.2	10.0	0.00	0.00
24956	23	340.37875, -64.235778	0.000	0.000	/	3.2	Ph	
33846	24	340.36354, -64.297972	22.937	21.543	-42.5 ± 10.3	5.3	0.00	0.00
42547	25	340.52042, -64.357194	22.577	21.207	105.9 ± 8.6	4.9	Ph	
30098	26	340.50979, -64.272278	17.807	16.986	123.9 ± 1.1	109.6	Ph	
20262	27	340.21804, -64.200806	22.595	20.826	36.0 ± 18.1	8.6	0.00	0.00
28726	28	340.55079, -64.263167	23.994	21.447	16.6 ± 18.2	5.7	Ph	
28435	29	340.56392, -64.261222	0.000	0.000	9.2 ± 13.2	3.8	Ph	
36322	30	340.44375, -64.315444	22.305	20.703	30.3 ± 11.8	10.2	0.00	0.00
40890	31	340.42958, -64.346389	23.053	21.507	-62.0 ± 23.8	5.7	0.00	0.00
22014	32	340.56696, -64.213194	22.229	20.861	-22.4 ± 10.0	7.9	0.00	0.00
24597	33	340.53050, -64.233250	23.047	21.985	/	2.4	Ph	

TABLE B.3— continued.

Object	Fiber	R.A., Dec (J2000) (deg)	V	I	v_{hel} (km/s)	S/N (pxl^{-1})	P P_1	P P_2
20184	34	340.44471, -64.200333	22.705	20.813	119.3 ± 12.0	6.8	0.00	0.00
25301	35	340.69692, -64.238194	23.488	22.373	/	3.1	Ph	
21919	36	340.63321, -64.212528	22.609	21.043	61.9 ± 7.7	6.1	0.00	0.00
31878	37	340.64842, -64.284611	22.696	21.652	/	4.3	Ph	
24201	38	340.67017, -64.230417	22.557	21.386	/	2.9	Ph	
4032	39	340.50846, -64.087278	22.940	21.389	/	1.5	Ph	
16892	40	340.56733, -64.178917	22.773	21.559	/	1.9	Ph	
31326	41	340.62975, -64.280972	22.065	20.503	12.7 ± 7.2	13.4	0.00	0.00
5642	42	340.45183, -64.099333	0.000	0.000	169.0 ± 14.0	2.2	Ph	
36740	43	340.69904, -64.318389	22.802	21.257	226.6 ± 13.3	5.1	0.00	0.00
13690	44	340.76192, -64.156333	22.987	21.887	/	2.1	Ph	
32638	45	340.56775, -64.289861	22.388	20.678	111.2 ± 14.0	12.0	0.00	0.00
32163	46	340.58575, -64.286389	22.559	20.710	117.7 ± 10.7	10.4	0.00	0.00
30991	47	340.65567, -64.278278	18.715	17.675	-50.1 ± 1.0	42.5	Ph	
20980	48	340.70929, -64.205528	22.358	20.702	1.2 ± 6.3	10.9	0.00	0.00
18416	49	340.65187, -64.188583	22.400	21.031	30.2 ± 6.2	5.5	0.00	0.00
24848	50	340.61529, -64.235028	22.317	20.877	187.0 ± 40.5	7.5	Ph	
21528	51	340.70312, -64.209722	22.354	20.615	45.3 ± 3.8	7.0	0.00	0.00
23752	52	340.47312, -64.226722	23.407	20.383	-23.1 ± 8.4	10.2	Ph	
31071	53	340.76042, -64.279000	22.194	20.633	-49.6 ± 8.6	10.4	0.00	0.00
31001	54	340.52425, -64.278361	19.060	18.133	-8.5 ± 1.3	48.2	Ph	
16300	55	340.81579, -64.175000	22.232	20.746	/	6.2	Ph	
19109	56	340.75412, -64.193778	23.158	21.607	10.0 ± 28.4	3.2	Ph	
18966	57	340.82242, -64.192750	22.928	21.727	-45.0 ± 11.4	4.0	Ph	
32477	58	340.72533, -64.288583	22.329	20.713	166.8 ± 9.7	8.8	0.00	0.00
27434	59	340.42087, -64.254250	22.831	22.089	/	4.0	Ph	
23221	60	340.79529, -64.222528	22.896	21.570	/	3.7	Ph	
22156	61	340.92625, -64.214333	22.016	20.832	36.2 ± 5.0	4.6	Ph	
37211	62	340.60975, -64.322028	23.534	22.110	71.6 ± 8.9	3.9	Ph	
35540	63	340.60425, -64.309583	23.512	21.524	35.1 ± 8.0	6.0	0.00	0.00
20829	64	340.86492, -64.204417	22.850	21.214	64.4 ± 9.6	4.8	Ph	
35289	65	340.95317, -64.307861	22.275	21.177	150.2 ± 22.5	3.9	Ph	
35409	66	340.89879, -64.308722	22.419	20.780	-53.4 ± 5.6	7.1	0.00	0.00
32709	67	340.92150, -64.290306	22.070	20.786	145.1 ± 5.7	8.4	0.00	0.00
28348	68	340.93237, -64.260694	21.678	21.149	74.5 ± 15.9	1.2	Ph	
21201	69	340.56067, -64.207028	22.672	20.824	21.8 ± 7.2	6.3	0.00	0.00
34708	70	340.81462, -64.303722	22.380	21.111	31.0 ± 10.6	5.1	0.00	0.00
26258	71	340.91354, -64.245583	22.960	21.634	/	4.3	Ph	
40705	72	340.62008, -64.345167	23.701	22.204	/	4.1	Ph	
25087	73	340.92037, -64.236667	23.166	21.664	/	3.2	Ph	
43260	74	340.79483, -64.361667	21.816	20.598	119.6 ± 6.4	7.1	0.00	0.00
38186	75	340.82146, -64.328167	22.477	21.367	-3.6 ± 10.6	3.1	Ph	
44653	76	340.78854, -64.370306	23.135	22.253	247.6 ± 15.6	4.5	Ph	
27730	77	340.57954, -64.256472	19.371	17.200	33.2 ± 2.5	25.3	Ph	

TABLE B.3— continued.

Object	Fiber	R.A., Dec (J2000) (deg)	V	I	v_{hel} (km/s)	S/N (pxl^{-1})	P P_1	P P_2
32288	78	340.60825, -64.287361	21.536	19.870	7.0 ± 3.6	15.0	Ph	
43618	79	340.65275, -64.363917	22.909	21.618	18.2 ± 15.2	5.2	0.00	0.00
51984	80	340.82829, -64.415750	22.555	21.163	68.8 ± 9.9	3.5	Ph	
47042	81	340.80346, -64.387083	23.206	22.295	32.4 ± 10.2	2.5	Ph	
48384	82	340.67171, -64.396111	22.925	21.382	151.5 ± 14.7	5.6	0.11	0.09
40996	83	340.55800, -64.347111	21.789	19.157	8.5 ± 4.5	17.1	Ph	
48246	84	340.90804, -64.395111	23.503	22.183	75.9 ± 10.6	1.6	Ph	
7717	85	340.36279, -64.114750	23.246	22.057	-127.7 ± 16.4	2.0	Ph	
53621	86	340.76875, -64.422778	22.723	21.204	138.3 ± 7.6	4.5	Ph	
46156	87	340.69479, -64.381472	23.079	21.690	-78.4 ± 13.8	4.2	Ph	
100022	88	340.57396, -64.375972	21.449	20.089	-1.9 ± 3.9	15.0	0.00	0.00
48450	89	340.69687, -64.396500	23.093	22.168	51.1 ± 11.3	1.8	Ph	
54894	90	340.66104, -64.428417	23.263	21.835	165.0 ± 11.5	3.5	Ph	
100003	91	340.47454, -64.418306	0.000	0.000	178.5 ± 3.6	8.5	0.99	[a]
49630	92	340.52779, -64.403528	23.248	22.008	173.9 ± 9.5	3.2	Ph	
100014	93	340.45825, -64.394861	22.315	20.943	145.3 ± 5.4	8.7	0.17	[a]
100009	94	340.49612, -64.411722	0.000	0.000	188.7 ± 3.6	8.6	0.99	0.99
100013	95	340.50742, -64.407194	0.000	0.000	73.3 ± 11.1	1.7	Ph	
100021	96	340.56921, -64.383500	22.354	20.657	186.2 ± 12.6	6.8	0.80	[a]
52804	97	340.63075, -64.419389	22.454	21.103	-194.8 ± 5.2	6.5	0.00	0.00
52613	98	340.61704, -64.418556	23.114	21.918	188.8 ± 15.0	3.6	Ph	
39325	99	340.55700, -64.335500	23.549	20.742	6.0 ± 12.0	8.8	Ph	
100002	100	340.46446, -64.423806	21.317	20.260	188.0 ± 15.6	5.7	0.99	[a]
49958	101	340.42304, -64.405278	22.881	21.748	167.9 ± 12.7	3.4	Ph	
100016	102	340.40967, -64.402278	22.405	21.056	174.0 ± 6.1	6.0	0.99	[a]
100005	103	340.43446, -64.408333	22.420	21.021	180.9 ± 5.0	8.0	0.99	[a]
50951	104	340.44454, -64.410722	22.730	21.691	/	2.8	Ph	
9224	105	340.31279, -64.126778	22.600	21.255	-122.7 ± 10.2	3.7	Ph	
100018	106	340.35333, -64.414500	22.687	20.941	67.1 ± 3.9	7.1	0.00	[a]
100017	107	340.39833, -64.411361	22.249	20.909	173.4 ± 6.0	7.7	0.99	[a]
100006	108	340.49225, -64.423611	22.349	21.126	191.5 ± 8.2	5.6	0.99	[a]
100001	109	340.44696, -64.422306	21.427	20.323	175.1 ± 3.8	8.4	0.99	[a]
47569	110	340.34308, -64.390611	22.639	21.297	149.9 ± 11.1	5.3	0.63	0.54
46004	111	340.42396, -64.380417	22.728	21.480	18.6 ± 17.8	5.0	0.00	0.00
54972	112	340.25037, -64.428806	23.127	22.017	/	2.2	Ph	
43720	113	340.41837, -64.364556	21.006	19.251	63.2 ± 2.5	30.8	Ph	
21138	114	340.59517, -64.206583	23.023	21.318	105.6 ± 26.0	6.0	0.00	0.00
39993	115	340.32687, -64.340028	21.844	20.614	-43.2 ± 10.5	6.5	0.00	0.00
50864	116	340.38775, -64.410250	22.784	21.569	/	3.0	Ph	
39557	117	340.14258, -64.337139	22.481	21.281	/	2.7	Ph	
25558	118	340.42058, -64.240028	22.349	20.730	172.8 ± 8.6	5.9	0.00	0.00
33805	119	340.28633, -64.297639	22.541	21.346	-364.1 ± 7.5	3.3	Ph	
34818	120	340.29067, -64.304556	22.643	21.338	/	3.0	Ph	

TABLE B.3— continued.

Object	Fiber	R.A., Dec (J2000) (deg)	V	I	v_{hel} (km/s)	S/N (pxl^{-1})	P P_1	P_2
28959	121	340.13192, -64.264889	22.808	21.283	/	2.5	Ph	
26205	122	340.18454, -64.245194	22.136	20.540	-1.2 ± 6.2	5.3	0.00	0.00
32371	123	340.25575, -64.287861	22.674	20.963	161.0 ± 13.4	4.5	Ph	
26562	124	340.47250, -64.248028	22.589	21.159	-404.5 ± 8.8	4.3	Ph	
33199	125	340.05833, -64.293333	23.122	22.000	/	2.7	Ph	
38665	126	340.39025, -64.331333	20.370	19.311	100.5 ± 5.4	16.8	Ph	
15314	127	340.19367, -64.168111	22.785	21.271	193.8 ± 23.0	2.6	Ph	
25202	128	340.42783, -64.237500	23.155	21.857	319.1 ± 12.4	2.7	Ph	
22526	129	340.27612, -64.217083	22.241	19.161	6.8 ± 7.8	11.0	Ph	
28804	130	340.29137, -64.263722	22.447	21.320	-419.7 ± 3.3	3.0	Ph	
22297	131	340.13142, -64.215389	21.895	20.688	-37.1 ± 10.1	5.1	0.00	0.00
25382	132	340.18987, -64.238778	0.000	0.000	/	3.0	Ph	
13504	133	340.24646, -64.155139	22.938	21.329	136.9 ± 15.8	3.6	Ph	
19228	134	340.57158, -64.194472	23.355	22.151	/	2.9	Ph	
5411	135	340.47821, -64.097583	22.284	21.120	/	3.0	Ph	
7674	136	340.45483, -64.114306	22.383	21.151	/	3.2	Ph	
24957	137	340.75162, -64.235778	22.854	21.301	/	4.2	Ph	
24991	138	340.76054, -64.235972	23.274	22.108	/	2.6	Ph	
31905	139	340.54608, -64.284778	22.730	21.167	45.5 ± 16.0	5.6	0.00	0.00
20561	140	340.84067, -64.202861	21.969	20.723	199.4 ± 10.7	6.1	0.00	0.00
13652	141	340.89246, -64.156111	22.599	20.829	/	3.2	Ph	
29029	142	340.98737, -64.265417	23.359	22.117	/	1.9	Ph	
28008	143	340.92996, -64.258472	0.000	0.000	83.4 ± 14.9	4.8	Ph	
43939	144	340.83217, -64.366000	22.510	20.554	40.1 ± 5.4	7.1	0.00	0.00
41813	145	340.53267, -64.352583	22.750	21.276	142.6 ± 18.3	6.3	0.01	0.01
40477	146	340.93167, -64.343667	19.724	18.922	168.6 ± 3.4	19.6	Ph	
38363	147	340.56947, -64.329389	23.588	21.699	-44.2 ± 9.7	3.2	Ph	
54686	148	340.83783, -64.427528	22.108	20.905	180.1 ± 11.6	3.4	Ph	
41818	149	340.48062, -64.352611	0.000	0.000	160.9 ± 21.5	3.5	Ph	
52574	150	340.77154, -64.418333	23.343	22.174	68.4 ± 5.3	2.0	Ph	
50194	151	340.45900, -64.406667	23.010	21.531	/	3.8	Ph	
52007	152	340.54187, -64.415889	23.029	21.919	/	2.8	Ph	
100015	153	340.51367, -64.411667	22.436	20.912	181.9 ± 6.3	5.2	0.99	[a]
52859	154	340.60392, -64.419611	22.947	21.748	/	2.3	Ph	
54691	155	340.63350, -64.427556	23.203	22.063	/	2.5	Ph	
60765	156	340.69737, -64.465083	22.639	21.274	147.8 ± 17.3	3.0	Ph	
50636	157	340.61592, -64.409111	23.031	21.272	/	3.2	Ph	
50350	158	340.45050, -64.407500	22.775	21.648	197.8 ± 9.3	2.6	Ph	
46819	159	340.41362, -64.385528	22.469	20.773	-34.9 ± 11.4	6.6	0.00	0.00
100007	160	340.42029, -64.416056	22.412	21.129	-88.3 ± 6.2	4.7	Ph	
53700	161	340.46612, -64.423111	0.000	0.000	185.6 ± 11.5	2.5	Ph	
51422	162	340.36446, -64.413167	23.310	22.180	204.1 ± 4.6	2.8	Ph	
51322	163	340.18804, -64.412694	22.476	21.120	/	3.0	Ph	

TABLE B.3— continued.

Object	Fiber	R.A., Dec (J2000) (deg)	V	I	v_{hel} (km/s)	S/N (pxl^{-1})	P P_1	P P_2
43254	164	340.23679, -64.361611	22.178	21.031	229.1 ± 9.0	2.0	Ph	

Bibliography

Abbott, T. M. C., Abdalla, F. B., Allam, S., et al. 2018, ApJS, 239, 18

Albers, S. M., Weisz, D. R., Cole, A. A., et al. 2019, MNRAS, 490, 5538

Albert, L., Demers, S., & Kunkel, W. E. 2000, AJ, 119, 2780

Allende Prieto, C., Fernández-Alvar, E., Schlesinger, K. J., et al. 2014, A&A, 568, A7

Alonso, A., Arribas, S., & Martínez-Roger, C. 1999, A&AS, 140, 261

Amorisco, N. C., & Evans, N. W. 2012a, ApJL, 756, L2

—. 2012b, MNRAS, 419, 184

Amorisco, N. C., Evans, N. W., & van de Ven, G. 2014, Nature, 507, 335

Aparicio, A., Carrera, R., & Martínez-Delgado, D. 2001, AJ, 122, 2524

Aparicio, A., & Gallart, C. 2004, AJ, 128, 1465

Appenzeller, I., Fricke, K., Fürtig, W., et al. 1998, The Messenger, 94, 1

Arraki, K. S., Klypin, A., More, S., & Trujillo-Gomez, S. 2014, MNRAS, 438, 1466

Asplund, M., Grevesse, N., Sauval, A. J., & Scott, P. 2009, ARA&A, 47, 481

Bacon, R., Accardo, M., Adjali, L., et al. 2010, Society of Photo-Optical Instrumentation Engineers (SPIE) Conference Series, Vol. 7735, The MUSE second-generation VLT instrument, 773508

Battaglia, G., Helmi, A., & Breddels, M. 2013, NewAR, 57, 52

Battaglia, G., Helmi, A., Tolstoy, E., et al. 2008a, ApJL, 681, L13

Battaglia, G., Irwin, M., Tolstoy, E., et al. 2008b, MNRAS, 383, 183

Battaglia, G., & Starkenburg, E. 2012, A&A, 539, A123

Battaglia, G., Tolstoy, E., Helmi, A., et al. 2011, MNRAS, 411, 1013

—. 2006, A&A, 459, 423

Beers, T. C., Carollo, D., Ivezić, Ž., et al. 2012, ApJ, 746, 34

Begum, A., & Chengalur, J. N. 2004, A&A, 413, 525

Belokurov, V. 2013, NewAR, 57, 100

Belokurov, V., & Koposov, S. E. 2016, Monthly Notices of the Royal Astronomical Society, 456, 602

Benítez-Llambay, A., Navarro, J. F., Abadi, M. G., et al. 2016, MNRAS, 456, 1185

Berger, T. A., Kudritzki, R.-P., Urbaneja, M. A., et al. 2018, ApJ, 860, 130

Bernard, E. J., Aparicio, A., Gallart, C., Padilla-Torres, C. P., & Panniello, M. 2007, AJ, 134, 1124

Bernard, E. J., Monelli, M., Gallart, C., et al. 2009, ApJ, 699, 1742

—. 2010, ApJ, 712, 1259

Bettinelli, M., Hidalgo, S. L., Cassisi, S., Aparicio, A., & Piotto, G. 2018, MNRAS, 476, 71

Binney, J. 1978, MNRAS, 183, 501

Binney, J., & Tremaine, S. 1987, Galactic dynamics

Blumenthal, G. R., Faber, S. M., Primack, J. R., & Rees, M. J. 1984, Nature, 311, 517

Borissova, J., Georgiev, L., Kurtev, R., et al. 2000, RMxAA, 36, 151

Boylan-Kolchin, M., Bullock, J. S., & Kaplinghat, M. 2012, MNRAS, 422, 1203

Breddels, M. A., & Helmi, A. 2014, ApJL, 791, L3

Bresolin, F., Urbaneja, M. A., Gieren, W., Pietrzyński, G., & Kudritzki, R.-P. 2007, ApJ, 671, 2028

Bressan, A., Marigo, P., Girardi, L., et al. 2012, MNRAS, 427, 127

Brook, C. B., & Di Cintio, A. 2015, MNRAS, 450, 3920

Brooks, A. M., & Zolotov, A. 2014, ApJ, 786, 87

Buchner, J., Georgakakis, A., Nandra, K., et al. 2014, A&A, 564, A125

Buck, T., Macciò, A. V., Dutton, A. A., Obreja, A., & Frings, J. 2019, MNRAS, 483, 1314

Bullock, J. S., & Boylan-Kolchin, M. 2017, ARA&A, 55, 343

Carrera, R. 2012, A&A, 544, A109

Carrera, R., Aparicio, A., Martínez-Delgado, D., & Alonso-García, J. 2002, AJ, 123, 3199

Carrera, R., Pancino, E., Gallart, C., & del Pino, A. 2013, MNRAS, 434, 1681

Carroll, B. W., & Ostlie, D. A. 2006, An introduction to modern astrophysics and cosmology

Cayrel, R. 1988, in IAU Symposium, Vol. 132, The Impact of Very High S/N Spectroscopy on Stellar Physics, ed. G. Cayrel de Strobel & M. Spite, 345

Cenarro, A. J., Cardiel, N., Gorgas, J., et al. 2001, MNRAS, 326, 959

Chambers, K. C., Magnier, E. A., Metcalfe, N., et al. 2016, arXiv e-prints, arXiv:1612.05560

Chun, S.-H., Jung, M., Kang, M., Kim, J.-W., & Sohn, Y.-J. 2015, A&A, 578, A51

Cicuéndez, L., & Battaglia, G. 2018, MNRAS, 480, 251

Cicuéndez, L., Battaglia, G., Irwin, M., et al. 2018, A&A, 609, A53

Cioni, M. R. L. 2009, A&A, 506, 1137

Cioni, M. R. L., Girardi, L., Marigo, P., & Habing, H. J. 2006, A&A, 448, 77

Cole, A. A., Smecker-Hane, T. A., Tolstoy, E., Bosler, T. L., & Gallagher, J. S. 2004, MNRAS, 347, 367

Cole, A. A., Weisz, D. R., Dolphin, A. E., et al. 2014, ApJ, 795, 54

Cole, A. A., Tolstoy, E., Gallagher, John S., I., et al. 1999, AJ, 118, 1657

Collins, M. L. M., Chapman, S. C., Rich, R. M., et al. 2013, ApJ, 768, 172

de Blok, W. J. G., Walter, F., Brinks, E., et al. 2008, AJ, 136, 2648

de Boer, T. J. L., Belokurov, V., & Koposov, S. 2015, MNRAS, 451, 3489

Deason, A. J., Belokurov, V., & Evans, N. W. 2011, MNRAS, 416, 2903

Demers, S., Battinelli, P., & Kunkel, W. E. 2006, ApJL, 636, L85

Dutton, A. A., & Macciò, A. V. 2014, MNRAS, 441, 3359

Dutton, A. A., Macciò, A. V., Frings, J., et al. 2016, MNRAS, 457, L74

Einasto, J., Saar, E., Kaasik, A., & Chernin, A. D. 1974, Nature, 252, 111

Fattahi, A., Navarro, J. F., & Frenk, C. S. 2020, MNRAS, 493, 2596

Fattahi, A., Navarro, J. F., Frenk, C. S., et al. 2018, MNRAS, 476, 3816

Fernández-Alvar, E., Allende Prieto, C., Schlesinger, K. J., et al. 2015, A&A, 577, A81

Feroz, F., Hobson, M. P., & Bridges, M. 2009, MNRAS, 398, 1601

Ferrero, I., Abadi, M. G., Navarro, J. F., Sales, L. V., & Gurovich, S. 2012, MNRAS, 425, 2817

Fillingham, S. P., Cooper, M. C., Kelley, T., et al. 2019, arXiv e-prints, arXiv:1906.04180

Foreman-Mackey, D., Hogg, D. W., Lang, D., & Goodman, J. 2013, PASP, 125, 306

Fouquet, S., Łokas, E. L., del Pino, A., & Ebrová, I. 2017, MNRAS, 464, 2717

Fraternali, F., Tolstoy, E., Irwin, M. J., & Cole, A. A. 2009, A&A, 499, 121

Fritz, T. K., Battaglia, G., Pawlowski, M. S., et al. 2018, A&A, 619, A103

Gaia Collaboration, Helmi, A., van Leeuwen, F., et al. 2018, A&A, 616, A12

Gallart, C., Monelli, M., Mayer, L., et al. 2015, ApJL, 811, L18

Garcia, M., Herrero, A., Najarro, F., Lennon, D. J., & Alejandro Urbaneja, M. 2014, ApJ, 788, 64

Garcia, M., Herrero, A., Vicente, B., et al. 2009, A&A, 502, 1015

Garrison-Kimmel, S., Wetzel, A., Hopkins, P. F., et al. 2019a, MNRAS, 489, 4574

Garrison-Kimmel, S., Hopkins, P. F., Wetzel, A., et al. 2019b, MNRAS, 487, 1380

Geha, M., Wechsler, R. H., Mao, Y.-Y., et al. 2017, ApJ, 847, 4

Girardi, L., Bressan, A., Bertelli, G., & Chiosi, C. 2000, A&AS, 141, 371

Gonneau, A., Lançon, A., Trager, S. C., et al. 2016, A&A, 589, A36

Goodman, J., & Weare, J. 2010, Communications in Applied Mathematics and Computational Science, Vol. 5, No. 1, p. 65-80, 2010, 5, 65

Gregory, A. L., Collins, M. L. M., Read, J. I., et al. 2019, MNRAS, 485, 2010

Hanuschik, R. W. 2003, A&A, 407, 1157

Hargreaves, J. C., Gilmore, G., Irwin, M. J., & Carter, D. 1994, MNRAS, 269, 957

Hausammann, L., Revaz, Y., & Jablonka, P. 2019, A&A, 624, A11

Hendricks, B., Koch, A., Walker, M., et al. 2014, A&A, 572, A82

Hermosa Muñoz, L., Taibi, S., Battaglia, G., et al. 2020, A&A, 634, A10

Hidalgo, S. L., Monelli, M., Aparicio, A., et al. 2013, ApJ, 778, 103

Ho, N., Geha, M., Tollerud, E. J., et al. 2015, ApJ, 798, 77

Holtzman, J. A., Afonso, C., & Dolphin, A. 2006, ApJS, 166, 534

Husser, T. O., Wende-von Berg, S., Dreizler, S., et al. 2013, A&A, 553, A6

Huxor, A. P., & Grebel, E. K. 2015, MNRAS, 453, 2653

Ibata, R. A., Lewis, G. F., McConnachie, A. W., et al. 2014, ApJ, 780, 128

Iorio, G., Fraternali, F., Nipoti, C., et al. 2017, MNRAS, 466, 4159

Iorio, G., Nipoti, C., Battaglia, G., & Sollima, A. 2019, MNRAS, 487, 5692

Jacobs, B. A., Tully, R. B., Rizzi, L., et al. 2011, AJ, 141, 106

Janesh, W., Morrison, H. L., Ma, Z., et al. 2016, ApJ, 816, 80

Jordi, K., Grebel, E. K., & Ammon, K. 2005, Astronomische Nachrichten, 326, 657

Kacharov, N., Battaglia, G., Rejkuba, M., et al. 2017, MNRAS, 466, 2006

Kamann, S., Wisotzki, L., & Roth, M. M. 2013, A&A, 549, A71

Karachentsev, I. D., Makarov, D. I., & Kaisina, E. I. 2013, AJ, 145, 101

Kazantzidis, S., Łokas, E. L., Callegari, S., Mayer, L., & Moustakas, L. A. 2011, ApJ, 726, 98

Kazantzidis, S., Łokas, E. L., & Mayer, L. 2013, ApJL, 764, L29

Kazantzidis, S., Mayer, L., Callegari, S., Dotti, M., & Moustakas, L. A. 2017, ApJL, 836, L13

Kirby, E. N., Bullock, J. S., Boylan-Kolchin, M., Kaplinghat, M., & Cohen, J. G. 2014, MNRAS, 439, 1015

Kirby, E. N., Cohen, J. G., & Bellazzini, M. 2012, ApJ, 751, 46

—. 2013a, ApJ, 768, 96

Kirby, E. N., Cohen, J. G., Guhathakurta, P., et al. 2013b, ApJ, 779, 102

Kirby, E. N., Gilbert, K. M., Escala, I., et al. 2020, AJ, 159, 46

Kirby, E. N., Lanfranchi, G. A., Simon, J. D., Cohen, J. G., & Guhathakurta, P. 2011, ApJ, 727, 78

Kirby, E. N., Rizzi, L., Held, E. V., et al. 2017, ApJ, 834, 9

Klypin, A., Kravtsov, A. V., Valenzuela, O., & Prada, F. 1999, ApJ, 522, 82

Koch, A., Grebel, E. K., Gilmore, G. F., et al. 2008, AJ, 135, 1580

Koch, A., Grebel, E. K., Wyse, R. F. G., et al. 2006, AJ, 131, 895

Koleva, M., Prugniel, P., Bouchard, A., & Wu, Y. 2009, A&A, 501, 1269

Koposov, S. E., Irwin, M., Belokurov, V., et al. 2014, Monthly Notices of the Royal Astronomical Society: Letters, 442, L85

Koposov, S. E., Gilmore, G., Walker, M. G., et al. 2011, ApJ, 736, 146

Koposov, S. E., Belokurov, V., Evans, N. W., et al. 2012, The Astrophysical Journal, 750, 80

Lake, G., & Skillman, E. D. 1989, AJ, 98, 1274

Lavery, R. J., & Mighell, K. J. 1992, AJ, 103, 81

Law, D. R., & Majewski, S. R. 2010, ApJ, 714, 229

Leaman, R., Venn, K. A., Brooks, A. M., et al. 2012, ApJ, 750, 33

—. 2013, ApJ, 767, 131

Leaman, R., Mendel, J. T., Wisnioski, E., et al. 2017, MNRAS, 472, 1879

Lee, H., Grebel, E. K., & Hodge, P. W. 2003, A&A, 401, 141

Lee, M. G., Aparicio, A., Tikonov, N., Byun, Y.-I., & Kim, E. 1999, AJ, 118, 853

Lemasle, B., Hill, V., Tolstoy, E., et al. 2012, A&A, 538, A100

Lemasle, B., de Boer, T. J. L., Hill, V., et al. 2014, A&A, 572, A88

Lewis, G. F., Ibata, R. A., Chapman, S. C., et al. 2007, MNRAS, 375, 1364

Li, T. S., Koposov, S. E., Zucker, D. B., et al. 2019, MNRAS, 490, 3508

Lokas, E. L., Ebrova, I., Del Pino, A., & Semczuk, M. 2014, MNRAS, 445, L6

Lozinskaya, T. A., Moiseev, A. V., & Podorvanyuk, N. Y. 2003, Astronomy Letters, 29, 77

Lux, H., Read, J. I., & Lake, G. 2010, MNRAS, 406, 2312

Marcolini, A., D'Ercole, A., Battaglia, G., & Gibson, B. K. 2008, MNRAS, 386, 2173

Martin, N. F., & Jin, S. 2010, ApJ, 721, 1333

Massari, D., Breddels, M. A., Helmi, A., et al. 2018, Nature Astronomy, 2, 156

Massari, D., Helmi, A., Mucciarelli, A., et al. 2020, A&A, 633, A36

Mateo, M. L. 1998, ARA&A, 36, 435

Mayer, L. 2010, Advances in Astronomy, 2010, 278434

McConnachie, A. W. 2012, AJ, 144, 4

McConnachie, A. W., Arimoto, N., Irwin, M., & Tolstoy, E. 2006, MNRAS, 373, 715

McConnachie, A. W., & Irwin, M. J. 2006, MNRAS, 365, 1263

McConnachie, A. W., Irwin, M. J., Ferguson, A. M. N., et al. 2005, MNRAS, 356, 979

McQuinn, K. B. W., Boyer, M. L., Mitchell, M. B., et al. 2017, ApJ, 834, 78

Menzies, J. W., Whitelock, P. A., & Feast, M. W. 2015, MNRAS, 452, 910

Miyoshi, T., & Chiba, M. 2020, arXiv e-prints, arXiv:2003.07006

Moiseev, A. V., & Lozinskaya, T. A. 2012, MNRAS, 423, 1831

Monelli, M., Gallart, C., Hidalgo, S. L., et al. 2010, ApJ, 722, 1864

Monelli, M., Bernard, E. J., Gallart, C., et al. 2012, MNRAS, 422, 89

Moore, B., Ghigna, S., Governato, F., et al. 1999, ApJL, 524, L19

Munari, U., Sordo, R., Castelli, F., & Zwitter, T. 2005, A&A, 442, 1127

Navarro, J. F., Frenk, C. S., & White, S. D. M. 1997, ApJ, 490, 493

Newberg, H. J., Yanny, B., & Willett, B. A. 2009, The Astrophysical Journal Letters, 700, L61

Noll, S., Kausch, W., Kimeswenger, S., et al. 2014, A&A, 567, A25

Oh, S.-H., de Blok, W. J. G., Brinks, E., Walter, F., & Kennicutt, Robert C., J. 2011, AJ, 141, 193

Oh, S.-H., Hunter, D. A., Brinks, E., et al. 2015, AJ, 149, 180

Oman, K. A., Navarro, J. F., Fattahi, A., et al. 2015, MNRAS, 452, 3650

Ordoñez, A. J., & Sarajedini, A. 2016, MNRAS, 455, 2163

Papastergis, E., Giovanelli, R., Haynes, M. P., & Shankar, F. 2015, A&A, 574, A113

Papastergis, E., & Shankar, F. 2016, A&A, 591, A58

Peñarrubia, J., Navarro, J. F., McConnachie, A. W., & Martin, N. F. 2009, ApJ, 698, 222

Peebles, P. J. E. 1982, ApJL, 263, L1

Planck Collaboration, Ade, P. A. R., Aghanim, N., et al. 2016, A&A, 594, A13

Pont, F., Zinn, R., Gallart, C., Hardy, E., & Winnick, R. 2004, AJ, 127, 840

Proxauf, B., da Silva, R., Kovtyukh, V. V., et al. 2018, A&A, 616, A82

Pucha, R., Carlin, J. L., Willman, B., et al. 2019, ApJ, 880, 104

Puls, J., Urbaneja, M. A., Venero, R., et al. 2005, A&A, 435, 669

Read, J. I., & Erkal, D. 2019, MNRAS, 487, 5799

Read, J. I., Iorio, G., Agertz, O., & Fraternali, F. 2016, MNRAS, 462, 3628

Revaz, Y., & Jablonka, P. 2018, A&A, 616, A96

Richardson, J. C., Irwin, M. J., McConnachie, A. W., et al. 2011, ApJ, 732, 76

Robin, A. C., Reylé, C., Derrière, S., & Picaud, S. 2003, A&A, 409, 523

Rocha, M., Peter, A. H. G., & Bullock, J. 2012, MNRAS, 425, 231

Roderick, T. A., Jerjen, H., Da Costa, G. S., & Mackey, A. D. 2016, MNRAS, 460, 30

Roth, M. M., Sandin, C., Kamann, S., et al. 2018, A&A, 618, A3

Rutledge, G. A., Hesser, J. E., & Stetson, P. B. 1997, PASP, 109, 907

Sales, L. V., Helmi, A., & Battaglia, G. 2010, Advances in Astronomy, 2010, 194345

Sales, L. V., Navarro, J. F., Abadi, M. G., & Steinmetz, M. 2007, MNRAS, 379, 1475

Sánchez-Blázquez, P., Peletier, R. F., Jiménez-Vicente, J., et al. 2006, MNRAS, 371, 703

Sandage, A. 1971, ApJ, 166, 13

Saviane, I., Held, E. V., & Piotto, G. 1996, A&A, 315, 40

Savino, A., Tolstoy, E., Salaris, M., Monelli, M., & de Boer, T. J. L. 2019, A&A, 630, A116

Sawala, T., Frenk, C. S., Fattahi, A., et al. 2016, MNRAS, 457, 1931

Schlafly, E. F., & Finkbeiner, D. P. 2011, ApJ, 737, 103

Schroyen, J., De Rijcke, S., Koleva, M., Cloet-Osselaer, A., & Vandenbroucke, B. 2013, MNRAS, 434, 888

Shapley, H. 1938, Harvard College Observatory Bulletin, 908, 1

Sibbons, L. F., Ryan, S. G., Irwin, M., & Napiwotzki, R. 2015, A&A, 573, A84

Silich, S., Lozinskaya, T., Moiseev, A., et al. 2006, A&A, 448, 123

Simon, J. D. 2018, ApJ, 863, 89

—. 2019, ARA&A, 57, 375

Simpson, C. M., Grand, R. J. J., Gómez, F. A., et al. 2018, MNRAS, 478, 548

Skilling, J. 2006, Bayesian Anal., 1, 833

Skillman, E. D., Tolstoy, E., Cole, A. A., et al. 2003, ApJ, 596, 253

Skillman, E. D., Hidalgo, S. L., Weisz, D. R., et al. 2014, ApJ, 786, 44

Slater, C. T., Bell, E. F., Schlafly, E. F., et al. 2013, The Astrophysical Journal, 762, 6

Spencer, M., Loebman, S., & Yoachim, P. 2014, ApJ, 788, 146

Spencer, M. E., Mateo, M., Walker, M. G., & Olszewski, E. W. 2017, ApJ, 836, 202

Starkenburg, E., Hill, V., Tolstoy, E., et al. 2010, A&A, 513, A34

Stilp, A. M., Dalcanton, J. J., Skillman, E., et al. 2013, ApJ, 773, 88

Strigari, L. E., Frenk, C. S., & White, S. D. M. 2018, ArXiv e-prints

Swan, J., Cole, A. A., Tolstoy, E., & Irwin, M. J. 2016, MNRAS, 456, 4315

Taibi, S., Battaglia, G., Rejkuba, M., et al. 2020, A&A, 635, A152

Taibi, S., Battaglia, G., Kacharov, N., et al. 2018, A&A, 618, A122

Tammann, G. A. 1994, in European Southern Observatory Conference and Workshop Proceedings, Vol. 49, European Southern Observatory Conference and Workshop Proceedings, 3

Tautvaišienė, G., Geisler, D., Wallerstein, G., et al. 2007, AJ, 134, 2318

Teyssier, M., Johnston, K. V., & Kuhlen, M. 2012, MNRAS, 426, 1808

Tollerud, E. J., Boylan-Kolchin, M., & Bullock, J. S. 2014, MNRAS, 440, 3511

Tollerud, E. J., Beaton, R. L., Geha, M. C., et al. 2012, ApJ, 752, 45

Tolstoy, E., Hill, V., & Tosi, M. 2009, ARA&A, 47, 371

Tolstoy, E., Irwin, M. J., Cole, A. A., et al. 2001, MNRAS, 327, 918

Tolstoy, E., Irwin, M. J., Helmi, A., et al. 2004, ApJL, 617, L119

Tonry, J., & Davis, M. 1979, AJ, 84, 1511

Udalski, A., Wyrzykowski, L., Pietrzynski, G., et al. 2001, AcA, 51, 221

Valdes, F., Gupta, R., Rose, J. A., Singh, H. P., & Bell, D. J. 2004, ApJS, 152, 251

van den Bergh, S. 1994, AJ, 107, 1328

—. 2000, The Galaxies of the Local Group

van Dokkum, P. G. 2001, PASP, 113, 1420

Vásquez, S., Zoccali, M., Hill, V., et al. 2015, A&A, 580, A121

Vazdekis, A., Koleva, M., Ricciardelli, E., Röck, B., & Falcón-Barroso, J. 2016, MNRAS, 463, 3409

Vazdekis, A., Ricciardelli, E., Cenarro, A. J., et al. 2012, MNRAS, 424, 157

Vinko, J., Remage Evans, N., Kiss, L. L., & Szabados, L. 1998, MNRAS, 296, 824

Walker, M. G. 2013, Dark Matter in the Galactic Dwarf Spheroidal Satellites, ed. T. D. Oswalt & G. Gilmore, Vol. 5, 1039

Walker, M. G., Mateo, M., & Olszewski, E. W. 2008, ApJL, 688, L75

—. 2009a, AJ, 137, 3100

Walker, M. G., Mateo, M., Olszewski, E. W., et al. 2006, AJ, 131, 2114

—. 2009b, ApJ, 704, 1274

Walker, M. G., Mateo, M., Olszewski, E. W., Sen, B., & Woodroofe, M. 2009c, AJ, 137, 3109

Walker, M. G., Olszewski, E. W., & Mateo, M. 2015, MNRAS, 448, 2717

Walker, M. G., & Peñarrubia, J. 2011, ApJ, 742, 20

Weilbacher, P. M., Streicher, O., Urrutia, T., et al. 2012, Society of Photo-Optical Instrumentation Engineers (SPIE) Conference Series, Vol. 8451, Design and capabilities of the MUSE data reduction software and pipeline, 84510B

Weisz, D. R., Dolphin, A. E., Skillman, E. D., et al. 2014, ApJ, 789, 147

—. 2015, ApJ, 804, 136

Wetzel, A. R., Deason, A. J., & Garrison-Kimmel, S. 2015, ApJ, 807, 49

Wetzel, A. R., Hopkins, P. F., Kim, J.-h., et al. 2016, ApJL, 827, L23

Wheeler, C., Pace, A. B., Bullock, J. S., et al. 2017, MNRAS, 465, 2420

White, S. D. M., & Rees, M. J. 1978, MNRAS, 183, 341

Whiting, A. B., Hau, G. K. T., & Irwin, M. 1999, AJ, 118, 2767

Willman, B., & Strader, J. 2012, AJ, 144, 76

Wolf, J., Martinez, G. D., Bullock, J. S., et al. 2010, MNRAS, 406, 1220

Wolf, M. 1906, MNRAS, 67, 91

Yam, W., Carlin, J. L., Newberg, H. J., et al. 2013, The Astrophysical Journal, 776, 133

Yanny, B., Newberg, H. J., Johnson, J. A., et al. 2009, The Astrophysical Journal, 700, 1282

Young, L. M., van Zee, L., Lo, K. Y., Dohm-Palmer, R. C., & Beierle, M. E. 2003, ApJ, 592, 111

Zhu, L., van de Ven, G., Watkins, L. L., & Posti, L. 2016, MNRAS, 463, 1117

Zoccali, M., Gonzalez, O. A., Vasquez, S., et al. 2014, A&A, 562, A66

Zolotov, A., Brooks, A. M., Willman, B., et al. 2012, ApJ, 761, 71

.

Acknowledgements

I'm pretty sure I couldn't have done this PhD all by myself. For this reason I would like to thank all the people who have accompanied me, even for a while, in this adventure.

First of all, I would like to thank my supervisor Giuseppina. Penso che non potrò mai ringraziarti abbastanza. Grazie per avermi dato l'opportunità di lavorare su questo progetto e per avermi supportato (e sopportato!) durante questi anni. La tua infinita pazienza, i tuoi consigli e la tua disponibilità sono stati un tesoro per me, mi hanno aiutato ad essere più indipendente sul lavoro e a pensare criticamente.

A big thank also goes to my tutor Carme and to all the members that have been part of the work group at the IAC during these years. I really enjoyed our meetings, in and out of the IAC, and the useful discussions. A special thanks to Matteo, for bringing me to observe at the INT and for being a big fan of all the sweets I brought from Sicily.

To those who have welcomed me on my stays abroad goes a huge thanks! To Marina, for giving me the precious opportunity to spend a month at ESO, it's been amazing to work with you and meet so many interesting people at the institute. I can certainly say the same to Ryan, for the valuable experience at the MPIA, to Martin, at the AIP, and to Michele, at INAF-Bologna.

Pero no solo he estado afuera, tambien he pasado mucho (pero mucho!) tiempo en mi escritorio del IAC. Asi que quería agradecerles a mis vecinos y amigos Raúl, Diego y Efsan con los que he convivido estos años, por todas las galletas compartidas y los consejos de programación, que sin ellos estaría todavía ahí sentado. Citaría tambien a Felipe, pero como quiso mudarse... es broma, amigo, ¡te agradezco más abajo! Y a mis otros compañeros de despacho, que sois muchos, ¡les agradezco por no haberme matado cada vez que me preparaba una capsulita de café!

Me gustaría tambien agradecer algunas personas del IAC que difícilmente

olvidaré: Eva, Gabi, Rosi y Juan Pedro. Gracias por todas las buenas conversaciones, el apoyo moral y por haber sido tan amables conmigo.

Al grupo de amigos que se ha formado gracias a este hilo común que es la astrofísica: sé que muchos estais lejos ya, pero espero que las distancias no nos separen demasiado y que volvamos a vernos pronto. A Simón, que es un grande, gracias por haberme cuidado cuando más lo necesitaba, por haberme vuelto famoso como "El ruedas" y por todos los buenos consejos. Y Zaira, ¿cuándo vamos a Islandia? Bueno, ¡supongo que también desde Canada se podrá ver el aurora! A Feli y Cris, gracias por ser tan buenos amigos y estimadores de la buena comida. Sé que ahí tienen muchos canguros pero si necesitan uno italiano para cuidar al Lucas me dicen :) Alla mia amica Alejandra, al mitico Andrés y la pequeña Julia, difícilmente olvidaré nuestras tardes de juegos y pelis, las clases magistrales de historia, y escuchar el mar desde vuestro balcón ¡les quiero mucho! A Paula, aunque nuestro trío de escalada con Camilo no ha durado mucho, nos ha vuelto más amigos y esto es lo que cuenta. A Franci y Rayco, estar en Heidelberg sin el calor que habéis traido desde Tenerife no hubiese sido lo mismo. A Marco y Vivi, gracias por haberme enseñado que significa enchilarse. Ahora, ¡a enseñárselo a la pequeña Ainhoa! A Simone, grazie per essere stato il nostro sherpa personale, y a Natacha, por ser mi compañera de verduras. Gracias a los dos por apreciar tanto los libros, no olvidaré aquel viaje al centro de la tierra que me habéis regalado. Y a todos los amigos que no he nombrado, "la mancanza non è assenza" como decimos en italiano, les va un gracias de corazón.

A Kuba y Camilo, no hay palabras suficientes para expresar lo mucho que les quiero y cuánto les admiro como personas. Kuba, y por supuesto Laura y Mar, cada vez que veo Gran Canaria pienso en ustedes, pronto les haré una sorpresa en Vespa. Camilo, gracias por sacarme siempre de mi zona de confort, y aunque a veces las cosas no van como nos esperábamos y acabamos lisiados, me tranquiliza saber que ayudándonos podemos sacar las cosas adelante.

Alla mia famiglia, a Papà, Mamma, Luisa e Calogero, grazie per esserci sempre e per sopportare le mie discussioni sul perché dovremmo essere tutti un po' più scientifici. Grazie veramente, senza di voi non ci sarei arrivato a finire questo dottorato.

A Paz, que de verdad me ha aguantado en lo mejor y lo peor de este doctorado, por apoyar mis ideas, por hacer la magnífica portada de esta tesis, por darme preciosos consejos, y por estar a mi lado siempre, no sabes lo agradecido que estoy por haberte encontrado en aquella winter school.

Y a los que ya no están, gracias por tu sonrisa Rebe, e grazie a te Nonno, per esserti interessato alle cose che mi appassionano e per avermi dimostrato che ci credevi veramente in me. L'abbiamo vinta questa corsa!